WGRID-49 GMLC Project Report

Understanding the Role of Short-Term Energy Storage and Large Motor Loads for Active Power Controls by Wind Power

August 2019

National Renewable Energy Laboratory
Idaho National Laboratory
Clemson University
General Electric
University of Denver

NREL/TP-5D00-72888

GRID MODERNIZATION LABORATORY CONSORTIUM
U.S. Department of Energy

NREL/TP-5D00-72888

NOTICE

This work was authored in part by the National Renewable Energy Laboratory, operated by Alliance for Sustainable Energy, LLC, for the U.S. Department of Energy (DOE) under Contract No. DE-AC36-08GO28308. Funding provided by U.S. Department of Energy Office of Energy Efficiency and Renewable Energy Wind Energy Technologies Office. The views expressed in the article do not necessarily represent the views of the DOE or the U.S. Government.

NREL/TP-5D00-72888

WGRID-49 GMLC Project Report

Understanding the Role of Short-Term Energy Storage and Large Motor Loads for Active Power Controls by Wind Power

V. Gevorgian, P. Koralewicz, H. Villegas, S. Shah, R. Wallen, D. Corbus, and J. Keller[1]
R. Hovsapian, M. Mohanpurkar, R. Kadavi, and M. Pnawar[2]
J. Leonard[3]
M. Richwine and N. Miller (retired)[4]
D. Gao, W. Yan, and W. Gao[5]

August 2019

[1] National Renewable Energy Laboratory.
[2] Idaho National Laboratory.
[3] Clemson University.
[4] GE Energy Consulting.
[5] University of Denver.

Abstract

The GMLC project is built upon the results of pioneering research funded by the U.S. Department of Energy (DOE) and conducted by the National Renewable Energy Laboratory (NREL)—in collaboration with the Electric Power Research Institute and the University of Colorado—on active power controls (APC) by wind power during 2013–2016 [1]. The studies detailed in the first APC by wind power project have shown tremendous promise for the potential for wind power plants to provide APC.

The goal of this project was to continue the previous work and develop and validate coordinated controls of APC by wind generation, short-term energy storage, and large industrial motor drives for providing various types of ancillary services to the grid and minimizing loading impacts on wind turbines (e.g., drivetrains), thereby reducing operation-and-maintenance (O&M) costs and subsequently reducing the cost of energy generated by wind power. This work used the $30 million, multiyear DOE investments and the unique characteristics of NREL's existing National Wind Technology Center test site, including a combination of multimegawatt utility-scale wind turbine generators, a 1-MW/1-MWh battery energy storage system (BESS), industrial variable-frequency motor drives, a 1-MW solar photovoltaic (PV) array, and a 7-MVA controllable grid interface. This combination of technologies allows for the optimization, testing, and demonstration of various types of APC by wind power in coordination with other generation sources (including regenerative loads) and energy storage to allow for enhancing or, in some cases, substituting the APC services by wind power and reducing impacts on wind turbine component life and thus increasing the availability and reliability of the power supply from wind.

This 3-year project (Fiscal Year 2016–2018) was aimed toward the full-scale demonstration of advanced coordinated APC by using the existing DOE assets at NREL in collaboration with Idaho National Laboratory (INL), Clemson University, and GE. This project addressed DOE goals in the area of Devices and Integrated Systems within the Grid Modernization Laboratory Consortium Foundational Topics 1–4, specifically by demonstrating how wind power can be tied to other technologies (energy storage and responsive regenerative loads, in this case) for enhanced APC services and reduced wind O&M costs. A major accomplishment of this project was developing and demonstrating controls for wind power and energy storage combined with solar PV power to operate as a hybrid renewable plant with elements of dispatchability and provision of all types of the existing essential and future advanced reliability services. Another major achievement was the development of an advanced and one-of-a-kind power-hardware-in-the-loop test system to evaluate the impacts of developed controls on power systems. Additionally, new methods of characterizing wind turbine and BESS inverters were developed and implemented, such as inverter impedance-measurement-based characterization, full-range dynamic reactive power capability characterization, and impedance-based characterization of power system frequency response. With participation of the INL team, the concept of a distributed platform based on the virtual interconnection of digital real-time simulators for using assets and investments from geographically distant research facilities has been demonstrated. This includes a Global Real-Time Super Laboratory demonstration involving NREL, INL, Sandia National Laboratories, and five universities in the United States and Europe.

Executive Summary

Introduction

This project validates advanced controls for active power from wind generation, short-term energy storage, and large industrial motor drives for various types of ancillary grid services. It also evaluates wind turbine loading impacts such as drivetrain loads. The National Renewable Energy Laboratory (NREL), in collaboration with the Electric Power Research Institute (EPRI) and the University of Colorado, demonstrated active power controls (APC) by wind power during a 2013–2016 DOE research project [1]. This 3-year project (FY 2016–2018) was aimed at conducting a full-scale demonstration of advanced coordinated grid controls by utilizing the existing DOE assets at NREL in collaboration with Idaho National Laboratory (INL), Clemson University, and GE. This project addressed DOE goals in the area of Devices and Integrated Systems within the GMLC Foundational Topics 1–4, specifically by demonstrating how wind power can be tied to other technologies (energy storage and responsive regenerative loads in this case) for enhanced services and optimized wind O&M costs.

This work utilized the $30 million, multiyear DOE investments and unique characteristics of NREL's existing NWTC grid-integration site, including a combination of multi-MW utility-scale wind turbine generators, 1-MW/1-MWh battery energy storage system (BESS), industrial variable-frequency motor drives (VFD), 1-MW solar PV array, and 7-MVA controllable grid interface (CGI). This combination of technologies allows for the optimization, testing, and demonstration of various types of advanced grid controls by wind power, in coordination with other generation sources including PV systems, variable-speed pumping, and energy storage.

Another achievement of this project was that it developed and demonstrated controls for wind power and energy storage—combined with solar PV power—for operation of hybrid renewable plants with elements of dispatchability and provision of all types of the existing essential and future advanced reliability services. This was achieved by developing an advanced, one-of-a-kind power-hardware-in-the-loop (PHIL) test system to evaluate impacts of developed controls on power systems. It resulted in implementing new methods for characterizing wind turbine and BESS inverters, such as inverter impedance measurement–based characterization, full-range dynamic reactive power capability characterization, and impedance-based characterization of power system frequency response. With participation from the INL team, the concept of a distributed platform based on virtual interconnection of real-time digital simulators (RTDS) for utilizing assets and investments from geographically distant research facilities was demonstrated. This included a real-time Super Laboratory demonstration involving NREL, INL, Sandia National Laboratories, and five universities in the United States and Europe.

Description of Project Activities

A first-of-its kind multimegawatt grid simulator, the CGI was commissioned at the National Wind Technology Center (NWTC) at NREL in Boulder, Colorado, during 2013–2014. It became the central point of a testing infrastructure that enables electrical integration testing of various types of renewable energy sources (Figure ES-1). This system makes it possible to test devices in fully controllable conditions, including wind turbine nacelles in dynamometer buildings as well as devices operating on-site, including wind turbines, PV arrays, and energy storage systems.

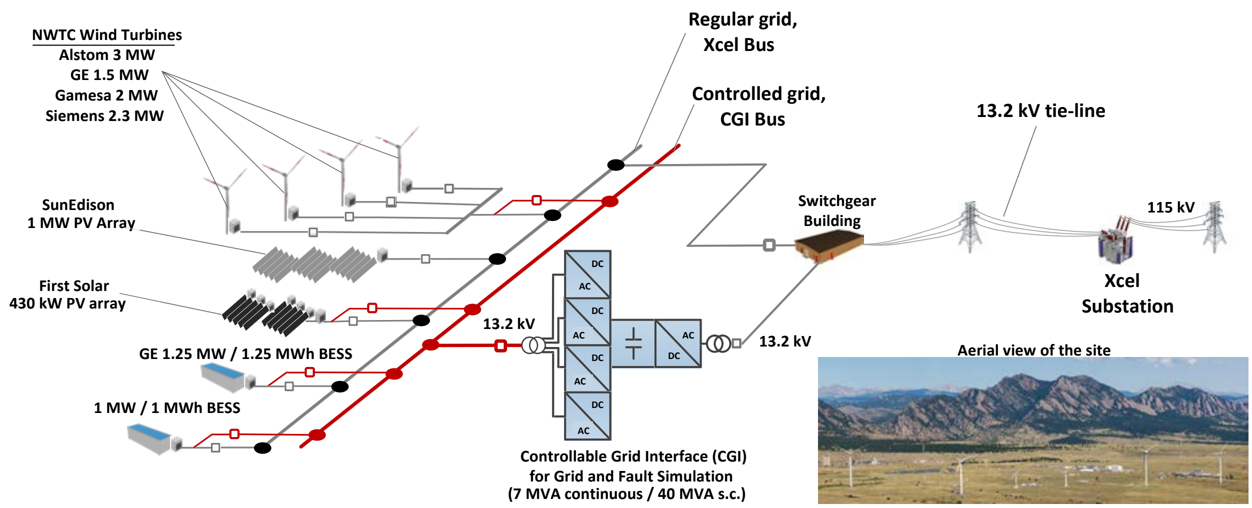

Figure ES-1. NWTC multimegawatt dual-bus validation platform

The GE WindCONTROL system—a standard GE wind power plant (WPP) control system—was commissioned during Year 1 of this project. The WindCONTROL system communicates with each wind turbine generator (WTG) located in the WPP and is a closed-loop control system that reads the actual WPP electrical parameters (voltage, reactive power, megawatt output) at the point of interconnection (POI) , or location of current transformers (CT) and potential transformers (PT), used by the WindCONTROL system, and adjusts the individual WTG's parameters to affect the overall WPP parameters toward its set points.

The following turbine- and plant-level APCs have been commissioned and tested in both grid-connected and CGI-connected modes.

- WindINERTIA control—ability of a single turbine to provide inertial response
- Plant-level frequency droop control—ability of the plant to provide frequency droop response (tested in "plant-of-one" configuration)
- Plant-level APC—ability of the plant to follow an active power set point (tested in "plant-of-one" configuration)
- Plant-level reactive power/voltage/power factor control (tested in "plant-of-one" configuration).

In 2017, NREL acquired a 1-MW/1-MWh BESS from Renewable Energy Systems (RES) Americas based on a competitive procurement process. The purpose of the procurement was to own and continuously operate a utility-scale BESS at the NWTC site for research purposes and demonstrate various uses case for energy storage applications in the following combinations.

- Test the BESS as a system connected directly to the Xcel Energy electric grid.
- Test the BESS connected to the NREL CGI for grid and fault simulation.
- Test the BESS in combination with NWTC renewable generation sources, such as wind turbines and PV arrays, connected to the Xcel Energy grid.
- Test the BESS in combination with NWTC renewable generation sources connected to the CGI grid/fault simulator.

- Test the BESS as a grid-forming unit for islanded microgrid operation with NWTC renewable generation sources.

Wind Plant Inertia Response

The unique characteristics of the NWTC site—where utility-scale wind turbines are co-located with the CGI—allows for conducting repetitive tests under fully controlled conditions so response of the wind power to the same grid events can be tested under different wind-resource variability conditions. This capability is especially useful for testing inertial response by wind power. We used this CGI capability to test the ability of a GE 1.5-MW WTG to provide inertial response when exposed to the same frequency event so that the aggregated inertial response of much greater levels of wind generation under diverse wind-speed conditions could be evaluated. Results of one such experiment are shown Figure ES-2. The GE 1.5-MW generator was exposed to a real decline in frequency at a very high rate of change of frequency (ROCOF) (1 Hz/sec) emulated by the CGI on its 13.2-kV voltage bus. The same test was conducted 65 times at different wind-speed conditions, so the ability of the turbine to provide inertial response was verified for all portions of the power curve, as shown in Figure ES-2.

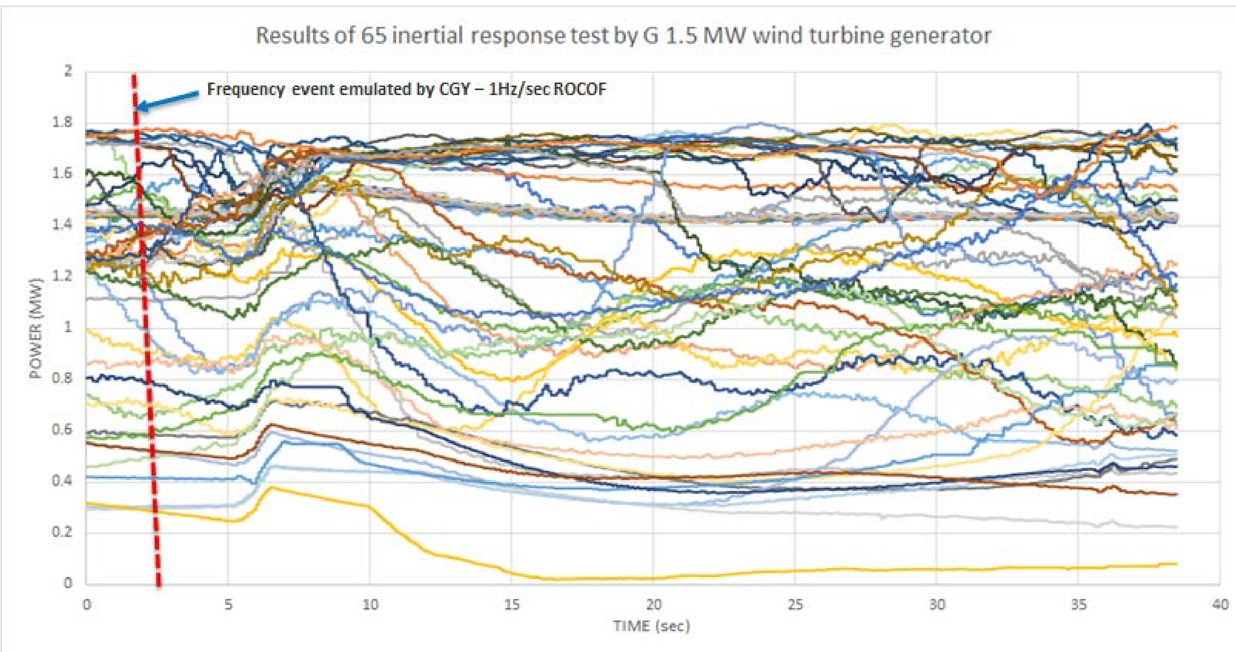

Figure ES-2. Results of inertia response tests

During data post-processing, the summation of all time-series produced an aggregate response that resembled the total inertial response of an approximate 100-MW WPP, as shown in Figure ES-3. In this case, the large WPP produced about 8 MW (or 10.7% of prefault power) of inertial response within 2 sec from the beginning of the event. Because of the rotor deceleration during tests at below-rated wind-speed conditions, there was some production loss after the event with a continued decline caused by changing wind conditions.

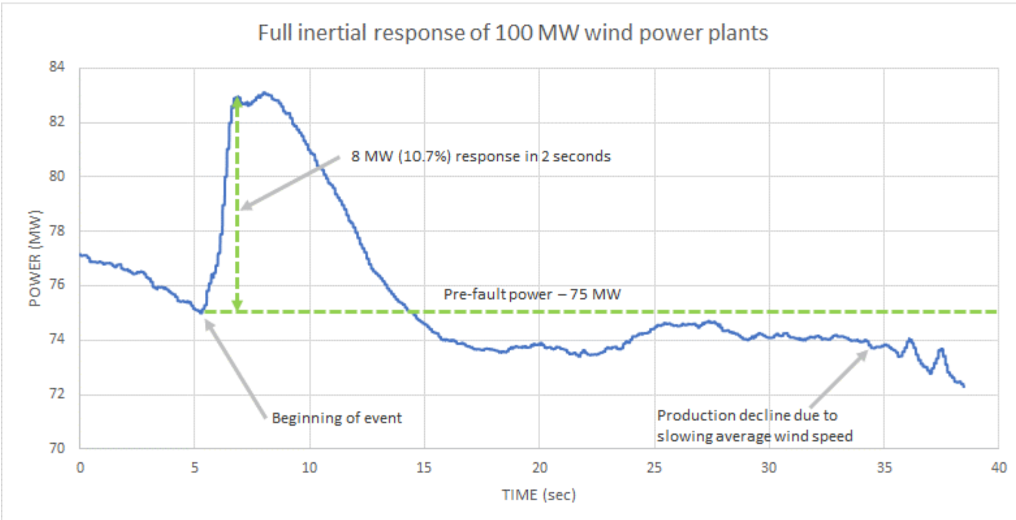

Figure ES-3. Wind inertia results aggregation

As part of this project, the NREL team developed an advanced PHIL platform using the CGI and RTDS systems. The configuration for a typical PHIL experiment setup is shown in Figure ES-4. The power side consists of various devices under test and a 7-MVA CGI acting as a low-latency controllable voltage source. Figure ES-4 shows a 1.5-MW wind turbine with a commercial WPP controller and the embedded capability to provide ancillary services. The RTDS is capable of the real-time execution of the generation and distribution models with a typical time step of 50 µs. A detailed description of the model used to conduct the tests described in this report is given in the main body content of this report. The voltage at a single node of the simulated model is monitored and commanded to the CGI. At the same time, the current at the POI is measured using Rogowski coils and fed back to the real-time digital simulator (RTDS).

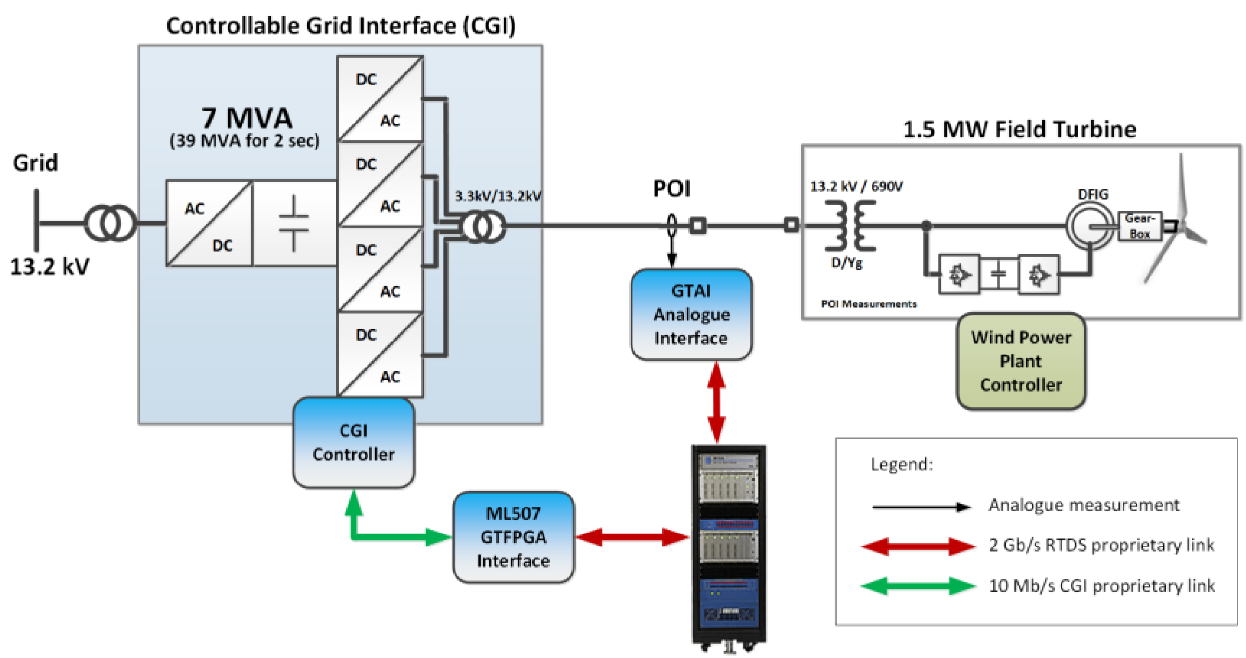

Figure ES-4. PHIL platform for wind turbine testing

Significant theoretical and experimental efforts were conducted by the NREL team in developing a PHIL interface between the CGI and RTDS because it was an important link for the successful implementation of this research project. This PHIL test setup using a fast (40-kHz) deterministic interface between the CGI and RTDS was used to conduct many experiments involving various types of active and reactive power control by wind generation, including inertial response, primary frequency response (PFR), wind participation in automatic generation control (AGC), reactive power and voltage control, and fault ride-through performance.

Impact on Wind Turbine Loads When Providing Advanced Grid Services

The NREL team conducted a number of experiments with the GE 1.5-MW wind turbine in CGI-connected mode under severe frequency events (a 1-Hz decline in frequency with a 1-Hz/s ROCOF setting). Some representative test results are shown in Figure 32 to Figure 35, with measured traces for electric frequency, turbine active power, high-speed shaft torque, and speed. During all inertial tests, we did not observe any significant impacts of inertial control on the gearbox loading. In fact, any high-speed shaft torque changes during inertial response did not seem to be any more "severe" than torque variations caused by wind-speed turbulence conditions at the NWTC. These results confirm theoretical findings from prior NREL research and demonstrate that the provision of inertial response by wind power is not going to become a cause of O&M cost increases if wind power is required to regularly provide inertial response in power systems.

Impacts of inertial response on drivetrain loading were measured using an instrumentation system that the NREL team installed on the GE 1.5-MW wind turbine gearbox and bearings as part of another research program supported by DOE at Argonne National Laboratory and NREL to examine the causes of white-etching cracks in wind turbine gearbox bearings. An instrumented Winergy 4410.4 gearbox was installed in the NWTC's GE 1.5-MW wind turbine and operated in 2018. The instrumentation included sensors to measure rotational speed in rotations per minute (rpm), bending moments, and torque on the gearbox's high-speed shaft and a slip ring to collect the mechanical loading data from the rotational frame. The mechanical loading data stream is GPS-synchronized with NREL's medium-voltage data-acquisition system so the mechanical and electrical time-series data can be aligned and analyzed during post-processing.

Inertia from Wind, Water Pumping, and BESS

The progressive incorporation of converter-based generation is displacing synchronously connected machines, which provide natural inertial response. The reduction of inertia constants negatively impacts the performance of power systems because relatively large load-generation unbalances can cause relatively large frequency deviations from nominal. Therefore, the risk of activating predefined schemes for underfrequency load-shedding during these disturbances increases, which is detrimental for the reliability of bulk power systems. To address this problem, the NREL team studied the symbiotic operation of controllable wind, pumping, and battery stations to provide synthetic inertia and droop response to prevent large frequency deviations. We derived relatively simple models of these assets that are helpful to simulate and understand their positive influence on the power system frequency response.

A singular component of the study is that it considers the impact of wake effects on the performance of wind turbines, because the upstream wind speed observed by each turbine influences its dynamic behavior when providing synthetic inertia. Many model simulations showed that wind, storage, and pumping stations can provide a significant amount of synthetic frequency response to power systems. These technologies were modeled with additional control loops that respond in proportion to the ROCOF. Hence, these assets can reliably emulate the inertial response of synchronous machines to frequency events. To compensate for the power changes that wind turbines can introduce when losing optimality after providing synthetic inertia, pumping stations are proposed to be furnished with droop-like frequency control strategies. This control strategy, in addition to synthetic inertia control loop, implies that pumped flow will be impacted momentarily, which might not be problematic—for example, for irrigation subsystems. To confirm the findings of this theoretical modeling task, we first conducted a number of experiments to characterize and measure inertial response characteristics on NREL's 2.5-MW VFD in conjunction with a wind turbine (Figure ES-5).

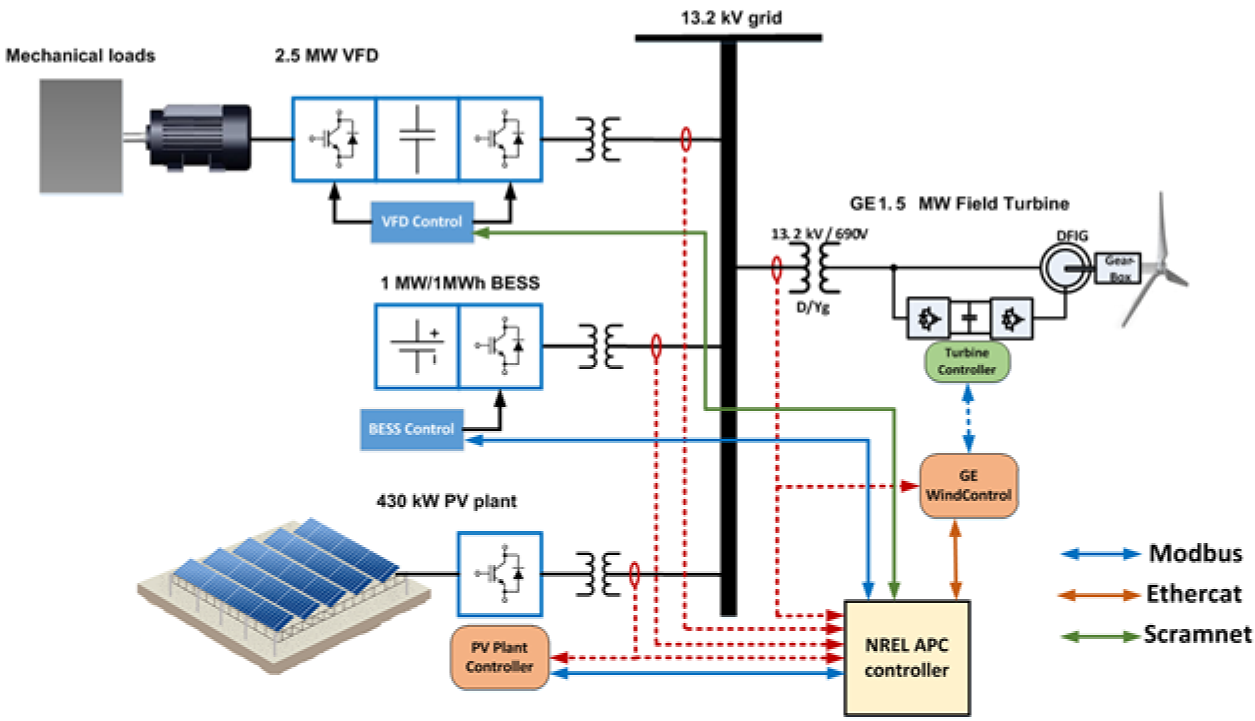

Figure ES-5. Components of NWTC test setup

After conducting a number of inertial response tests for the GE 1.5-MW WTG, it was determined that the average beginning time for the underproduction period resulting from wind-rotor deceleration was about 5–6 sec after the beginning of a frequency event. The VFD inertial controller was commanded to emulate its own inertial response by slowing down the motor about 5 sec after the beginning of the event. The results of one such test are shown in Figure ES-6. The inertial response of the WTG has a period of underproduction, which is depicted by the blue trace in the upper graph. The VFD controller commanded the rpm set points to modulate the exact shape of the underproduction profile with a 250-kW peak but with an opposite sign (Figure ES-6, lower graph). As a result, the aggregate power of the GE 1.5-MW WTG and 2.5-MW VFD did not have an underproduction period (orange trace in the upper graph of Figure ES-6).

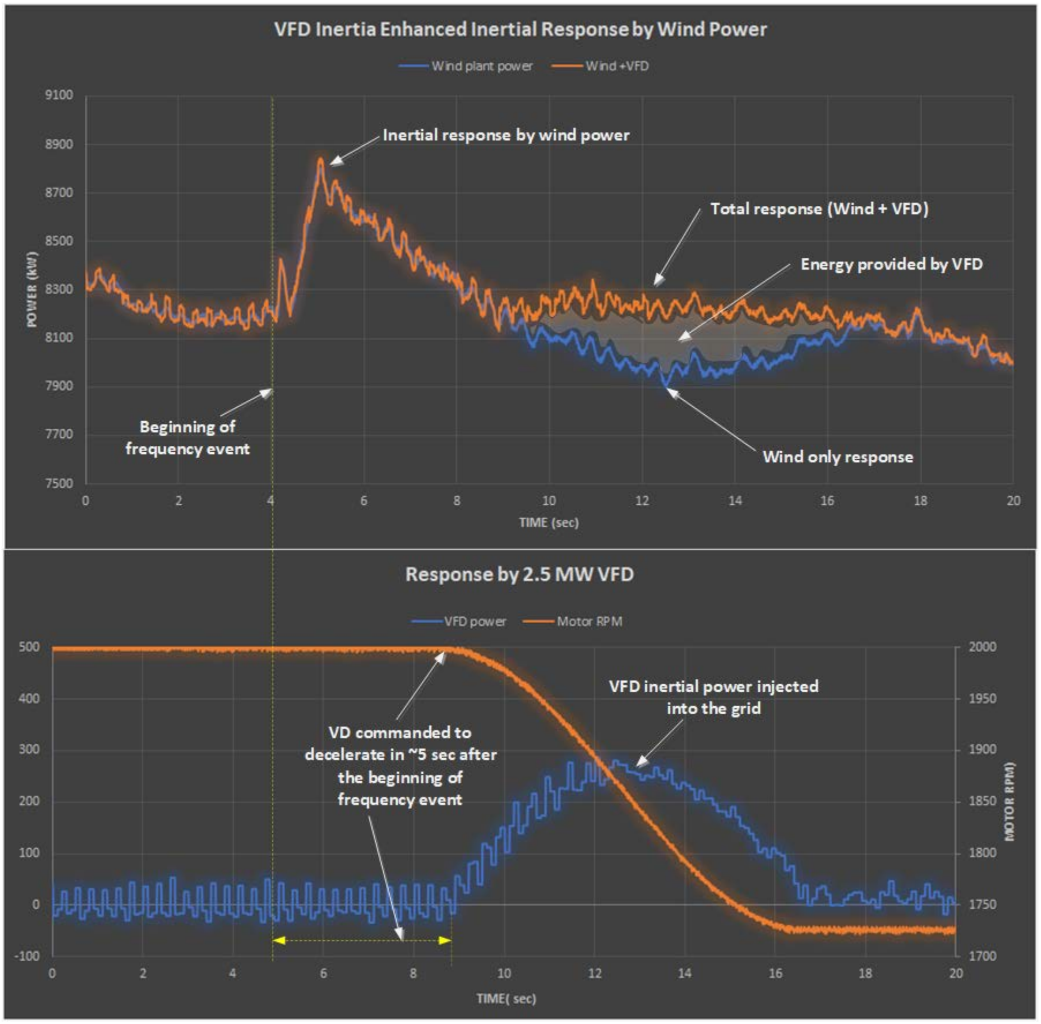

Figure ES-6. Results of wind inertia–enhancing test

Advanced Grid Services with Battery Storage

Fast-responsive BESS technologies have the potential to provide fully controllable, synthetic, inertia-like response to keep the frequency response metrics within the limits required by reliability standards. The focus of the BESS testing for the provision of inertial response is on the time interval of the first 10–15 sec after large system contingencies that cause a rapid decline in frequency. New battery controls were developed and implemented by the NREL team in a 1-MW/1-MWh BESS during this project. First, the battery controls were used in simulations in the PSCAD model to validate assumptions, then they were used in PHIL simulations using the CGI and RTDS interface with a real battery system and WTG. The results of the simulations for all use cases with their impacts on system frequency response after a 3% generation drop in the 9-bus Institute of Electrical and Electronics Engineers (IEEE) test case are shown in Figure ES-7. These scenarios included 30% of variable generation in total (20% wind and 10% solar PV), and the installed capacity of the BESS was about 3.1% of total system capacity. The BESS was dispatched to operate at zero active power, so it had headroom for full up- and down-regulation response after the event. The frequency nadir was the deepest for the base case when renewables did not provide any frequency response (Case 1). WindINERTIA alone helped improve the frequency nadir and shift it further right because of its impact on the initial ROCOF (Case 2). Even this improvement, however, did not guarantee avoiding underfrequency load-shedding (UFLS) because the frequency nadir was still in close proximity to typical UFLS thresholds (59.5 Hz for the Western Interconnection). A combination of WindINERTIA and droop control by wind power further significantly improved the frequency nadir (Case 3). This behavior is consistent with findings from a similar study for the whole Western Interconnection, shown in Gevorgian et al. [60]. Inertial response combined with an aggressive 1% droop response by the BESS (Case 4) produced a worse result than that of Case 3 (WindINERTIA only) because the installed capacity of the BESS was much less than it was for wind, therefore the impact by the BESS was smaller. The BESS, however, still produced a significant improvement compared to the base case. A combination of WindINERTIA and wind droop with the BESS inertial response (Case 5) further improved system performance. Case 6, with added BESS droop control, continued the trend, producing superior frequency response.

In Case 7, we combined droop control by curtailed PV generation with wind response. As shown in Figure 75, this provided marginal improvements compared to the previous case with the BESS. Finally, we tested the fast frequency response (FFR) control by the BESS with various time delays (Case 9, Case 10). The BESS also provided inertial response from the beginning of the event until it received an external set point command. In the case of a conservative 2-sec FFR delay (Case 8), the response of the system was worse than that of the less conservative 1-sec FFR delay (Case 9), and, of course, the response was the best for the optimistic (and likely not realistic) 0.1-sec FFR delay (Case 10).

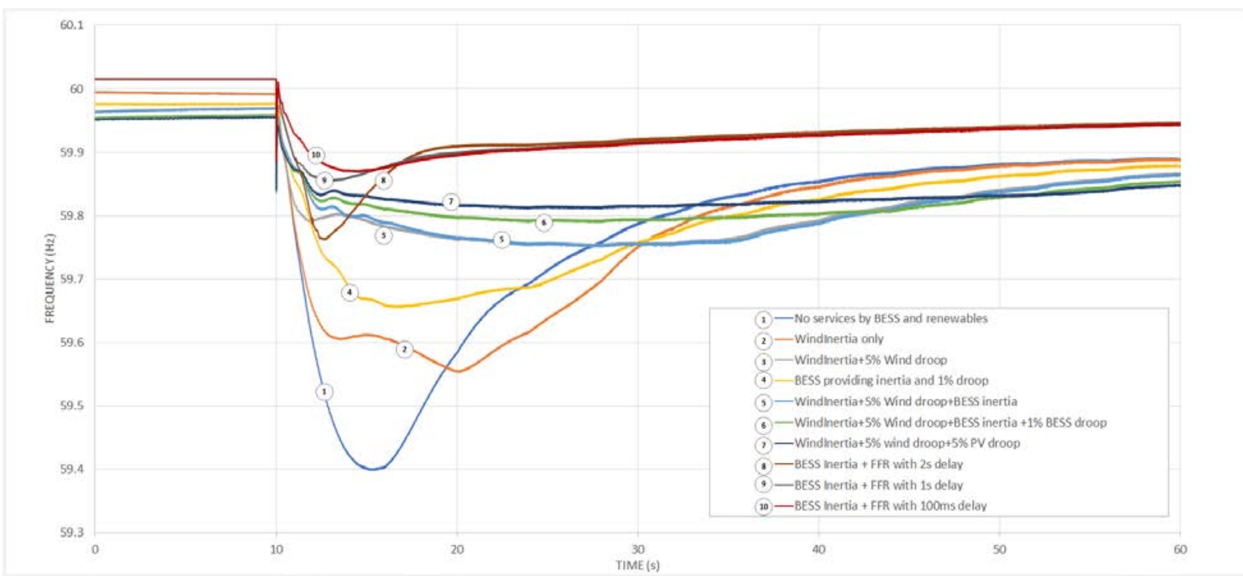

Figure ES-7. Comparison of frequency response for all simulation cases

Dispatchable Power Plant Controller

As part of project activities, the NREL team developed a controller for a dispatchable renewable power plant involving the NWTC's renewable wind and solar generation, and we integrated the BESS into this plant control. The plant control also is integrated with wind and solar resource forecasts and, along with full dispatchability, it can provide all types of existing and future evolving reliability services to the grid, including frequency regulation, primary frequency control, and inertial response. The main control panel of the dispatchable plant developed in the National Instruments LabVIEW environment is shown in Figure ES-8. The following control features for a dispatchable renewable plant were developed and implemented during this project.

- Dispatchable renewable plant operation (ability to operate at active and reactive power external set points received from system operator)

- Ramp limiting, variability smoothing, cloud-impact mitigation
- Provision of spinning reserve
- AGC functionality
- PFR (programmable droop control)
- FFR
- Inertial response (programmable synthetic inertia for a wide range of H constants emulated by the BESS)
- Reactive power/voltage control
- Advanced controls—The ability of the plant to modulate its output for the provision of power system oscillations damping services was tested
- Stacked services—The ability to provide several services at the same time
- Battery state-of-charge management controls

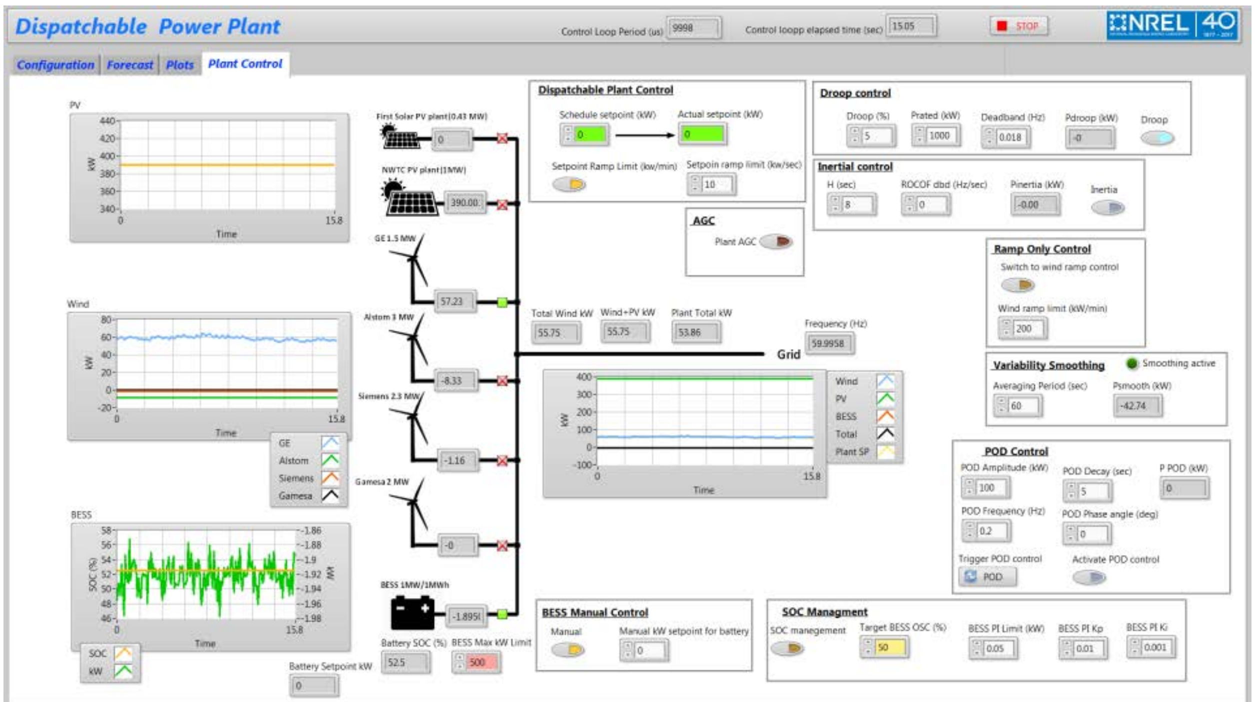

Figure ES-8. Main control panel of the NREL dispatchable power plant with BESS

Several new characterization methods and testing capabilities for wind power generation that also are applicable for any inverter-coupled technology were developed during the course of this project. In particular, in this work we presented an impedance-based approach for the characterization of power system frequency response. The impedance-based approach addresses the drawbacks of the existing frequency-response characterization methods and provides an analytical basis for the control development of the frequency support function in renewable generation and storage. The proposed method is demonstrated on a modified IEEE 9-bus system with 33% wind and PV penetration. The proposed method can estimate system inertia, PFR, and also the speed of primary frequency control in a noninvasive manner in the absence of a transient event. We also showed how the network impedance embeds the information on the power system frequency response behavior.

The NREL team also developed and validated a new automated test method allowing the use of the CGI for measuring the small- and large-signal impedance response of a multimegawatt-scale wind turbine, storage, and PV inverters. The CGI injects voltage perturbations into its 13.2-kV bus, and our developed measurement system captures the impedance response at different perturbation levels. An example of a measured positive sequence impedance response of a 1-MW BESS inverter from small-signal (0.5%) and large-signal (5%) voltage perturbations using the CGI is shown in Figure ES-9.

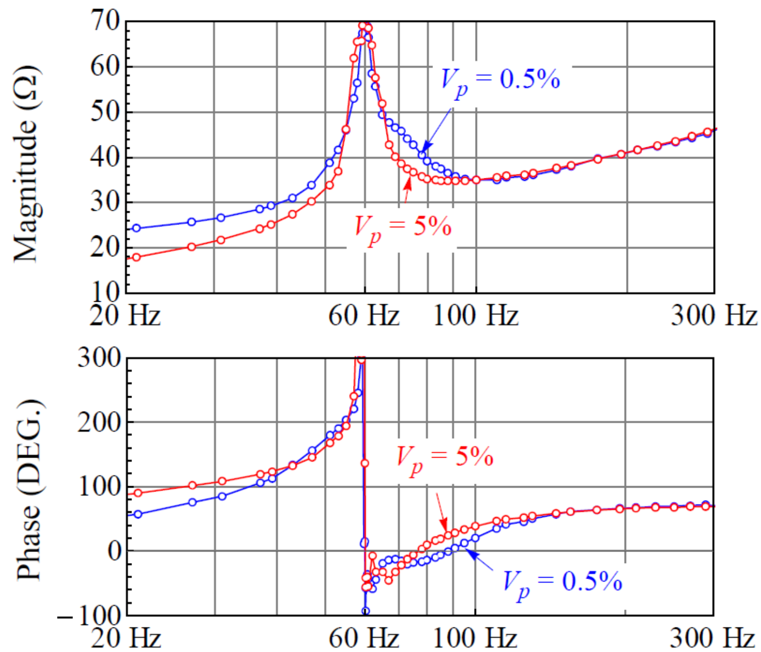

Figure ES-9. Measured impedance response of 1-MW BESS inverter

Additionally, we developed a new, unique, phasor-measurement unit–based test bed that can be used to validate wide-area stability control services by wind power and other technologies.

Distributed Real-Time Simulations and Laboratory-Laboratory PHIL Testing

Under this project, a new unique concept of distributed real-time simulations (RTS) and PHIL testing for wind power and other technologies was developed by the INL-NREL team. Real-time simulations increasingly are being used to understand the complex device- and system-level interactions in power grids. The evolution of power grids with the introduction of distributed-energy resources—including wind and solar—is rapid and complex. Wind and solar penetration levels are increasing at both the distribution and transmission levels of power grids. The increasing penetration levels of distributed energy resources presents certain challenges with grid integration, including a reduction of inertia and power system stability. Performing distributed RTS via the Internet can augment simulation capacity and leverage unique infrastructure that is dispersed in academia and research laboratories.

Performing geographically distributed RTS (GD RTS) between INL and the NWTC at NREL was one of the more technically challenging tasks of this project. It essentially involved performing a large power-systems simulation in real time with two digital real-time simulators (DRTS) that are located in different places—in this context, the simulators are located at INL and at NREL. A power systems model was partitioned to create two subsystems to enable the GD RTS. The power systems portion that was simulated at the NWTC connects with the GE 1.5-MW wind turbine with the proposed APC connected.

The subsystems simulated at INL connect to the hundreds of controller cards that model a WPP. The WPP is based on the characterization of the GE 1.5-MW WTG. More details are provided in Section 10. The significance of this simulation is the enhanced computation capability and enabling remote characterization and use of the NWTC.

Conclusions

Simulations and field tests using wind turbines with a BESS, VFD, and PV coupled with advanced controls showed that wind power inertial response, primary responses, and AGC participation can be significantly enhanced with the assistance of these technologies. Power-system dynamic studies show that wind generally can improve the reliability of the power system when providing primary frequency and synthetic inertial control. Coordinated control with other technologies allows notable improvements in system reliability in terms of frequency response. Control simulations showed that providing these responses will have a negligible effect on the structural loading of WTGs.

In particular, it was demonstrated that the symbiosis of frequency-responsive technologies can notably improve the frequency performance of power systems. In particular, wind, storage, and pumping stations can provide a significant amount of synthetic frequency response to power systems. These technologies have been furnished with control loops that respond in proportion to the ROCOF. Hence, these assets can reliably emulate the inertial response of synchronous machines to frequency events. To compensate for the power changes that wind turbines can introduce when losing optimality after providing synthetic inertia, pumping stations are proposed to be furnished with droop-like frequency control strategies. These control strategies, in addition to synthetic inertia control loop, imply that pumped flow will be impacted momentarily, which might not be problematic—for example, for irrigation subsystems.

In this work, the control constants that determine the synthetic inertia response for the considered assets originate from rational choices only. A rigorous framework to tune these constants—for example, as a function of displaced synchronous inertia—is a future research direction. A possible course could be to rely on system identification theory, because control constants could be identified to match a desired frequency trajectory in time. Another possibility is to rely on optimal control to minimize the perturbed pumped flow in pumping stations and the change in the performance coefficient in wind turbines but maintain power system frequency within desirable bounds. Another line of research pertains to ascertaining whether a particular penetration of wind, pumping, and battery capacity could be appropriate to compensate for the displaced synchronous inertia. In particular, it might be useful to elucidate the capability of these assets to replace synchronous inertia in a one-to-one manner.

We also demonstrated a use of a new impedance-based, noninvasive approach for the characterization of frequency response of a power system in real time in the absence of a transient event. It showed that the transfer function from the active power injected at the POI to the frequency at the same bus can be used to characterize the power system frequency response, and estimate system inertia, PFR, and the speed of the primary frequency control. The method essentially performs the fundamental frequency response adequacy evaluation in real time—a capability that has never existed within the energy industry. We also showed how the frequency response function is related with the network impedance. Such a relationship can support the development of grid-friendly controls for inverters and simultaneously optimize the inverter behavior for resonance or stability and frequency adequacy. Future work will use the proposed frequency response function for the frequency support control design using the BESS and renewable generation. An equivalent approach for the characterization of the voltage response of a power system also will be developed.

The following control features for a dispatchable renewable plant have been developed and successfully implemented during this project.

- Dispatchable renewable plant operation: Ability to operate at active and reactive power external set points received from the system operator)
- Ramp limiting, variability smoothing, cloud-impact mitigation
- Provision of spinning reserve
- AGC functionality
- PFR: Programmable droop control
- FFR
- Inertial response: Programmable synthetic inertia for a wide range of H constants emulated by the BESS
- Reactive power/voltage control
- Advanced controls: The ability of the plant to modulate its output for the provision of power system oscillations-damping services was tested
- Stacked services: The ability to provide several services at the same time
- Battery state-of-charge management controls

Additionally, new unique testing concepts and capabilities have been developed at the NWTC during the course of this project, including a phasor-measurement unit–based test bed for wide-area controls validation, and a novel method for the impedance characterization of converter-coupled generation using the CGI. The research under this project will continue through FY 2019 with the expectation of producing more interesting results and concept-validation activities.

Acknowledgments

The authors thank Charlton Clark and Jian Fu of the U.S. Department of Energy's Wind Energy Technologies Office for their continuous support of this project.

We also thank and acknowledge the substantial contributions to this work provided by the staff of the National Wind Technology Center at the National Renewable Energy Laboratory and the NREL Power Systems Engineering Center during the various stages of this project, as well as research staff from Idaho National Laboratory. Additionally, we thank Matthew Richwine and Nick Miller (recently retired) of GE Energy Consulting, and Jesse Leonard and Curtiss Fox of Duke Energy's eGRID Center at Clemson University's SCE&G Energy Innovation Center. We also thank the University of Denver team—led by Professor D. Gao—for its valuable contributions.

Acronyms and Abbreviations

AGC	automatic generation control
APC	active power control
BA	balancing authority
BESS	battery energy storage system
BMS	battery management system
CAISO	California Independent System Operator
CGI	controllable grid interface
CHIL	controller-hardware-in-the-loop
COE	cost of energy
CT	current transformer
DC	direct current
DOE	U.S. Department of Energy
DPI	Deep Packet Inspection
dq	direct-quadrature
DRTS	digital real-time simulator
DUT	device under test
EPRI	Electric Power Research Institute
FACTS	flexible AC transmission systems
FERC	Federal Energy Regulatory Commission
FFR	fast frequency response
FRO	frequency response obligations
GD RTS	geographically distributed real-time simulation
GE	General Electric
GW	gigawatts
HIL	hardware-in-the-loop
HVAC	high-voltage alternating current
HVDC	high-voltage direct current
HVRT	high-voltage ride-through
I2P	instantaneous-to-phasor
IA	interface algorithm
ICMP	Internet Control Message Protocol
IDS	intrusion detection systems
IEC	International Electrotechnical Commission
IEEE	Institute of Electrical and Electronics Engineers
IFRO	interconnection frequency response obligation
IN	Idaho National Laboratory
ITM	Ideal Transformer Model
kA	kiloamperes
kW	kilowatt
kNm	kilo-Newton-meter
LBNL	Lawrence Berkeley National Laboratory
LGIA	Large Generator Interconnection Agreement
LVRT	low-voltage ride-through
MHz	megahertz
ms	millisecond
MV	medium voltage
MVA	megavolt ampere
MVAR	megavolt-ampere reactive

MW	megawatt
NPC	neutral point clamped
NREL	National Renewable Energy Laboratory
NWTC	National Wind Technology Center
O&M	operation and maintenance
OpenADR	open automated demand response
p.u.	per-unit
PCC	point of common coupling
PFR	primary frequency response
PHIL	power-hardware-in-the-loop
POI	point of interconnection
PMU	phasor measurement unit
PT	potential transformer
PV	photovoltaic
QI	Quebec Interconnection
RMS	root mean square
ROCOF	rate of change of frequency
rpm	rotations per minute
RT	real time
RTAC	real-time automation controller
RTPESIL	Real-Time Power and Energy Systems Laboratory
RTDS	real-time digital simulator
RTS	real-time simulation
RTT	roundtrip time
SC	synchronous condenser
SOC	state of charge
SOE	state of energy
STATCOM	static synchronous compensator
THD	total harmonic distortion
UDP	user datagram protocol
UFLS	underfrequency load-shedding
VAR	volt-ampere reactive
VFD	variable-frequency drive
VSC	voltage source converter
WAN	wide area network
WECC	Western Electricity Coordinating Council
WPP	wind power plant
WTG	wind turbine generator

Contents

Figures

Tables

1.0 Introduction

This project is a continuation of pioneering research on active power controls (APC) by wind power, funded by the U.S. Department of Energy (DOE), and conducted during 2013–2016 by the National Renewable Energy Laboratory (NREL) in collaboration with the Electric Power Research Institute and the University of Colorado [1]. The studies detailed in the first APC by wind project have shown tremendous promise for the potential for wind power plants (WPPs) to provide APC. Close consideration of these responses will improve power system reliability. Careful design of the ancillary services markets will result in increased revenue for wind generators and reduced production costs for consumers when these services are provided. Precise design of control systems will result in responses that are in many ways superior to those of conventional thermal generation, and also results in very little effect on the loading and life of the wind turbine and its components. Meticulous engineering analysis can generate these benefits, thus there should be no reason that WPPs could not provide full automatic generation control (AGC) response to support the electric grid [1].

The goal of this project was to build on the previous work and develop and validate coordinated controls of active power by wind generation, short-term energy storage, and large industrial motor drives for providing various types of ancillary services to the grid and minimizing loading impacts, thereby reducing operation and maintenance costs (O&M) and subsequently reducing the cost of energy (COE) generated by wind power. This work used the $30 million, multiyear DOE investments and unique characteristics of NREL's existing National Wind Technology Center (NWTC) test site, including a combination of multimegawatt utility-scale wind turbine generators (WTGs), 1-MW/1-MWh battery energy storage system (BESS), industrial variable-frequency drives (VFD), a 1-MW solar photovoltaic (PV) array, and a 7-MVA controllable grid interface (CGI). This combination of technologies allows for the optimization, testing, and demonstration of various types of APC by wind power in coordination with other generation sources (including regenerative loads) and energy storage that allows for enhancing or, in some cases, substituting the APC services by wind power and reducing impacts on wind turbine component life and thus increasing the availability and reliability of the power supply from wind. This 3-year project (Fiscal Years 2016–2018) was aimed toward the full-scale demonstration of advanced coordinated APC by using the existing DOE assets at NREL in collaboration with Idaho National Laboratory (INL), Clemson University, and General Electric (GE). This project addressed DOE goals in the area of Devices and Integrated Systems within the Grid Modernization Laboratory Consortium Foundational Topics 1–4, specifically by demonstrating how wind power can be tied to other technologies (energy storage and responsive regenerative loads, in this case) for enhanced APC services and reduced wind O&M costs.

A major accomplishment of this project was developing and demonstrating controls for wind power and energy storage combined with solar PV power to operate as a hybrid renewable plant with elements of dispatchability and provision of all types of the existing essential and future advanced reliability services. Another major achievement was the development of an advanced, one-of-a-kind, power-hardware-in-the-loop (PHIL) test system to evaluate the impacts of developed controls on power systems. Additionally, new methods of characterizing wind turbine and battery energy storage system (BESS) inverters were developed and implemented, such as inverter impedance-measurement-based characterization, full-range dynamic reactive power capability characterization, and impedance-based characterization of power system frequency response. With participation of the INL team, the concept of a distributed platform based on the virtual interconnection of real-time dynamic simulators (RTDS) for using assets and investments from geographically distant research facilities was demonstrated as part of the Global Real-Time Superlaboratory [2].

The researched control concept can be adapted by different segments of the industry: power system operators, plant owners/operators, and various technology vendors (wind power, energy storage, and industrial VFD vendors). Such adoption will lay a foundation for establishing new market mechanisms that will provide additional revenue streams for wind power and industrial loads, and also will help reduce existing O&M costs for wind power, which are estimated to be on the order of $1.5–$2 billion annually. The control methods that were developed and tested under this project can be used to improve power system reliability.

Wind turbine generators are quite different from conventional steam, combustion, and hydro turbines. The APC response provided by wind power is different from the response from conventional plants, and it is essential that this response (especially in coordination with other technologies, such as energy storage and responsive loads) is analyzed and understood to support power system reliability under high penetration levels of wind power. The results of this work can be used to improve existing designs as well as provide input to new ancillary service market designs that allow wind to earn additional revenue and reduce overall costs to consumers. This will increase the economic competitiveness of wind power. The results of this work are expected to benefit various groups of stakeholders, including WTG vendors, WPP operators, utilities, transmission system operators, and reliability organizations.

The work conducted under this project helped further the development of a new, one-of-a-kind, world-class DOE capability for testing multitechnology controls at multimegawatt scales for future research and demonstration in the areas of smart grids, microgrids, and advanced energy management systems.

2.0 Description of NWTC Test and Validation Platform

2.1 Description of NWTC Site

Power systems throughout the world are undergoing a significant transition from those that are based on large, centralized power plants to more distributed systems that have large numbers of generation units based on renewable energy sources [1]. Integrating high levels of power converter–coupled variable renewable energy resources (wind and solar) into an electric grid requires significant changes to electricity system planning and operations to ensure continued reliability [3]. It therefore is important to better understand how power converter–based renewable energy systems interact with the grid, and how to use the advanced grid-friendly controls by renewables to maintain or enhance grid reliability. Several national and international standards and test procedures ensure that variable renewable technologies can meet the evolving reliability and controllability requirements of grid operators.

Manufacturers, developers, and power plant operators of renewable energy systems should perform a series of tests to demonstrate plant operation under grid disturbances and the systems' abilities to provide various types of ancillary services to enhance reliability. For instance, the latest edition of International Electrotechnical Commission (IEC) Standard 61400-21 for power-quality testing of utility-scale WTGs provides procedures for low-voltage ride-through (LVRT), active power and frequency responsive controls, and reactive power controls [5]. The newer, in-process edition of the same standard will be setting test requirements for an even greater scope of advanced controls, such as inertial response by WTGs. The performance of converter-coupled generation requires verification at all power ranges under realistic operating conditions. In conventional field-testing, the device under test (DUT) is connected to a specific grid for long periods; however, this does not guarantee that the DUT will experience the entire range of possible grid conditions—for example, frequency variations, balanced or unbalanced voltage fault conditions for testing LVRT or high-voltage ride-through (HVRT) controls—and changing grid characteristics, such as the inertia of the grid and stronger or weaker interconnections.

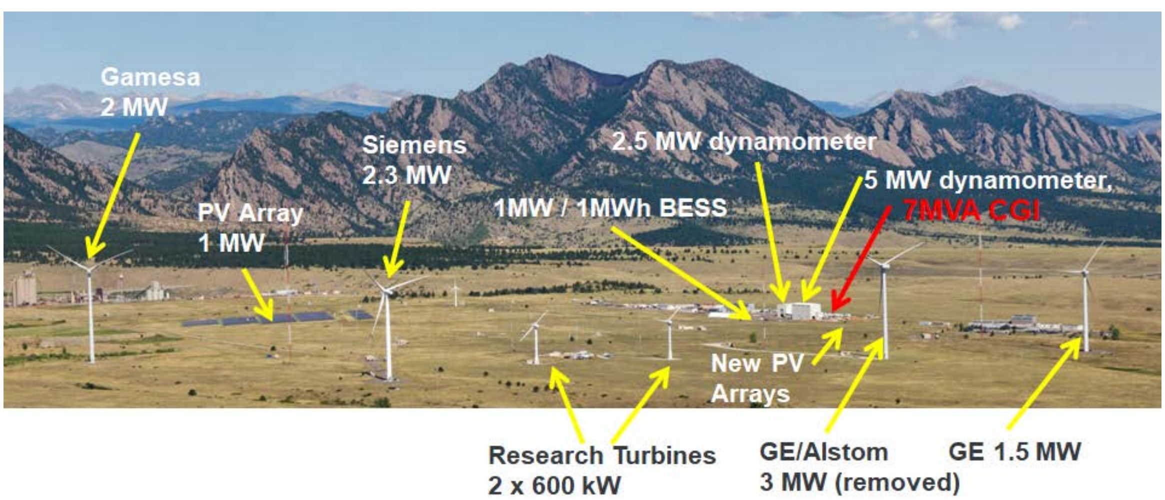

Figure 1. Aerial view of NWTC test site[1]

[1] Please note that the GE/Alstom 3-MW wind turbine was removed from the NWTC site while this report was in development.

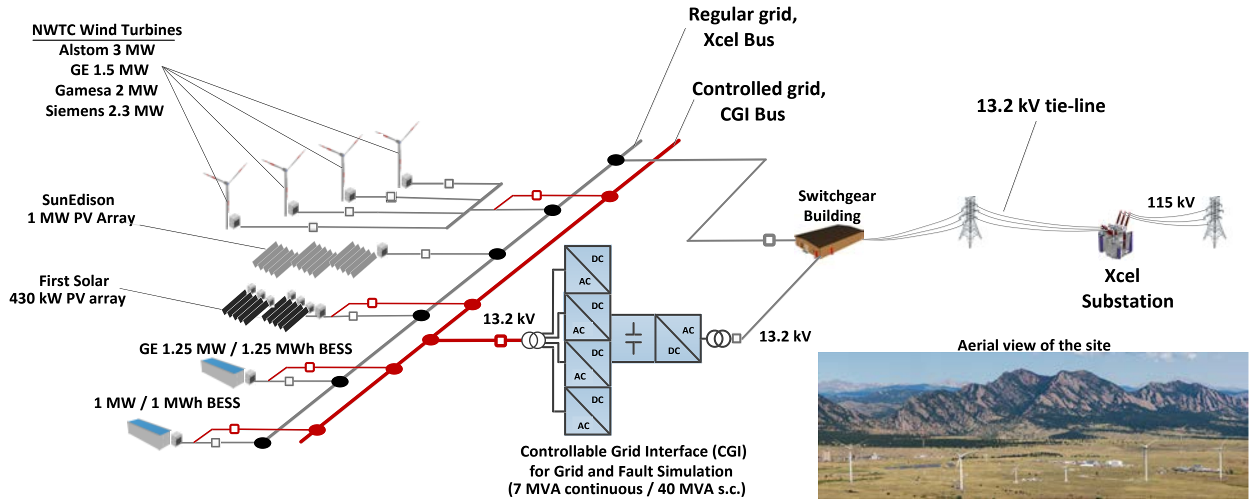

Figure 2. NWTC multi-MW validation platform

The first multimegawatt grid simulator of this kind, the CGI was commissioned at the NWTC at NREL in Boulder, Colorado, during 2013–2014 [6]. It became the central point of a testing infrastructure that enables the electrical integration testing of various types of renewable energy sources (*see* Figure 1, and Figure 2). This system makes it possible to test devices in fully controllable conditions, including wind turbine nacelles in dynamometer buildings, as well as devices operating on-site: wind turbines, photovoltaic arrays, and energy-storage systems. The first results from wind power–related tests conducted with NREL's CGI were demonstrated in Zeni et al. (2015)[7] and Zeni et al. (2016)[8], which showed examples of experiments to validate dynamic models of WTGs and test advanced active power controls by wind power. More in-depth review of the grid simulator's functionality, controls, and emulation of voltage fault and frequency fluctuation conditions that occur in real power systems is described elsewhere in this report.

2.2 Controllable Grid Interface Description

The unit power capacities of renewable energy systems are increasing. This imposes certain challenges for testing infrastructure because test apparatuses often must meet more-stringent standards than the DUT itself. The continuous power rating of the CGI is 7 MVA. It includes a 9-MVA active line-side rectifier unit that allows power to flow from the DUT to the steady grid with a controllable power factor. The test-side converter faces many challenges, however, because it must provide grid simulator functionality and maintain full controllability under transient conditions that can exist at the point of common coupling (PCC). Transient overcurrent capability is one important feature of the grid simulator because certain types of generators under test can inject high short-circuit currents that exceed their nominal rating multiple times [9]. For example, a wind turbine that uses a doubly fed induction generator topology can produce currents up to 10 times stronger than its nominal rating under zero-voltage conditions for short periods [42]. Therefore, substantial short-term overcurrent capacity is needed by the grid simulator to maintain stable operation during such transient events. For this purpose, the CGI topology is based on four 3.3-kV medium-voltage, neutral-point-clamped (NPC) inverter units that are normally used to drive industrial-grade motors, and a custom step-up transformer to produce 13.2 kV on the test article terminals, as shown in Figure 3**.** Under continuous 7-MVA) operation, the amplitude of the nominal continuous current at the inverter side of the transformer is at 500 A. To allow for a significant overcurrent capability, the selected medium-voltage NPC inverters are based on integrated gate-commutated thyristor devices. Their maximum current is 2.7 kiloamperes (kA), which allows for a 540% overcurrent margin assuming a 7-MVA DUT. The custom transformer is designed to match DUTs with various nominal voltages by using multiple transformer taps. The transformer is rated for 7-MVA continuous operation and 560%

short-term overcurrent operation to handle short-circuit currents that can be produced by the test articles. The special configuration of the transformer allows synthesizing 17-level low-distortion voltage waveforms by interleaving three-level phase voltages. Main technical specifications architecture of CGI is shown in Figure 3.

For a given semiconductor device, the power capacity can be increased by decreasing the switching frequency, which in turn can lead to voltage-quality degradation, which normally is measured as total harmonic distortion (THD). Normally, the desired THD level in power converters can be maintained by a harmonic filter; however, filters also decrease the dynamic range of operation. To maintain dynamic performance as fast as possible, the CGI uses advanced modulation-control methods rather than a hardware filter. Thus, a balance is found among three conflicting requirements of power conversion: multimegawatt power ratings, sub-1% THD, and extremely fast response times, typically smaller than 1 ms.

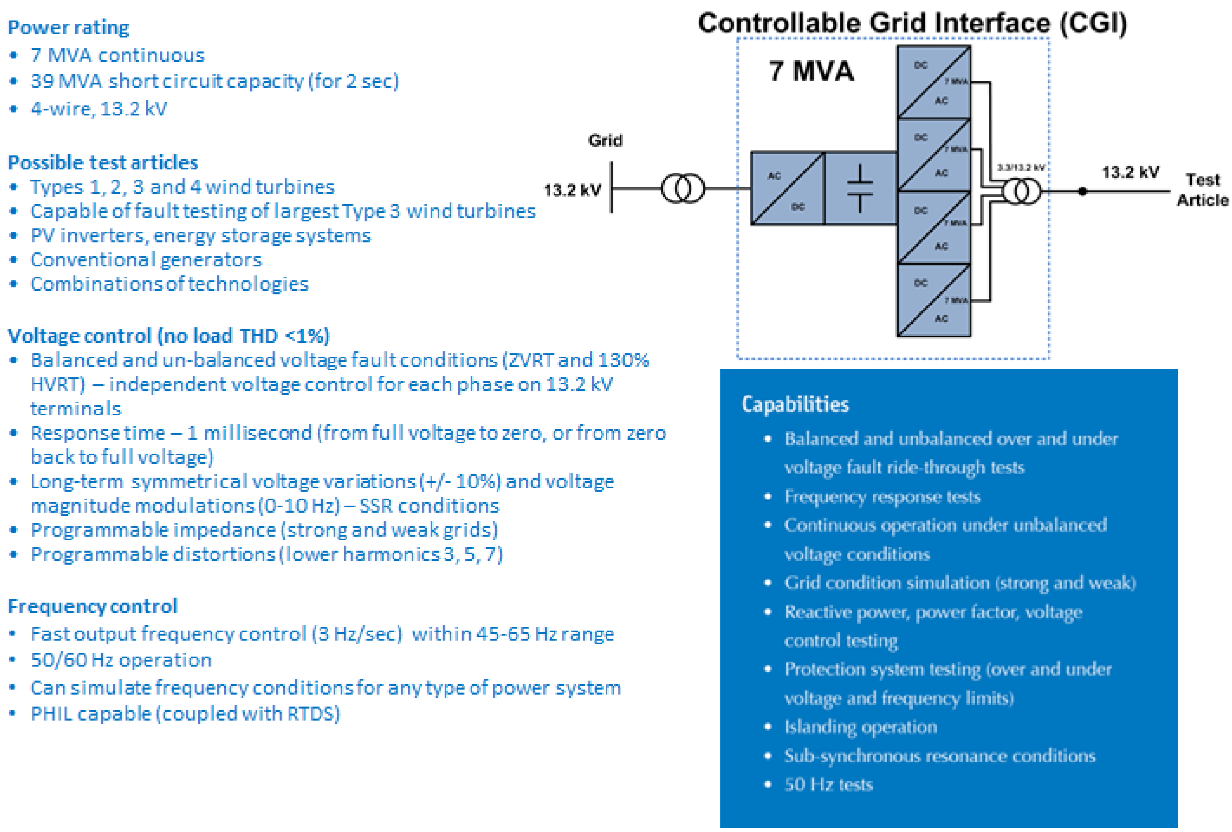

Figure 3. National Wind Technology Center CGI—main characteristics

2.3 Commissioning of General Electric WindCONTROL

The GE WindCONTROL system (standard GE WPP control system) was commissioned during year 1 of this project. The WindCONTROL system communicates with each WTG located in the WPP and is a closed-loop control system that reads the actual WPP electrical parameters (voltage, reactive power, MW output) at the POI (or the location of CTs and PTs used by WindCONTROL System) and adjusts the individual WTG's parameters to affect the overall WPP parameters toward its set points.

The following turbine and plant-level active power controls have been commissioned and tested in both grid- and CGI-connected modes.

- WindINERTIA control—ability of a single turbine to provide inertial response
- Plant-level frequency droop control—ability of the plant to provide frequency droop response (tested in "plant-of-one" configuration)
- Plant-level active power control—ability of the plant to follow active power set point (tested in "plant-of-one" configuration)
- Plant-level reactive power/voltage/power factor control (tested in "plant-of-one" configuration)
- WindINERTIA control (diagram shown in Figure 4) has been tested under different wind-speed conditions with CGI emulating a frequency event at the turbine's medium voltage (MV) terminals. Results of WindINERTIA testing during commissioning stage are shown in Figure 5.

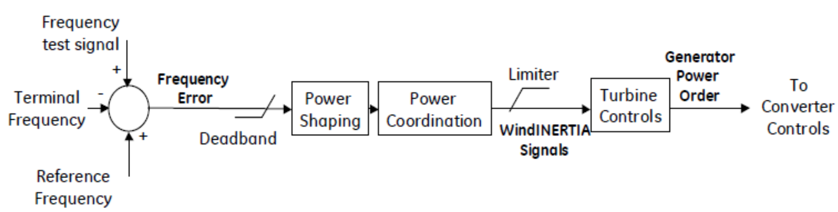

Figure 4. Functional diagram of WindINERTIA control (source: GE)

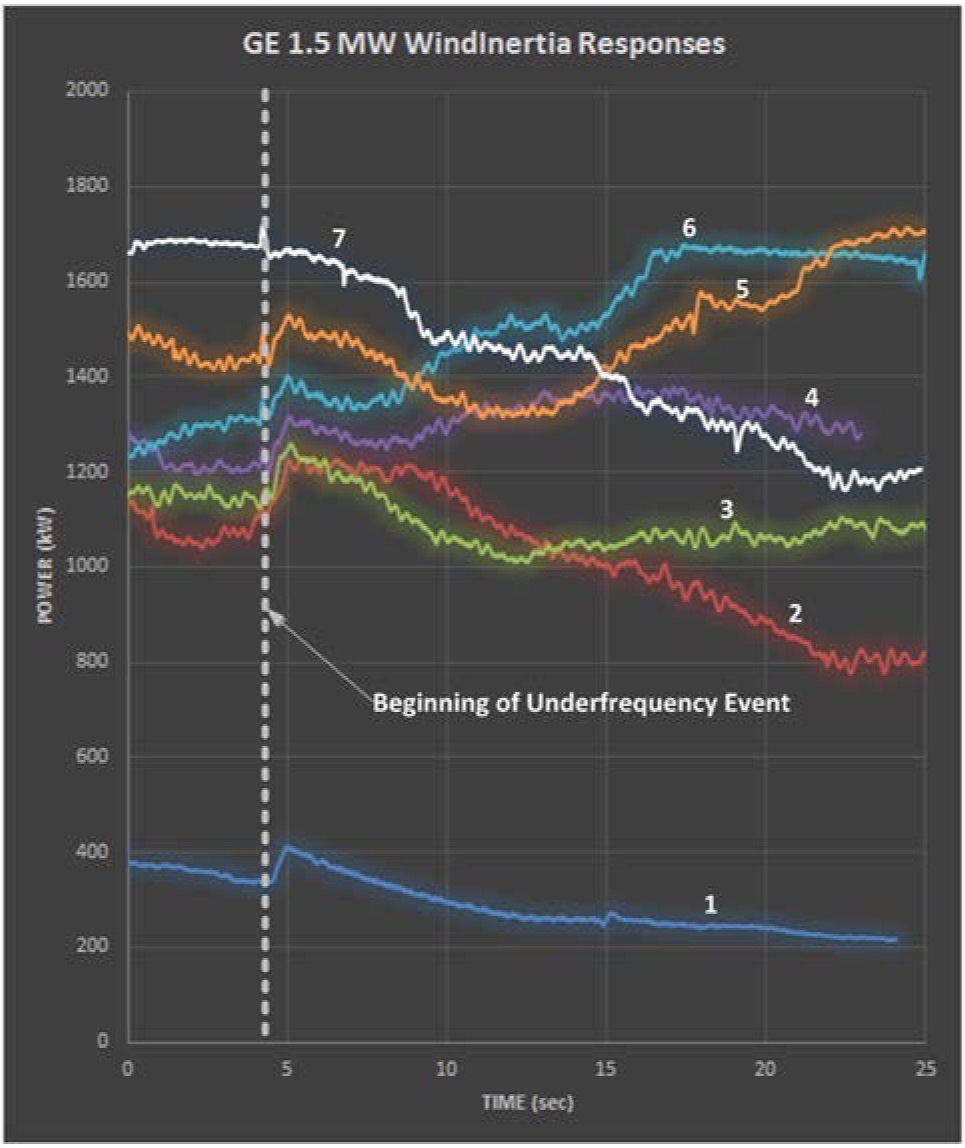

Figure 5. Initial results of WindINERTIA tests at different wind-speed conditions

Inertial control provides an inertial response capability for wind turbines for large underfrequency events. The response is provided by temporarily increasing the power output of the wind turbines in the range from 5% to 10% of the rated turbine power by extracting the inertial energy stored in the rotating masses. This short, quick power injection can benefit the grid by essentially limiting the rate of change of frequency (ROCOF) at the inception of the load/generation imbalance event. Figure 5 shows the measured frequency response of a 1.5-MW WTG triggered by the same frequency profile under different and highly turbulent wind-speed conditions. The profile of each individual response is highly dependent on the initial turbine conditions (wind speed, power level, rotational speed) at the beginning of the underfrequency event and also the wind speed during the event. As shown in Figure 5, the turbine under test consistently produced a short-term increase in power production at different power levels (traces 1–6). Subsequently, the turbine's production decreased briefly because of the wind-rotor deceleration. The level of the decline and the speed of the recovery, however, depend on the wind-speed conditions. During Test 7, the turbine produced no inertial response because the inverter already was at its thermal limit.

The control diagram of frequency droop function implemented in WindCONTROL is shown in Figure 6. It sets a proportional wind-plant response to grid frequency variations. Two different grid frequency response characteristics can be programmed into the WindCONTROL system. The parameters for setting the frequency droop characteristic are shown in Figure 7, with the exception of the hysteresis setting.

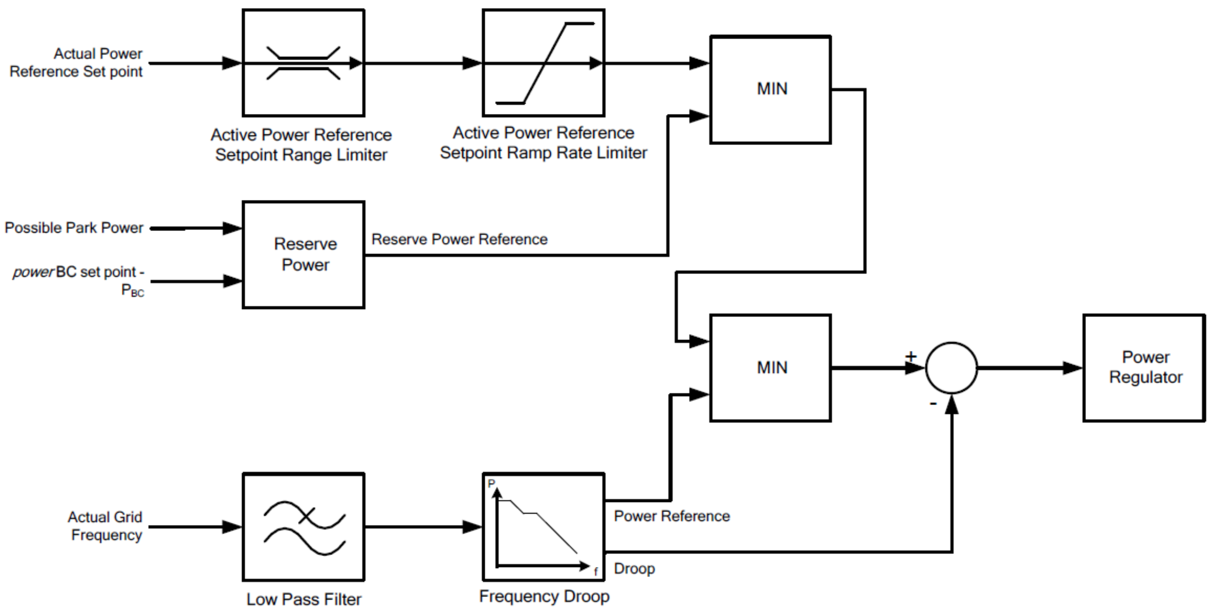

Figure 6. Frequency droop control implemented in GE-WindCONTROL (source: GE)

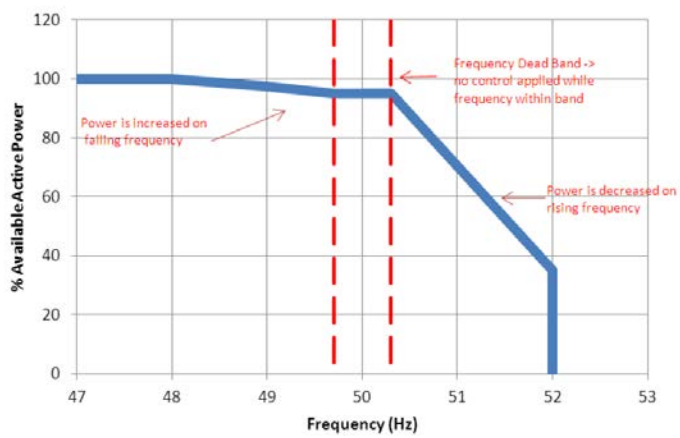

Figure 7. Power-frequency droop settings (source: GE)

The droop control function testing started in early October 2016, after wind conditions improved at NWTC. Some preliminary results of testing with CGI are shown in Figure 8 CGI was set to emulate up and down step changes in frequency of 13.2 kV voltage as shown in Figure 8. So far, the turbine was able to produce droop response for overfrequency events. For underfrequency events, the turbine produced inertial responses only and did not produce droop response. NREL has worked with the GE team to resolve this issue, so by the end of 2017 the droop response for underfrequency events was demonstrated as well.

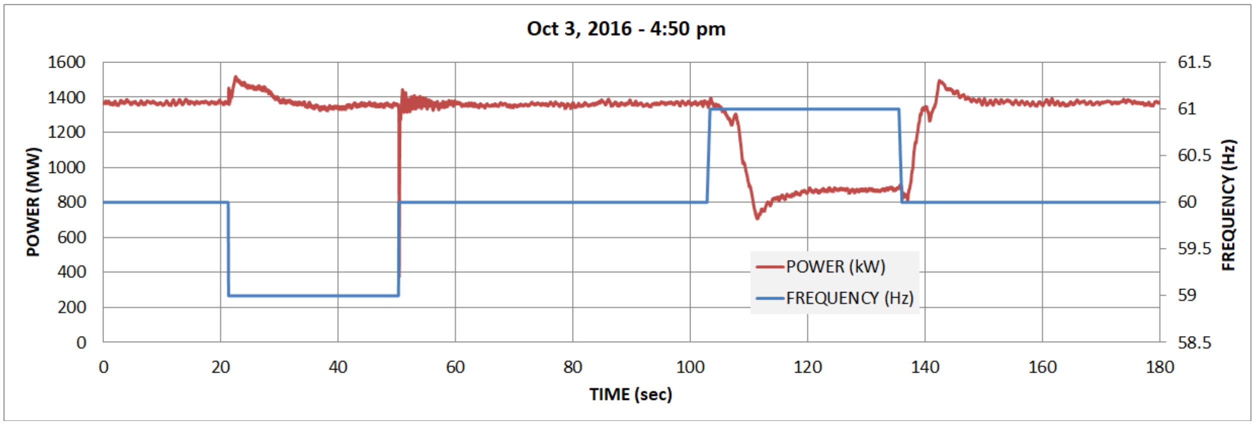

Figure 8. Results of 5% droop test

Results of the WTG providing 3% droop in response to real frequency event measured by NREL in Colorado are shown in Figure 9. This real frequency time series data was emulated at CGI terminals, so the turbine response can be measured as if it was operating in the field was and exposed the same frequency event in real time. The data shown in Figure 9 were collected at 25-Hz sampling frequency; this explains the scatter in measured droop as shown in right x-y graph. The figure shows that the turbine provides linear droop response during this event, and the turbine returns to normal operation with 15% headroom after frequency returns to normal prefault level.

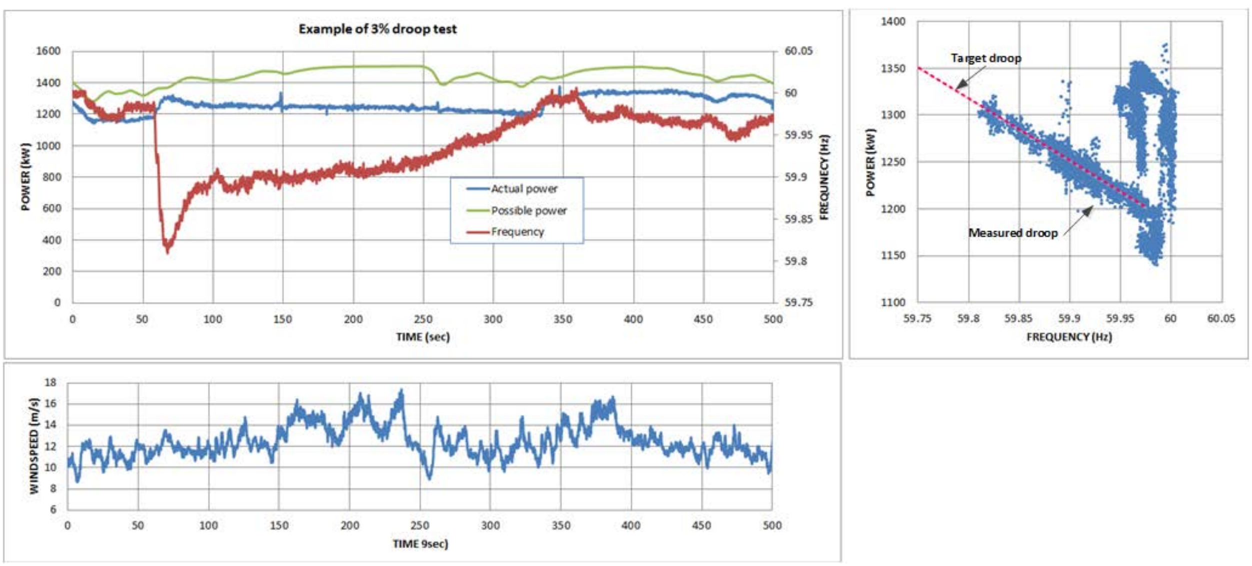

Figure 9. Results of 3% droop test

The control diagram for active power set point operation is shown in Figure 10. The active power regulator in the WindCONTROL system receives active power measurements by means of a three-phase set of potential and current transformers located in the wind plant substation or another location on the electric utility system where the WindCONTROL system is assigned to regulate the system active power. The voltage from the potential and current transformers is connected to the grid-monitoring device in the WindCONTROL enclosure which then sends the calculated active power information to the WindCONTROL sequence processing control unit. The measured active power from the three-phase set of potential and current transformers is subtracted from power reference to produce an active power error signal as shown in Figure 10. A feed-forward term is included as well as a compensation term that includes the power losses of the collector system and the turbine unit step-up transformer. The output of the integrator block is clamped to +/- 10% of the rated power of the online turbines.

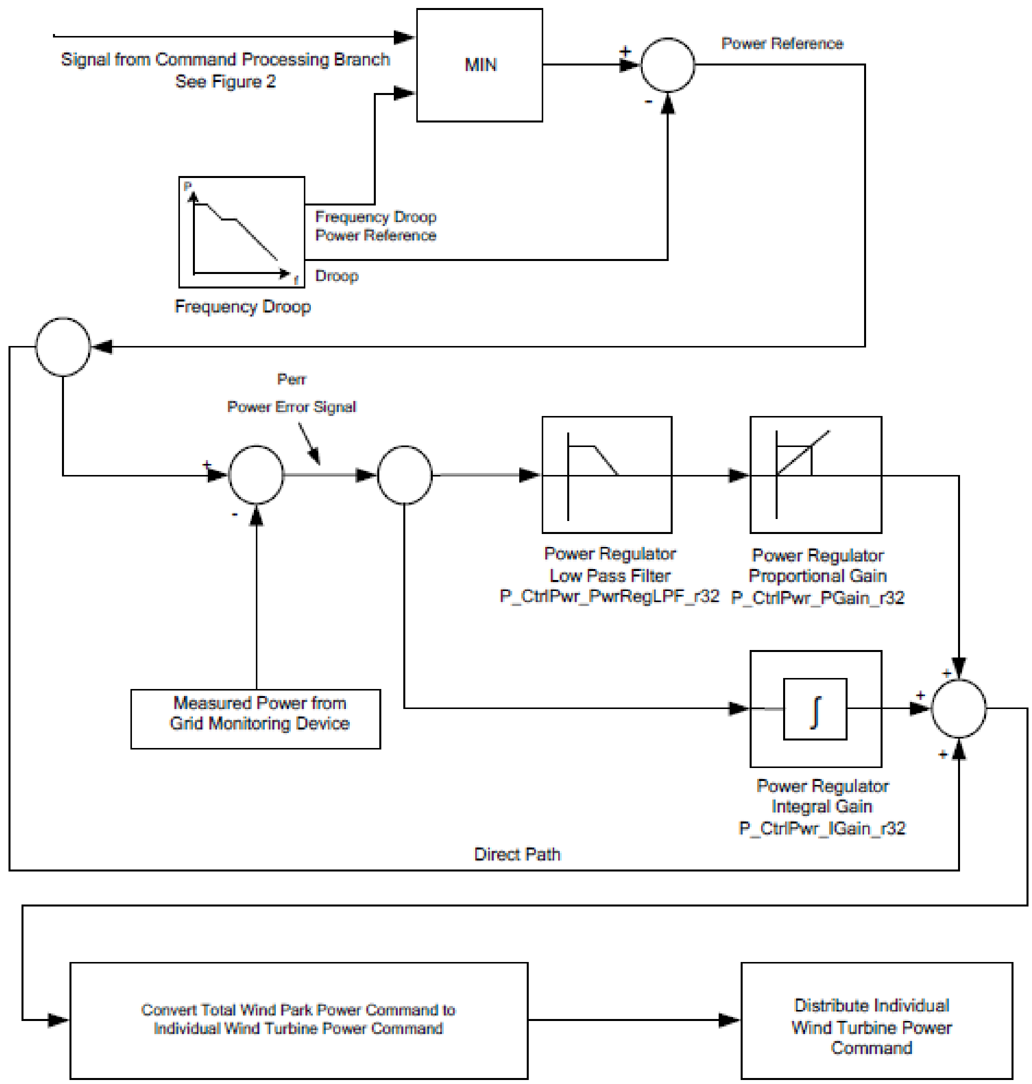

Figure 10. Active power regulator implemented in WindCONTROL (source: GE)

The power error signal then is sent to a low-pass filter that is used to supply the input signal to the proportional control section of the active power regulator. The purpose of the low-pass filter is to remove higher-frequency components that can appear in the active power error signal. Some results of turbine APC tests are shown in Figure 11. The turbine ramp rate limiter was active and set to 1.5 MW/min rate. The turbine was able to follow the set point under steadier wind conditions. Due to turbulent nature of wind resource at NTWC, however, the turbine production was decreasing rapidly during fast wind down-ramps, causing mismatch between commanded and actual power as shown in Figure 11.

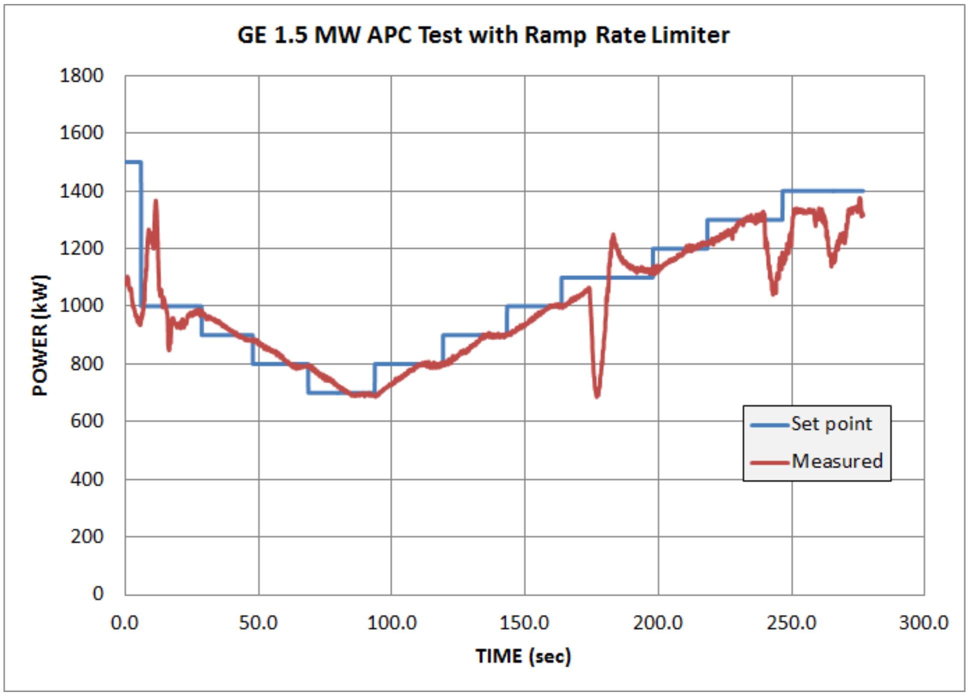

Figure 11. Results of APC test during WindCONTROL commissioning

2.4 NWTC BESS

Energy storage is expected to play an increasing role in the successful integration of electricity generated by variable renewable sources into existing and future power grids. The goal of this research effort is to conduct a 1-year testing and demonstration of several types of grid-supporting services by a utility-scale BESS in conjunction with wind generation at NREL's NWTC.

In 2017, NREL acquired a 1-MW/1-MWh BESS from RES Americas based on competitive procurement process. The purpose of the procurement was to own and continuously operate a utility-scale BESS at the NWTC site for research purposes, and to demonstrate various uses case for energy-storage applications in the following combinations.

- Test BESS as a system connected directly to the Xcel electrical grid
- Test BESS connected to the NREL CGI for grid and fault simulation
- Test BESS in combination with NWTC renewable generation sources, such as wind turbines and PV arrays connected to the Xcel grid
- Test BESS in combination with NWTC renewable generation sources connected to the CGI grid/fault simulator
- Test BESS as grid-forming unit for islanded microgrid operation with NWTC renewable generation sources

To achieve this type of flexible testing configuration, NREL used the NWTC's Energy Storage Test facility, which incorporates a system of electrically prewired concrete pads integrated with medium voltage (MV) infrastructure to provide operation for all configurations described above.

The battery system was delivered and installed at the NWTC test site in April 2017. Figure 12 shows the aerial photo of the BESS system, including the battery enclosure, SMA inverter, step-up transformer, and MV switchgear. Figure 2 shows how the BESS was integrated into NWTC's dual-bus system (note that the flow battery shown in Figure 2 is not yet installed). The BESS can operate continuously when connected to the regular Xcel grid for testing "slower" grid services and connected to the CGI bus as needed for testing fast-responsive services such as frequency control, voltage control, and transient fault ride-through.

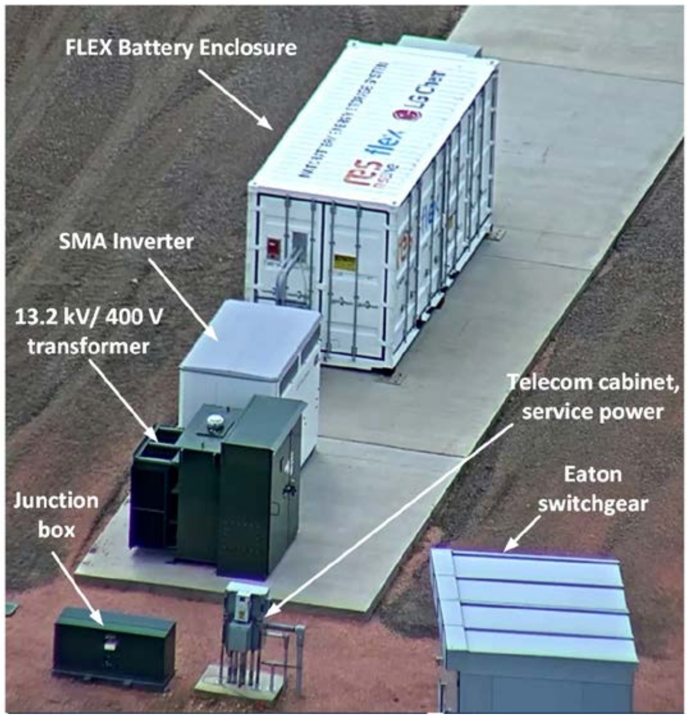

Figure 12. 1-MW/1-MWh BESS at NWTC test site

NREL's main technical objectives were focused to ensure delivery of the hardware and associated internal control system portions of BESS, capable to interconnect with NWTC's 13.2-kV utility system by means of an input transformer from 13.2 kV down to power converter operational voltage. Specific components making up the BESS included the following.

- Outdoor-rated, industrial container–size enclosure for batteries and associated climate-control and battery-management equipment
- Power electronic converter (inverter/rectifier and DC/DC converter for battery charging) in standalone container that meets the same requirements, or embedded into the same container with batteries
- BESS controller and battery management system (BMS)
- 13.2-kV grid-coupling transformer
- Necessary switchgear and protection equipment consistent with National Electric Code (NEC) and typical safety practices
- High-speed data interface for two-way communication with NREL hierarchical computer control

The power converter was intended to be sized for passing at least 1 MW continuous real power with intermittent overload capability with VAR absorption/contribution capability (1.25 MVA rating desirable). The BESS also was intended for use in the research involving the following utility-controlled and self-directed services, and distribution-level and customer energy management services.

- Transmission infrastructure services (upgrade deferrals, congestion relief)
- Electric energy time-shift (arbitrage)
- Peak load management
- Load following and ramping support for renewables
- Renewables curtailment reduction
- Renewables variability smoothing
- Frequency regulation and area control, primary frequency response (PFR), fast frequency response (FFR), synthetic inertia-like response
- Spinning, non-spinning, and supplemental reserves
- Electrical supply capacity
- Reactive power and voltage support
- Critical load support during outages (islanding), black-start
- Advanced controls: power systems oscillation damping controls
- Power reliability
- Retail energy time-shift
- Demand charge management
- Stacked services—use case combinations

3.0 Description of PHIL Validation Platform for Wind Power and BESS

As part of this project, the NREL team developed an advanced PHIL platform using CGI and RTDS systems. Configuration for a typical PHIL experiment setup is shown in Figure 13. The power side consists of various DUTs and a 7-MVA CGI acting as a low-latency controllable voltage source. Figure 13 shows a 1.5-MW wind turbine with a commercial WPP controller and the embedded capability to provide ancillary services. The RTDS is capable of the real-time execution of the generation and distribution models with a typical time step of 50 µs. A detailed description of the model used to conduct the tests described in this report is given elsewhere in this report. The voltage at a single node of the simulated model is monitored and commanded to the CGI. At the same time, the current at the point of interconnection (POI) is measured using Rogowski coils and fed back to the RTDS.

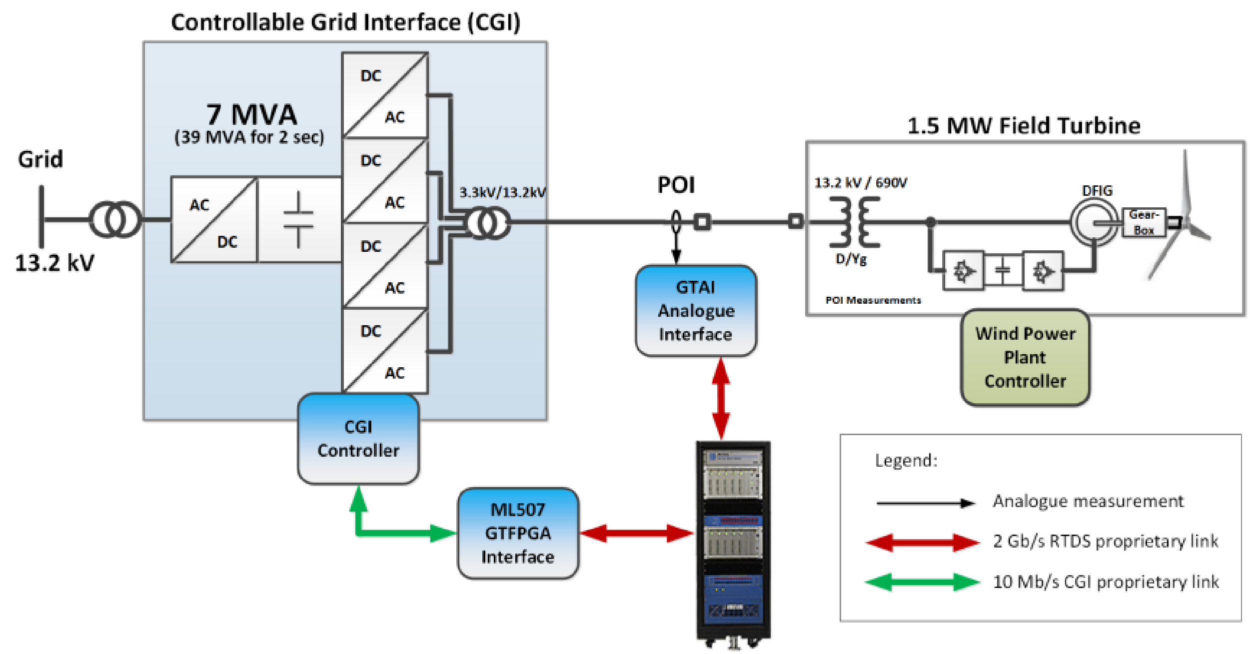

Figure 13. PHIL platform for wind turbine testing

Because of the large physical footprint of the test setup, a dedicated fiber-optic network communication system was implemented to exchange measurements and set points among the CGI, DUT, and RTDS using the minimum latency required by the closed-loop systems instead of traditional analog signal interfaces [10]–[12]. The DUT voltage (u_{dut}) and current (i_{dut}) waveforms are measured with a standard RTDS analog input card located near the DUT's POI, which is far from the main RTDS rack. Voltages and currents are collected with a high sampling rate of 25 µs, digitally filtered for antialiasing effects, and transmitted back to the central RTDS unit using a 2 Gb/sec fiber-optic channel, thus reducing the latency of the measurement to less than 25 µs. At the same time, the voltage commands from the RTDS are transmitted after every 50 µs time step by using the 2 Gb/sec optical link to the ML507 Xilinx evaluation board, which acts as a protocol translator allowing an interface with the CGI by using proprietary optical protocol and making it possible to deterministically exchange 20 x 16-bit words every 25 µs.

The following sections of this chapter describe both theoretical and experimental activities performed by the NREL team in developing a PHIL interface between CGI and RTDS, because it was an extremely important but "missing link" for successful implementation of this research project.

3.1 Development of Power-Hardware-in-the-Loop Interface

The PHIL interface is a coupler between a model of the grid implemented in the RTDS and a real DUT in the field. The block diagram is shown in Figure 14. The PHIL's basic principle is that voltage measured at the simulated model's single bus is replicated at the real system's bus using grid simulation. Simultaneously, the current flowing into the grid simulator is measured and injected back into the simulated model. Model and real-world per-unit (p.u.) systems can differ, so voltage scaling (k_V) and current-scaling (k_I) factors are used. Additionally, the impact of the DUT on the grid model can be adjusted by manipulating the multiplication factor "*m*." In the case of $m=0$, the test is called an open loop, and allows the DUT to "see" the voltage of the modeled grid but no feedback is enabled. Increasing the *m* factor multiplies the impact of power flowing from the DUT on the modeled grid, which thus allows for testing variables such as the penetration levels of renewable energy on a given grid.

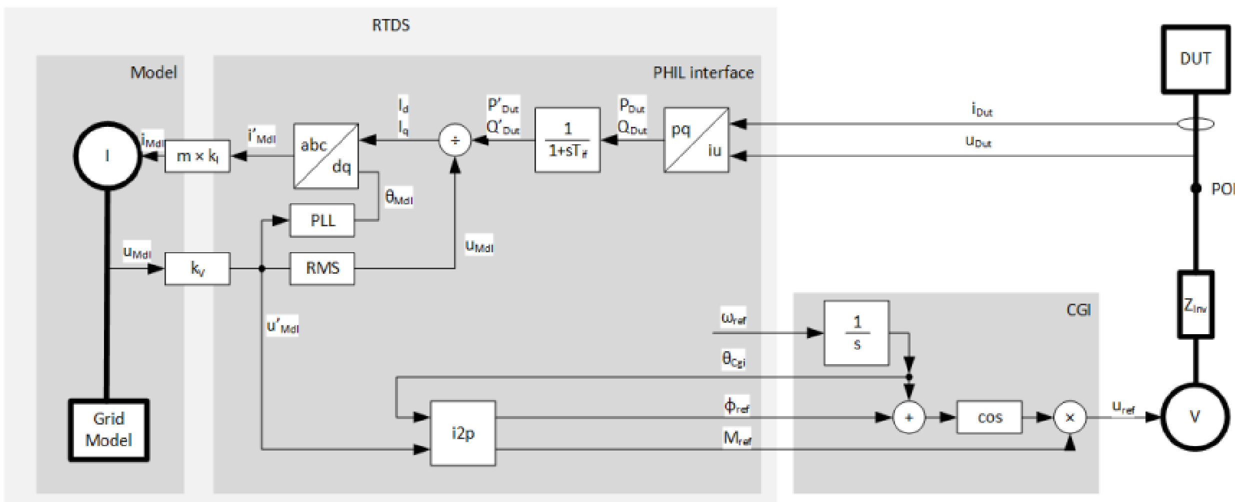

Figure 14. Block diagram of the PHIL interface

The main objectives of the NWTC's PHIL interface implementation are as follows.

- Accurate, low-latency, instantaneous voltage tracking of the modeled voltage, u'_{mdl}, by actual CGI voltage, u_{ref}
- Accurate tracking of positive, negative, and zero sequence components of modelled voltage u'_{mdl} by actual CGI voltage
- Accurate tracking of actual DUT active and reactive power (measured using i_{dut} and u_{dut}) in the model.

Fulfilling the above objectives allows for multiple tests validating the DUT's ancillary services, including frequency response, voltage regulation, and volt/volt-ampere reactive (VAR) support. Voltage tracking by the CGI is complicated by the fact that the CGI is intended to operate using phasor set points rather than instantaneous set points, whereas researchers desired to implement an instantaneous model in the real-time simulation (RTS). An instantaneous-to-phasor (I2P) algorithm therefore is developed to convert the modeled instantaneous voltages u'_{mdl} into phasor magnitudes, M_{ref}, and angle set points, φ_{ref}, for each phase independently, so that the CGI's instantaneous voltage u_{ref} is able to track the modeled voltages in terms of phase, magnitude, and frequency both in steady state and during transient states. The next section further describes the I2P algorithm's design and performance validation.

Power tracking in the real-time model is implemented using active and reactive power measurements taken at the POI. These then are filtered to ensure the stability of the closed-loop PHIL experiment, and they are divided by the voltage, U_{rms}, to extract the I_d and I_q components of the current. The angle of the modeled voltage, θ_{mdl}, is reconstructed using a phase-locked loop and used to synthesize the instantaneous current references, i_{mdl}, which control the current sources in the grid model.

3.2 Single-Phase Instantaneous-to-Phasor Algorithm

As an electromagnetic transient model program, most of the variables observed within an RTDS simulation model correspond to instantaneous values of voltage and current. Because the CGI accepts only polar phasor references, an algorithm was developed to allow for real-time conversion. Due to the requirement of accurately tracking positive, negative, and zero sequence voltages, and the fact that CGI inputs are independent single-phase phasors, it was desired to implement the I2P algorithm as a single-phase module. Three identical blocks are used to implement the three-phase PHIL algorithm. The block design is described elsewhere in this section. Figure 15 shows the voltage vector rotating on a complex plane and the principles of smooth optimization. Figure 16 shows a block diagram of calculations done in the I2P algorithm.

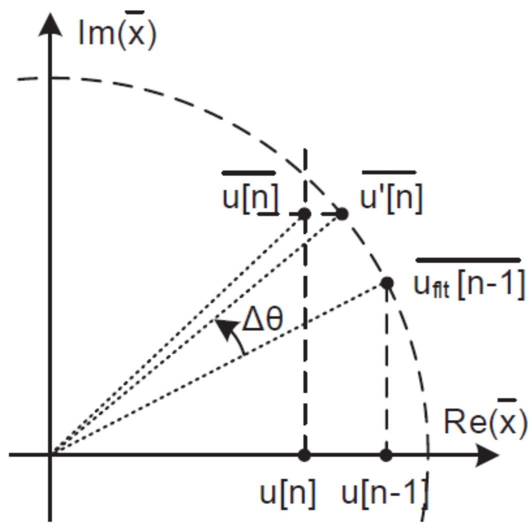

Figure 15. Instantaneous-to-phasor algorithm step calculation presented on complex plane

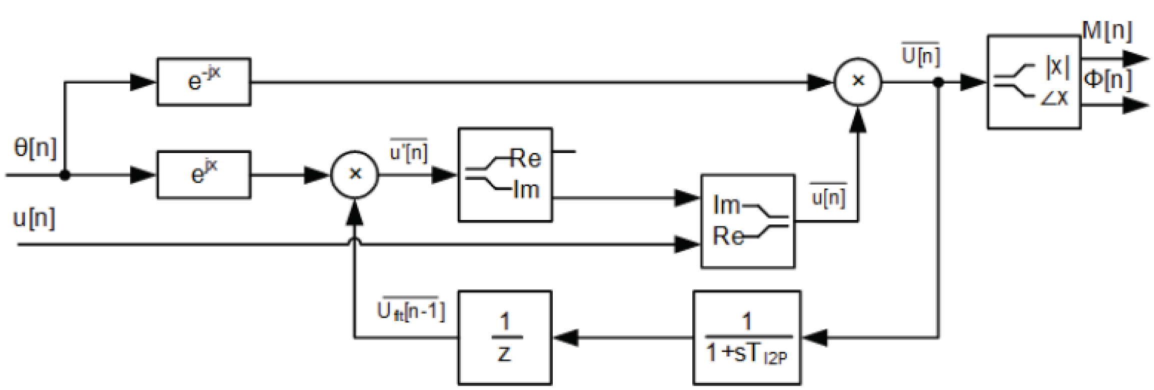

Figure 16. Block diagram showing calculations within the I2P algorithm

Because the I2P algorithm needs to be implemented in a real-time environment with calculations executed in constant time step, discrete equations are used. Calculating the actual step outputs M[n] and $\phi[n]$ is based on actual inputs $u[n]$ and $\theta[n]$, and the previous state of the rotating phasor vector, $\overline{u_{flt}[n-1]}$.

The algorithm's main objective is to calculate the magnitude, $M[n]$, and angle, $\varphi[n]$, that will be sent to CGI based on the instantaneous value of voltage in any given phase, $u[n]$, and the actual angle of the CGI's integrator, $\theta[n]$. The CGI modulator rotates the phasor using the cosine function, thus, as long as formula (Equation 3.1) is met, then the actual instantaneous voltage at the output of the modulator will be equal to the instantaneous input voltage.

$$u[n] = M[n]cos(\Phi[n] + \theta[n]) \tag{3.1}$$

Because two variables must be calculated, and only one equation satisfies the main objective, it means that there is one degree of freedom which can be used to satisfy the secondary objective of a smooth phasor reference to the CGI, both in steady state and during transitions. Point $\overline{u_{flt}[n-1]}$ corresponds to an actual phasor reference sent to the CGI in a previous cycle, $\overline{U_{flt}[n-1]}$, rotated by the integrator angle from a previous calculation step, $[n-1]$, as shown in Equation 3.2.

$$\overline{u_{flt}[n-1]} \;=\; \overline{U_{flt}[n-1]}e^{i\theta[n-1]} \tag{3.2}$$

Projection of this point on a real axis corresponds to the actual instantaneous output voltage at previous step $u[n-1]$.

Based on the previous phasor reference, a $\overline{u'[n]}$ point coordinates are calculated by rotating the actual CGI's reference from the previous step by the actual integrator angle, $\theta[n]$.

$$\overline{u'[n]} = \overline{U_{flt}[n-1]}e^{i\theta[n]} \tag{3.3}$$

Thus, this point can be interpreted as the first estimate of the $\overline{u[n]}$ point assuming that the input voltage phasor is oscillating steadily with nominal frequency and equals to $\overline{U_{flt}[n-1]}$. Essentially, when Equation 3.4 is met, $\overline{u'[n]}$ becomes $\overline{u[n]}$.

$$\overline{U_{flt}[n-1]} = \overline{U_{flt}[n]} \tag{3.4}$$

This assumption is not always met in the dynamic system, however, so the algorithm must be able to respond to transients and lack of synchronization issues. To address this, $\overline{u[n]}$ point is built as shown in Equation 3.5.

$$\overline{u[n]} = u[n] + i\, Im\{\overline{u'[n]}\} \tag{3.5}$$

Equation 3.6 ensures that the actual instantaneous voltage at the output of modulator is equal to the instantaneous input by setting the real part to $u[n]$. The imaginary part of the point is selected so that $\overline{u[n]}$ is closest to the estimated point $\overline{u'[n]}$. This is always achieved when the imaginary parts are equal. A new point calculated in the rotating plane must be reverted to the stationary frame before sending the reference to the CGI.

$$\overline{U[n]} = \overline{u[n]}e^{-i\theta[n]} \tag{3.6}$$

Because the CGI uses polar coordinates as references, they must be converted to M[n] and $\phi[n]$ before sending.

The real and reactive part of actual phasor values are filtered through a single pole, low-pass filter to assure that a steady state always is achieved for voltages oscillating with nominal frequency and steady magnitude and angle. Then, a single-cycle delay is applied to avoid an algebraic loop before this point is used for the next cycle calculations.

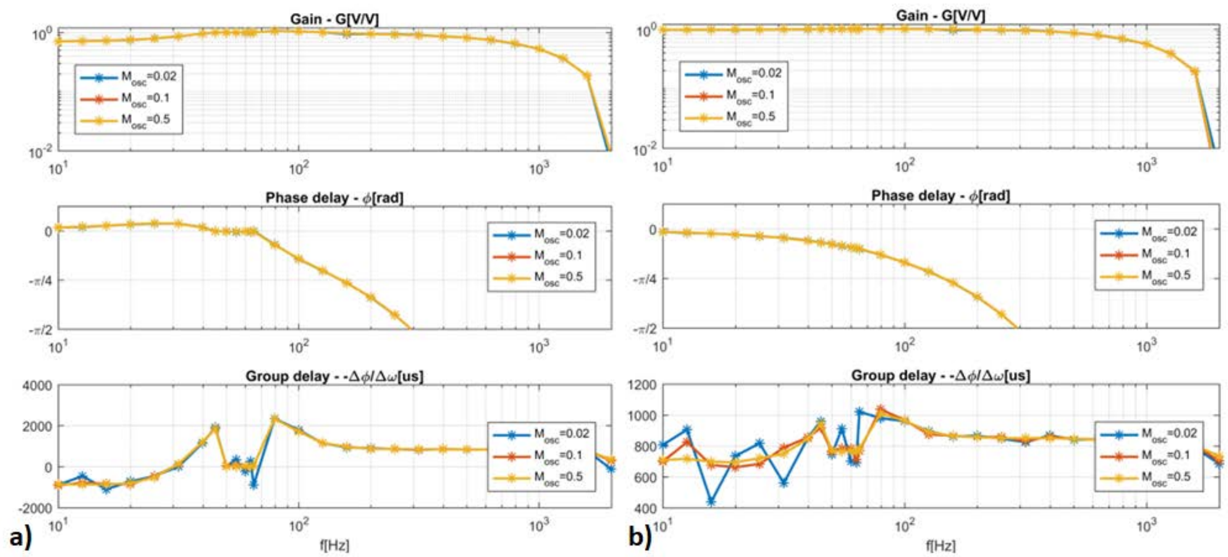

Figure 17. Voltage tracking path transfer function analysis; (a) without delay compensation (b) with delay compensation using T_C

3.3 Transfer Function Analysis and Delay Compensation

The design of the I2P algorithm shown in a previous section is idealized and assumes no delays between the RTDS and the CGI. Various delays do exist in the system, however, because of communications and processing times. These delays are summarized and visualized in Figure 14 as the e^{sT_d} block. If no delay-compensation technique is used, then the voltage tracking will be optimized to reproduce the voltage's fundamental component with the highest precision and minimum delay between the simulated and actual voltage, although other frequency components will show various delays. The system transfer function was analyzed using a detailed Simulink model of the system, which included all the delays and a modulator model. Small signal oscillation sweeping through the frequency range from 10 Hz to 2 kHz was generated as voltage at modeled RTDS side (u_{Mdl}). Simultaneously, the given frequency was measured at the modulator's output (u_{ref}). Figure 17a shows the Bode plot of this transfer function. For frequencies at the CGI's nominal operating range, 45–65 Hz of magnitude, the gain (G) is close to 1.0 and phase shift (ϕ) is close to 0 radians, which indicates good synchronization of the fundamental frequency signal. Below the nominal operating range, the frequency phase shift is slightly positive, indicating that output voltage slightly leads against the model. Above the nominal operating range, the frequency phase shift veers negative—thus, the output voltage is slightly delayed as compared to the input voltage. The last plot shows group delay calculated as a phase shift derivative with respect to frequency. A flat group delay plot versus frequency indicates that fewer distortions have been added to the output signal, because more frequencies are delayed by the same amount of time. With no delay compensation, the plot shows significant variability with values ranging between -800 µs and 2,000 µs, which indicates that distortions could be significant in wide-frequency spectrum signals.

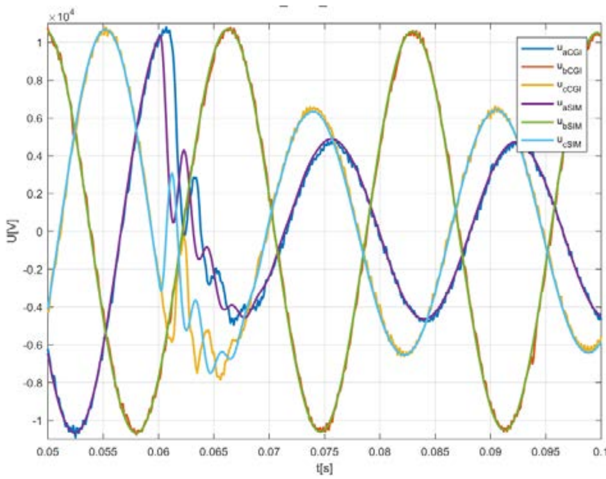

Figure 18. Voltage fault tracking through the PHIL interface without delay compensation

Figure 18 shows the PHIL interface's voltage tracking capabilities for wide-frequency spectrum voltage signals—a single line-to-line voltage fault. Before the event at t=0.06s, voltage tracking is excellent—the CGI and the simulated voltages are synced. A step change in modeled voltage is observed during the fault. Due to the wide-frequency spectrum of this kind of signal, the voltage distortion is visible. After t=0.075s, the voltage reaches steady state and, much like the period before the event, synchronization can once again be observed.

Figure 17b shows the same transfer function after applying a delay compensation, T_c, which is equal in value to the sum of all system delays, T_d, to the angle signal feed to the RTDS from the CGI's integrator, θ_{cgi}. The delay compensation changed the phase-delay profile; it now decreases steadily with frequency and always is negative. The output voltage is delayed when compared to the simulation. The group delay also shows a substantial difference, and a flatter plot is observed.

An example of a wide-spectrum signal passing through the PHIL interface is provided in Figure 19a. There are negligible voltage-tracking errors during steady state and transition, indicating that the delay compensation was correctly added. The measured CGI's output voltage signal was shifted in time by T_d to enable a better comparison of the delayed signal distortions. Additionally, Figure 19b shows that in the steady state before the event, both magnitude and phase are smooth, indicating that the CGI's optimal operation has been achieved. During the transient reference voltage, the vector changes dynamically. Due to the CGI's limitations, however, the rate of change is not fast enough to cause disturbances. The delay compensation drawback is that output signals are delayed as compared to simulated signals, thus limiting the maximum bandwidth of simulation that can be achieved in a PHIL type of experiment.

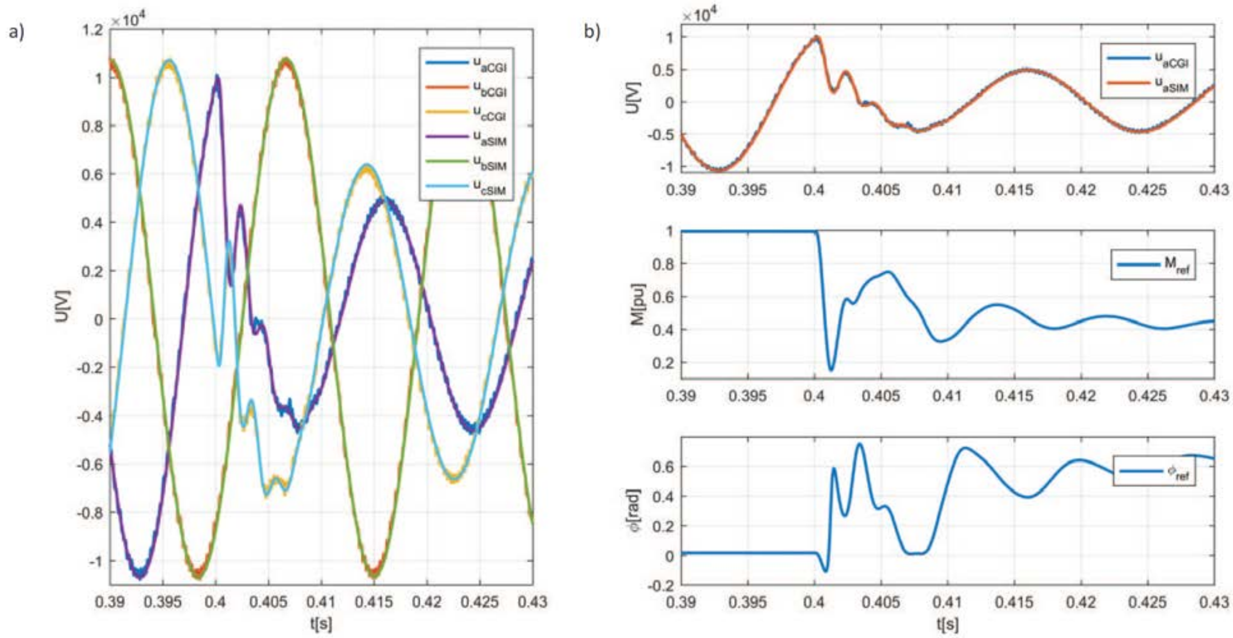

Figure 19. Single phase line-to-line fault example; (a) voltage tracking during transition, (b) CGI voltage reference of phase A during the fault event

3.4. Grid Modeling and Power-Hardware-in-the-Loop

During the initial stages of the PHIL platform development, the model of the modified Institute of Electrical and Electronics Engineers (IEEE) 9-bus test case for 230-kV transmission grid (shown in Figure 20) was developed by the NREL team and used in experiments. The model consists of four generators with a total capacity of 617 MW [3]. During the experiment, the steady-state total system load is 400 MW. The AGC has been implemented to control overall system frequency.

The IEEE model allowed multiple types of tests that show the interaction between transmission system and DUT (1.5-MW GE WTG, in this case). With this model, it is possible to conduct PHIL experiments using both active and reactive power controls by wind power. Contingency underfrequency and overfrequency events can be triggered by tripping one of the generators or loads in the 9-bus system. This way, various types of active power controls including inertial response and droop response by wind power can be tested under realistic conditions. Similarly, transient undervoltage and overvoltage can be triggered in the system to test LVRT and HVRT performance of the WTG being tested.

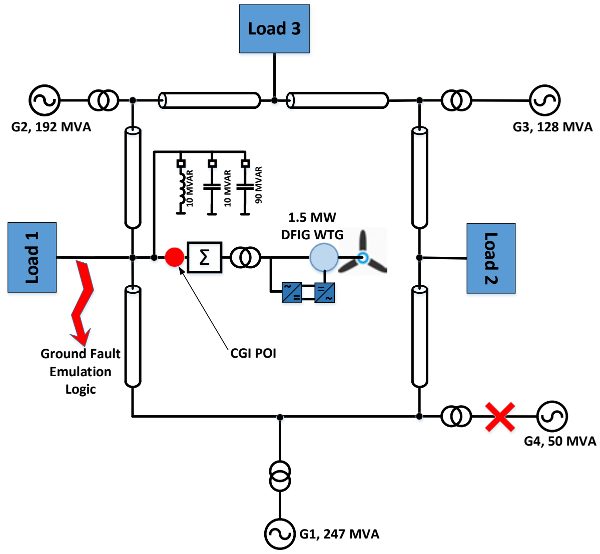

Figure 20. Diagram of 9-bus real-time dynamic simulators model

An example of the results of a closed-loop PHIL frequency test realized with the 9-bus test system is shown in Figure 21. The example shows a very close match between the commanded frequency and the measured frequency during the generation and load-loss events triggered in the model. These are the initial results of testing to demonstrate the CGI PHIL capability.

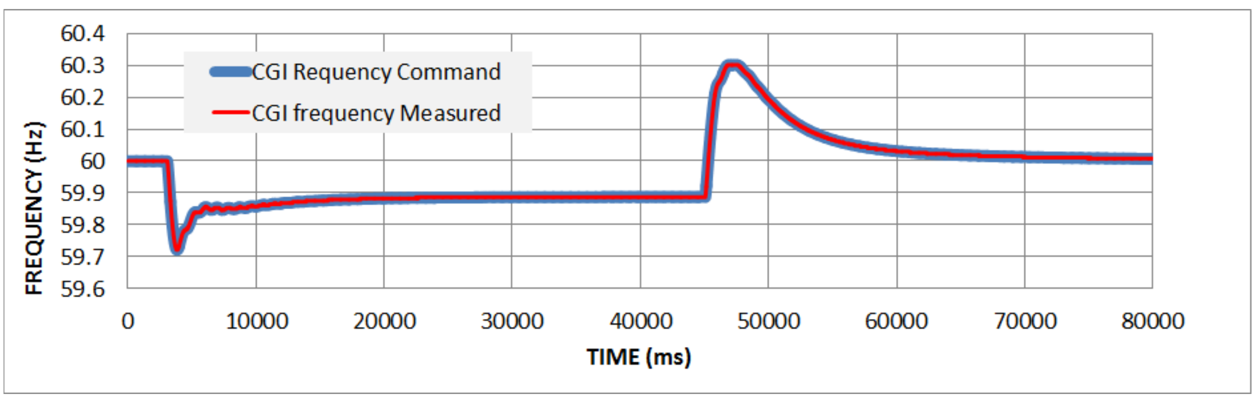

Figure 21. Comparison of RTDS model and CGI-emulated frequency

3.4.1. Voltage Fault PHIL Testing

Various types of faults can occur in a power grid. The PHIL interface allows evaluation of an impact of the fault simulated in one of busses of the model on a real DUT. Various ride-through techniques can be tested. At the same time, the DUT's grid-supporting features—such as injecting a reactive current—can be tested. Verifying these features usually requires an open-loop approach; however, the PHIL interface verifies the efficiency of such a scheme at a system level.

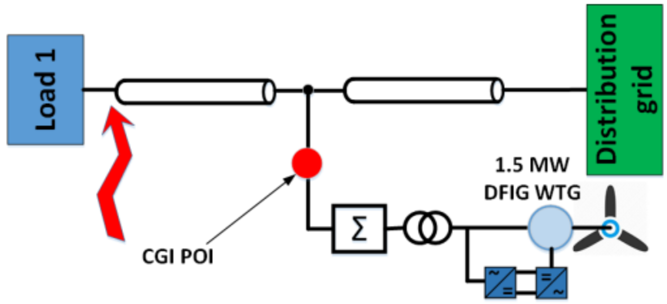

Figure 22. Voltage fault testing circuit

Figure 22 shows a testing circuit embedded in the RTDS model that was used for evaluating various fault scenarios. A fault was located at the Load 1 bus, which is connected to the main transmission grid ring through impedance Z_L. The POI for the PHIL test was located at 20% of the line length from Load 1, thus the fault effectively was happening behind $0.2Z_L$ impedance, as seen from the DUT perspective.

Both line-to-line and line-to-ground voltage fault tests have been conducted to validate the PHIL interface's capability to track fast-changing and highly asymmetric voltages during such faults. Some of the tests are presented in this report, including single-phase line-to-line tests (Figure 19), three-phase line-to-ground tests (Figure 23), and two-phase line-to-line faults (Figure 24). All of these tests show the superior tracking capabilities of the PHIL interface. Apart from step change, which is precisely emulated, PHIL also can track oscillation with about 400 Hz characteristic frequency of modelled circuit that happens after the step change and typically is damped within 10–20 ms because of the high bandwidth of the PHIL interface and the CGI.

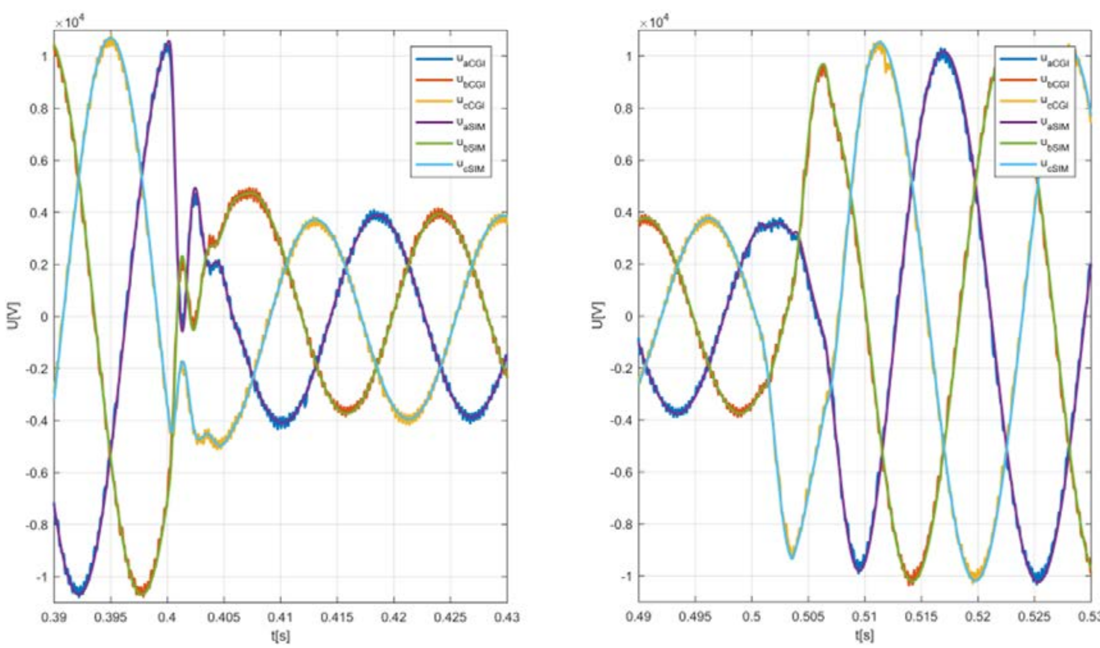

Figure 23. Three-phase line-to-ground fault test

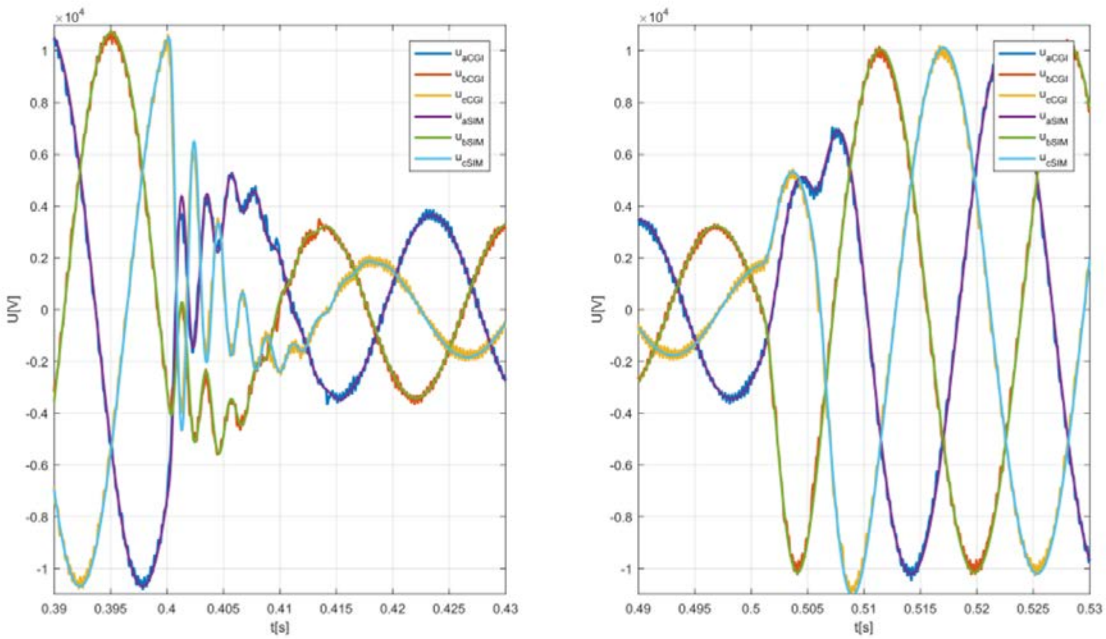

Figure 24. Two-phase line-to-line fault

3.4.2. Frequency Response Testing

Multiple tests were conducted to show the impact of a generator-loss contingency event on grid frequency; selected results are shown in Table 1. Prior to the contingency emulation, the wind turbine was set to operate in curtailed mode with maximum power at 1 MW, thus allowing 0.5 MW of headroom for regulation purposes. At $t = 0.9\ s$, a circuit breaker from Generator 4 was commanded to open, causing the instantaneous loss of 50 MW of generation out of 450 MW of total generation.

Table 1. Results of PHIL Tests for Frequency Response by Wind Power

m, Number of turbines	f_{nadir} [Hz]
0	59.606
3	59.609
60	59.621
100	59.625

Due to a combination of primary frequency control and AGC implemented in the RTDS model, the system frequency declines to 59.606 Hz and then slowly recovers. (Note that it is important to limit the depth of the frequency event because it can cause various grid protective devices to trip an entire system). The wind turbine supports the grid by injecting additional active power to the grid during the underfrequency event, using synthetic inertia and Hz/kW droop curves. All four events in Figure 25 show the inertial response of the turbine; the turbine's active power is increased by approximately 100 kW within 1 sec, starting after the frequency fell to less than 59.8 Hz. This aligns with the DUT configuration. The droop starts to operate later because it is implemented in the WPP controller instead of the turbine's inertial controller. For comparison, see the case where $m = 0$ shows the system's frequency response without the PHIL feedback. At $m = 3$, nearly no impact on system frequency can be observed because the inertial response of 3 x 100 kW is negligible as compared to a 50-MW loss. At m = 60 and m = 100, the impact of the turbine's grid support is visible because its inertial response translates to 6 MW and 10 MW, respectively, of additional generation, thus helping to reduce the frequency dip to 59.621 Hz and

59.625 Hz. The PHIL experiment also demonstrates how AGC interacts with the droop response by causing a slight oscillation and overshoot of the frequency that needs to be damped.

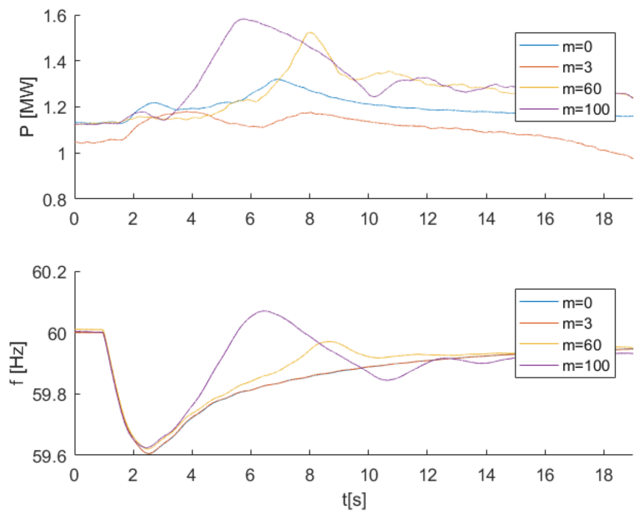

Figure 25. Wind power and frequency in 9-bus system

It is important to note that there was a 200-mHz deadband set as a default value in GE WindCONTROL for inertial response for the GE 1.5-MW wind turbine, and the NREL team did not have the means to change that value during these initial tests. This is why the inertial response triggers "later" than expected. Even with such large deadband, however, the improvement in frequency nadir can be observed for different levels of wind penetration in this test 9-bus system.

3.4.3. PHIL Testing of Wind Power Controlling the Voltage at Point of Interconnection

Another useful case for a PHIL experiment is voltage control verification and its impact on grid stability and operation. In this case, a WPP controller operates with a volt/VAR droop that is intended to support the grid with voltage control by injecting reactive power into the system. Figure 26a and Figure 26b show the response of a WPP to a step in the system voltage caused by the 10-MVAR capacitor bank connection and disconnection. According to the droop curve marked with the dotted line on the bottom subplot, without the wind turbine's support, the turbine injects reactive power at $m = 0$. Because the impact to the grid is not modeled, additional reactive current does not help correct the voltage, and thus the turbine operates at a different set point than that for when the feedback was enabled: $m = 100$. The PHIL experiment also allows for studying the dynamic response of the voltage controller and its interaction with the grid impedance which, in some cases, could lead to power oscillations and would not be captured if only an open-loop system is analyzed. For example, an overshoot just after an event might be assumed; although, in this case, it would be very well damped.

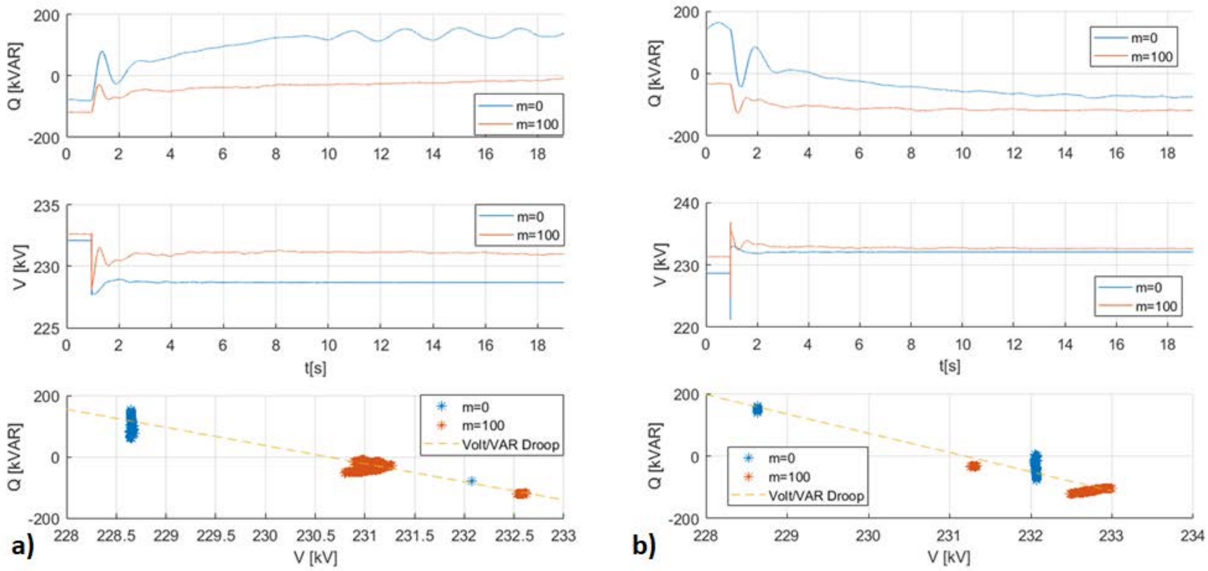

Figure 26. A WPP's voltage regulator response to a capacitor bank disabling event (a), and enabling event (b)

The PHIL system developed at the NWTC is a breakthrough in utility-scale grid integration testing capability that allows for studies of system stability, including detailed models of generation and distribution combined with real distributed-power assets that already are installed at the NWTC, and testing devices that can be installed at the NWTC temporarily. Results shown confirm the system's performance and allow for further studies of systems that are highly penetrated by low-inertia distributed resources with power electronics. This report shows high flexibility and improved system performance of the system that can be used for multiple type of tests—from testing high-bandwidth fault events to evaluating long-term algorithms through various type of closed-loop, grid-connected inverters with features such as droop or inertia. PHIL testing of newly commissioned systems is considered an intermediate step between offline modeling and final commissioning of many complex systems, such as microgrids.

3.4.4 Controllable Grid Interface Virtual Impedance and Reactive Power Control Tests

In addition to active power control tests, the ability of WindCONTROL to operate the 1.5-MW wind turbine in reactive power control mode was tested. These tests were conducted in CGI connected mode as depicted in Figure 27. Reactive power control tests in normal grid connected mode are undesirable because injection or absorption of greater levels of reactive power will cause overvoltage or undervoltage conditions in the NWTC grid, impacting site loads and generation. CGI provides full isolation between the test grid and normal grid in terms of reactive power, so the all reactive power can be provided or absorbed by CGI without impacting voltage stability in the rest of the NWTC grid.

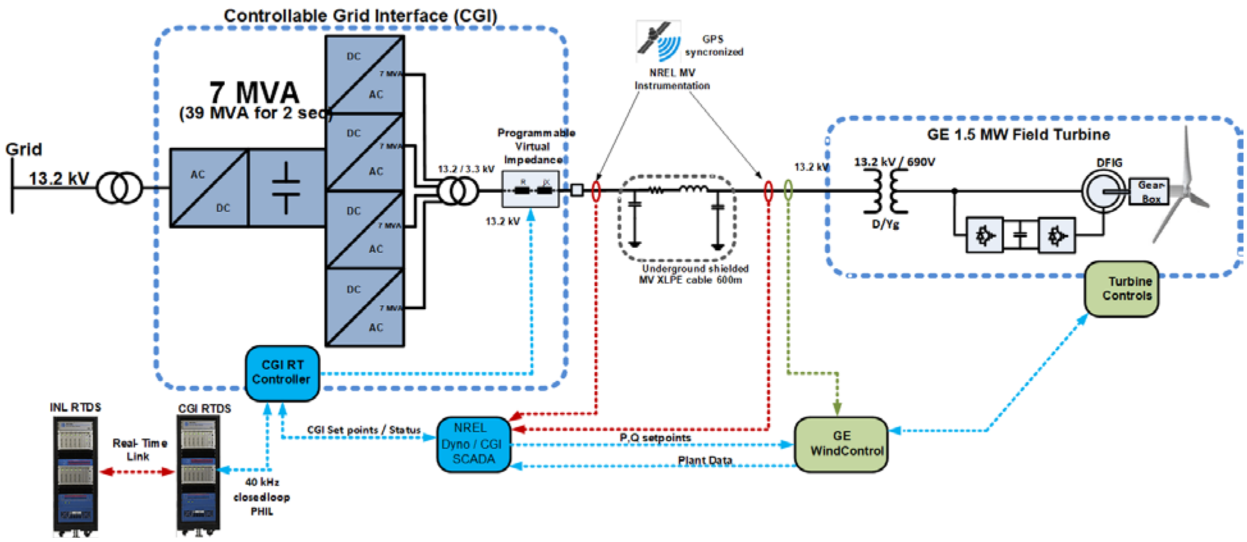

Figure 27. GE 1.5-MW WTG and CGI interconnection used for reactive power control tests

The electrical characteristics of the grid, such as line impedance and short-circuit ratio at the PCC, might impact the ability of inverter-coupled generation to ride through various types of voltage faults and other transient conditions. For example, some wind turbine electrical topologies—such as doubly-fed induction generators—need to absorb reactive power from the grid for magnetization, which can deteriorate weak grids. During voltage faults, wind turbines, photovoltaic, and energy-storage inverters are capable of supplying reactive current to weak grids to increase the grid voltage and assist with recovery. Also, inverter-coupled generators can provide voltage, reactive power, or power factor control to enhance stability.

With simplifications, the CGI can be viewed as an ideal voltage source inverter with a series impedance of the matching transformer. Therefore, the transformer impedance has a significant impact on the parameters of the emulated grid. A short-circuit power (S_{SC}) that allows for the evaluation of grid strength can be estimated using Equation 3.7.

$$S_{SC} = \frac{U_N}{Z_t} = \frac{S_N}{Z_{tPU}} \tag{3.7}$$

The impedance of the CGI transformer Z_{PU} is 5% for 50-Hz operation and 6% for 60-Hz operation; therefore, the short-circuit ratio of the emulated grid S_{SC} is 20 or 16.66 times greater than the nominal power of grid simulator (S_N) for 50 Hz an 60 Hz, respectively ($S_{SC} = 140\ MVA$ at 50 Hz and 116 MVA at 60 Hz). This value is significantly greater than the rating of any DUT, so the CGI naturally emulates a strong grid interconnection. Note that the impedance of the emulated grid can be accurately estimated at any frequency, making it a useful feature when analyzing the transients with current waveforms consisting of any harmonic or subharmonic components.

To test the WTG performance under emulated strong and weak grid conditions, a programmable line impedance feature has been implemented in the CGI's controls. The impedance control is implemented for the reference frequency, and it allows for (a) compensating the transformer impedance, Z_t, and (b) introducing an additional impedance, Z_D. Depending on the commanded reference voltage, U_{Ref}, the controller sets the impedance value so the voltage at the PCC follows Equation 3.8, whereas in reality it is the sum of the inverter voltage and voltage drop of the transformer, as indicated in Equation 3.9.

$$\overline{U_{PCC}} = \overline{U_{Ref}} + \overline{Z_d}\overline{I} \tag{3.8}$$

$$\overline{U_{PCC}} = \overline{U_{INV}} + \overline{Z_t}\overline{I} \tag{3.9}$$

To ensure that the CGI emulates the requested impedance, a voltage vector is generated by the inverter based on Equation 3.10.

$$\overline{U_{INV}} = \overline{U_{Ref}} + (\overline{Z_d} - \overline{Z_t})\overline{I} \tag{3.10}$$

The CGI controller calculates the output current vector in real time and modifies the inverter voltage by adding an equivalent of voltage drop on the requested impedance and negative transformer impedance. This enables the CGI to emulate any impedance requested. If zero impedance is requested, then the SGI will act as a strong grid because only the transformer voltage drop will be compensated. The impedance control is implemented in the CGI's hardware-in-the-loop (HIL) emulator. Figure 28 shows the CGI voltage measured at the 13.2-kV PCC for different levels of reactive power injected at three different impedance settings. A case with transformer-only compensation (green trace) corresponds to $S_{SC} = 5118$ MVA, which can be considered nearly infinite as compared to the nominal rating of 7 MVA. Other cases for $Z_{dPU} = 6\%$ and $Z_{dPU} = 10\%$ are shown in red and blue, respectively. Measured S_{SC} values in Table 2 show that grid impedance can be controlled with sufficient accuracy.

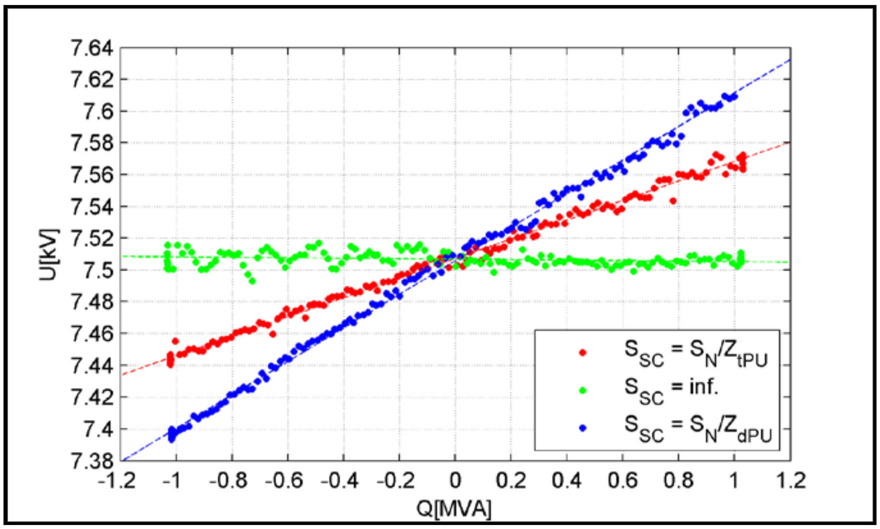

Figure 28. Impedance compensation results using PHIL emulation

Table 2. Grid Impedance Levels Emulated by CGI

Impedance Setting	Expected S_{sc}	Measured S_{sc}
$Z_{PU} = Z_{tPU} = 6\%$	116 MVA	123 MVA
$Z_{PU} = Z_{dPU} = 0\%$	inf	-5,118 MVA
$Z_{PU} = Z_{dPU} = 10\%$	70 MVA	71.1 MVA

Results of one reactive power set point operation test for GE 1.5-NW WTG are shown in Figure 29 and Figure 30 for strong and weaker grid cases, respectively. In first case (Figure 29), there was no line impedance emulated by CGI, so the voltages measured at both wind turbine terminals and CGI terminals (with about 0.3 miles of underground cable in the middle) are not changing with reactive power produced or absorbed by the wind turbine. At the same time, the turbine was producing active power during this test. The Figure 29 shows active and reactive power (left graph) under emulated strong grid conditions (no impedance) measured at the turbine and CGI terminals (sending and receiving ends), and voltage versus reactive power (right graph). Figure 30 shows the same under an emulated 10% grid impedance. The impact of turbine reactive power on voltage is clearly visible in the right graph.

The results shown in Figure 29 and Figure 30 also demonstrate the ability of the turbine converter to control active and reactive power independently. The WTG is capable of following the reactive power set points without impact on active power production.

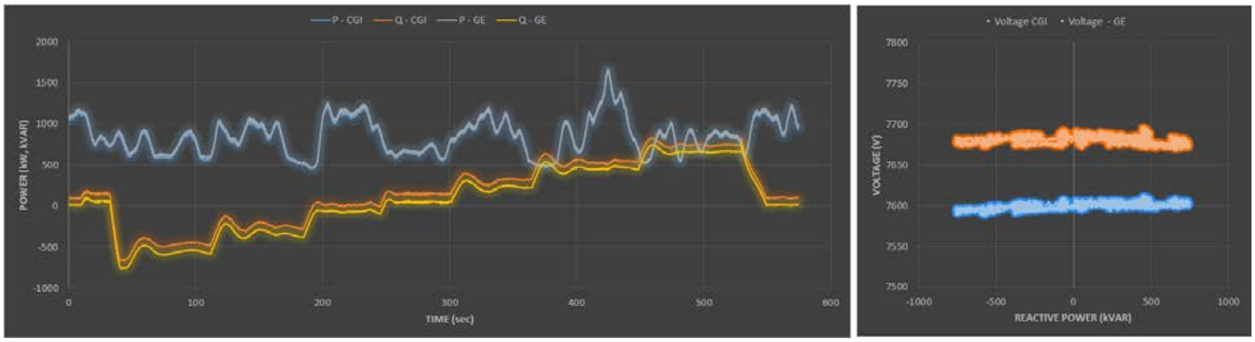

Figure 29. GE 1.5 reactive power set point operation—no impedance emulated by CGI (strong grid)

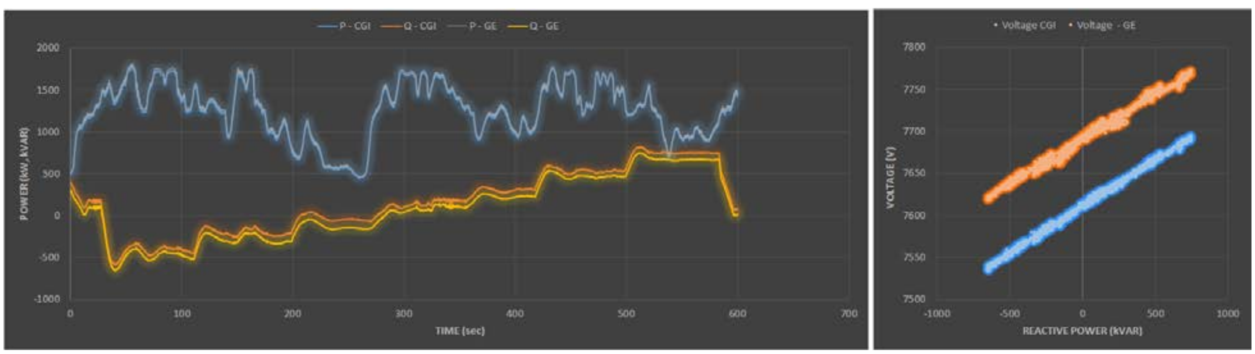

Figure 30. GE 1.5 reactive power set point operation—10% impedance emulated by CGI (weaker grid)

3.4.5. Voltage Fault Ride-Through Tests

The test setup shown in Figure 27 is also used to test the fault ride-through characteristics of the GE 1.5-MW WTG. Figure 31 shows results of one LVRT test (50% symmetric voltage drop). CGI was commanded to emulate a 200 ms rectangular voltage fault (Figure 31). The turbine response is shown in Figure 31a and 31c for active/reactive power and total current measured on the medium-voltage side of transformer. It can be seen that the turbine rides through this fault and restores full production after the fault is cleared. Some current oscillation can be observed during the recovery.

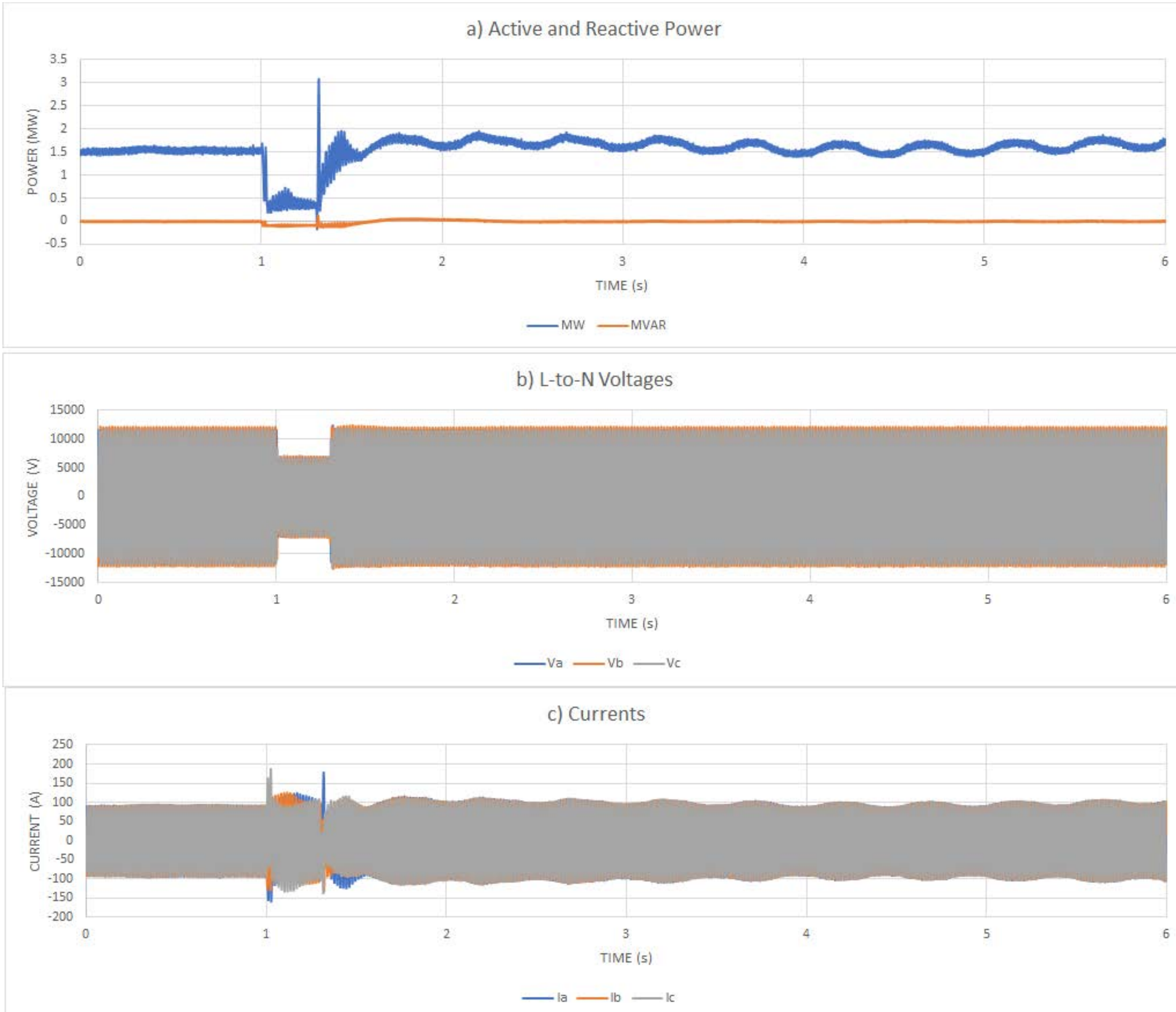

Figure 31. Results of low-voltage ride-through test

3.5 Impacts of Inertial Response on WTG Loads

During recent years, NREL researchers investigated impacts of provision of inertial response by WTGs on the mechanical loads of Type-3 WTG drivetrains [53]. For this purpose, detailed dynamic time domain simulation models have been built by integrating the aeroelastic wind turbine model in FAST (developed by NREL) with the electro-mechanical drivetrain model in SimDriveline and SimPowerSystems. Simulations on these models were performed in the MATLAB/Simulink environment to investigate the dynamic loads experienced by the drivetrain components during the inertial response. Theoretical findings for Type-3 WTG showed that drivetrain loads were not impacted by the grid frequency variations. Additional loads on Type-3 WTG drivetrain during its inertial response caused by the transient vibrations attributed to the change in output power also were insignificant.

These findings were confirmed during the testing stage of this project. The WTG was exposed to large high-ROCOF frequency variations created by the CGI. The impacts of inertial response on drivetrain loading were measured using an instrumentation system that an NREL team installed on the GE 1.5-MW wind turbine gearbox and bearings as part of another research program supported by DOE at Argonne National Laboratory and NREL. The program examined the causes of white-etching cracks in wind turbine gearbox bearings [54]. An instrumented Winergy 4410.4 gearbox was installed in the NWTC's GE 1.5-MW wind turbine and operated in 2018. The instrumentation included sensors to measure rotational speed in rpm, bending moments, and torque on the gearbox's high-speed shaft and slip ring. The mechanical loading data was collected from the rotational frame. The mechanical loading data stream is GPS-synchronized with NREL's medium-voltage data-acquisition system, so mechanical and electrical time series data can be aligned and analyzed during post-processing.

Several dozens of inertial tests were conducted with the GE 1.5-MW wind turbine in CGI-connected mode under severe frequency events (1 Hz decline in frequency with 1 Hz/s ROCOF setting). Some representative test results are shown in Figure 32 through Figure 35 with measured traces for electric frequency, turbine active power, high-speed shaft torque, and speed. During all inertial tests we did not observe any significant impacts of inertial control on the gearbox loading. In fact, any high-speed shaft torque changes during inertial response do not seem to be any more "severe" than torque variations caused by wind-speed turbulence conditions at the NWTC. These results confirm theoretical findings from prior NREL research and demonstrate that provision of inertial response by wind power is not going to become a cause of O&M cost increases if wind power is required to regularly provide inertial response in power systems.

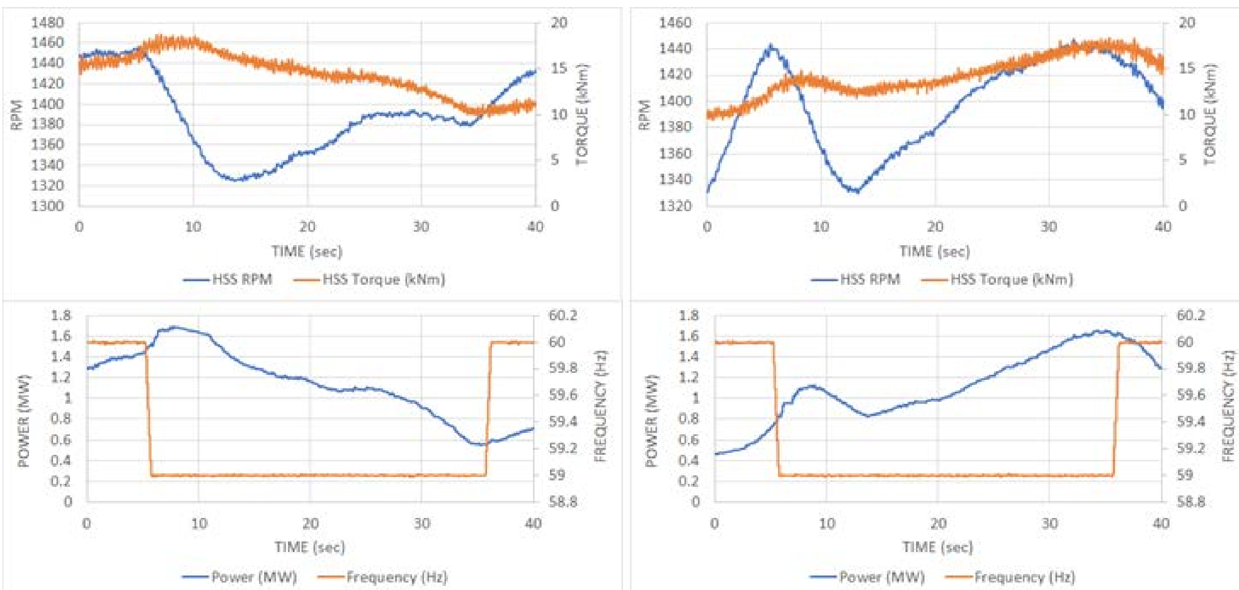

Figure 32. Measured electric power and high-speed shaft torque during inertial response; Test 1 (left) and Test 2 (right)

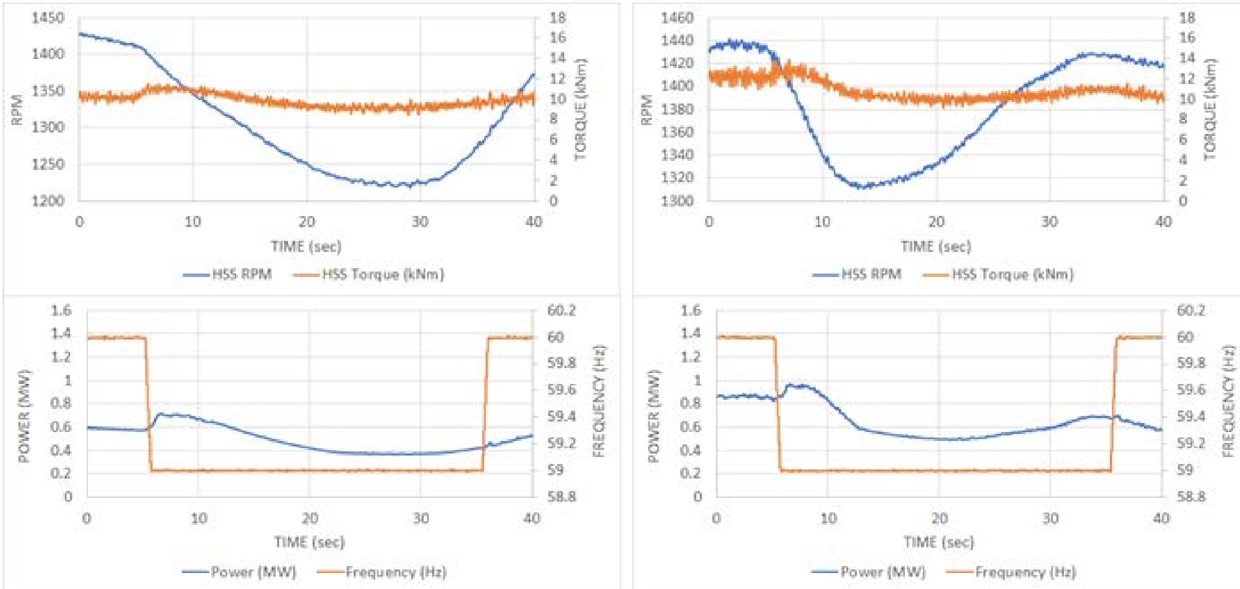

Figure 33. Measured electric power and high-speed shaft torque during inertial response; Test 3 (left) and Test 4 (right)

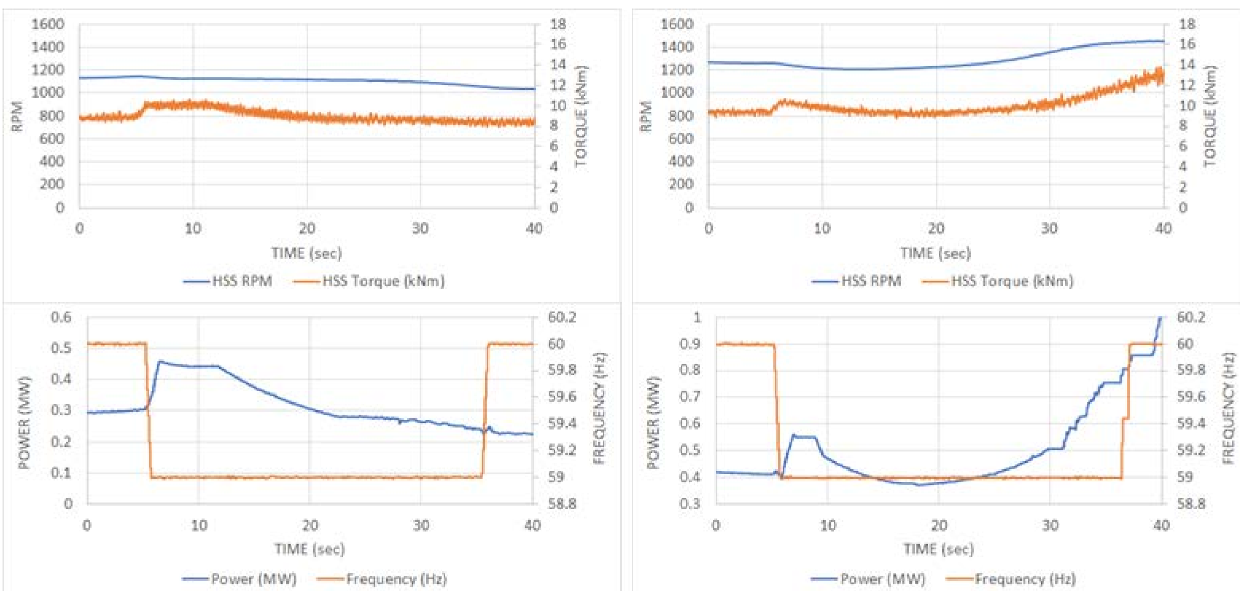

Figure 34. Measured electric power and high-speed shaft torque during inertial response; Test 5 (left) and Test 6 (right)

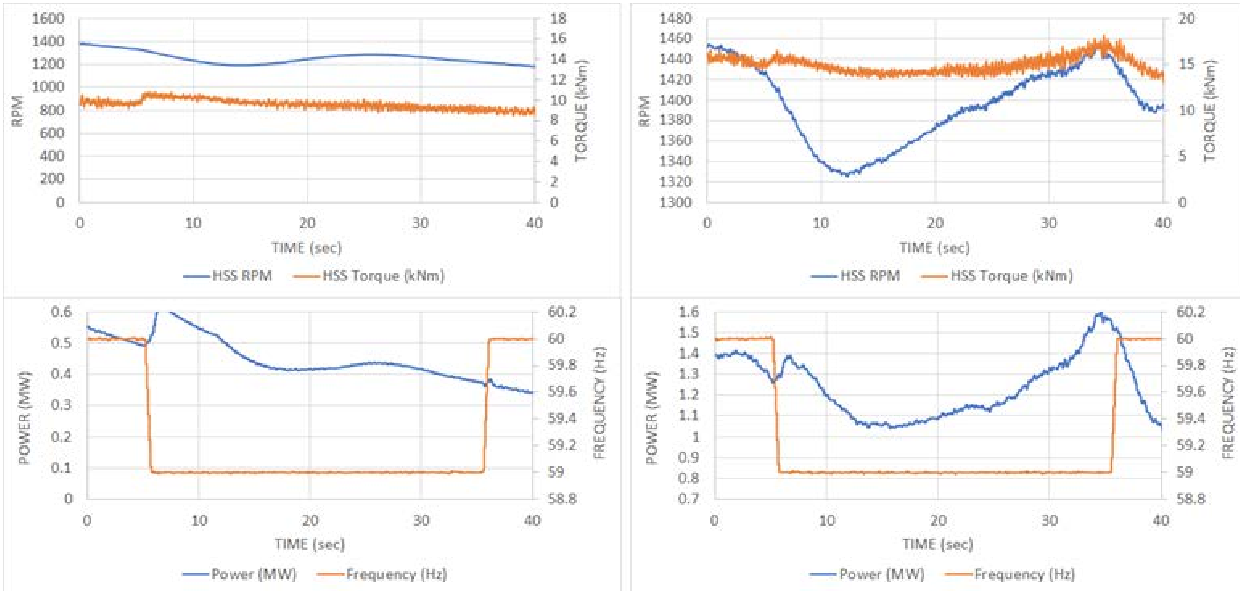

Figure 35. Measured electric power and high-speed shaft torque during inertial response; Test 7 (left) and Test 8 (right)

4.0 Understanding the Symbiotic Operation of Wind, Battery, and Variable-Frequency Drive Motor Loads to Support Frequency

4.1 Introduction

The progressive incorporation of converter-based generation is displacing synchronously connected machines which provide natural inertial response. The reduction of inertia constants negatively impacts the performance of power systems because relatively large load-generation unbalances can cause relatively large frequency deviations from nominal. Therefore, the risk of activating predefined schemes for underfrequency load-shedding (UFLS) during these disturbances increases, which is detrimental for the reliability of bulk power systems. To address this problem, we study the symbiotic operation of controllable wind, pumping, and battery stations to provide synthetic inertia and droop response to prevent large frequency deviations. To this end, we derive relatively simple models of these assets that are helpful to simulate and understand their positive influence on the power system frequency response. A singular component of the study is that it considers the impact of wake effects on the performance of wind turbines because the upstream wind speed observed by each turbine influences its dynamic behavior when providing synthetic inertia.

The power system frequency or simply "frequency" is the number of complete cycles that quasi-steady state voltage or current waveforms repeat during a specified period [13]. Frequency commonly is estimated at particular locations of a power system as being indicative of system generation-load equilibrium [14]. Although frequency can reflect the average speed of interconnected synchronous machinery [15], this metric: (a) is not linked to any particular physical equipment [1] and (b) is meaningful only if a power system is in quasi-steady state [16]–[17], for example, when not riding through a transmission fault [19]–[21]. A time-domain frequency trajectory, $f(t)$ for $t \in (t_0, t_d]$, as a result of loss of generation is illustrated in Figure 36.

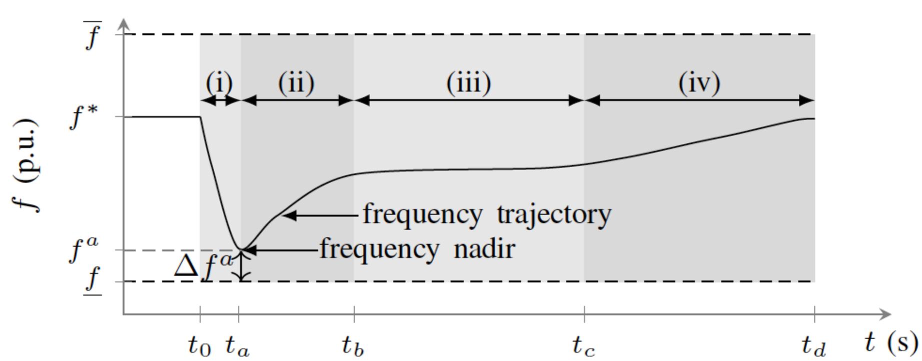

Figure 36. Illustration of a frequency trajectory $f(t)$ for all $t \in (t_0, t_d]$ [22]

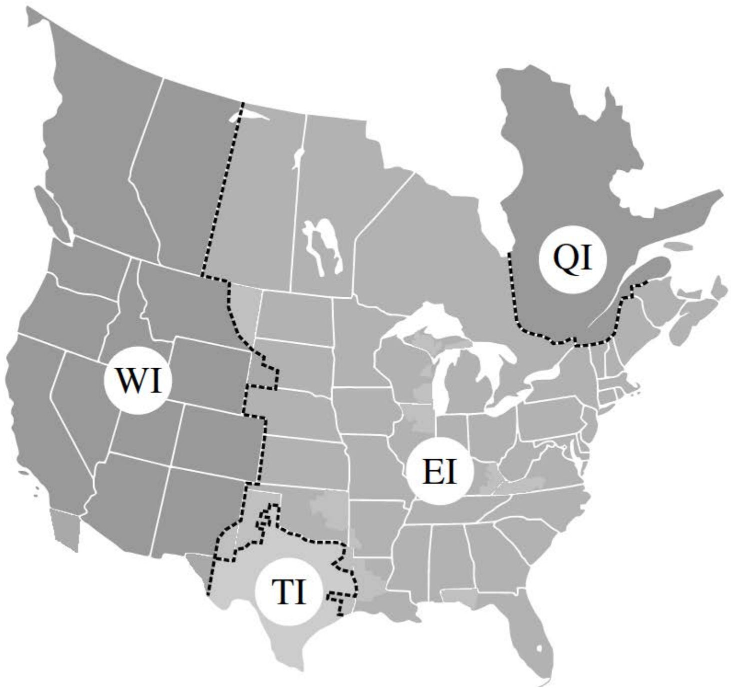

Figure 37. Major North American interconnections: Western Interconnection (WI), East Interconnection (EI), Texas Interconnection (TI), and Quebec Interconnection (QI).

Typically, a frequency trajectory is characterized by [22] the following.

- An *arresting* period in which deviations of $f(t)$ from a stablished set point f^* (e.g., $f^* = 60$ Hz) is being hindered by the response of rotor inertial dynamics, frequency-sensitive assets, and initial action of slow acting controls.
- A *rebound* stage which materializes because speed controls notoriously steer machine rotors to a common synchronous speed which typically is greater than the minimum reached frequency or frequency nadir, for example, $f(t) = f^a$ at $t = t_a$.
- A *stabilization* phase in which rotors achieve a relatively constant speed which "droops" slightly from f^* and purposely conceived to achieve speed regulation harmony.
- A *recovery* period where frequency is steered toward f^* by action of AGC, for example, $f(t) \rightarrow f^*$ for $t \in [t_c, t_d]$.

To defend a power system against load-generation mismatches that cause significant frequency excursions, protective relays usually are employed to shed load or trip generation, for example, if $f(t) < \underline{f}$ or $f(t) > \underline{f}$ in Figure 36, respectively.

To avoid unnecessary disconnections, it is critical to ensure via suitable control strategies that $f(t) \in \left[\underline{f}, \overline{f}\right]$ at all times. Of particular importance is the power system risk associated to underfrequency excursions, which is measured via the margin $\Delta f^a = f^a - \underline{f}$ [9] (Figure 36). This indicates how close the execution of underfrequency load-shedding (UFLS) is during a disturbance, being $\Delta f^a \leq 0$ undesirable.

In 2017, a lowest frequency nadir of $f^a = 59.697$ Hz has been reported for the Western Interconnection in North America (*see* Figure 37) caused by 2,650-MW load-generation unbalance [22]. This nadir implies $\Delta f^a = 0.197$ Hz because a first step for UFLS is planned in the Western Interconnection if $f(t) < \underline{f} = 59.5$ Hz [9]. Notably, the margin $\Delta f^a = 0.197$ Hz has worsened with respect to those in 2015 and 2016, which were 0.345 Hz and 0.319 Hz, respectively. Additionally, the progressive penetration of renewable power sources is projected to negatively impact this metric as displacing synchronous generation inertia [22]–[24]. In view of the aforementioned metric trend and projected changes in the generation mix, the development of methods to minimize the risk of activating UFLS (or improve Δf^a) via frequency responsive reserves is still a significant and timely problem to address [22]–[24].

The available literature that studies the improvement of the margin Δf^a using renewable generation and responsive demand assets is extensive and diverse (*see, e.g.,* [24]–[29]). The most common and effective technique is to apply controls that are sensitive to the ROCOF, that is, df/dt [23], [26], [28]. The objective of this strategy is to *impede* significative changes of $f(t)$ during the arresting period by controlling relatively fast-acting generation and load assets in proportion to the ROCOF. In power engineering, this classical derivative control strategy [30], [31]is called artificial inertia, inertia emulation, synthetic inertia, and virtual inertia [23], [26], [27], [28], [32], to name a few. In addition to this strategy, droop controls, that is, regulators proportional to frequency deviations $f^* - f(t)$, could be furnished to support the frequency-stabilization phase.

This section studies the operational symbiosis of frequency-responsive technologies and its impact on frequency performance. In particular, we illustrate via simulations that wind, pumping, and storage stations can provide a significant amount of synthetic inertial response, hence causing positive impacts on the power system frequency. In contrast to available literature we consider the aerodynamic wake effects, because the upstream wind speed observed by each wind turbine influences how fast the harvested power can change when providing synthetic inertia. This is problematic to the power system frequency because the amount of extracted aerodynamic power reduces after rotor speed changes, given that the turbine was operating optimally. To compensate for this behavior until regaining optimality after a frequency event, pumping stations controlled by speed drives can be furnished with droop frequency controls in addition to synthetic inertia regulators. This rationale implies that pumped flow will be impacted momentarily in proportion to the ROCOF and the magnitude of frequency deviations which cannot be deemed problematic for irrigation subsystems, for example.

Section 4.2 briefly describes dynamic models of conventional generation as well as measurements of frequency and ROCOF from the modeled variables. Section 4.3 presents a model of a WPPs that recognized wake effects for frequency studies. Section 4.4 describes dynamic models of a pumping and battery stations. Section 4.5 develops illustrative case studies to show the positive impacts of controllable assets on frequency. Section 4.6 concludes the exposition.

4.2 Preliminary Assumptions

This section considers a low-order system frequency response model comprising of a mix of gas, steam, hydro, and wind power generation, as well as battery storage and motor loads [14]. For expositional simplicity, controls of other generation technologies (e.g., photovoltaic operating at maximum power point tracking) are considered insensitive to frequency events. The variables that follow in this section represent deviations from an equilibrium operating condition, and are normalized with respect to given speed, ω_b, and volt-ampere, S_b, bases.

The dynamics of the average system speed are [14] showing in Equation 4.1.

$$\frac{d}{dt}\omega_e = \frac{1}{2H}(P_G + P_S + P_H + P_W + P_B - P_P - P_D - D\omega_e) \tag{4.1}$$

Where H and D capture system inertia and damping constants. The variables P_G, P_S, P_H, P_W, P_B represent the power generated by gas, steam, hydro, wind turbines, and battery storage. The variables P_P and P_D

model the power demand of a pumping station and generation-load disturbances occurring by generation disconnection, respectively. In the small-signal sense, we note that

$$\omega_e \approx \frac{f - f^*}{f^*} \tag{4.2}$$

with f and f^* discussed in the Introduction.

4.2.1 Conventional Generation

Gas power generation is modeled by Equation 4.3 [33].

$$P_G = k_g W_f \tag{4.3}$$

Where the dynamics of gas fuel-flow, W_f, are:

$$\frac{d}{dt} W_f = \frac{1}{\tau_f}\left(-W_f + W_f^*\right). \tag{4.4}$$

The command, W_f^*, is from a proportional-integral regulator:

$$W_f^* = K_{g,P}\left(-\omega_e - R_g P_G + R_g P_G^*\right) + z_g \tag{4.5}$$

$$\frac{d}{dt} z_g = K_{g,I}\left(-\omega_e - R_g P_G + R_g P_G^*\right) \tag{4.6}$$

that considers power droop R_g and AGC command P_G^*.

Steam generation is represented by the following [15].

$$P_S = K_m\left(P_r - \frac{F_h}{R_s}\omega_e + F_h P_S^*\right) \tag{4.7}$$

$$\frac{d}{dt} P_r = \frac{1}{\tau_r}\left(-P_r - \frac{1 - F_h}{R_s}\omega_e + (1 - F_h) P_S^*\right) \tag{4.8}$$

Where R_s is a power-droop constant and P_S^* is an AGC command.

An ideal hydro turbine is modeled with [16]:

$$\frac{d}{dt} P_H = -\frac{2}{\tau_w}\left(P_H - P_v + \tau_w \frac{d}{dt} P_v\right) \tag{4.9}$$

and its control is accomplished with the speed-droop governor:

$$\frac{d}{dt} P_v = \frac{1}{\tau_v}\left(-P_v + P_c + \frac{\tau_{c,1}}{\tau_{c,2}}\left(P_c^* - P_c\right)\right) \tag{4.10}$$

$$\frac{d}{dt} P_c = \frac{1}{\tau_{c,2}}\left(-P_c + P_c^*\right) \tag{4.11}$$

$$P_c^* = P_H^* - \frac{\omega_e}{R_h} \tag{4.12}$$

having transient droop compensation control via the state P_c [34]. The power command P_H^* is also set by an AGC command.

The AGC control is modeled by

$$\frac{d}{dt}P_A = -B\omega_e \tag{4.13}$$

$$\frac{d}{dt}P_F = \frac{1}{\tau_a}(-P_F + P_A)\,. \tag{4.14}$$

Thus, $P_G^* = \gamma_G P_F$, $P_S^* = \gamma_S P_F$, and $P_H^* = \gamma_H P_F$ in (4.5)-(4.6), (4.7)-(4.8), and (4.12) , respectively. The time constant τ_a models the delayed response of generating units to the AGC commands. The AGC participation factors $\gamma_G, \gamma_S, \gamma_H \geq 0$ of each conventional generator satisfy $\gamma_G + \gamma_S + \gamma_H = 1$.

4.2.2 Frequency Measurement and ROCOF Approximation

Measured frequency for control purposes is modeled by:

$$\frac{d}{dt}\tilde{\omega}_e = \frac{1}{\tau_e}(-\tilde{\omega}_e + \omega_e) \tag{4.15}$$

because low-pass filters are recommended to damp sub-cycle frequency transients (not modeled here) [20]. A frequency dead zone, to avoid unnecessary control action for relatively small frequency deviations, is modeled with:

$$f_e = \begin{cases} \tilde{\omega}_e - d_\omega & \text{if } \tilde{\omega}_e > d_\omega \\ \tilde{\omega}_e + d_\omega & \text{if } \tilde{\omega}_e < -d_\omega \\ 0 & \text{otherwise} \end{cases} \tag{4.16}$$

for $d_\omega = 2.5 \cdot 10^{-4}$ p.u. (or 15 mHz) in North America.

The measured ROCOF is approximated with Equation 4.17 [18].

$$\frac{d}{dt}f_e \approx \dot{\tilde{f}}_e = \frac{1}{\epsilon}(f_e - f_d) \tag{4.17}$$

Where

$$\frac{d}{dt}f_d = \frac{1}{\epsilon\tau_d}(-f_d + f_e) \tag{4.18}$$

for appropriate choices of τ_d and ϵ (usually $\epsilon = 0.1$). The approximation (4.17) commonly is adopted in derivative control loops to realize proper transfer functions [31].

To simplify exposition in the next sections, the measured frequency, f_e, in (4.15) and ROCOF estimation, $\dot{\tilde{f}}_e$, in (4.17) are assumed to be the same for any frequency-sensitive control system.

4.3 Wind Power Plant Model

We consider a WPP composed of I equal turbines. The harvested power by an i-th turbine, $i = 1, \ldots, I$, is [35]:

$$P_{m,i} = \pi\frac{\rho}{2}C_p(\lambda_i, \beta_i)R_w^2 v_{w,i}^3,\ \ \lambda_i = \frac{R_w\omega_i}{v_{w,i}} \tag{4.19}$$

with ρ the air density, C_p a performance coefficient, λ_i the tip-speed ratio, ω_i the turbine angular speed, $v_{w,i}$ the turbine's observed upstream wind speed (no necessarily equal for all $i = 1, \ldots, I$ as a result of wake effects), β_i the blade pitch angle, and R_w the radius of the blade sweeping area. A single-mass rotational dynamic model of the i-th turbine-generator system is given in Equation 4.20.

$$\frac{d}{dt}\omega_i = \frac{1}{J_w}T_{a,i} \text{ with } T_{a,i} = T_{m,i} - GT_{e,i}\,. \tag{4.20}$$

Here, $T_{a,i}$ is the net torque whereas $T_{m,i} = P_{m,i}/\omega_i$ and $T_{e,i}$ are the mechanical and electromagnetic torques produced by the wind turbine and its generator, respectively. The constant J_w models the inertia of the turbine-generator assembly observed at the wind turbine shaft. A nondynamic gearbox model is considered, hence the generator to wind turbine rotor speed ratio is $G = \omega_{r,i}/\omega_i$.

Considered mechanical operational constraints are:

$$\omega_i(t) \in [\underline{\omega}, \overline{\omega}] \text{ and } T_{a,i}(t) \in [-\overline{T}_a, \overline{T}_a] \tag{4.21}$$

because the rotatory components are designed for a limited range of speed and mechanical stress [23].

4.3.1 Blade Pitch Angle Control

The servo-motor controlled dynamics of β_i in (4.19) are

$$\frac{d}{dt}\beta_i = \begin{cases} R_\beta & \text{if } R_\beta < \dfrac{(-\beta_i + \beta_i^*)}{\tau_\beta} \\ -R_\beta & \text{if } -R_\beta > \dfrac{(-\beta_i + \beta_i^*)}{\tau_\beta} \\ \dfrac{(-\beta_i + \beta_i^*)}{\tau_\beta} & \text{otherwise} \end{cases} \tag{4.22}$$

where R_β the slew rate limits of servomotors. To ensure $\omega_i(t) \leq \overline{\omega}$ (e.g., during relatively high wind speed conditions), the blade-pitch angle is commanded by

$$\beta_i^* = \begin{cases} \overline{\beta} & \text{if } \beta_i^{**} > \overline{\beta} \\ 0 & \text{if } \beta_i^{**} < 0 \\ \beta_i^{**} & \text{otherwise} \end{cases} \tag{4.23}$$

where

$$\beta_i^{**} = K_{c,\beta}(\omega_i - \overline{\omega}) + \beta_{c,i} \tag{4.24}$$

$$\frac{d}{dt}\beta_{c,i} = \frac{1}{\tau_{c,\beta}}\left(-\beta_{c,i} + \beta_i^*\right) \tag{4.25}$$

is an anti-windup proportional-integral regulator.

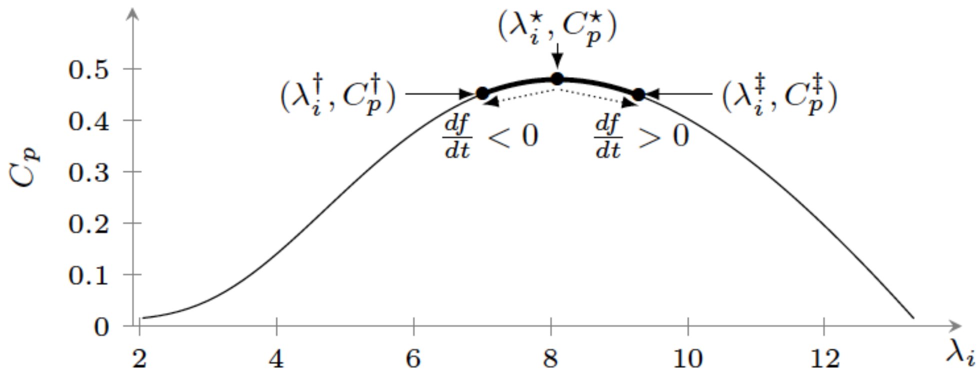

Figure 38. Performance coefficient as function of tip-speed ratio with optimal pair $(\lambda_i^\star, C_p^\star) = (8.1, 0.48)$ for $\beta_i = 0°$.;The pair $(\lambda_i^\star, C_p^\star)$ can progressively move toward $(\lambda_i^\dagger, C_p^\dagger)$ or $(\lambda_i^\ddagger, C_p^\ddagger)$ as a result of contributing with synthetic inertia during underfrequency or overfrequency events, respectively

4.3.2 Electromagnetic Torque and Synthetic Inertia Control

To operate optimally and emulate synthetic inertia, the control command to regulate $T_{e,i}$ in (4.20) is:

$$T_{e,i}^{*} = T_{e,i}^{\star} + T_{f,i}^{*} \tag{4.26}$$

where: (*i*) the optimal torque command [22], [37]:

$$T_{e,i}^{\star} = k_w^{\star} \omega_i^2 \text{ with } k_w^{\star} = \frac{\pi\rho}{2G} R_w^5 \frac{C_p^{\star}}{\lambda_w^{\star 3}} \tag{4.27}$$

regulates ω_i so that the pair (λ_i, C_p) of (4.19) is ideal to harvest maximum wind power (*see, e.g.,* $(\lambda_i^\star, C_p^\star)$ Figure 38), and (ii) the synthetic-inertia torque command:

$$T_{f,i}^{*} = \begin{cases} \overline{T}_a/G & \text{if } T_{f,i} > \overline{T}_a/G \\ \underline{T}_a/G & \text{if } T_{f,i} < -\overline{T}_a/G \\ T_{f,i} & \text{otherwise} \end{cases} \tag{4.28}$$

with

$$T_{f,i} = -\kappa_W \left(\frac{\overline{T}_a}{G}\right) \dot{\tilde{f}}_e \tag{4.29}$$

is conceived to support the grid during frequency events. Note in (4.29) that $T_{f,i}$ is proportional to the approximation of the ROCOF in (4.17) and $\kappa_W > 0$ is an emulated inertia constant.

The generator electromagnetic torque, $T_{e,i}$, in (4.20) is modelled by:

$$T_{e,n} = \begin{cases} \min\{\frac{S_{w,max}}{G\omega_i}, T_{e,n}^{*}\} & \text{if } T_{e,n}^{*} \geq 0 \\ \max\{-\frac{S_{w,max}}{G\omega_i}, T_{e,n}^{*}\} & \text{if } T_{e,n}^{*} < 0 \end{cases} \tag{4.30}$$

because controls are designed to follow relatively fast (with respect to the time scale of interest herein) the command $T_{e,i}^{*}$ in (4.26) without surpassing the wind turbine (generator and power electronics) rated power $S_{w,max}$.

The total WPP generated power for (4.1) is:

$$P_W = \frac{\eta_w}{S_b} \sum_{i=1}^{I} (\,\omega_i G T_{e,i} - P_{m,i0}) \tag{4.31}$$

with $P_{m,i0}$ the i-th predisturbance wind turbine power, which remains fixed throughout the study. An aggregate efficiency factor $\eta_w \in (0,1)$ is introduced to capture power losses in the WTGs and power electronics.

4.3.3 Turbine Wind Speed and Wake Effects

Pretransient wind speed $v_{w,i}$ impacts the rate of change of tip-speed ratio, λ_i in (4.19), during variations of ω_i, that is:

$$\frac{d}{dt}\lambda_i = \left(\frac{R_w}{v_{\omega_i}}\right)\frac{d}{dt}\omega_i \,. \tag{4.32}$$

In particular, tip-speed ratio changes caused by fluctuations of the rotor speed will be more sensitive during relatively low wind speeds (assuming they remain constant). Hence, the harvested wind power will change accordingly during frequency events because λ_i impacts the performance coefficient C_p (*see* Equation 4.19).

To estimate the upstream wind speed observed by each wind turbine, we consider the wake effects which can be modeled using various approaches [38]. These aerodynamic interactions occur because energy extraction by the blades of a wind turbine can reduce the upstream wind speed observed by others. The Jensen wake model is considered here because it models the wake behavior relatively well [38]. We calculate [39]:

$$v_{w,i} = v_{w,\infty}\left(1 - \sqrt{\sum_{j=1}^{N} w_{ij}^2}\right) \tag{4.33}$$

where $v_{w,\infty}$ is the WPP upstream wind speed and

$$w_{ij} = \frac{a_{ij}}{\pi r_{w,ij}^2}\left[1 - \sqrt{1 - C_t(\lambda_j, \beta_j)}\right] \tag{4.34}$$

models the wake deficit factor induced by a j-th turbine on an i-th one. The wind stream geographical direction is SϕW with ϕ a director angle. The immediate previous formulation uses [39] the following.

$$a_{ij} = \begin{cases} 0 & \text{if } d_{ij} > 2R_w + \alpha x_{ij} \\ \pi R_w^2 & \text{if } d_{ij} < \alpha x_{ij} \\ \psi_{ij} & \text{otherwise} \end{cases} \tag{4.35}$$

$$\psi_{ij} = r_{w,ij}^2 \overset{-1}{\cos}\left(\frac{b_{ij}}{r_{w,ij}}\right) + R_w^2 \overset{-1}{\cos}\left(\frac{d_{ij} - b_{ij}}{R_w}\right) - \frac{d_{ij} z_{ij}}{2} \tag{4.36}$$

$$r_{w,ij} = R_w + \alpha x_{ij} \,. \tag{4.37}$$

The physical significance of some of these variables is illustrated in. Pelletier et al. [26]. In particular, we note in (4.34) that $C_t(\lambda_j, \beta_j)$ is the thrust coefficient of a j-th turbine, a_{ij} is the area of the i-th turbine rotor disk intersecting the wake of the j-th turbine, and $r_{w,ij}$ is the wake radius caused by a j-th turbine and observed by an i-th one.

4.3.4 Wind Turbine Speed Recovery Operation

To provide synthetic inertia when $\dot{\hat{f}}_e < 0$, $T_{f,i}^* > 0$ of Equation 4.28 momentarily increases the injection of generated power to the grid. This nonetheless causes deceleration of the rotating masses of the wind turbine assembly, that is, $d\omega_i/dt < 0$ and $d\lambda_i/dt < 0$ (4.32). Hence, the optimal pair $(\lambda_i^\star, C_p^\star)$ is driven progressively toward a suboptimal pair $(\lambda_i^\dagger, C_p^\dagger)$ as illustrated in Figure 38. To regain optimality after the frequency arresting and stabilization period (i.e., when $\dot{\hat{f}}_e \approx 0$), the rotor needs to reaccelerate(i.e., $d\omega_i/dt > 0$) which requires lowering slightly the generated electric power supplied to the grid. Similarly, when $T_{f,i}^* < 0$ caused by $\dot{\hat{f}}_e > 0$ [36], the optimal pair $(\lambda_i^\star, C_p^\star)$ moves toward $(\lambda_i^\ddagger, C_p^\ddagger)$ as depicted in Figure 38. To regain the optimum, electric power generation must slightly increase so that $d\omega_i/dt < 0$.

The aforementioned operation is conflicting because extracted wind power will decrease with respect to its initial generation magnitude during low-frequency events, for example. Such undesirable behavior nonetheless can be compensated for by using pumping stations with motors controlled by speed drives. Further, battery storage systems can be employed to boost the power and compensate power loss during wind-generation recovery.

4.4 Motor Loads and Battery Storage

This section considers pumping and storage power stations interfaced by fully rated converters.

4.4.1 Fully Controllable Motor Loads

We model a pumping station composed of N equal capacity motor-driven centrifugal pumps. Breaking power developed by an n-th ($n = 1, \dots, N$) pump is modeled in Equation 4.38 [30].

$$P_{p,n} = P_{r,n} \left(\frac{\omega_{p,n}}{\omega_{r,n}}\right)^3 . \tag{4.38}$$

The constant $P_{r,n}$ is a reference breaking power at a reference speed $\omega_{r,n}$ as to develop a particular differential pressure and flow (given by pump characteristic tables). The density of the pumped fluid is assumed invariant for the study.

The rotor speed dynamics are modeled by the following.

$$\frac{d}{dt}\omega_{p,n} = \frac{1}{J_p}\left(T_{e,n} - T_{p,n}\right) \tag{4.39}$$

With $T_{e,n}$ the electromagnetic torque induced by the driving motor and $T_{p,n} = P_{p,n}/\omega_{p,n}$ the pump breaking torque. The combined motor-pump rotating mass have inertia constant J_p.

The electromagnetic torque for (4.39) (positive power flow is from battery to grid)

$$T_{e,n} = \begin{cases} \min\{\dfrac{S_{p,max}}{\omega_{r,n}}, T^*_{e,n}\} & \text{if } T^*_{e,n} \geq 0 \\ \max\{-\dfrac{S_{p,max}}{\omega_{r,n}}, T^*_{e,n}\} & \text{if } T^*_{e,n} < 0 \end{cases} \tag{4.40}$$

is regulated by a power converter with rating limit, $S_{\max,p}$, whose torque command, $T^*_{e,n}$, originates from a proportional-integral regulator.

$$T^*_{e,n} = K_P\left(\omega^{**}_{p,n} - \omega_{p,n}\right) + z_{p,n} \tag{4.41}$$

$$\frac{d}{dt} z_{p,n} = \frac{K_P}{\tau_P}\left(\omega^{**}_{p,n} - \omega_{p,n}\right). \tag{4.42}$$

Here, the filtered commanded speed [31] is shown in Equation 4.43.

$$\frac{d}{dt}\omega^{**}_{p,n} = \frac{1}{\tau_\omega}\left(-\omega^{**}_{p,n} + \omega^*_{p,n}\left(1 + K_{p,D} f_e + K_{p,I}\dot{\tilde{f}}_e\right)\right) \tag{4.43}$$

With $\omega^*_{p,n}$ a specified speed set-point by the pump operator, f_e of (4.16), and $\dot{\tilde{f}}_e$ of (4.17). The filter time constant, τ_w, is used to prevent hammering in the pumps. Note in (4.43) that during frequency events f_e and $\dot{\tilde{f}}_e$ cause the commanded $\omega^{**}_{p,n}$ to droop from $\omega^*_{p,n}$. Further, the tunable constants $K_{p,D}$ and $K_{p,I}$ are used to provide frequency droop and inertial response, respectively. The frequency droop capability is attractive to support wind turbines to regain optimality after providing synthetic inertia without negatively impacting the power system. Please, refer to Section 4.

The power withdrawn by the pumping station is:

$$P_P = \frac{1}{\eta_p S_b}\sum_{n=1}^{N}\left(\omega_{p,n} T_{e,n} - P_{r,n}\right) \tag{4.44}$$

with $\eta_p \in (0,1)$ an efficiency factor because of losses in the energy conversion subsystem. The impact of motor speed changes on per-unit pumping flow changes is modeled with the following [27].

$$Q_{p,n} = \frac{\omega_{p,n}}{\omega_{p,r}} - 1\,. \tag{4.45}$$

The latter expression signifies that the pumped flow will be impacted momentarily during frequency events which could be acceptable for irrigation subsystems.

4.4.2 Fully Controllable Battery Station

The battery station layout is composed of various battery racks, each interfacing to the power system via a power converter. For expositional simplicity, the battery station is represented by a single battery rack and converter. (A holistic battery station dynamic model can be found in Schimpe *et al.* [41].) The battery station power P_B for (4.1) (e.g., measured at the ac-side terminals of the converter) is modeled by (assuming ideal generator torque control) the following.

$$\frac{d}{dt}P_B = \frac{1}{\tau_B}\left(-P_B + P^*_B\right) \tag{4.46}$$

$$P_B^* = -\kappa_B \dot{\hat{f}}_e \tag{4.47}$$

with $P_B^* \in [-P_{B,r}, P_{B,r}]$ and $P_{B,r}$ the total battery station converter rating. The command P_B^* is nonzero only when providing synthetic inertia because this variable depends on the ROCOF approximation in (4.17). The time constant τ_B is used to not abruptly charge or discharge the battery and κ_B is a synthetic inertia constant. Changes of the state-of-charge (or stored energy) is modeled with:

$$\frac{d}{dt}E_B = \begin{cases} -\dfrac{1}{\eta_B}P_B & \text{if } P_B \geq 0 \\ -\eta_B P_B & \text{if } P_B < 0 \end{cases} \tag{4.48}$$

4.5 Case Studies

We demonstrate the positive impacts by the combined operation of WPPs as well as pumping stations and battery storage on the power system frequency. These assets are furnished with synthetic inertia and droop controls as modeled in Section 4.3 through Section 4.4. We consider a power system composed of 8% wind, 39% gas, 15% steam, and 27% hydro generation to resemble the generation mix of the Western Interconnection [42]. The remaining 11% of generation is assumed to be supplied by non-inertial generation sources that do not have frequency-sensitive controls, for example, photovoltaic power generation operating at maximum power point tracking. The total generation capacity of the considered power system is 562.5 MW. The system bases are $S_b = 100$ MVA and $\omega_b = 120\pi$ rad/s. Parameters of the gas, steam, and hydro generation models of Section 4.2 as well as frequency-related measurements are shown in Table 3.

Table 3. Parameters for Conventional Plants and ROCOF Measurement

Parameter	Value	Unit	Parameter	Value	Unit
R_g	0.0228	p.u.	τ_f	0.2	s
$K_{g,P}$	10	p.u.	$K_{g,I}$	5	p.u./sec
R_s	0.0593	p.u.	τ_r	8.0	sec
K_m	0.95	p.u.	F_h	0.3	p.u.
R_h	0.0329	p.u.	τ_w	2.0	sec
$\tau_{c,1}$	9.0	p.u.	$\tau_{c,2}$	117.6	sec
τ_v	0.5	sec	τ_a	0.5	sec
D	2	—	H	36.08	sec
γ_g	0.2	—	γ_s	0.3	—
γ_h	0.5	—	τ_e	3.3	ms
τ_d	40	sec	ϵ	0.1	—
B	0.4	p.u./sec			

The WPP comprises 30 turbines (i.e., $I = 30$), and each of its electromechanical conversion systems is rated $S_{w,max} = 1.5$ MVA. The turbines form a geographical array of six columns and five rows with inter-turbine spacing of $14R_w$. The array columns and rows are parallel to the South and West geographical axes, respectively. The upstream wind speed is $v_{w,\infty} = 8$ m/s, and the wind direction is S5°W, hence $\phi = 5°$. The aforementioned information enables calculation of the upstream wind speed observed by each turbine, as explained in Section 4.3. Relevant turbine data to construct the overall model of Section 3 is presented in Table 4.

Table 4. Parameters for WPP

Parameter	Value	Unit	Parameter	Value	Unit
ρ	1.225	kg/m³	R_w	35.25	m
J_w	4.26810^6	kg·m²	G	97.5	—
R_β	10	Deg/sec	τ_β	0.1	sec
$K_{c,\beta}$	95.49	Deg/(rad/sec)	$\tau_{c,\beta}$	5	sec
$\underline{\omega}$	1.15	rad/sec	$\overline{\omega}$	2.5	rad/sec
$C_p^\star$	0.48	—	$\lambda_w^\star$	8.1	—
κ_W	$36.9 \cdot 10^3$	Nm/(p.u./sec)	α	0.07	—
η_w	0.95	—	$\overline{T}_a$	$1.59 \cdot 10^5$	Nm

The pumping station is made of 40 motor-driven pumps (i.e., $N = 40$), which are actively controlled by $S_{\max,p} = 500$ kVA power converters. The reference braking power $P_{r,n} = 400$ kW and speed $\omega_{r_n} = 180$ rad/s for all $n = 1, \dots, N$. The battery storage system capacity is rated 3.24 p.u. (i.e., 90 kWh in the volt-ampere base $S_b = 100$ MVA) and is interfaced by a set of power converters which combined can provide up to 5 MW (i.e., $P_{B,r} = 0.05$ p.u.). Relevant parameters to model the pumping and battery stations as shown in Section 4 are detailed in Table 5.

Table 5. Parameters for Pumping and Storage Stations

Parameter	Value	Unit	Parameter	Value	Unit
$\omega_{p,n}^*$	180	rad/sec	$\omega_{r,n}$	180	rad/sec
J_p	300	Kg·m²	$P_{r,n}$	400	kW
K_P	$2.98 \cdot 10^3$	Nm/(rad/sec)	τ_P	0.396	sec
τ_W	10	ms	η_p	0.88	—
$K_{p,D}$	5	—	$k_{p,I}$	0.4	—
τ_B	10	ms	κ_B	2	—
η_B	0.8	—			

We simulate the power system frequency response to generation loss $P_d = 0.3$ p.u. (e.g., 30 MW of photovoltaic disconnection) at $t = 50$ sec, q.v. (1.1). To study the individual and some combinatory performance instances of the wind, pumping, and storage assets, we consider seven case studies by activating or deactivating their frequency-sensitive controls as specified in Table 6 . The frequency-sensitive controls are deactivated by setting pertinent control gains to zero. The corresponding traces for each case study are illustrated in Figure 39 through Figure 41. In Table 7, we specify the percentage of the frequency nadir deviation from a nominal set point (i.e., $f^a - f^*$ for $f^* = 100\%$ of 60 Hz) which is obtained from the minimum values of ω_e in Figure 39 for the different cases. Similarly, the UFLS activation margin $\Delta f^a = f^a - \underline{f}$ for $\underline{f} = 99\%$ is presented. It is desirable that $\Delta f^a > 0$ to ensure that UFLS will not be initiated, which also is presented in Table 7.

Table 6. Activation Matrix of Frequency-Sensitive Controls

Asset	Case 0	Case 1	Case 2	Case 3	Case 4	Case 5	Case 6
Wind	No	Yes	No	No	Yes	Yes	Yes
Pump	No	No	No	Yes	No	Yes	Yes
Battery	No	No	Yes	No	Yes	No	Yes

Table 7. Percent Off-Nominal Frequency Deviations

Metric (%)	Case 0	Case 1	Case 2	Case 3	Case 4	Case 5	Case 6
$f^a - f^*$	-1.19	-1.08	-0.99	-0.92	-0.95	-0.89	-0.80
Δf^a	-0.19	-0.08	0.01	0.08	0.05	0.11	0.20
UFLS Risk	Yes	Yes	No	No	No	No	No

In Table 7, Figure 39, and Figure 40, we note that the nadir is improved significantly when all frequency-sensitive controls of the considered assets are active with respect to when all are inactive. On an individual basis, as illustrated in Figure 40, the pumping station provides better frequency support than battery and wind assets because it is capable of reducing the system load by reducing the motor speed (*see, e.g.,* Figure 41). The battery station, conversely, seems to have better impacts on the frequency performance than wind assets because it can sustain the injection of active power during frequency events. This behavior, however, is dependent on the control gains (or synthetic inertia constants) that are chosen for each subsystem. It is interesting to observe in Figure 39 (blue trace for "Case 1") that the net contribution $P_W + P_B - P_P$ resulting from wind only can be negative after providing synthetic inertia—a situation that is explained in Section 4.4. Nonetheless, this impact can be canceled out by using the frequency-sensitive controls of the pumping station; hence, the impact only can become positive. For example, observe that magenta trace for Case 5 in the plot corresponding $P_W + P_B - P_P > 0$, that is, it is always positive which is desirable during frequency events under nominal conditions.

Figure 41 depicts per-unit motor speed and pumped flow deviation as well as the energy stored in the battery system. In the developed case studies, the pumped flow could reduce from 4% to 6% during frequency events, which could have a minor impact on the pumping station operation that serves irrigation systems, for example. Conversely, the stored energy of the battery, E_B, shown in Figure 41, indicates that it can reduce momentarily in 0.75 p.u.-sec (or 20.83 kWh) from its initial state of charge (SOC).

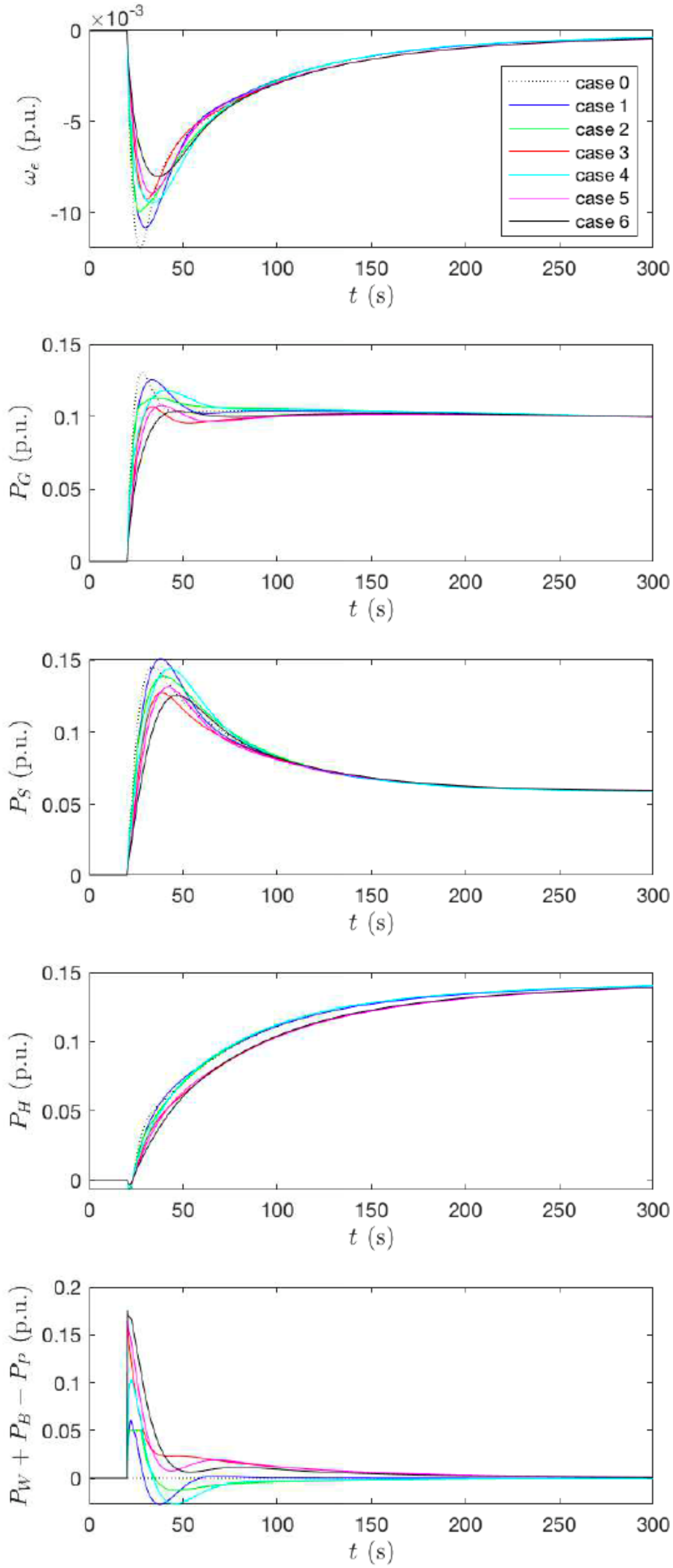

Figure 39. Frequency response of power system to the case studies specified in Table 6

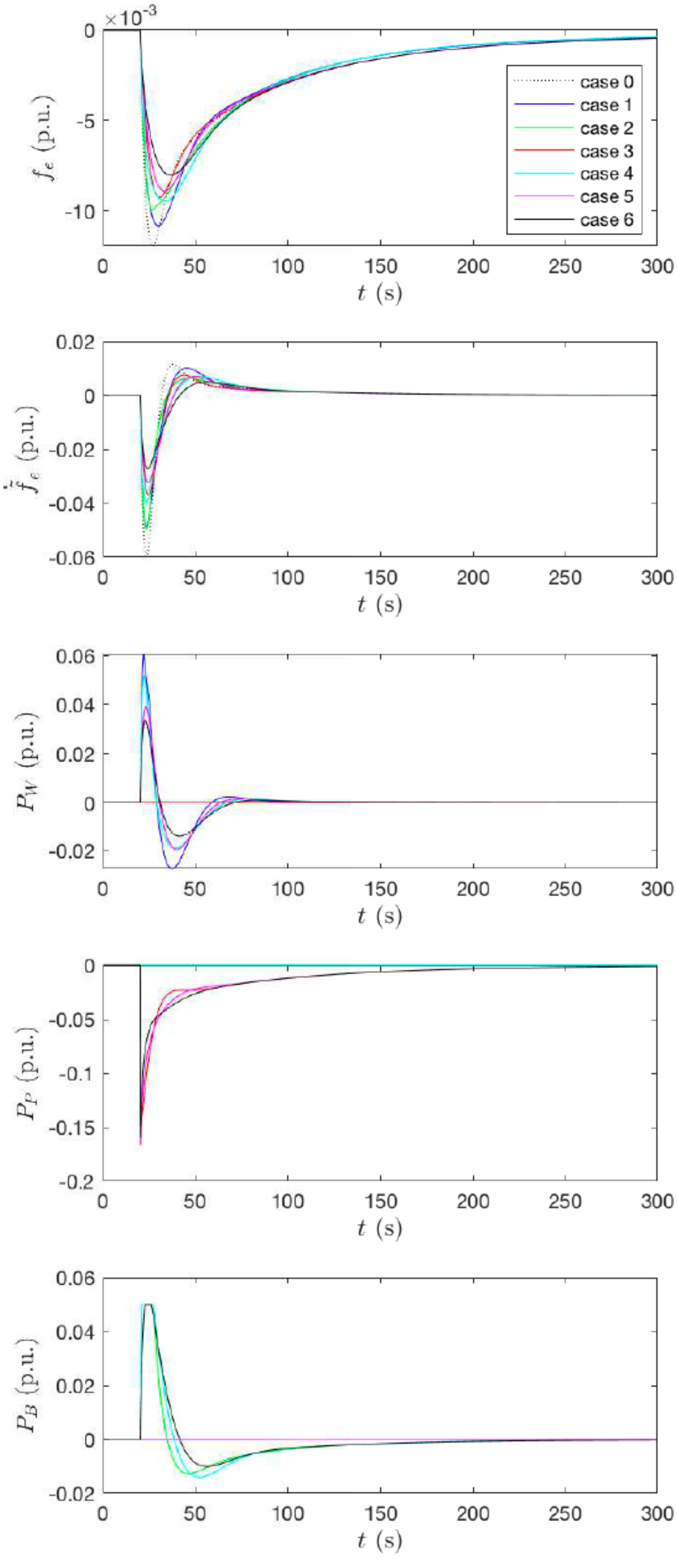

Figure 40. Response of frequency-sensitive assets to the case studies specified in Table 6

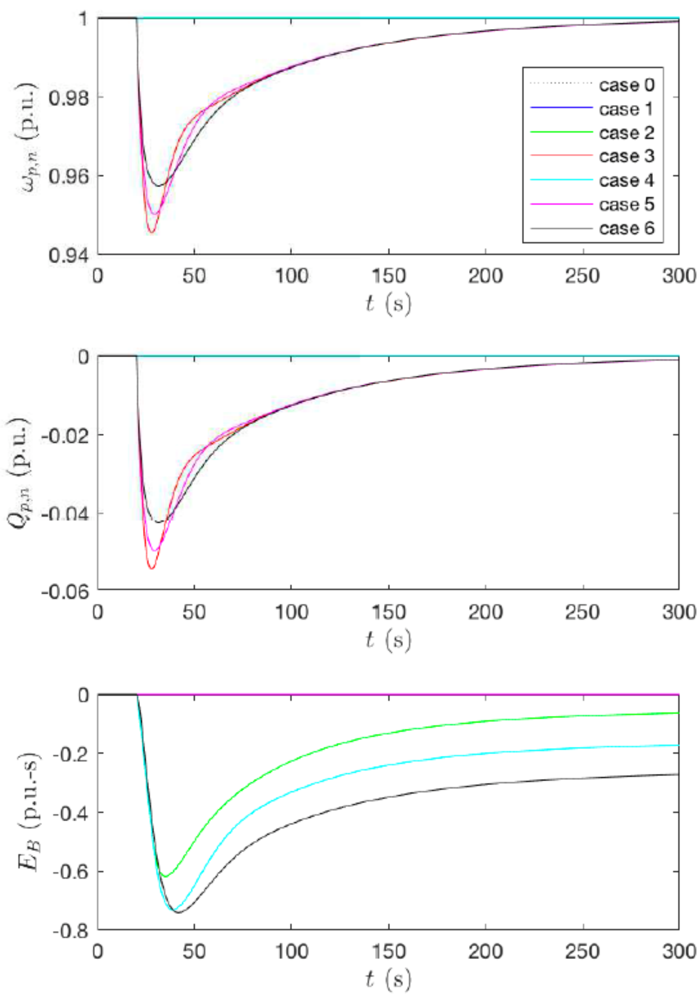

Figure 41. Response of pumping and battery variables to the case studies specified in Table 6

In Figure 42, we observe the response of some variables of interest of the WPP for Case 1. In particular, it is illustrated that the variation of the tip-speed ratio λ_i is different among turbines as depending on the upstream wind speed observed at each turbine, $v_{w,i}$, which is calculated as explained in Section 3. It also can be seen that the performance coefficient C_p in Figure 42 can drop from 0.48 to 0.46 in some turbines which signifies an approximately 4% momentarily loss of extracted wind power. We emphasize that although all wind turbines use the same control strategy to provide synthetic inertia, they behave differently, such as observing different wind speeds because of wake effects.

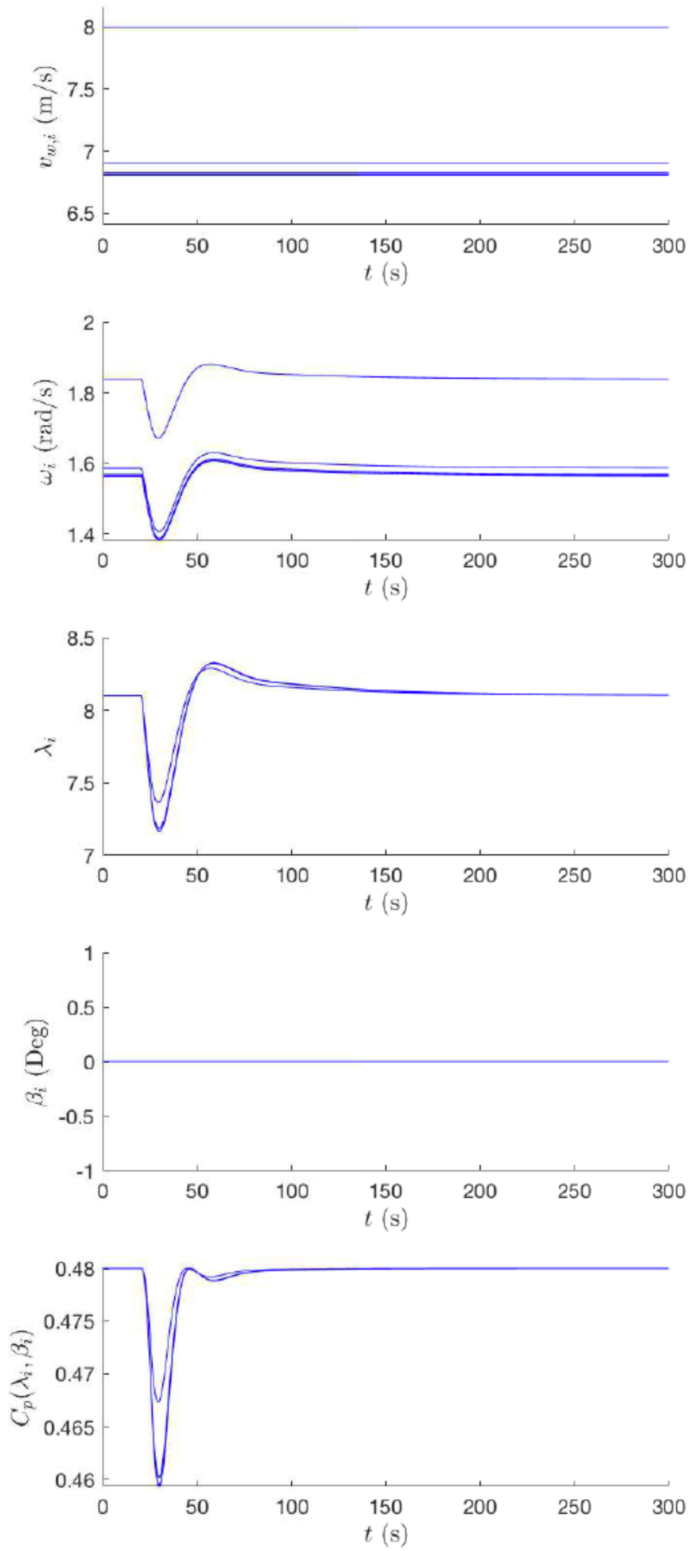

Figure 42. Response of WPP variables to the case study Case 0 specified in Table 6

4.6 Conclusions to Analytical Task

This section has illustrated that the symbiosis of frequency-responsive technologies can notably improve the frequency performance of power systems. In particular, wind, storage, and pumping stations can provide a significant amount of synthetic frequency response to power systems. Here, these technologies have been furnished with control loops that respond in proportion to the ROCOF. Hence, these assets can reliably emulate the inertial response of synchronous machines to frequency events. To compensate for the power changes that wind turbines can introduce when losing optimality after providing synthetic inertia, pumping stations are proposed to be furnished with droop-like frequency control strategies. This control strategy, in addition to synthetic inertia control loop, implies that pumped flow will be impacted momentarily which might not be problematic for irrigation subsystems, for example.

In this work, the control constants that determine the synthetic inertia response for the considered assets originate from rational choices only. A rigorous framework to tune these constants, for example, as a function of displaced synchronous inertia is a future research opportunity. A possible course could be to rely on system identification theory because control constants could be identified to match a desired frequency trajectory in time. Another possibility is to rely on optimal control to minimize the perturbed pumped flow in pumping stations and changes of performance coefficient in wind turbines and maintain the power system frequency within desirable bounds. Another line of research pertains to ascertaining whether a particular penetration of wind, pumping, and battery capacity could be appropriate to compensate the displaced synchronous inertia. In particular, it could be useful to elucidate the capability of these assets to replace synchronous inertia in a one-to-one manner.

4.7 Additional Background Information

This section shows how to select the proportional-integral control constants K_P and τ_P for Equation 4.42 and Equation 4.41. To this end, we use a small signal stability model described below.

$$\frac{d}{dt}\begin{bmatrix}\Delta\omega_{p,n}\\ \Delta z_{p,n}\end{bmatrix} = \begin{bmatrix}\frac{-K_P\omega_{r,n}^2 - 2P_{r,n}}{J_p\omega_{r,n}^2} & \frac{1}{J_p}\\ -\frac{K_P}{\tau_P} & 0\end{bmatrix}\begin{bmatrix}\Delta\omega_{p,n}\\ \Delta z_{p,n}\end{bmatrix} \tag{4.49}$$

Assuming an equilibrium speed $\omega_{p,n} = \omega_{p,n}^{**} = \omega_{r,n}$. The characteristic polynomial of the matrix in Equation 4.49 is shown in Equation 4.50.

$$P(\lambda) = \lambda^2 + \lambda\frac{K_P\omega_{r,n}^2 + 2P_{r,n}}{J_p\omega_{r,n}^2} + \frac{K_P}{\tau_P J_p}. \tag{4.50}$$

To design a critically damped system as to avoid oscillations, the characteristic polynomial must take the form:

$$P(\lambda) = \lambda^2 + 2\omega_o\lambda + \omega_o^2 \tag{4.51}$$

with ω_o the natural frequency of oscillation, hence:

$$\omega_o = \frac{5}{t_{ss}} = \frac{K_P\omega_{r,n}^2 + 2P_{r,n}}{2J_p\omega_{r,n}^2} \tag{4.52}$$

for a desired stabilization time t_{ss}.

In Equation 4.52, it is considered the controlled system stabilizes in five times of its time constant, $\tau_o = 1/\omega_o$, i.e., $t_{ss} = 5\tau_o$. The control constants thus are as follows.

$$K_P = 2J_p\omega_o - \frac{2P_{r,n}}{\omega_{r,n}^2} \tag{4.53}$$

$$\tau_P = \frac{K_P}{J_p\omega_o^2}. \tag{4.54}$$

Note that in Equation 4.53 that $K_P > 0$ should be enforced by an appropriate choice of t_{ss} as impacting ω_o, q.v. (Equation 4.52).

5.0 Testing Industrial VFDs to Enhance Inertial Response by Wind Power

5.1 Introduction

To confirm the theoretical findings described in the previous section, the project team conducted a number of experiments to characterize and measure inertial response characteristics on NREL's 2.5-MW VFD. Many system operators have been engaged in developing viable wholesale demand response with direct market participation capability to be used for power system reliability. In particular, ancillary services by responsive loads are being considered by many independent system operators (e.g., California Independent System Operator [CAISO], Electric Reliability Council of Texas). Various types of pumping loads (e.g., groundwater, irrigation, water treatment) have been considered as a demand response provider by many independent system operators. For example, large megawatt-size pumping loads in California have been considered for use as an ancillary service provider to CAISO in several studies (Kirby 2003; Stanford University 2012). Globally, the capacity of water-pumping loads is expanding and expected to grow significantly from the existing 30.8 gigawatt (GW) to the 200-GW level according to a 2012 study by Navigant. Most existing large pumping motors are equipped with soft starters for in-rush current mitigation. Retrofitting the existing pump motors and designing the future pumping systems with variable-frequency drives will significantly increase the ancillary service portfolio that pumping loads can provide to the grid. The simple on/off demand response type of functionality can be substituted with many advanced controls offered by modern regenerative motor drives, such as inertial response, primary and secondary frequency controls, and voltage control. In particular, the four-quadrant operation capability by VFD-coupled motors offers a capability of contributing into fast frequency regulation by injecting the energy stored in the rotating masses of large motors back into the grid in a very controlled manner, and absorbing energy from the grid when necessary—thus acting as a very short-term energy storage for the grid.

Municipal wastewater-treatment facilities were selected as a focus of the Lawrence Berkeley National Laboratory (LBNL) Demand Response Research Center since 2006 [1]. The Demand Response Research Center's Open Automated Demand Response (OpenADR) research program focused on such facilities in California because they are energy-intensive and have significant electricity demand during utility peak periods. Additionally, many wastewater-treatment facilities already have implemented energy-efficiency measures, making it more likely for them to participate in other actions in the value chain. In the United States, estimates for energy use in water and wastewater-treatment range from 75,000 GWh to 100,000 GWh annually. In the next 10 years, wastewater-treatment loads are expected to increase by 20% resulting from population growth and more-stringent regulations. The facility demand required to treat and transport wastewater is significant during peak energy-demand periods experienced by electrical utilities. Further, the majority of wastewater-treatment facilities in California have the capability to implement OpenADR. The Demand Response Research Center recently conducted a survey of control capabilities and Open ADR readiness in California's major industries, which revealed that more than 80% of wastewater-treatment facilities in California have a centralized control system that is capable of controlling all of the facility's major end uses [44].

Similarly, a recent study [45] indicates that optimal control of HVAC systems can achieve energy savings of up to 45% in various types of power grids. Therefore, optimized control of HVAC systems can potentially reduce a significant amount of global energy consumption [46]. Optimal control of building HVAC systems as a DR might have a potential to not only reduce energy costs in commercial and industrial buildings, but also to reduce energy demand in power grids, provide stability services, and promote evolving smart grids.

In this project, NREL's research focus is on active power control characteristics of regenerative industrial motor VFDs for grid services. Power regeneration is the process of recovering kinetic energy stored in the rotating mass of the motor during stopping or braking, converting that energy to electric power and feeding the power back into the power grid. This is especially applicable for VFD use cases with frequent starting and stopping loads, decelerating high-inertia load, and overhauling torque applications such as a downhill conveyors [47]. Aside from its obvious energy/cost savings and green footprint, power regenerative drives provide additional benefits in the form of inertial response, demand response, and energy efficiency.

In particular, at this stage of the project, NREL has investigated and demonstrated the ability of modern industrial voltage source converter (VSC)–based VFDs to provide inertial response to the grid with the specific purpose being to enhance the similar response by wind power. The idea is that decelerating motors coupled with VFDs can inject a short-term amount of energy back to the grid, thus mitigating the production loss resulting from decelerating wind rotors, as shown in Figure 43 (similar injection can be done by BESS as well).

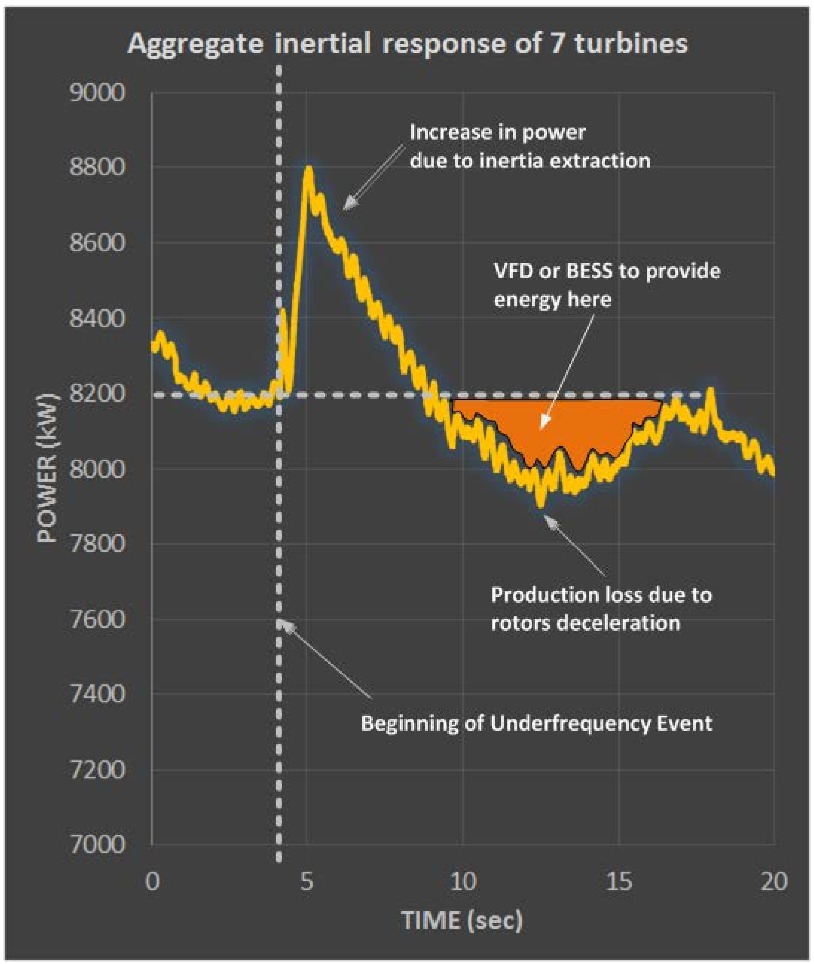

Figure 43. Illustration of wind power production loss after injecting inertial power back to the grid

5.2 Characterizing Operational Links of NREL's 2.5-MW VFD

NREL's 2.5-MW VFD is a part of larger dynamometer facility that was dedicated in 1997. Since then, the VFD went through several upgrades, the most recent one in 2013–2014, that included upgrade of the original line-commutated converter to more superior back-to-back VSC power electronic converters using

ABB's ACS-2000 drive family of products. For the VFD system, NREL conducted an analysis for characterizing the power and torque based operational envelope of the drive as shown in Figure 44 (torque referred to dynamometer's low-speed shaft).

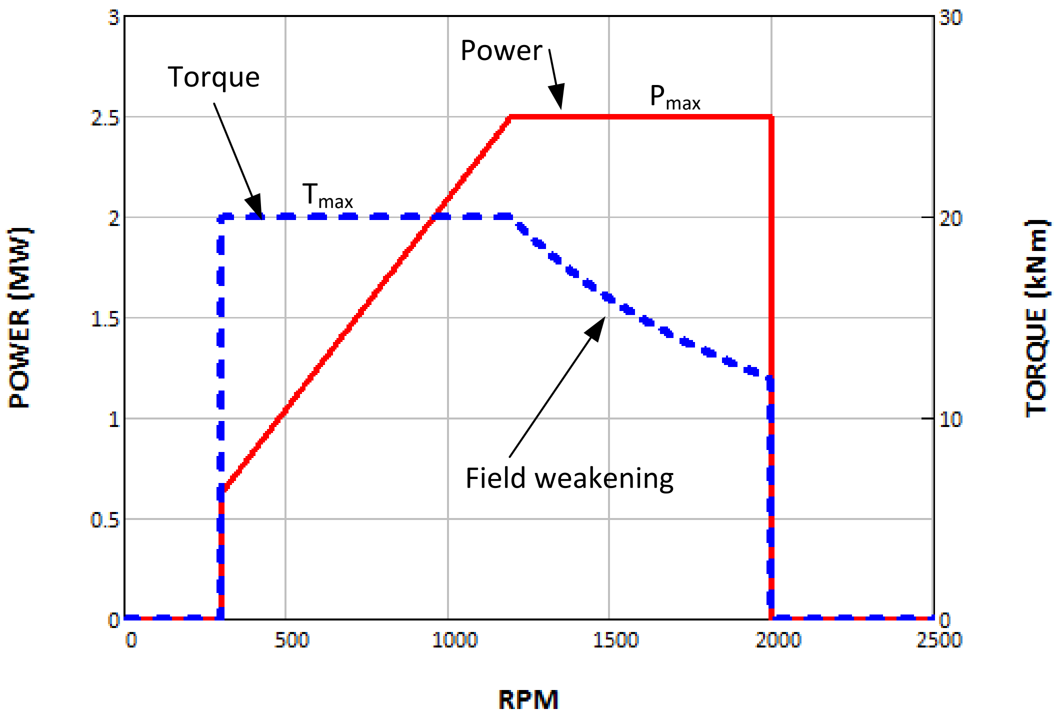

Figure 44. NREL's 2.5-MW VFD power and torque limits

The motor's maximum allowed power is 2.5 MW and maximum allowed mechanical torque level is 20 kNm, all within feasible motor speed range of 300–200 rpm. The system can operate at maximum torque within the whole range of rotational speeds. During the torque, however, it must be limited by providing motor field-weakening control to keep the active power at the maximum 2.5-MW level. Various torque limits can be provided, depending on the nature of mechanical loads and safety limits for a particular VFD use case. The power and torque profile of the VFD with implemented toque limits at 25%, 50%, 75%, and 100% of nominal are shown in Figure 45 and Figure 46, respectively.

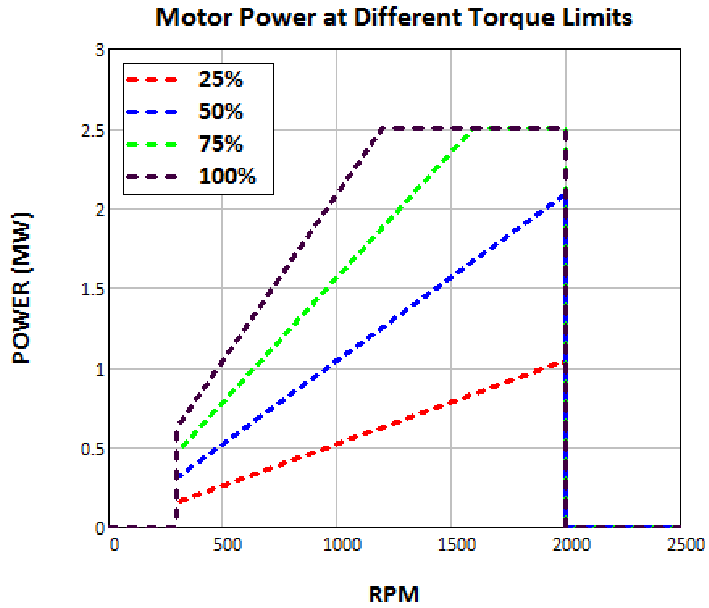

Figure 45. VFD maximum power at different toque limits

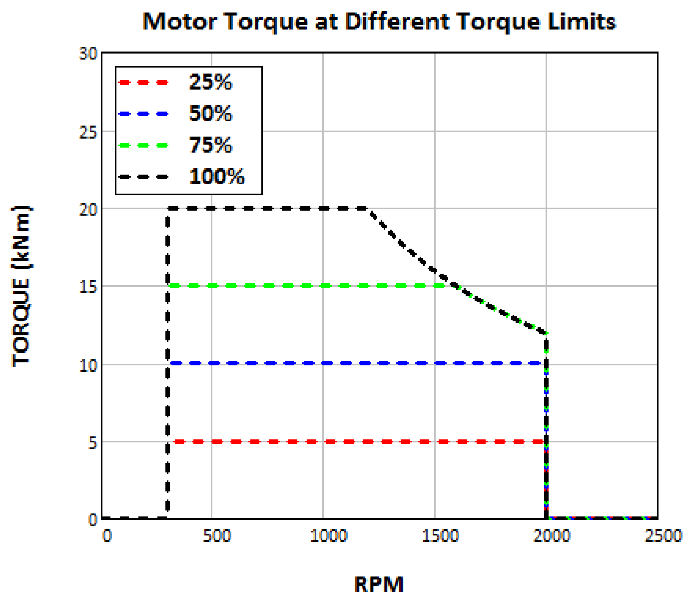

Figure 46. VFD maximum torque profiles at different toque limits

From previous testing and modeling efforts it was determined that the moment of inertia of 2.5-MW VFD motor is J=250 kg·m^2. The energy (*E*) stored in the total rotating mass at any given speed of motor shaft can be calculated as follows.

$$E(rpm) = \frac{1}{2} J \cdot \omega(rpm)^2 = \left(\frac{\pi}{30}\right)^2 \cdot \frac{1}{2} J \cdot rpm^2 \tag{5.1}$$

Where S_n is rated apparent power of the drive (2.5 MVA). The inertial energy stored in the drive for any given rpm is shown in Figure 47. The inertial constant of the drive (H) then can be calculated.

$$H = \frac{E(rpm)}{S_n} = \left(\frac{\pi}{30}\right)^2 \cdot \frac{\frac{1}{2}J \cdot rpm^2}{S_n} \tag{5.2}$$

The inertial constant of the drive at full speed then can be calculated (H=2.2 sec). Based on the calculations above, the full operational space of 2.a 5-MW VFD motor in terms of power and torque can be determined as shown in Figure 48 and Figure 49.

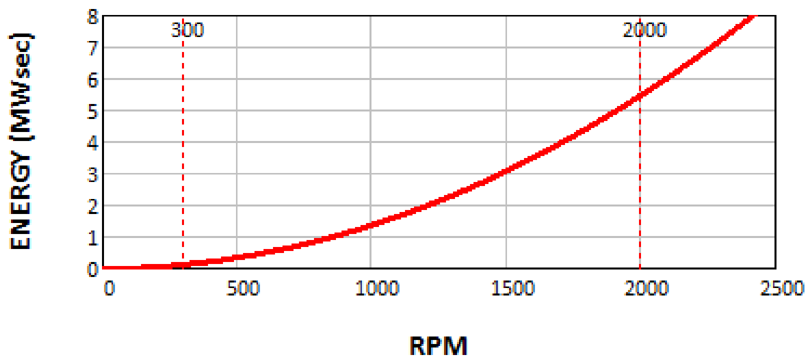

Figure 47. Kinetic energy stored in drive as a function of rotational speed

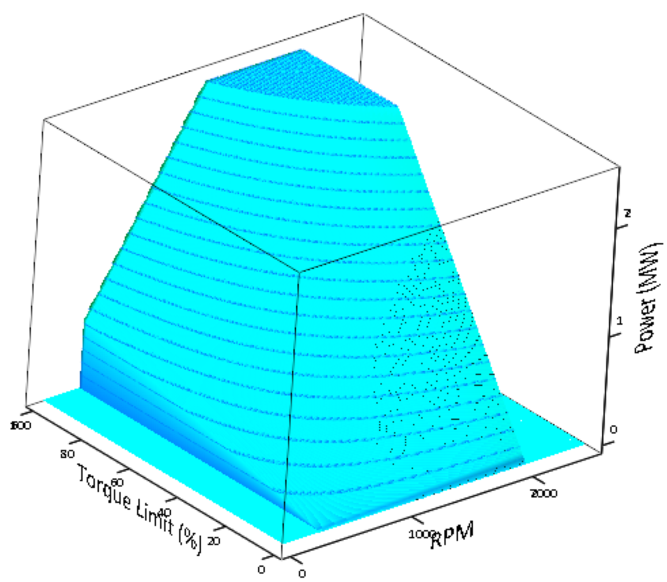

Figure 48. Full operational power envelope for 2.5-MW VFD motor

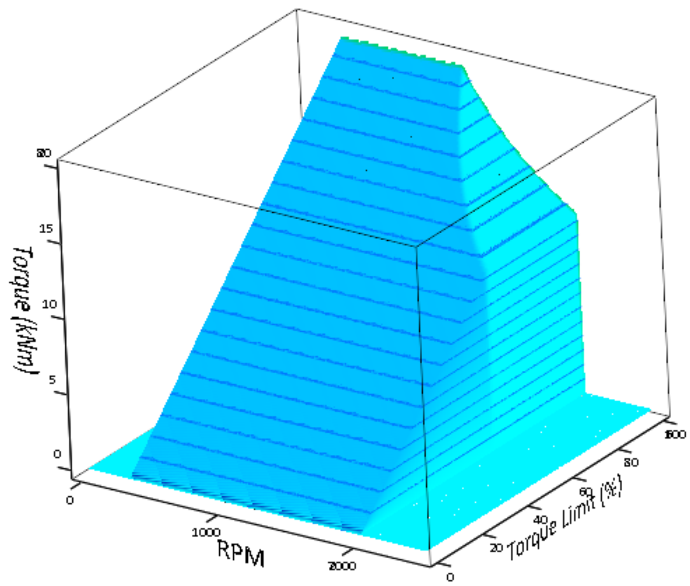

Figure 49. Full operational torque envelope for 2.5-MW VFD motor

An example power time series from NWTC's 5-MW dynamometer operation is shown in Figure 50 to demonstrate the responsiveness of the system. The positive and negative spikes in power represent the inertial component caused by motor acceleration or deceleration. This power can be injected into the turbine bus or absorbed by the VFD. The amplitude, profile, and duration of the spikes can be tightly controlled by controlling the rpm and torque command of the VFD and thus emulating a response in accordance to various profiles.

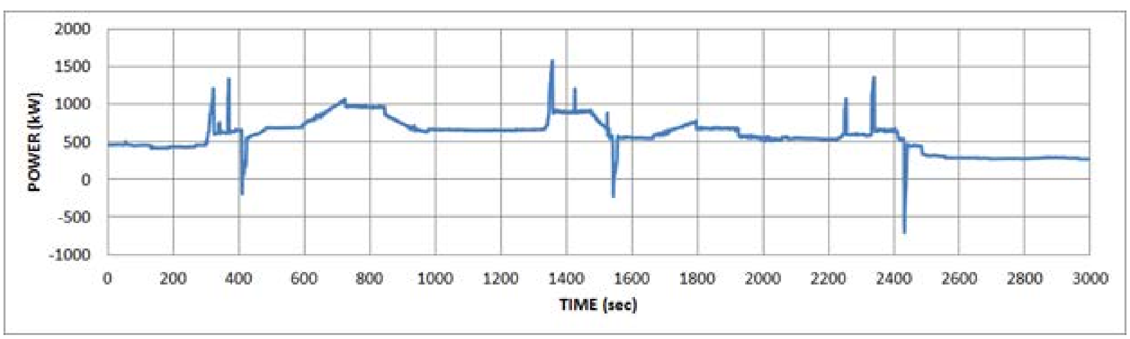

Figure 50. Example of 5-MW VFD power time series when injecting or absorbing active power

The measured active power time series from the same NWTC 5-MW dynamometer in four-quadrant operation is shown in Figure 51. The VFD demonstrated ability for fast inertial power injections and absorption at around ±2-MW/sec rates.

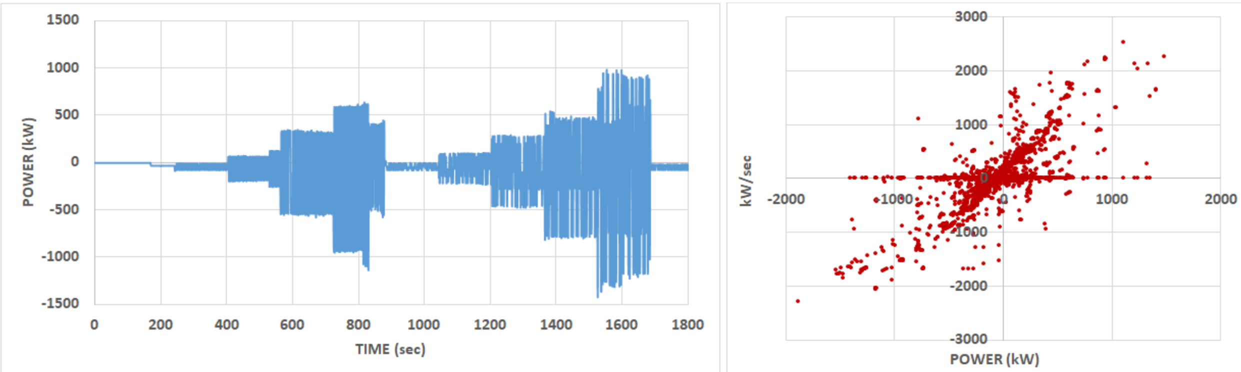

Figure 51. Measured inertial power of 5-MW VFD

5.3 Validation of VFD Inertial Model

Various modeled cases we simulated using the inertial model of the 2.5-MW VFD operating in a speed-control mode incorporated into the model of overall NWTC test setup (diagram shown in Figure 52).

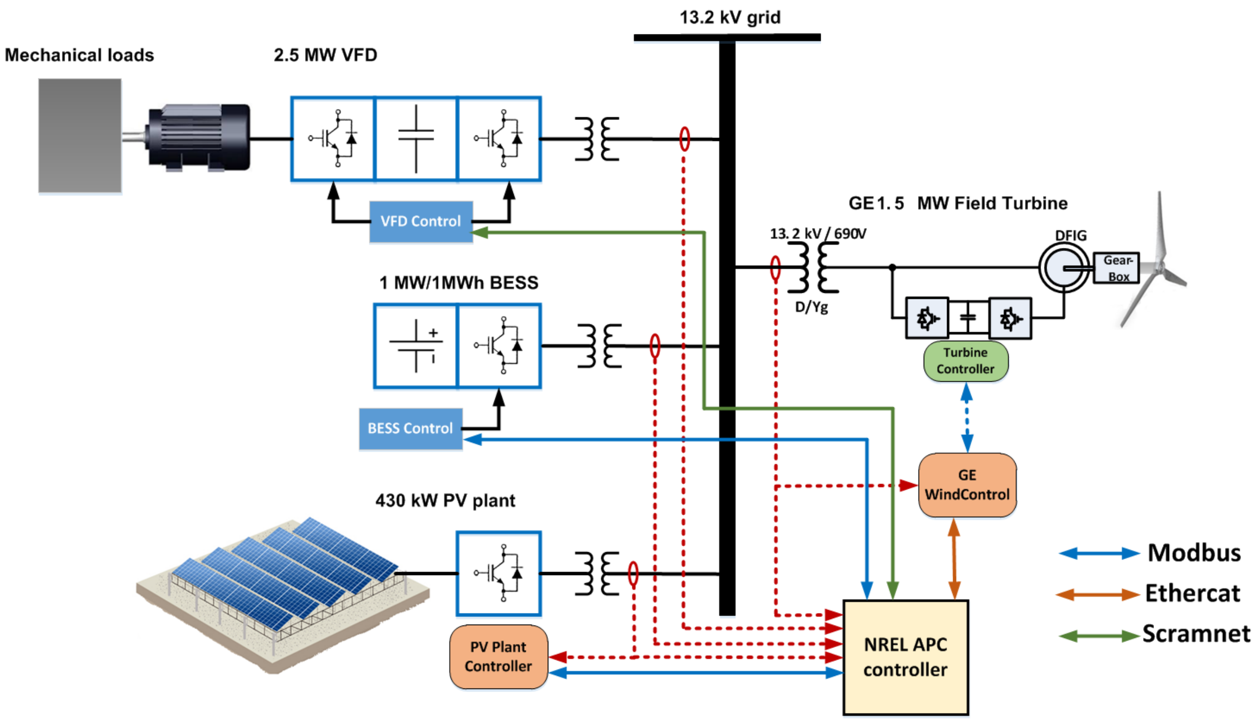

Figure 52. Components of NWTC test setup

The diagram of the controller to extract inertial energy from VFD or absorb energy by VFD rotating masses is shown in Figure 53. It was developed in the National Instruments LabVIEW software environment and implemented in PXI real-time controller. The control loop implemented in LabVIEW is shown in Figure 54. Several tests involving this controller have been conducted to demonstrate ability of 2.5-MW VFD to provide inertial controls.

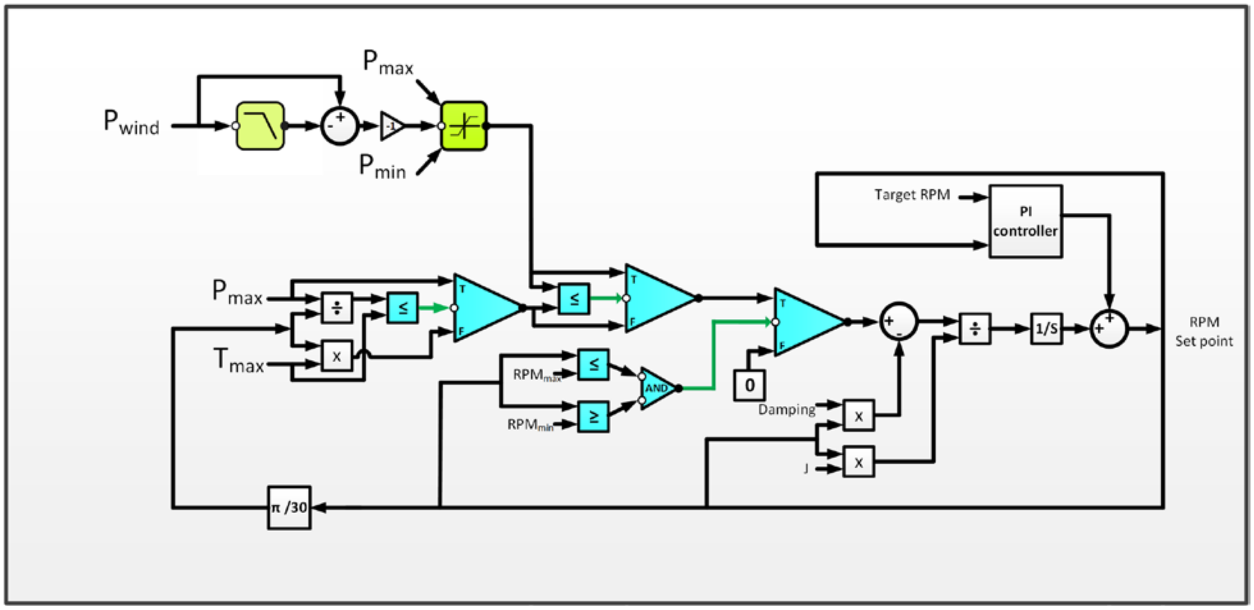

Figure 53. VFD inertial controller

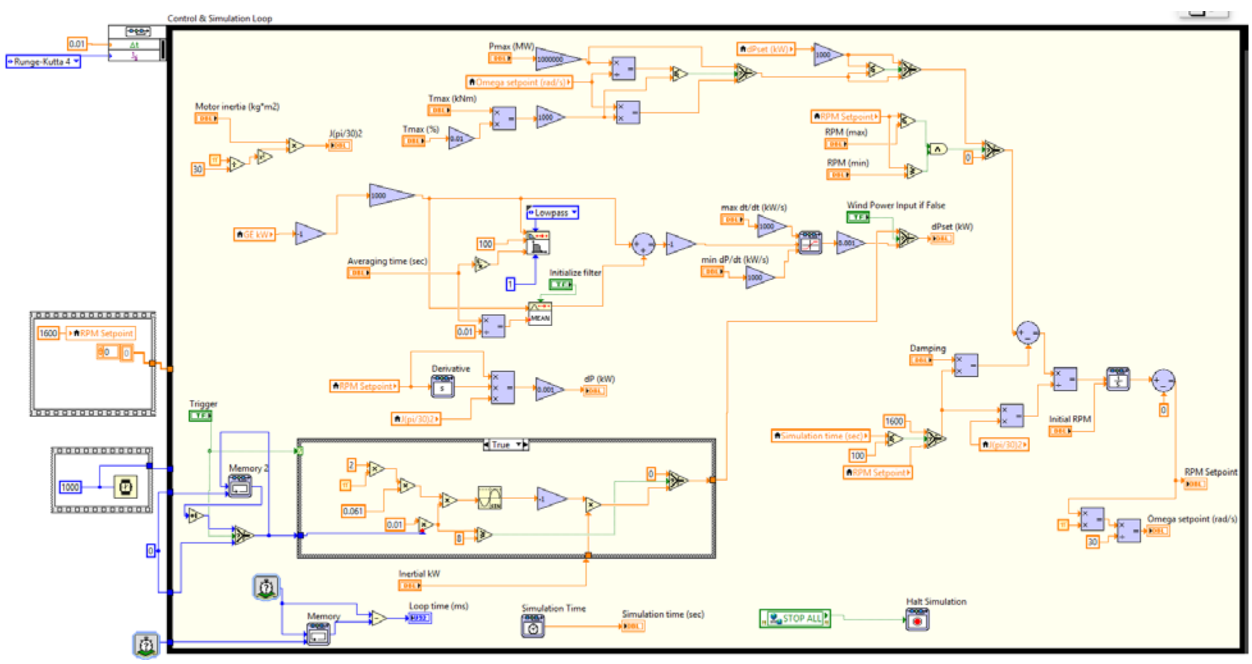

Figure 54. VFD inertial controller implemented in LabVIEW

Results of two VFD tests using the Figure 54 controller are shown in Figure 55 and Figure 56 for VFD power-injection and power-absorption cases, respectively. The VFD was operating in speed-control mode, and controller commanded speed set point to modulate the VFD power measured on 13.2-kV MV bus in accordance to predefined sinusoidal shapes.

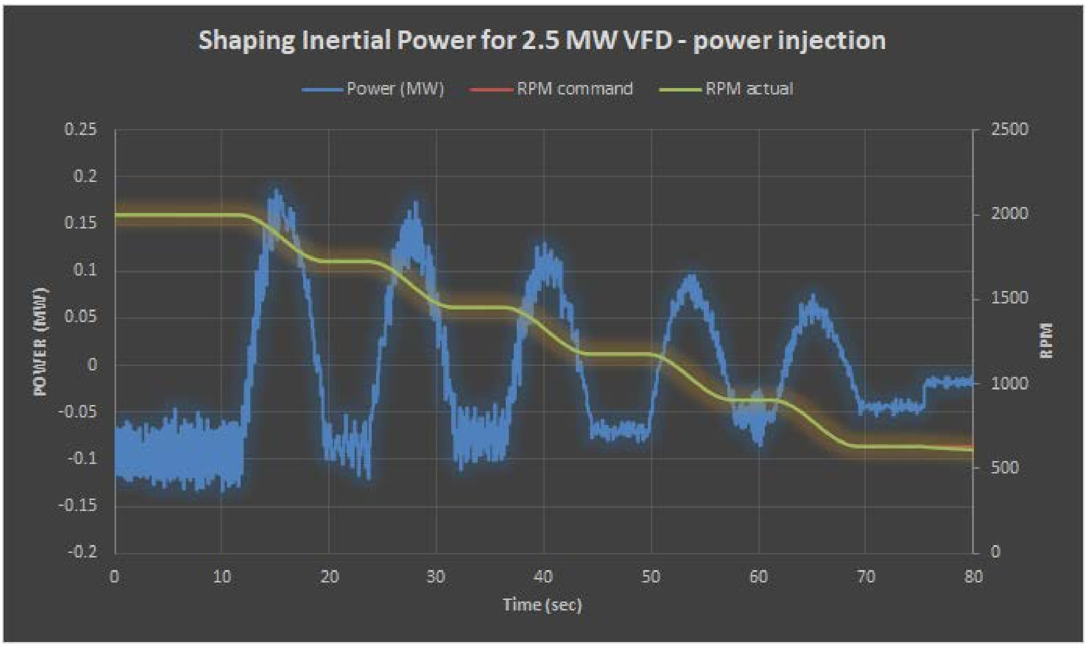

Figure 55. Injecting motor inertial power to the grid

Figure 56. VFD motor absorbing energy

The test results shown in Figure 55 and Figure 56 demonstrate that the power of VFD can be modulated in desired shapes depending on initial conditions (initial VFD motor speed) and within physical limits of the drive components. Further validation of VFD model and control method was conducted and the results are shown in Figure 57.

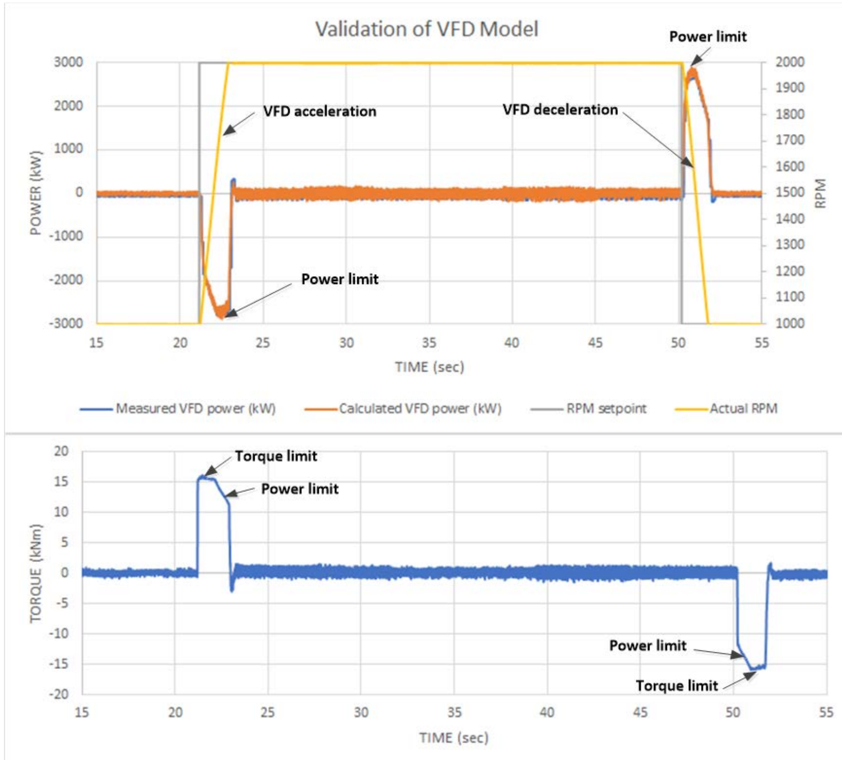

Figure 57. VFD model validation

The test was conducted with the motor accelerating and decelerating at a constant rate, so predicted power by the controller and actual measured power can be compared. Figure 58 shows a zoomed-in view of the acceleration portion of the test. A very good match between measured and predicted power is observed when the VFD was operating in unconstrained mode and at power or torque limit. Similarly, the same good match between measured and predicted power can be observed in the zoomed-in deceleration test view shown in Figure 59. Results of both tests also are consolidated in Figure 60. Both motor power and torque are shown as a function of motor speed. The measurement results in Figure 60 demonstrate drive operation and match between measured and modeled results at both power and torque limits of VFD, and explain the operational envelope of the drive for inertial control in terms of both power and torque.

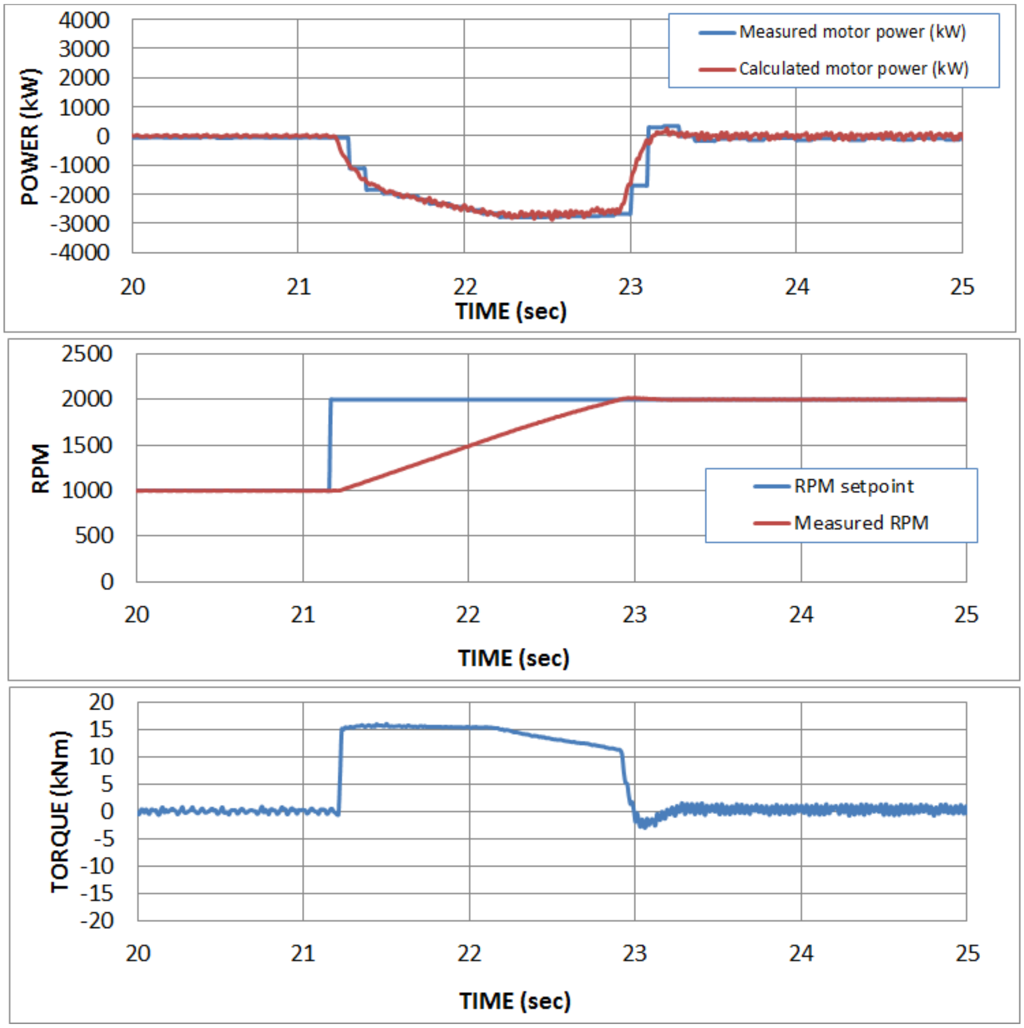

Figure 58. Model validation during acceleration test

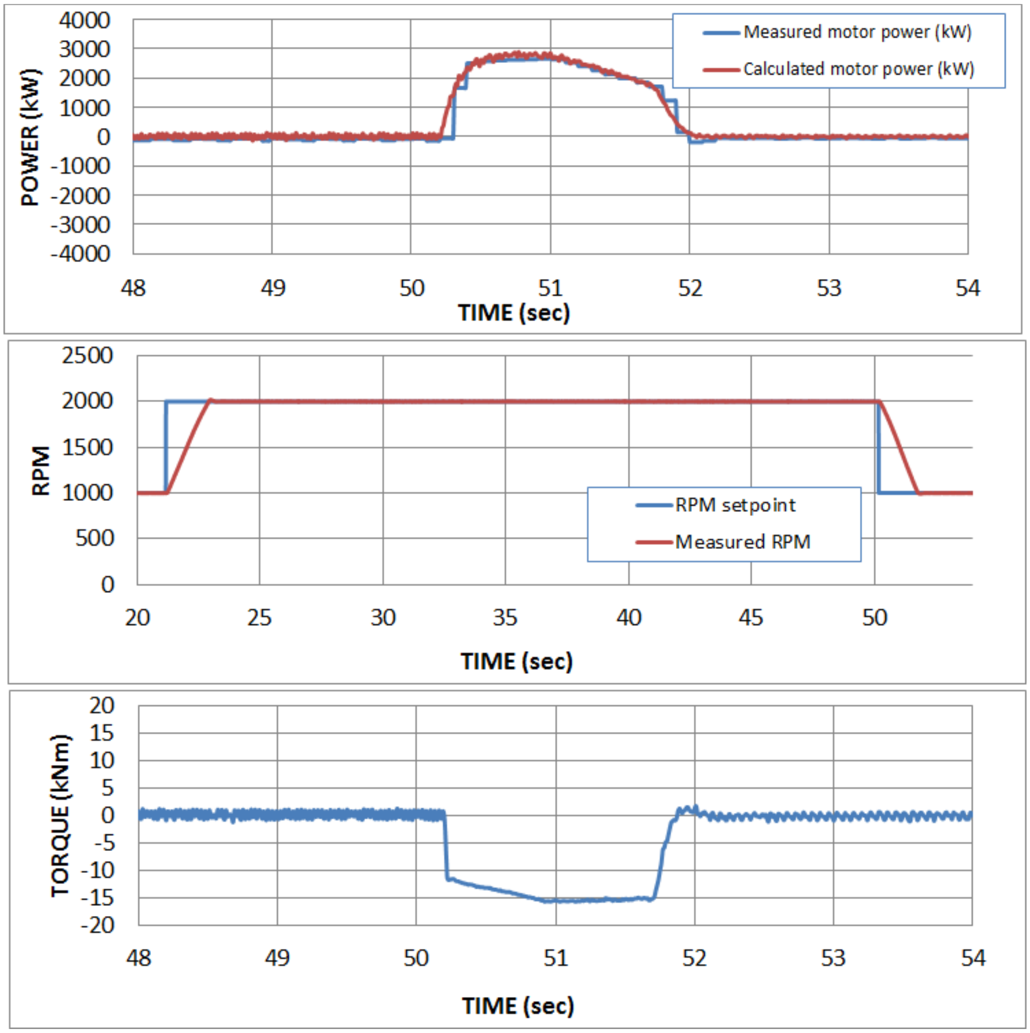

Figure 59. Model validation during deceleration test

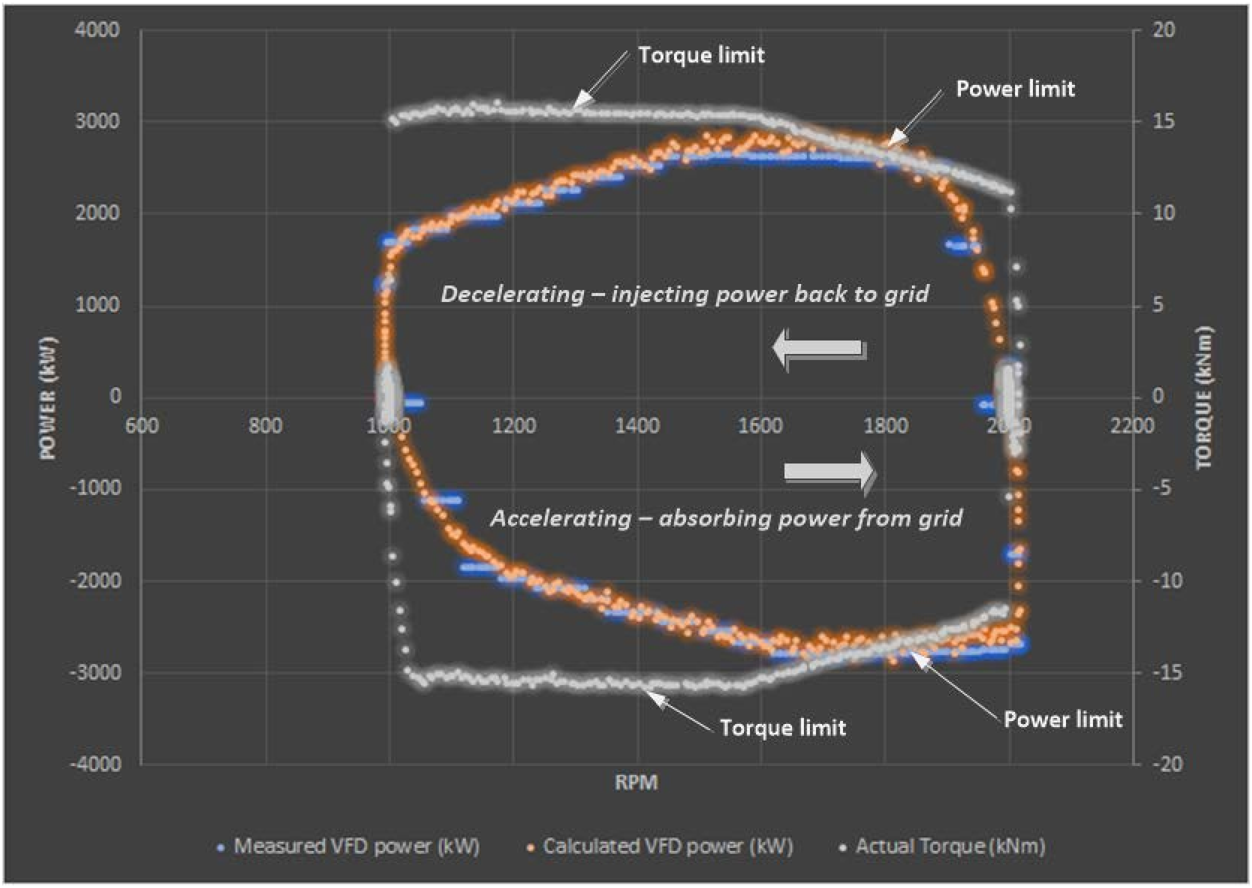

Figure 60. Measured VFD power and torque as a function of rotational speed

Additional interesting tests results were demonstrated with the VFD acting as a very short-term flywheel-like energy storage trying to smooth out the variable power production of GE 1.5-MW wind turbine under real wind-speed conditions.

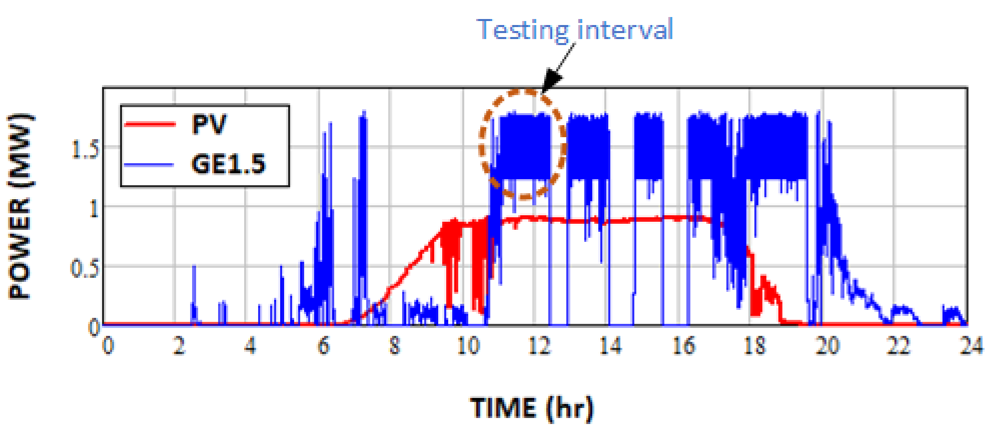

Figure 61. Wind and solar PV production profile at NWTC during the day of testing

Figure 61 shows the actual 1-sec wind-production data for a day of testing. The actual testing with VFD was conducted during one particular hour of the day when wind-speed conditions at NWTC tests site were close to rated wind speed for GE 1.5-MW WTG (as highlighted in Figure 61). A 30-sec moving-average window was applied to real wind power measured at the turbine MV bus, and the VFD was set to modulate its power to follow the smoothed 30-sec average wind-power generation profile. The results are shown in Figure 61, demonstrating that significant variability smoothing for WTG can be achieved by controlling the VFD this way. The lower-right plot in Figure 61 shows significant reduction in 1-sec variability. This type of operation of VFD in combination with wind power perhaps has a little practical value, but the purpose of this experiment is to demonstrate the ability and fast responses by VFD motor loads that can be used for various types of fast reliability services for the grid.

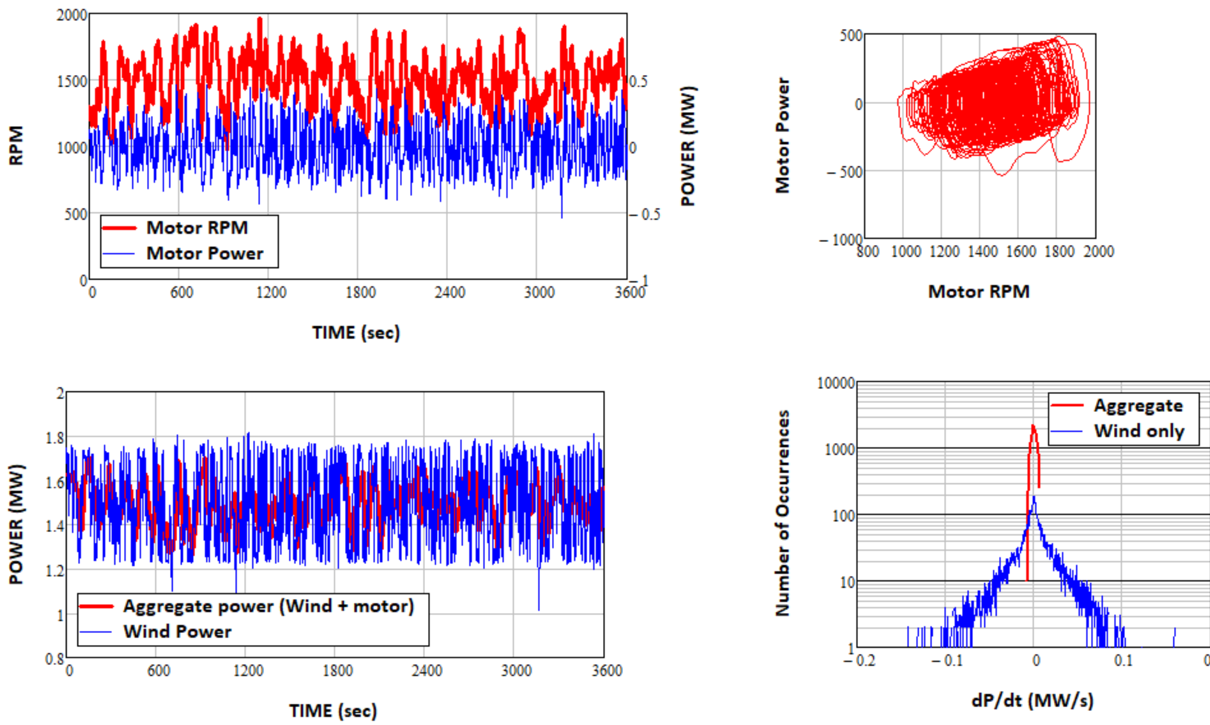

Figure 62. Power smoothing test results for 30-sec averaging window

After a number of inertial response tests for the GE 1.5-MW WTG, it was determined that the average beginning time for the underproduction period caused by wind rotor deceleration was about 5–6 sec after the beginning of frequency event. The VFD inertial controller was commanded to emulate its own inertial response by slowing down the motor about 5 sec after the beginning of the event. The results of one such test is shown in Figure 63. The inertial response of the WTG has a period of underproduction depicted by blue trace in the upper graph. The VFD controller commanded rpm set points to modulate the exact shape of underproduction profile with a 250-kW peak but with opposite sign (lower graph). As a result, the aggregate power of GE 1.5-MW WTG and 2.5-MW VFD does not have any underproduction period (orange trace in upper graph). Of course, the VFD will need energy from the grid to go back to normal prefault operation at 200 rpm. This can be done at the later time, however, when the power system recovers after the contingency.

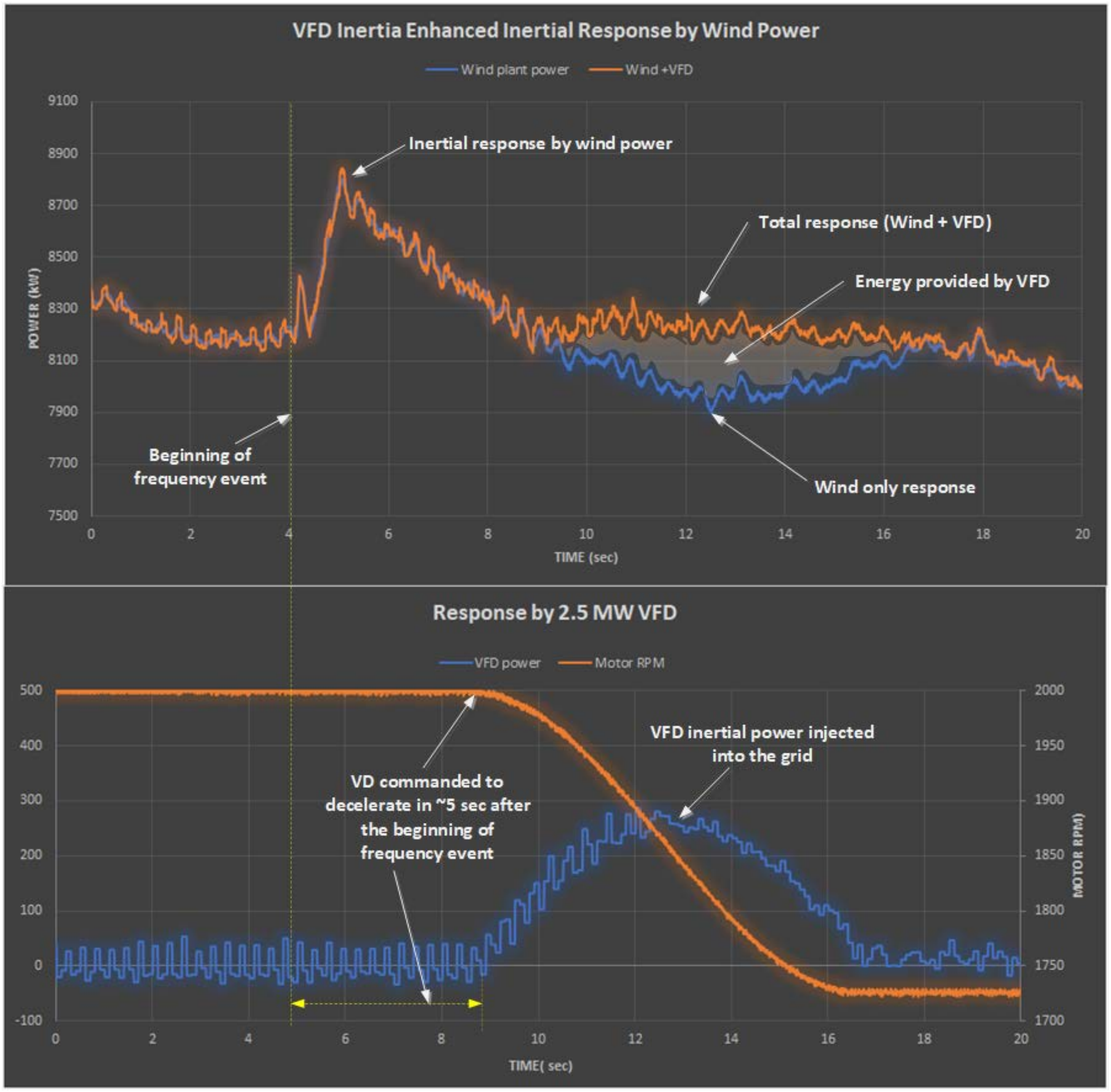

Figure 63. Results of wind inertia–enhancing test

6.0 Development of BESS Controls

6.1 BESS as a Provider of Reliability Services

The present grid is dominated by synchronous generators having large, rotational inertia with a relatively small amount of inverter-interfaced variable renewable energy (VRE) sources. The future grid will be realized as VRE penetration increases and conventional synchronous machines are gradually replaced with power electronics-based generation, storage, and loads[49].

From a physics standpoint, the turbines and rotors of synchronous generators exhibit mechanical inertia, so kinetic energy can be stored in their rotating masses. That kinetic energy can be extracted from or absorbed into these rotating masses during system disturbances helping interconnected power systems to withstand fluctuations in net load and generation. Specifically, a net excess (or deficiency) in generation delivers energy into (or extracts energy from) the rotating masses and subsequently leads to an increased (or decreased) system frequency; hence, the direction of the frequency deviation is an indicator of net energy excess or deficiency on loads and VRE when the magnitude of the frequency deviation is inversely proportional to the net inertia on the system. Consequently, a system with low inertia is vulnerable to larger and undesirable frequency deviations [49].

Another important factor determining the dynamic behavior of existing power systems is the synchronizing torque produced by synchronous generators. The synchronizing torque along with inertia has a crucial role in determining the initial rotor-speed behavior of conventional generators following a contingency event in the grid. The active power injected by synchronous machines maintains synchronism and damps mechanical oscillations through their synchronizing and the damping torque components of the total electric torque. The abundance of inertia and synchronous torque from synchronous machines along with their controls allows for the mitigation of the large active and reactive power imbalances in the grid. This fundamentally important characteristic of power systems would change dramatically with growing penetrations of inverter-based generation. In contrast, VRE technologies use a different set of technologies for energy conversion and interfacing to the grid.

The types of inertial response in power systems can be divided into three major categories, as follows.

1. Inertia based on kinetic energy stored in rotating masses of constant-speed generators and motor loads that are directly coupled with a grid (conventional generators and constant speed wind turbines, constant speed induction and synchronous motors, synchronous condensers). Directly coupled inertia is a physical property of rotating mass, system operators have no control over the shape of the response, it is strictly a function of mass and ROCOF, and does not depend on initial power level of the unit.
2. Inertia based on kinetic energy stored in rotating masses of inverter-coupled variable-speed generators and motor loads (Type 3 and Type 4 wind turbines, variable-speed hydro, variable-speed gas turbines, VFDs). This is still a real mechanical inertia but is decoupled from grid frequency. Operators can have certain control over the shape of inertial response by these systems, but it is limited by physical properties of rotating masses and constrains caused by electrical, mechanical, and structural limits for a given technology.
3. Inertia without kinetic energy—ability of a non-spinning generator (such as PV or fuel cells), electrical loads, and energy storage to virtually inject or absorb energy based on active power set points commanded by control systems. This is a synthetic inertia and operators have full control over the shape of response as long as it is within the limits for a given technology (speed of response and electric rating of power converters).

The Category 3 inertia usually is referred in the literature as synthetic inertia. Some sources also refer to it as virtual inertia, digital inertia, transient frequency response, and ROCOF response. Li-ion chemistry-based energy storage technologies are characterized by high efficiency, fast response, and long cycle life time [50]. NREL's 1 MW/1MWh BESS system is used in the project to demonstrate ability of battery technology to provide synthetic inertia and understand impacts of such service on power systems frequency response.

For synchronous machines, the inertial response is an inherent release of stored kinetic energy in the rotating rotor. This stored energy is determined by rotor moment of inertia *J* and rotational speed *ω*.

$$E = \frac{1}{2} J\omega^2 \tag{6.1}$$

If imbalance exists in the active power loading of a generator, then the ROCOF can be determined from a swing equation in per units.

$$2H \frac{d\omega}{dt} = P_{gen} - P_{load} \tag{6.2}$$

Where H is the inertia constant defined as follows.

$$H = \frac{E}{S_{rated}} = \frac{1}{2} \frac{J\omega^2}{S_{rated}} \tag{6.3}$$

For the whole power system with S_{total} power rating, total inertia constant can be calculated from inertia constants and power ratings of all *N* individual units as shown below.

$$H_{total} = \frac{\sum_{i=1}^{N} H_i S_i}{S_{total}} \tag{6.4}$$

During large disturbances, power systems with larger H_{total} have lower ROCOF, and therefore have the capability to better arrest the rate of frequency decline or increase after large contingencies. Inertia is an important system characteristic and, in combination with PFR, has an impact on the lowest frequency (nadir), which is shown as point C in Figure 64. Point C has to be higher than the highest set point for UFLS within an interconnection. Measuring the level of Point C based on what large credible disturbances the interconnection plans for helps determine the amount and characteristics of PFR that are needed to arrest frequency decline above UFLS settings. After the frequency decline has been arrested, continued delivery of PFR will stabilize frequency to a steady state (Point B). The point at which frequency is stabilized often is referred to as steady-state frequency. The B value is determined by averaging the frequency values from a period of 32 sec starting at t=20 sec after the disturbance [51].

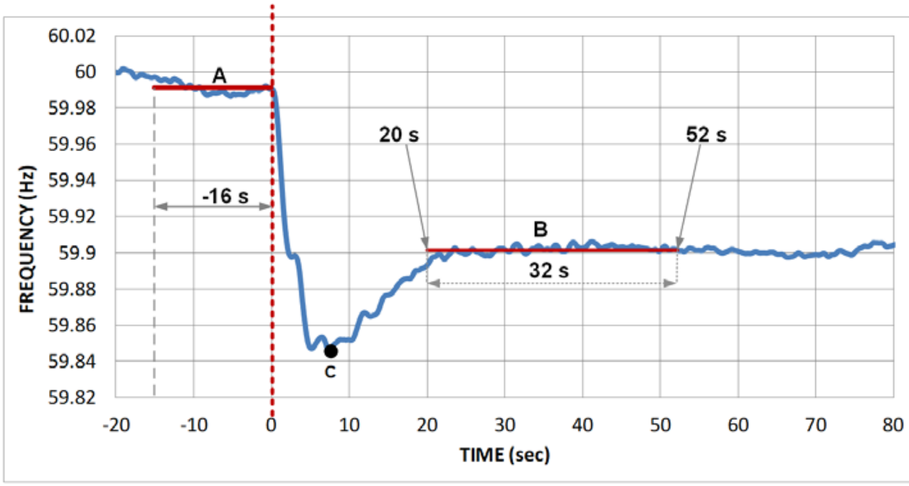

Figure 64. Description of BAL-003-1 frequency response metrics

The following main frequency metrics are used to evaluate the frequency response of an interconnection.

4. Initial rate of decline of frequency—determined by inertia only
5. Value of frequency nadir (Point C)—determined by inertia and PFR
6. Transition time between the beginning of the disturbance and the frequency nadir (transition time from Point A to Point C)—determined by inertia and PFR
7. Value of settling frequency (Point B)—determined by PFR only
8. Transition time between the frequency nadir and the settling frequency (transition time from Point C to Point B)—depends on PFR speed
9. Ratio of frequency value at Point C to value at Point B (CB_R)—determined by inertia and PFR

The first two frequency response metrics depend on system inertia, therefore any deficiencies in inertial response could cause decline in overall interconnection frequency response and jeopardize system reliability. The above metrics along with other parameters are used to calculate the interconnection frequency response obligation (IFRO) and frequency response obligations (FRO) of individual balancing areas. For example, in 2017, the Western Interconnection IFRO was 858 MW/0.1 Hz, and CAISO's FRO was 196.5 MW/0.1 Hz [52].

The fast-responsive BESS technologies have a potential to provide fully controllable synthetic inertia-like response to keep the above frequency response metrics within limits required by reliability standards. The focus of BESS testing for provision of inertial response is on the first 10–15-sec time interval after large system contingencies causing rapid decline in frequency (as shown for a hypothetical simulated example for a single-area power system in Figure 65). In this hypothetical case, the inertial response of a synchronous generator starts immediately after instantaneous airgap torque imbalance caused by change in airgap flux after the grid event. Kinetic energy stored in the generator rotor and turbine is injected into the grid, helping to arrest the initial ROCOF. As ROCOF starts declining, the inertial response is reduced as well in accordance with Equation 6.1.

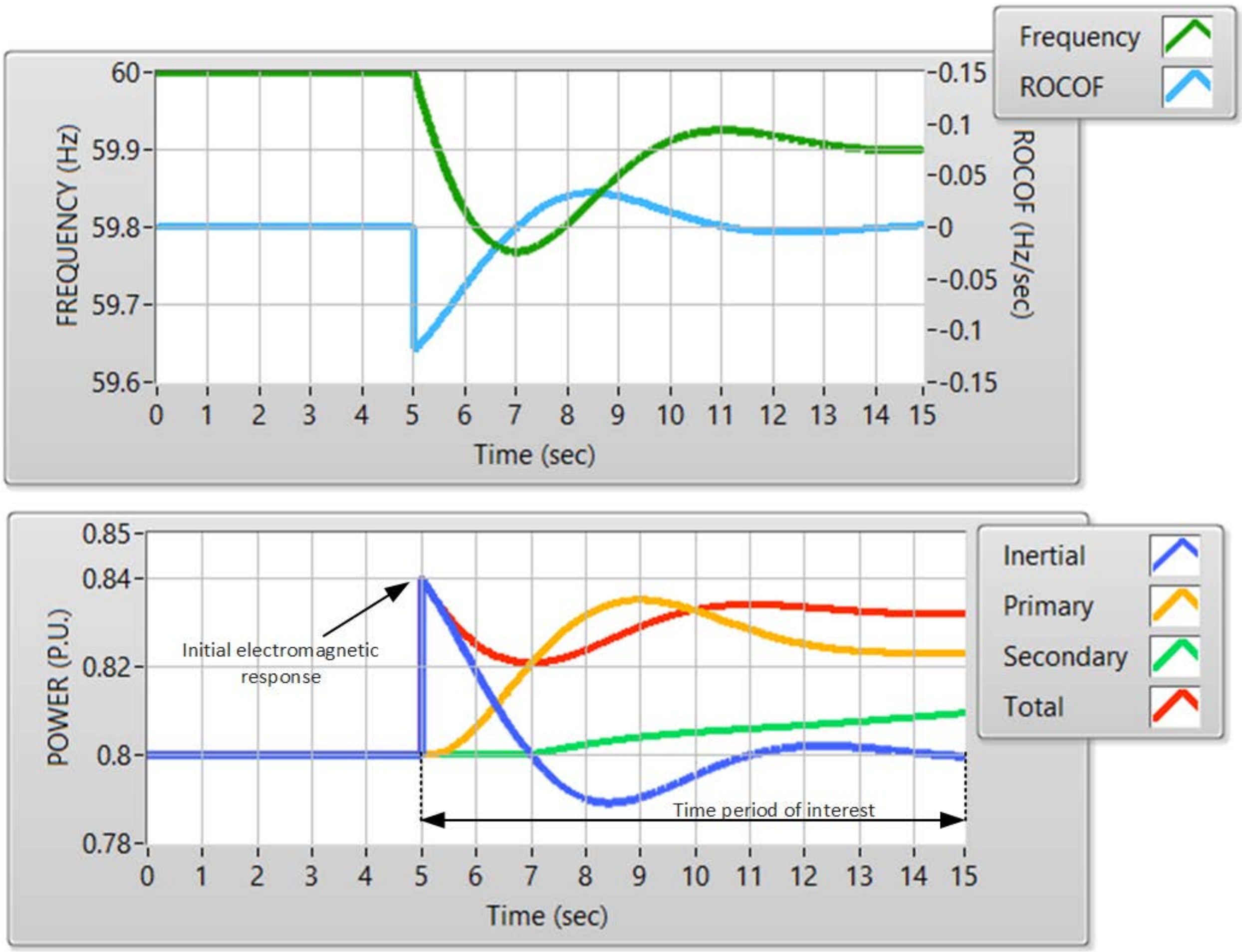

Figure 65. Generator frequency response segregated into individual components

For BESS to provide inertial response similar to a rotating generator, the output power of all participating battery systems must be modulated to inject/absorb active power, similar to the hypothetical case (blue line) shown in Figure 65. It is important to note, however, that the maximum level of inertial response by BESS at any given moment in time depends on the operating power level of the BESS just before the frequency event occurs. If 1-MW battery system is being charged at full power (-1 MW), for example, then it can deliver up to 2 MW of inertial response by quick transition to discharge at full power (+1 MW). This will correspond to very high levels of H constant. The ability of BESS to deliver inertial response in some cases also depends on the SOC or state of energy (SOE). Modern lithium-ion (Li-ion) battery systems can be designed to provide short-term response event at 0% or 100% SOE. For example, the NREL BESS was designed with following specs in terms of SOE.

- ±1.15 MW for 10 sec at 100% SOE occurring no more than 6 times per year
- ±1.1 MW for 30 sec at 100% SOE occurring no more than 6 times per year
- Deep discharge (0%) capable; ±500 kW at 0% SOE for 10 sec with cooling period of no longer than 10 min. Max number of deep discharge events—no more than 24 times per year

To characterize the inertial constant of NREL's 1 MW/1 MWh battery similar to rotating machines, we perform the following simple calculations.

- Maximum amount of energy stored in BESS is $E_{max} = 1\ MWh$
- BESS nominal apparent power is $S_{BESS} = 1MW$
- Battery inertial constant is $H_{BESS} = \frac{E_{max}}{S_{BESS}} = \frac{1\ MWh}{1MW} = 1h = 3{,}600\ sec$

This $H_{BESS} = 3{,}600\ sec$ is a large gain as compared to typical H of rotating generators (1 sec–10 sec). However, keep in mind that the actual value of H_{BESS} for the battery can be programmed only within the 1-MW rating of the converter (Equation 6.5).

$$\Delta P_{BESS} = -2H_{BESS}\frac{df}{dt}, |\Delta P_{BESS}| \leq P_{max}, P_{max} = 1MW\ for\ NREL\ BESS \tag{6.5}$$

The possible values of H_{BESS} as a function of ROCOF for maximum inverter rating of 1 MW is shown in Figure 66 (calculated using p.u. values of f and ΔP_{BESS}).

As shown in Figure 66, the theoretical values of H emulated by BESS for typical ROCOFs observed in the Western Interconnection are H=200–800 s—about two orders of magnitudes greater than for a typical rotating generator (in reality they can be less if considering time delays because of low-pass filtering of the ROCOF signal—this issue is discussed elsewhere in this report). If the battery happened to operate at full discharge level (+1 MW), however, then it won't be able to produce any inertial response. Therefore, the level of inertial response by BESS is greatly dependent on the initial conditions of the battery, and care must be taken to have adequate power headroom for desired inertial response if BESS is expected to provide such service at any time.

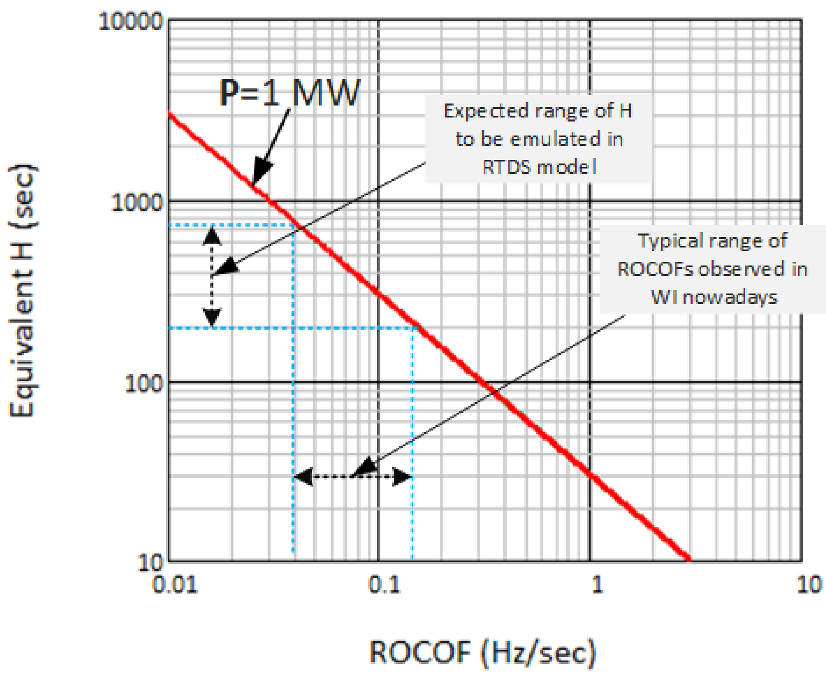

Figure 66. Range of programmable H for 1-MW/1-MWh BESS

Synchronous generators also can operate with power-frequency droop in accordance to the droop equation.

$$\frac{1}{droop} = \frac{\Delta P/P_{rated}}{\Delta f/60Hz} \tag{6.6}$$

Adequate droop response in combination with inertia is an important reliability factor for any power system and should be maintained at levels prescribed by BAL-003-1 for interconnections and individual balancing areas. The most common droop setting used in many power systems is 5%, but in some cases the more aggressive 3% droop also is used. For example, the Western Electricity Coordinating Council (WECC) governor droop criterion allows individual generator droop settings within a 3% to 5% range. Equation 6.6 above assumes a linear relationship between power and frequency (with some small deadband). For example, 5% droop means that a 5% change in frequency would result in a 100% change in power; a 3% droop means that a 3% change in frequency will result in a 100% change in power. Such a linear relationship is theoretical though, and with real governors there are many nonlinearities because of various types of control delays, unintentional deadbands, and physical characteristics of prime movers. For BESS, as was shown by previous testing at NREL, the relationship between power and frequency essentially is linear because of the fast response time (less than 50 ms) of battery inverters. Therefore, BESS can provide PFR with much greater levels of precision and speed for a wide range of droop settings (1%–5%, for example). The ability of BESS to provide adequate droop response, however, also is subject to its initial conditions. For the same per-unit of power and depending on initial conditions, the BESS can provide more benefits to a system's PFR than conventional generators. Theoretical comparison of frequency droop response of BESS and synchronous generator-based unit is shown in Figure 67.

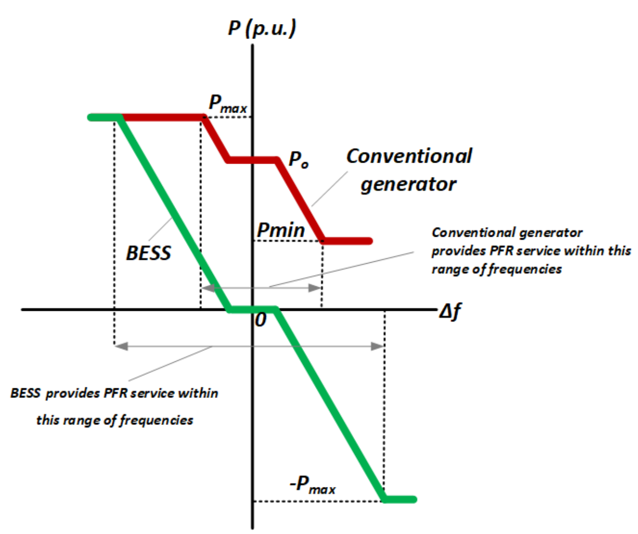

Figure 67. Droop response by conventional plant and BESS operating at zero active power (source: NREL)

BESS is assumed to operate at zero power, so it can set to operate at full power in both charging and discharging modes. For the same droop setting and same power rating, the BESS is capable of providing PFR for much wider range of frequency deviations than a conventional generator (*see* Figure 67). The minimum power level P_{min} at which a conventional generator can operate stably depends on many factors, including type of the plant and its operational limits set by stability and physical limits.

Fast frequency response is another method for using BESS to compensate for sudden generation or load losses. This can become a very efficient frequency response tool for system operators, but requires precise knowledge of loss magnitude, so that BESS can be commanded to change its power output accordingly.

This method is dependent on the ability of the control system to rapidly determine the magnitude of the loss and communicate the set point to BESS control. The speed of response (or how fast the BESS deploys all available reserves) depends on power system stability impacts: BESS can deploy all available reserves very rapidly, which can cause unwanted oscillations in the system. In some cases, FFR activation by BESS can be based on frequency thresholds similar to UFLS schemes or be based on ROCOF. This requires determination of precise FFR magnitudes based on system frequency or frequency ROCOF by conducting system-level modeling studies.

BESS also is capable of participating in frequency regulation (or AGC) by following the active power set point commands received from the system operator (usually every 4 sec). Similar to inertia and droop, the ability of BESS to provide both up- and down-regulation also depends on the average power level of battery operation at the time; it requires enough headroom to increase or decrease its power level or to change the operation mode from charging to discharging or vice versa.

All the above-mentioned active power control services by BESS have a potential to create additional revenue streams for BESS plant owners and operators. Some of these services already have existing or emerging markets (e.g., regulation, droop response). BESS must be dispatched in such a manner so that it can provide the services it has committed to when needed. Other possible services provided by BESS include participation in wide-area stability services such as power-system oscillation damping.

All components of the active power controls by BESS (discussed above) can be combined in a single equation; so, at any instance in time, the total BESS power is as shown in Equation 6.7.

$$P_{bess}(t) = P_o(t) + \Delta P_i(t) + \Delta P_{FFR}(t) + \Delta P_{droop}(t) + \Delta P_{AGC}(t) \tag{6.7}$$

Where $P_o(t)$ is the BESS dispatch set point; $\Delta P_i(t)$ is the BESS inertial response (or response proportional to ROCOF); $\Delta P_{FFR}(t)$ is the BESS FFR response; $\Delta P_{droop}(t)$ is the droop response; and $\Delta P_{AGC}(t)$ is the BESS AGC response.

Depending on the types of services that BESS is providing, the individual components in Equation 6.7 can be activated at proper times. For example, $\Delta P_i(t)$ starts first, at the beginning of the event as soon as a large ROCOF is detected. Then either $\Delta P_{FFR}(t)$ or $\Delta P_{droop}(t)$ occurs (BESS can provide either FFR or droop response but cannot do both at the same time). After the frequency reaches a particular settling level, the $\Delta P_{AGC}(t)$ component starts.

Equation 6.7 can be expanded to show the components of interest in more detail (Equation 6.8).

$$P_{bess}(t) = P_o(t) - 2H\frac{df(t)}{dt} + \Delta P_{FFR}(t) - \frac{f_o - f(t)}{droop} + \Delta P_{AGC}(t) \tag{6.8}$$

Where f_o is scheduled grid frequency, and $f(t)$ is the grid frequency at any point in time.

6.2 What Is the Best Way to Control BESS for Frequency-Responsive Services?

We explore the question of what frequency response service by BESS included in Equation 6.8 is most impactful in terms of improving power system performance during and after large contingencies. For this purpose, we use a simple (governor-only) power system model consisting of synchronous generators with steam and hydro governors, static loads, inertialess wind and solar generation, and BESS as shown in Figure 68. This simple governor-only model was realized in Mathcad using the full set of differential equations of the system. We adopted this approach to better understand the dynamics of this system based on real equations rather than using Simulink black boxes. In this hypothetical case there is a 20% share of combined wind and PV generation, and the combined rated power of BESS is 3.5% of total load. We simulate a large contingency by tripping off the generator G4, which supplies 3% of the load. Combined inertia constant for all conventional generators H=5 sec.

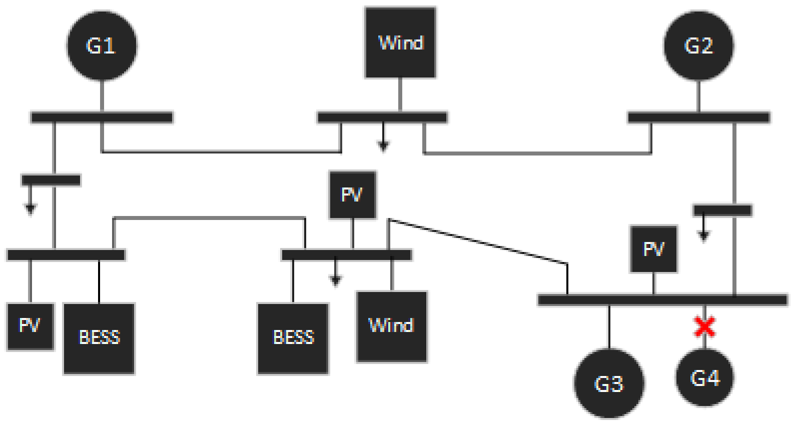

Figure 68. Simple governor-only model

In this simple test system, both wind and solar generation are providing bulk power only, and do not provide any reliability service. The BESS operates at zero power, so it has ability to operate at full power in both charge and discharge modes. At t=50 sec the G4 is tripped, thus causing the system frequency to decline as shown in Figure 69a. The base case (black trace) is when inertia and droop response by only conventional generators are available, causing frequency nadir at about the 59.6-Hz level (just below 59.7 Hz, the first stage of UFLS of the Western Interconnection). The results of simulations for this hypothetical case are explained below, in Figure 69a and 69b.

Then the following services by BESS are activated to demonstrate the impacts on system frequency.

- Case 1: BESS providing inertial response (200 ms delay)
- Case 2: BESS providing droop response (200 ms delay)
- Case 3: BESS providing inertial response and droop (200 ms delay)
- Case 4: BESS providing FFR (2 sec delay)
- Case 5: BESS providing inertia (200 ms delay) and FFR (2 sec delay)

In all above cases, governors of the synchronous generators in Figure 68 (G1, G2, and G3) are set to provide 5% droop and the BESS is set to operate at 50% SOC. The ability of the BESS to deliver inertial response in some cases also will depend on SOC or SOE. Modern lithium-ion battery systems can be designed to provide short-term response event at 0% or 100% SOE. For example, the NREL BESS was designed with following specs in terms of SOE.

- ±1.15 MW for 10 sec at 100% SOE occurring no more than 6 times per year
- ±1.1 MW for 30 sec at 100% SOE occurring no more than 6 times per year
- Deep discharge (0%) capable; ±500 kW at 0% SOE for 10 sec with cooling period of no longer than 10 min.; max number of deep discharge events—no more than 24 times per year

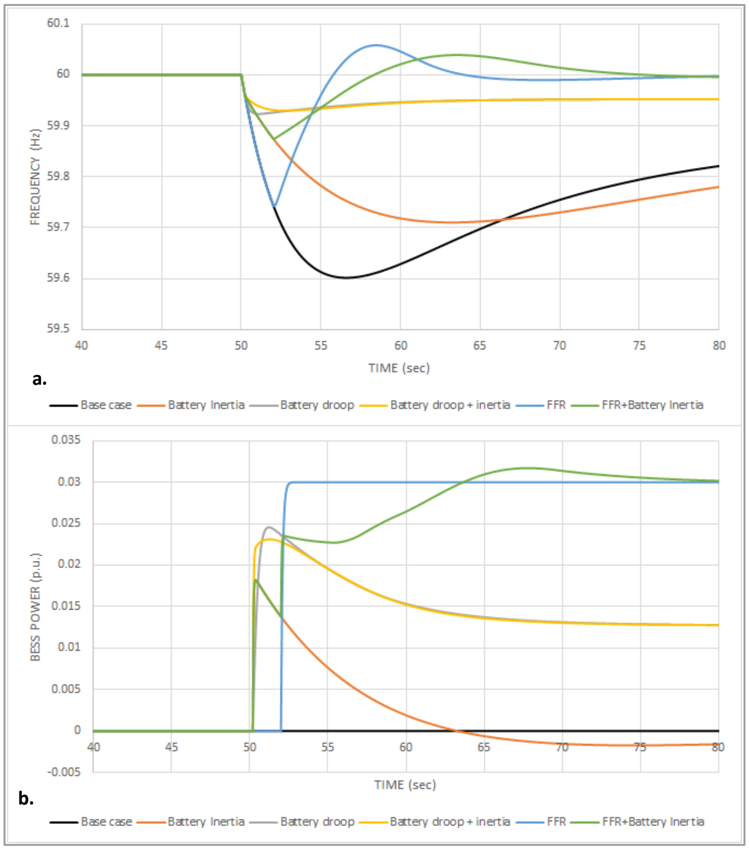

Figure 69. System frequency (a) and BESS response (b)

In Case 1, BESS provides inertial response in accordance to Equation 6.5, mimicking the inertial response of a rotating generator. In this case, the BESS is set to provide inertial response corresponding to H=10 sec in 200 ms after the beginning of the event (200 ms is a very conservative time delay and is introduced to represent a response time of BESS inertial control). Such boost in system inertia causes lower ROCOF and higher frequency nadir as seen in Figure 69a (orange trace). The BESS power output when providing inertial response for H=10 sec is shown in Figure 69b, where BESS is changing its output based only on ROCOF multiplied by H in accordance to Equation 6.5.

Next, we tested the system response with BESS providing 5% droop response only (Case 2) with the same 200 ms response delay. Both system frequency and BESS output for this case are shown as gray traces in Figure 69a and 69b, respectively. A significant improvement in system frequency response is observed for this case because the droop response provided by BESS is much faster than the same response provided by conventional generators. The frequency response becomes even more superior for Case 3 when BESS provides both inertial and droop response (yellow trace).

For Case 4 (blue trace), the BESS was set to provide FFR with very conservative 2-sec delay. The reason for a 2 sec delay was to introduce all computational and communication delays by a phasor measurement unit (PMU) wide-area control system that needs a certain amount of time to determine the exact magnitude of generation loss and communicate it to the BESS control (conceptual diagram of such system is shown in Figure 70). With such long delay, the frequency response of FFR-only case is worse than for the BESS droop or droop plus inertia cases (with some overshoot causing overfrequency) but still better than the base case and BESS inertia-only case. Further, we combined FFR with BESS inertia (Case 5) shown as the green trace. Combination of both gives better performance than the FFR-only case, with a much better frequency nadir and smaller overshoot.

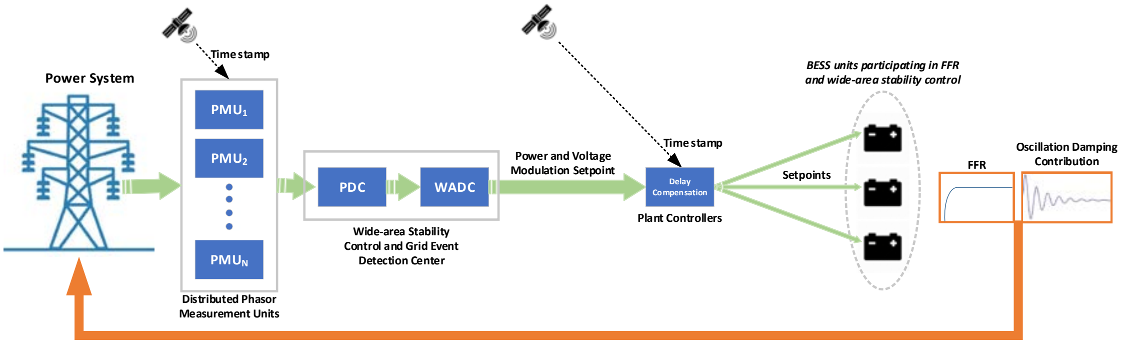

Figure 70. Concept of PMU-based network for provision of FFR and wide-area stability services by BESS

Before drawing any conclusions on best controls strategy for BESS, we decided to try shorter communication delays for the FFR-only case to show sensitivity of system frequency response to time delays caused by wide-area control system (results are shown in Figure 71a and 71b). For the theoretical and (not realistic) no-delay (0 sec) case, the system frequency remains practically undisturbed (black trace). The quality of frequency response is gradually declining with increasing FFR time delay (0.1 sec, 0.5 sec, 1 sec, 2 sec). Combining BESS FFR with inertia, however, yields much superior performance (Figure 72a and 72b) than the FFR-only case. Even for a conservative 2-sec delay, the performance of BESS FFR with inertia gives high-frequency nadir and fast recovery with small overshoot.

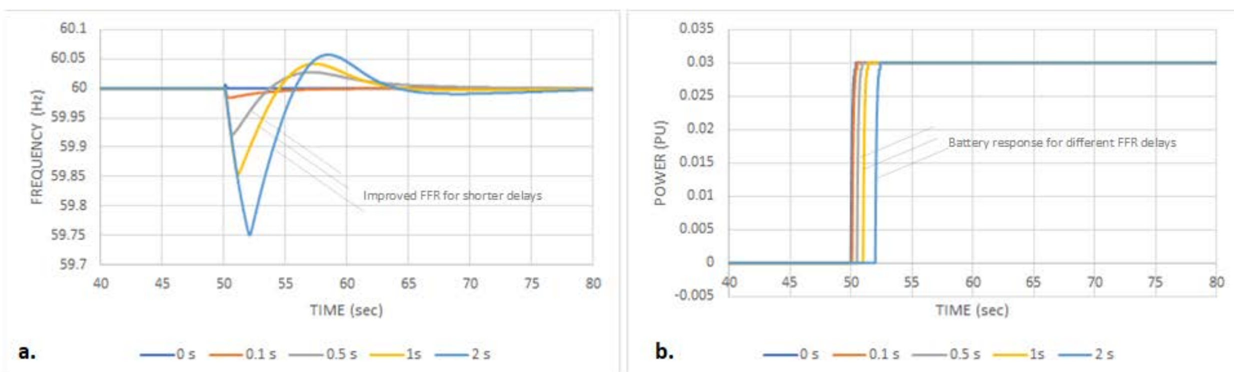

Figure 71. Impact of FFR-only time delay

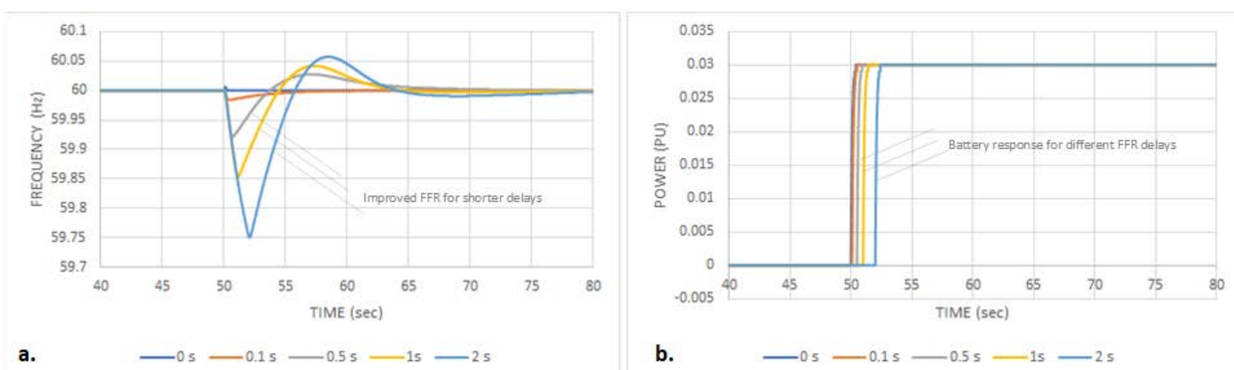

Figure 72. Impact of FFR plus inertia time delay

To verify findings of the simple governor-based model shown in Figure 68, a more-complex transient model of the IEEE 9-bus test system was developed in PSCAD (Figure 73) using NREL-developed models for wind and PV generation and BESS. These models include options to turn on all types of reliability services including GE WindINERTIA model for wind power, ROC) F-proportional inertial response by BESS and curtailed PV plants, droop response by all types of inverter-coupled generation, and reactive power controls. This test case includes a number of conventional steam and hydro-power conventional plants with frequency-responsive governors, automatic voltage regulators, and AGC. The model was tuned to resemble the frequency response of the U.S. Western Interconnection under TEPCC 2022 light spring load case.

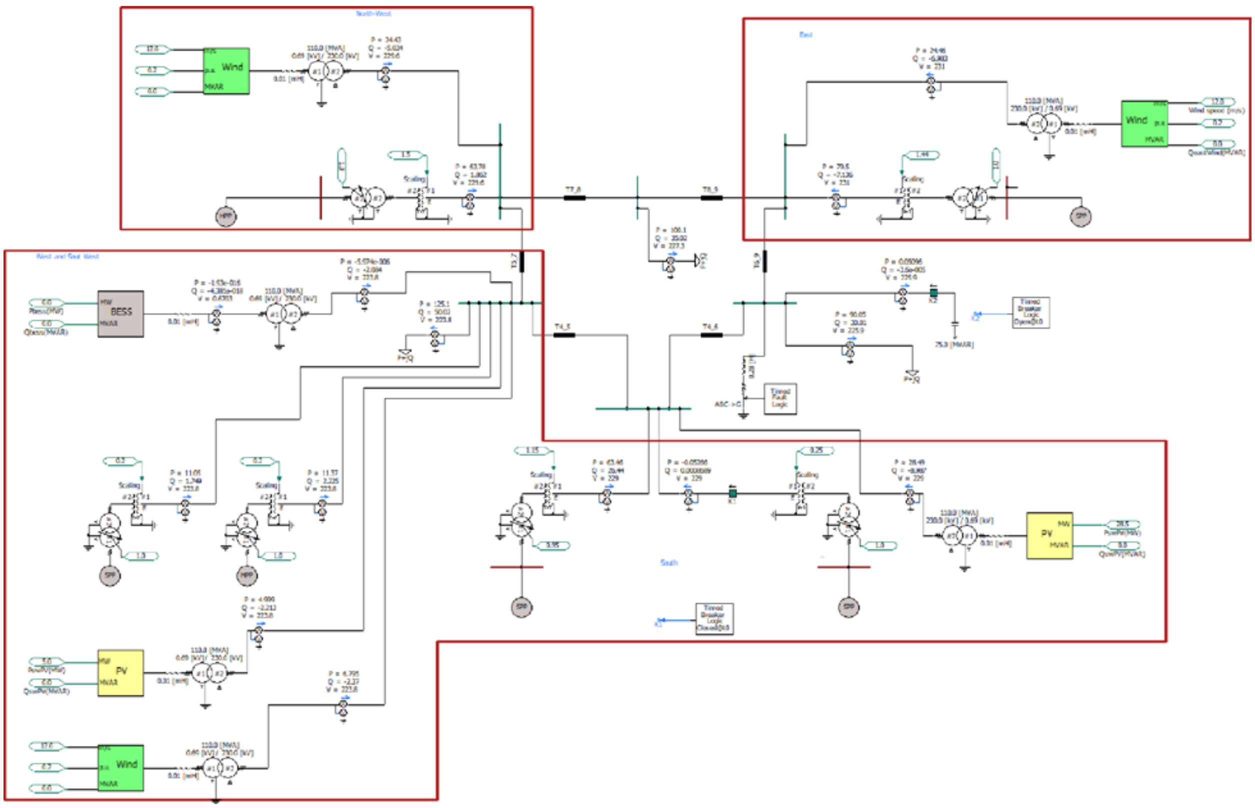

Figure 73. Modified 9-bus test system in PSCAD

Simulations were conducted under different instantaneous penetration levels by variable renewable generation in response to an approximately 3% generation trip for the use cases shown in Table 8.

Table 8. Use Case Description

Use Case #	Conventional Generation	Wind Power	Solar PV	BESS
1	Enabled governors with 5% droop, AGC	No service	No service	No service
2	Enabled governors with 5% droop, AGC	WindINERTIA only	No service	No service
3	Enabled governors with 5% droop, AGC	WindINERTIA and 5% droop, all wind dispatched with 10% headroom	No service	No service
4	Enabled governors with 5% droop, AGC	No service	No service	ROCOF-proportional inertial response and 1% frequency droop
5	Enabled governors with 5% droop, AGC	WindINERTIA and 5% droop, all wind dispatched with 10% headroom	No service	ROCOF-proportional inertial response
6	Enabled governors with 5% droop, AGC	WindINERTIA and 5% droop, all wind dispatched with 10% headroom	No service	ROCOF-proportional inertial response and 1% frequency droop
7	Enabled governors with 5% droop, AGC	WindINERTIA and 5% droop, all wind dispatched with 10% headroom	5% droop, all PV dispatched with 5% headroom	No service
8	Enabled governors with 5% droop, AGC	No service	No service	FFR, 2-sec delay
9	Enabled governors with 5% droop, AGC	No service	No service	FFR, 2-sec delay
10	Enabled governors with 5% droop, AGC	No service	No service	FFR, 0.1-sec delay

The battery controls used in simulations were developed and implemented in 1 MW/1 MWh by the NREL team during the course of this project. The same controls were used in simulations as well as scaled-up to the rated capacity of BESS in the power system PSCAD model shown in Figure 73. The functional diagram of BESS controls is shown in Figure 74. The model allows triggering an inertial response by BESS based on programmable constant H and proportional to ROCOF with programmable ROCOF deadbands. It also is capable of providing a droop response with programmable droop setting and frequency deadband. The FFR response deploys BESS reserves in accordance to external set point command after programmable communication delay. The BESS also is capable of providing reactive power droop. The response time of the model was based on measured response time of NREL's 1-MW/1-MWh Li-ion BESS system.

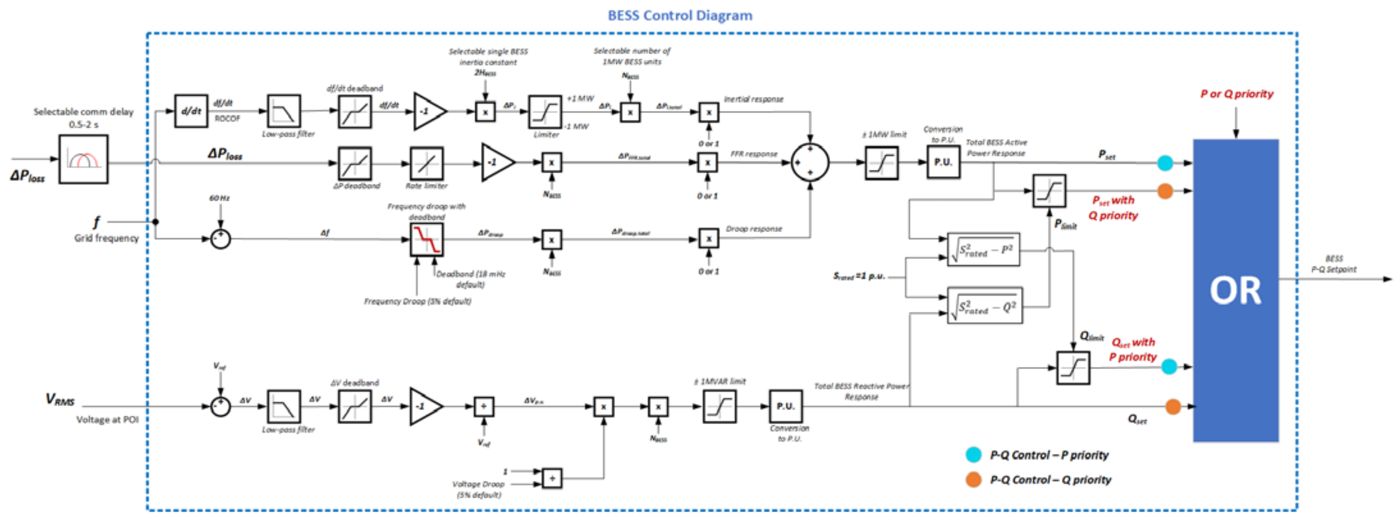

Figure 74. Diagram of NREL-developed BESS control systems

The following model settings were used during simulations for all use cases.

Table 9. Model Settings

	Wind	BESS	PV
Response time (sec)	0.1	0.03	0.05
Inertial response frequency deadband (mHz)	16	16	16
Inertial response ROCOF deadband (Hz/sec)	0 (WindINERTIA has none)	0.02	0.02
Time constant for df/dt filer (sec)	0.05	0.05	0.05
Frequency droop deadband (mHz)	16	16	16
Voltage droop (p.u.)	0.05	0.05	0.05
Voltage droop deadband (kV)	0.025	0.025	0.025

The results of simulations for all use cases with their impact on system frequency response after 3% generation drop is shown in Figure 75 (UFLS was disabled in these simulations). In this scenario, there was 30% of variable generation in total (20% wind and 10% solar PV) and the installed capacity of BESS was about 3.1% of total system capacity. The BESS was dispatched to operate at zero active power, so it has headroom for full up and down response after the event. The frequency nadir is deepest for a base case when renewables do not provide any frequency response (Case 1). WindINERTIA alone helps improve the frequency nadir and shifts it further right because of its impact on the initial ROCOF (Case 2). Even such improvement does not guarantee UFLS avoidance, however, because the frequency nadir still is in close proximity to typical UFLS 59.5-Hz thresholds (59.5 Hz for Western Interconnection). Combination of WindINERTIA and droop control by wind power causes further significant improvements in frequency nadir (Case 3). This behavior is consistent with the findings of a similar study for the whole Western Interconnection shown in Gevorgian et al. [60]. Inertial response combined with aggressive 1% droop response by BESS (Case 4) produces a worse result than Case 3 (WindINERTIA only) because the installed capacity of BESS is much smaller than for wind. Therefore, in this case, the impact by BESS is smaller. However, it still produces significant improvement compared to the base case. Combination of WindINERTIA and wind droop with BESS inertial response (Case 5) provides further improvement in system performance. Case 6, with added BESS droop control, continues the trend of producing more superior frequency response.

In Case 7, we decided to combine droop control by curtailed PV generation with wind response. As shown in Figure 75, it provides marginal improvements as compared to previous case with BESS. Finally, we tested the FFR control by BESS with various time delays (Case 9 to Case 10). The BESS also was providing inertial response from the beginning of the event until it received an external set point command. In case of conservative 2-sec FFR delay (Case 8), the response of the system is worse than the less-conservative 1-sec FFR delay (Case 9) and, of course, it the best for optimistic (and likely not realistic) 0.1-sec FFR delay (Case 10).

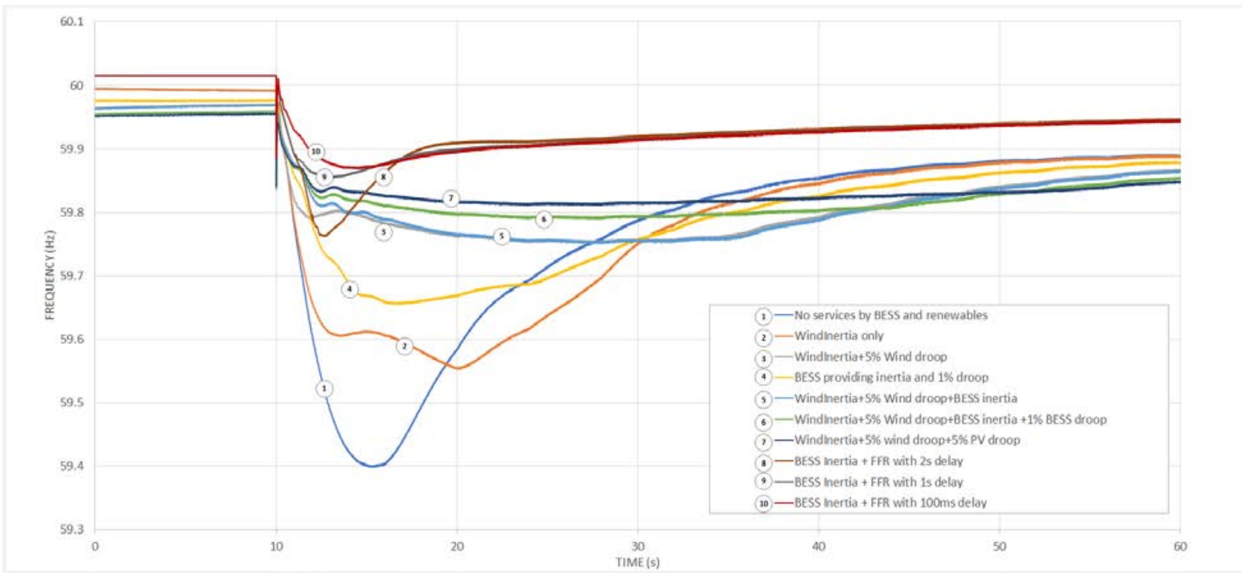

Figure 75. Comparison of frequency for all simulation cases

The responses by wind power for all the above cases are consolidated in Figure 76. It can be seen that wind power produces the greatest response in Case 3. The response by BESS for all use cases is shown in Figure 77. Overall system responses for all generation components are shown in Figure 78 for all use cases.

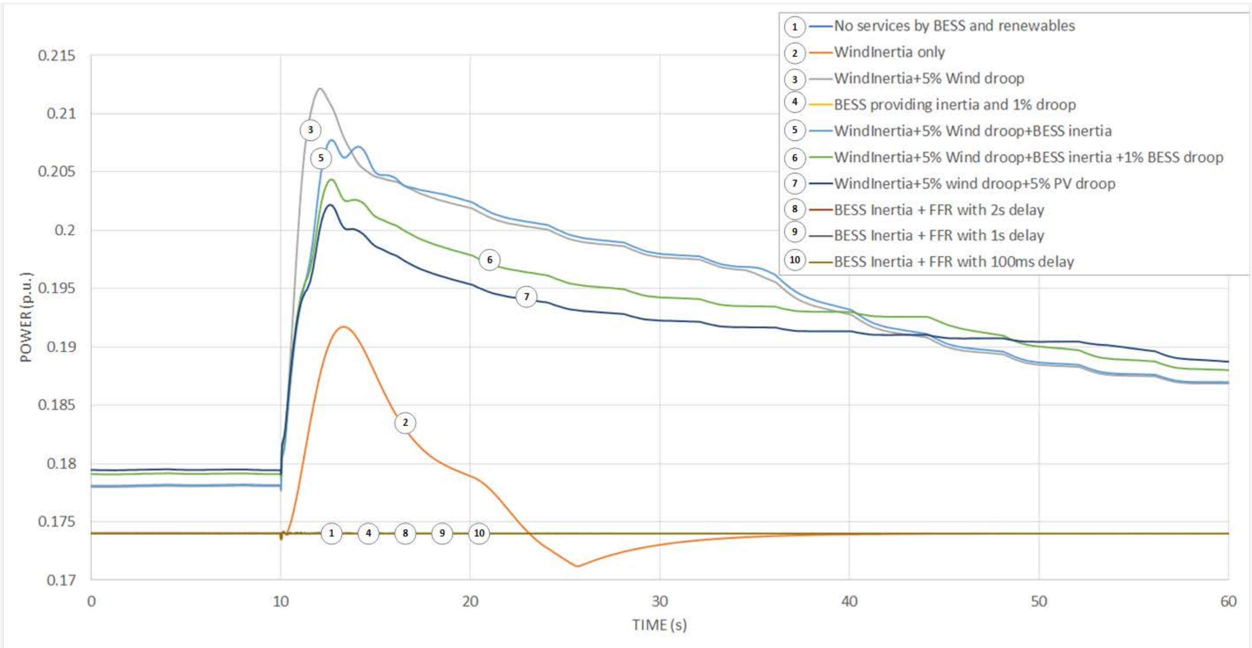

Figure 76. Comparison of wind power responses for all simulation cases

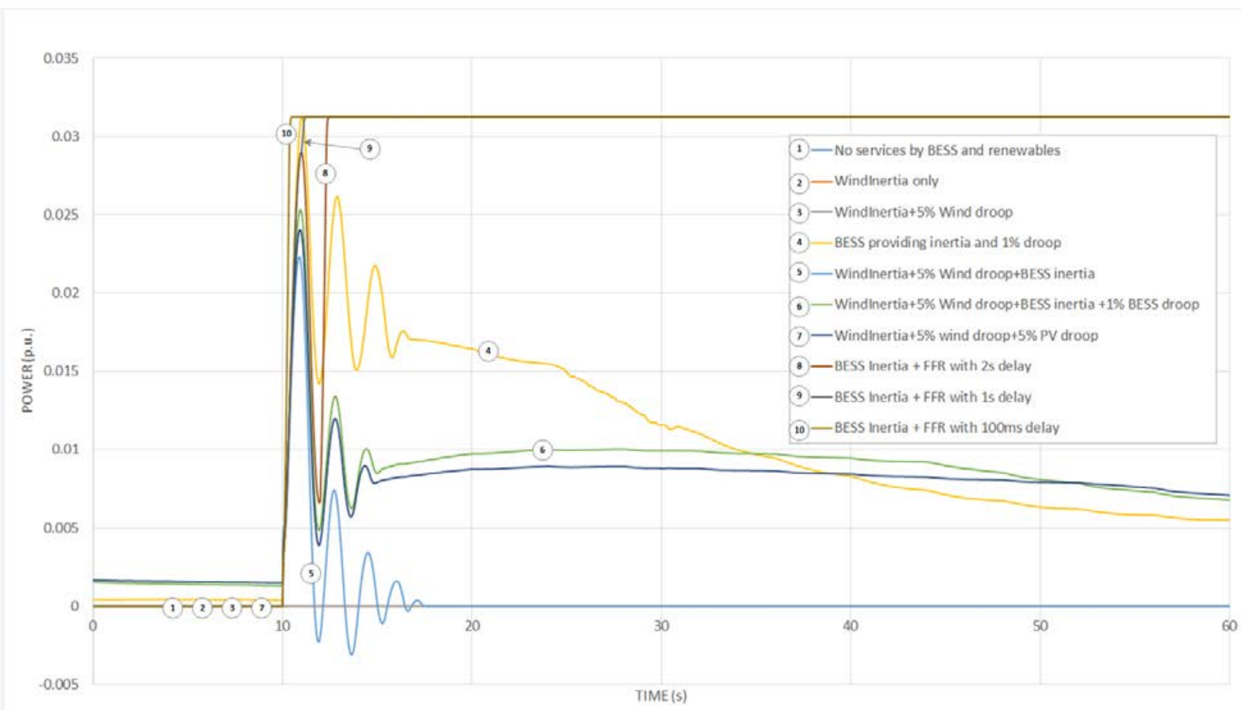

Figure 77. Comparison of BESS responses for all simulation cases

Figure 78. Comparison of system performance for all use cases

We also investigated the impact of average wind speed and consecutive ability of wind power to provide inertial and droop response on system frequency for the same level of generation loss as for previous cases described int this section. Figure 79 compares results for four different simulated cases for the power system shown in Figure 73.

- Case 1: All wind turbines operate at average 8 m/sec wind speed and set to provide both inertial and droop response with 10% headroom.
- Case 2: 10% of total wind power operates at or above rated wind speed (12 m/sec) with remaining 90% operating at 8 m/sec. All wind power is set to provide inertial and droop response with 10% headroom.
- Case 3: 30% of total wind power is operating at or above rated wind speed with remaining 70% operating at 8 m/sec. All wind power is set to provide inertial and droop response with 10% headroom.

- Case 4: 30% of total wind power is operating at or above rated wind speed with remaining 70% operating at 8 m/sec without curtailment. Only wind power operating at rated wind speed is set to provide inertial and droop response.

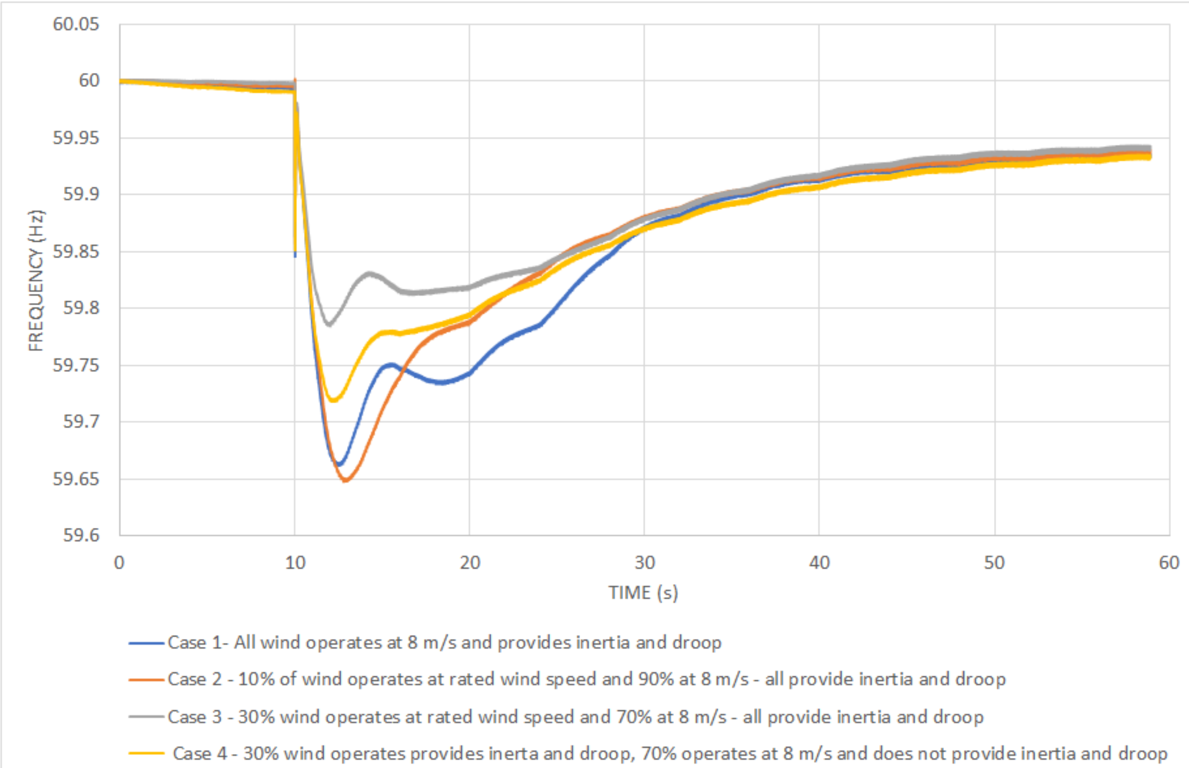

Figure 79. Wind-speed impact on frequency response

Comparison of results shown in Figure 79 leads to the conclusion that provision of inertial and droop response by only a portion of wind power that operates at high wind speeds in some cases can produce better frequency, response partially because of more superior inertial response (minimal deceleration of wind rotors). For example, despite of the fact that Case 4 has highest instantaneous penetration by wind power and with lower percentage of responsive wind turbines, it still produces better response than Case 1 and Case 2 with lower share of wind power in the system. Naturally, Case 3 exhibits the best frequency response because all wind power was set to provide both inertia and droop.

6.3 Reactive Power Controls by BESS

Voltage of the North American bulk system normally is regulated by generator operators, which typically are provided along with voltage schedules by transmission operators [55]. The growing levels of variable wind and solar generation have led to the need for them to contribute to power system voltage and reactive regulation because, in the past, the bulk system voltage regulation was provided almost exclusively by synchronous generators. According to the Federal Energy Regulatory Commission's (FERC's) LGIA Standard Large Generator Interconnection Agreement (LGIA) [55], the generally accepted power-factor requirement of a large generator is ±0.95. In conventional power plants with synchronous generators, the reactive power range normally is defined as dynamic, so synchronous generators must continuously adjust their reactive power production or absorption within a power factor range of ±0.95. For PV power plants, the reactive power requirements are not well defined. FERC Order 661-A [19] is applicable to wind generators but sometimes applies to PV plants as well. It also requires a power factor range of ±0.95 measured at the POI and requires that the plant provide sufficient dynamic voltage support to ensure safety and reliability (the requirement for dynamic voltage support is normally determined during interconnection studies). Utility-scale WPPs are designed to meet the ±0.95 power factor requirements. The common practice in the PV industry, however, is to configure PV inverters to operate at unity power factor. It is expected that similar interconnection requirements for power factor range and low-voltage ride-through will be formulated for PV in the near future. To meet this requirement, PV inverters must have MVA ratings great enough to handle full active and reactive current.

In its recent Order 827, FERC issued a final rule requiring all newly interconnecting nonsynchronous generators, including wind generators, to design their facilities to be capable of providing reactive power [58]. The generating facilities must be capable of maintaining a composite power delivery at continuous rated power output at the high side of the generation substation at ±0.95 power factors.

Conventional synchronous generators of power plants have reactive power capability that typically is described as a "D curve," as shown in Figure 80. The reactive power capability of conventional power plants is limited by many factors, including their maximum and minimum load capability, thermal limitations because of rotor and stator current-carrying capacities, and stability limits. The ability to provide reactive power at zero loads usually is not possible in many large plant designs. Only some generators are designed to operate as synchronous condensers with zero actives loads. The reactive power capability of a PV inverter and Type-4 wind turbine power converter is determined by their current limits only. With proper megawatt and MVA rating, the PV inverter and Type-4 WTG should be able to operate at full current with reactive power capability, similar to that shown in Figure 80. Reactive power capability of Type-3 WTGs is different because of partial rating of their power converters and specific characteristics of double-fed induction generator-based electric topology. For the same MVA rating, a PV power plant or Type-4 WPP is expected to have much superior reactive power capability than a conventional synchronous generator–based plant, as indicated in Figure 80. In principle, PV inverters and wind turbine power converters can provide reactive power support at zero power, similar to a static synchronous compensator (STATCOM); however, this functionality is not standard—especially for PV inverters, because they are disconnected from the grid at night. The reactive power control at night by wind inverters is more commonly a standard function for WPPs, for example, GE's WindFREE voltage-control feature. Synchronous condensers and STATCOMs are capable of reactive power control but these devices do not produce any active power (unless coupled with energy storage).

Unlike wind and PV inverters that can operate only in two quadrants of P-Q plane, the BESS systems are capable of operating in all four quadrants, as depicted in Figure 80. This superior reactive power capability can make BESS a unique provider of reactive power–related services for steady state, dynamic, and transient applications. In its proposed reactive power capability characteristic for asynchronous generation, for example, CAISO defined the requirements for dynamic and continuous reactive power performance by such resources [59]. A comparison between BESS reactive power capability and CAISO requirements is depicted in Figure 81 for both dynamic and continuous conditions. The ability of BESS inverters to operate in all four quadrants and provide both continuous and dynamic reactive power support allows BESS to provide superior P-Q capability than that required by system operators.

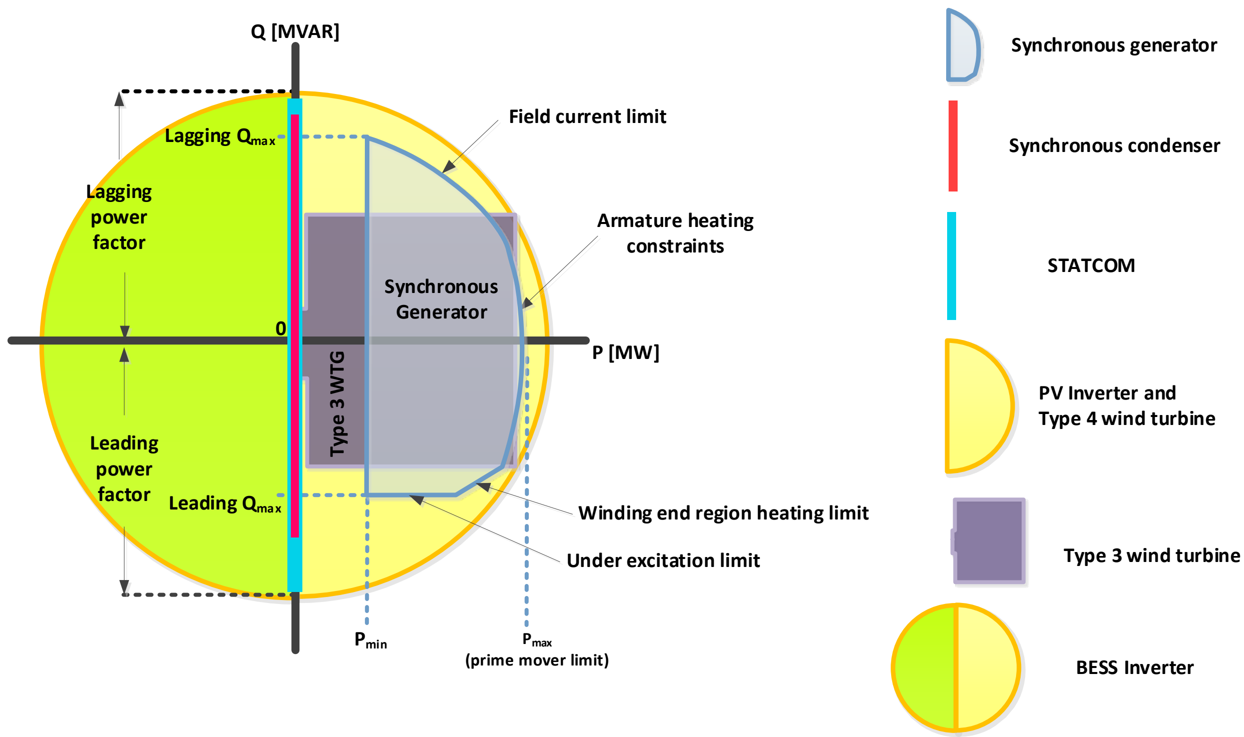

Figure 80. Comparison of reactive power capabilities

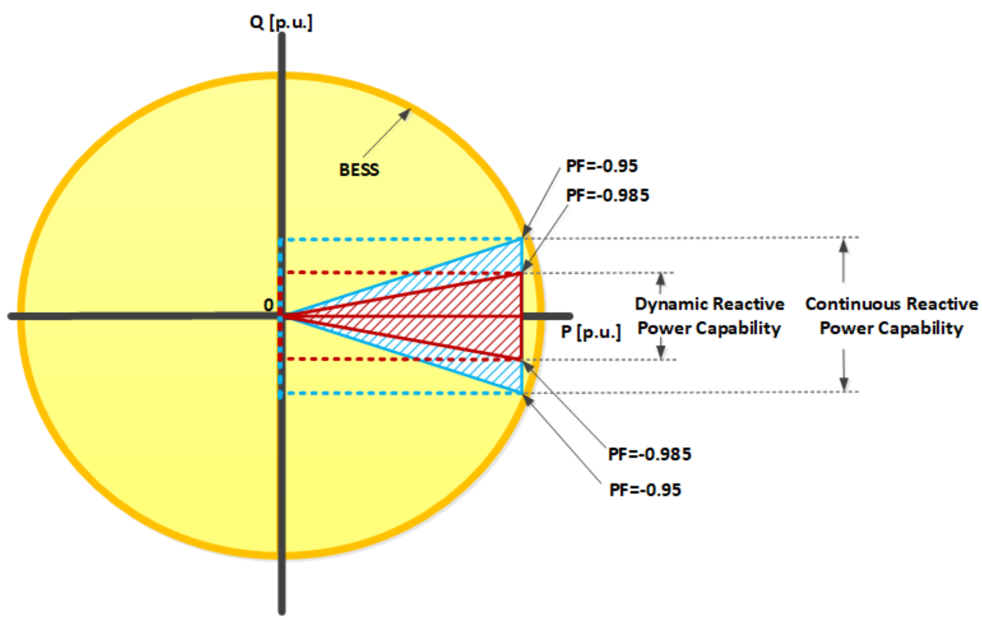

Figure 81. Comparison of BESS reactive power capability with proposed CAISO requirements

The reactive power/voltage droop has been implemented in BESS in accordance with the diagram shown in Figure 74. The controller allows prioritizing the reactive power provision by BESS over active power, based on a concept shown in Figure 82, if the current limit is exceeded.

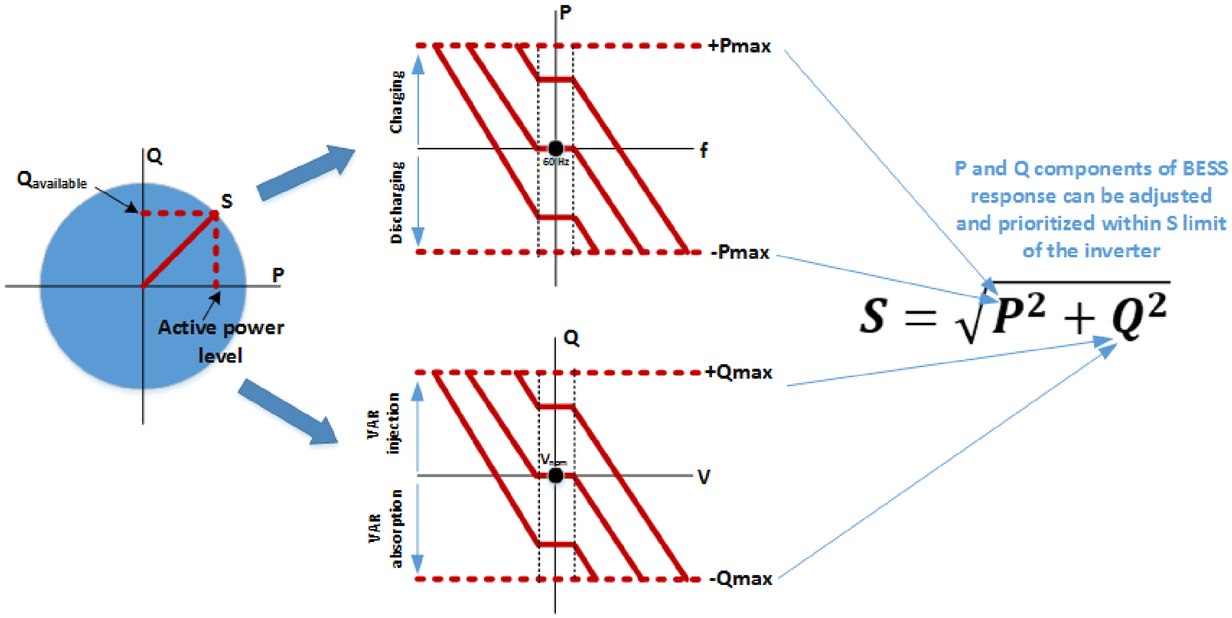

Figure 82. The P-Q control during steady-state and transient conditions with prioritizing

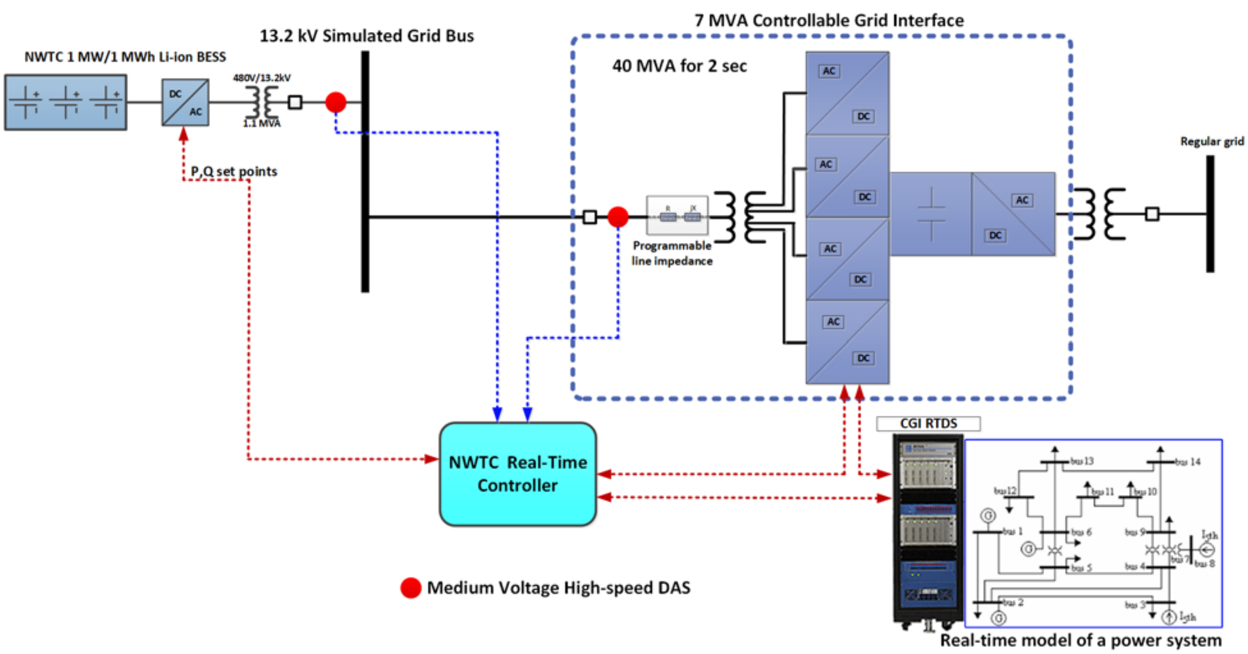

Figure 83. Experimental setup for testing the reactive power capability of BESS

The P-Q capability of NREL's 1 MW/1 MWh BESS consisting of LG Li-ion batteries and SMA 2.2 MVA, 400 VAC inverter/charger with 1.1 MVA 13.2 kV / 400V transformer was verified using experimental setup shown in Figure 83. The BESS inverter's full four-quadrant steady-state P-Q characteristic was tested in CGI connected mode to avoid impacts on NWTC grid. The inverter was commanded to use various combinations of active and reactive power set points to cover the whole range of P-Q operation. The results of one such test are shown in Figure 84. It was discovered that the SMA inverter limits only P_{max} and Q_{max} at 1 MW and 1 MVAR levels accordingly but does not limit the maximum apparent power S_{max} which is expected to be 1 MVA (green circle in Figure 84). Instead, the measured the P-Q characteristic is approaching to the square shape (orange area in Figure 84). Because of this characteristic, care must be taken not to exceed S_{max} set point for inverter transformer protection (the 400-V/132-kV step-up transformer is rated at 1.1 MVA).

The P-Q characteristic of the BESS system was measured on MV side (or CGI side) of BESS transformer as well. Comparison of both P-Q characteristics is shown in Figure 85. The shift between the two is caused by a 6% impedance of the BESS transformer, and some reactive losses in 100-m underground collector line. NREL is developing control to compensate for these reactive losses, so reactive power can be accurately controlled on the MV side of the BESS transformer.

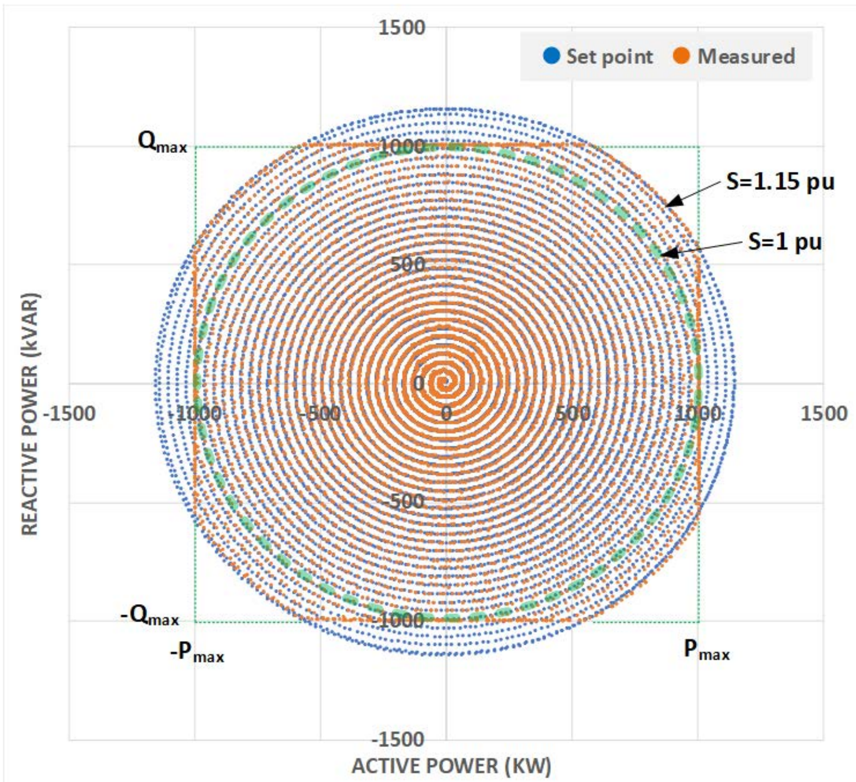

Figure 84. Results of BESS P-Q characterization test

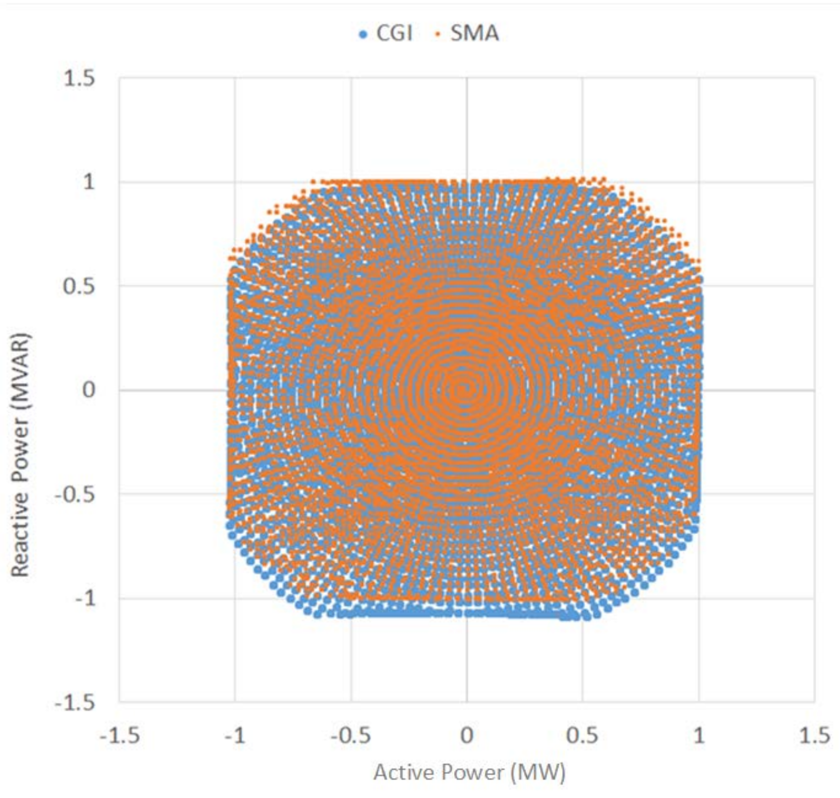

Figure 85. Reactive power capability measured on LV (SMA) and MV (CGI) sides of BESS trasmformer

7.0 Using CGI for Demonstrating Inertial Response by Wind Power Plants

The unique characteristics of the NWTC site—where utility-scale wind turbines are co-located with CGI—enable the conducting of repetitive tests under fully controlled conditions, so repose of the wind power to the same grid events can be tested under different wind resource variability conditions. As described in Section 2.3, this capability is especially useful for testing inertial response by wind power. We used this CGI capability to test ability of GE 1.5-MW WTG to provide inertial response when exposed to the same frequency event, so aggregate inertial response of much greater levels of wind generation under diverse wind-speed conditions can be evaluated. Results of one such experiment are shown Figure 86. The GE 1.5-MW generator was exposed to real decline in frequency at very high ROCOF (1 Hz/sec) emulated by CGI on its 13.2-kV voltage bus. The same test was conducted 65 times at different wind-speed conditions, so the ability of the turbine to provide inertial response was verified for all portions of the power curve, as shown in Figure 86.

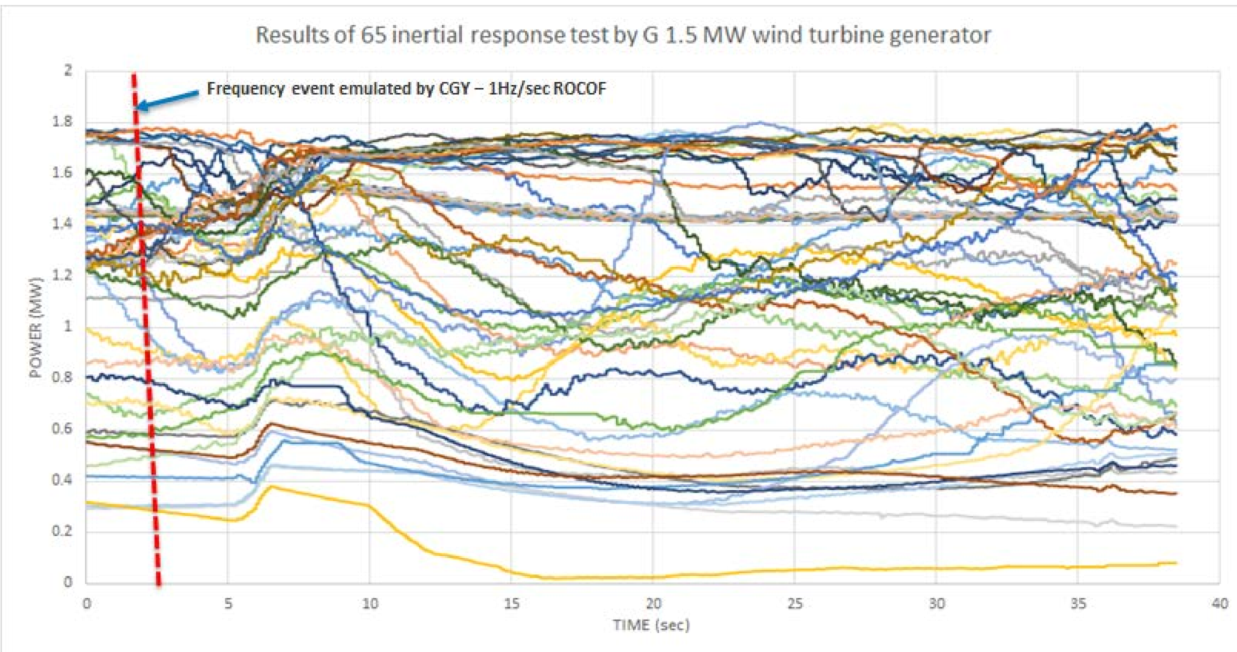

Figure 86. Results of inertia response tests

During data post-processing, the summation of all time series produces aggregate response that resembles total inertial response of ~100 MW wind power as shown in Figure 87. In this case, the large wind power plant would produce about 8 MW (or 10.7% of per-fault power) of inertial response within 2 sec from the beginning of the event. Due to rotor deceleration during tests at below-rated wind-speed conditions, there is some production loss after the event with continued decline because of changing wind conditions.

We also extracted time series demonstrating inertial response at rated or above-rated wind power (Figure 88). Initial wind speeds conditions are different for each test shown in the upper graph in Figure 88, but they all are at around or above the rated level. Note that turbines operating at this level produce predictable, scalable, and easy-to-model inertial response. Also, the production recovery occurs with very little energy loss, as shown in the lower graph in Figure 88.

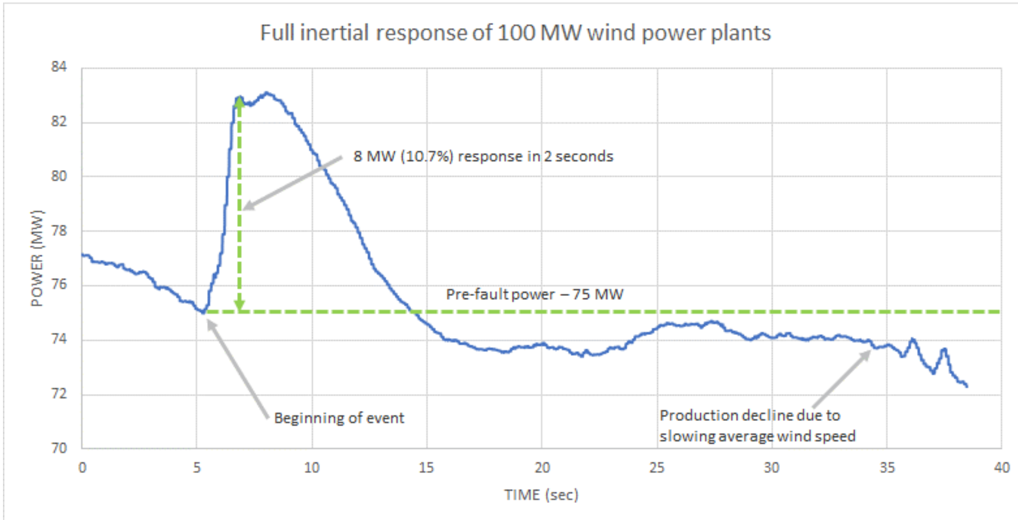

Figure 87. Wind inertia results aggregation

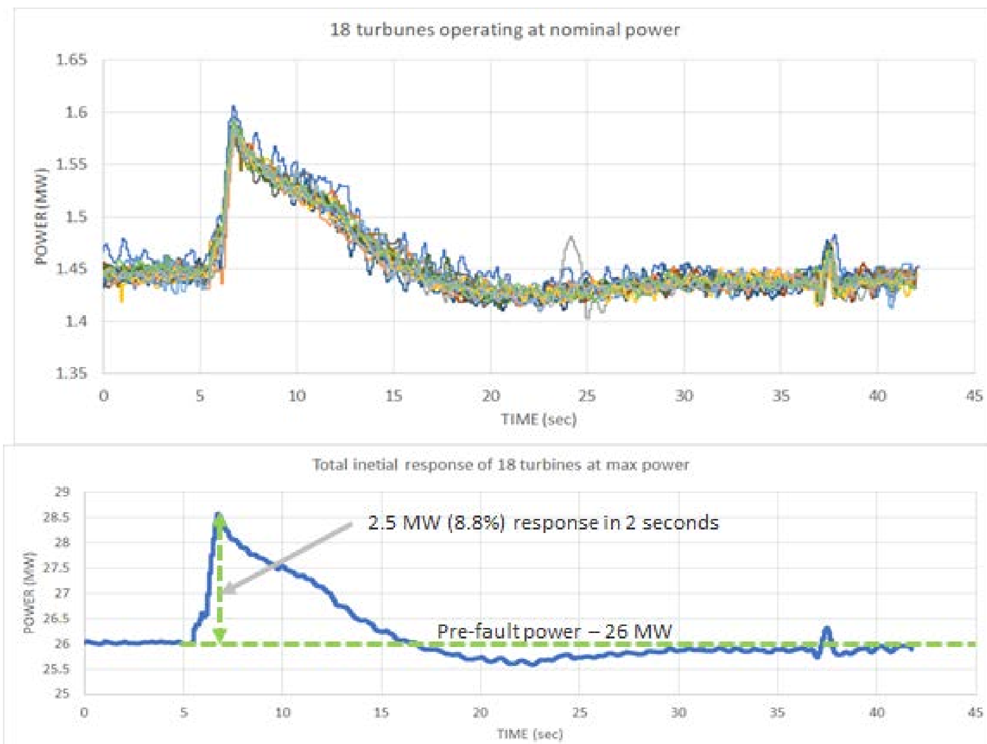

Figure 88. Inertial responses at rated or above rated wind speeds (upper graph), and equivalent inertial response (lower graph)

We also extracted inertial response by several wind turbines operating at lower wind speeds and produced aggregate response as shown in Figure 89. This equivalent of response of 31.5-MW WPP. The peal inertial response is 2.7 MW (8.7% of capacity, or 15.8% of prefault level). We also calculated the energy ratio for both power injection and underproduction stages as shown in Figure 89. It appears that during this particular experiment, under specific wind-speed conditions the injected energy was 38.6 kWh, and energy needed for production recovery was 69.7 kWh. This equals to 55% roundtrip energy efficiency. A short-term fast-acting energy storage system with appropriate power rating can provide energy to compensate the underproduction loss in cases like this.

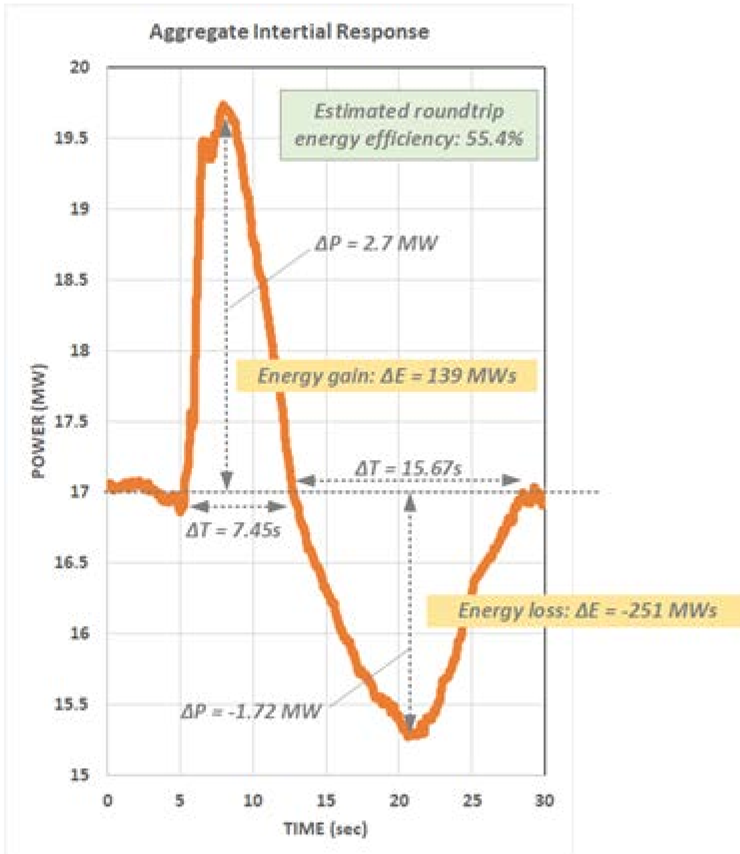

Figure 89. Equivalent inertial response at lower wind speeds

In general, inertial response tests conducted on GE 1.5-MW wind turbine using CGI demonstrated the turbine's ability to extract kinetic energy stored in the turbine's rotor in accordance with inertial control set points. Figure 90 shows the results of one inertial test when the WTG was set to operate at 1 MW with a small frequency deadband set at 16 mHz. The inertial response is triggered immediately after the declining frequency passes below 16 mHz, as shown in Figure 91 for the same test. After that, the inertial power is controlled to increase linearly with declining frequency until it reaches about 1.15 MW, and the injected inertial power starts declining to prefault level.

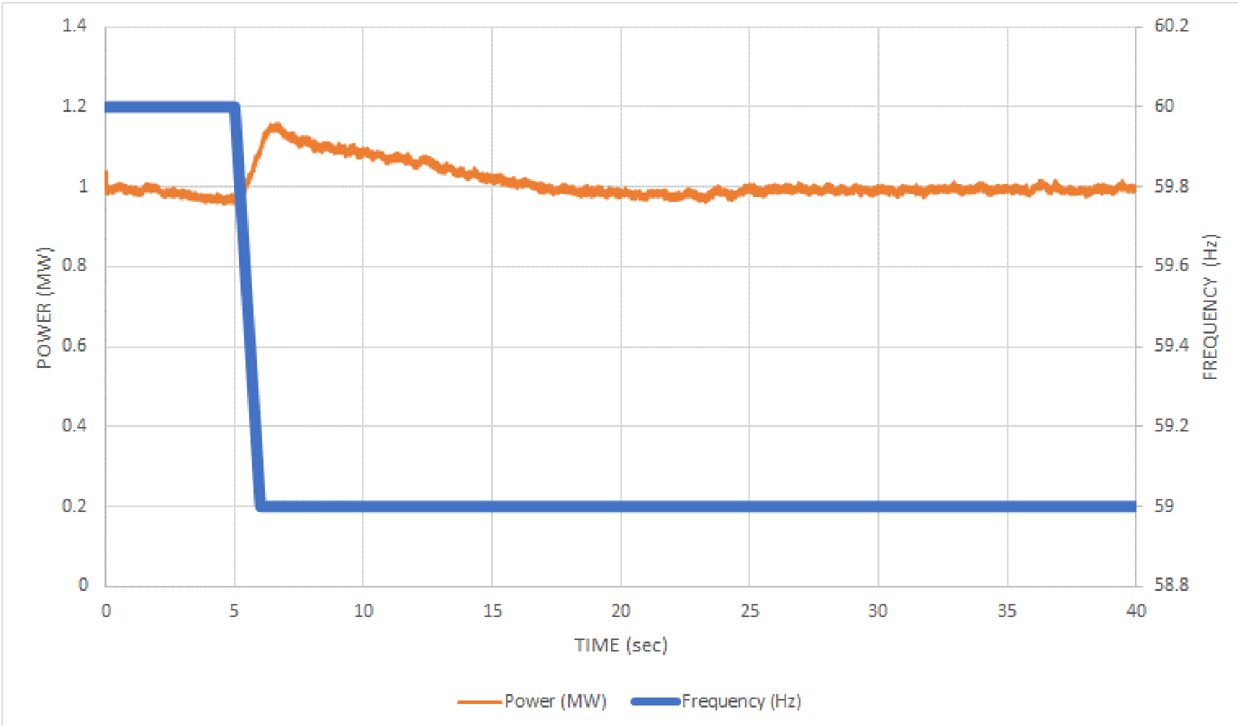

Figure 90. Inertial response test with 16-mHz deadband

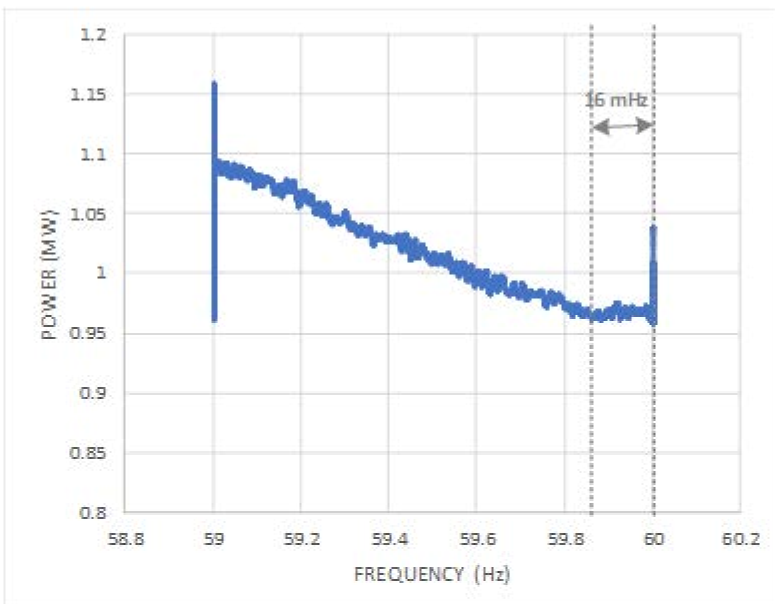

Figure 91. Inertial power versus frequency with 16-mHz deadband

7.1 Development of Controls for Dispatchable Operation with Provision of Reliability Services

As part of project activities, the NREL team developed a controller for a dispatchable renewable power plant involving NWTC's renewable wind and solar generation and integrated the BESS into this plant control. The plant control also is integrated with wind and solar resource forecast and, along with full dispatchability, it can provide many types of existing and future evolving reliability services to the grid, including frequency regulation, primary frequency control, and inertial response. The main control panel of dispatchable plant developed in NI LabVIEW environment is shown in Figure 92.

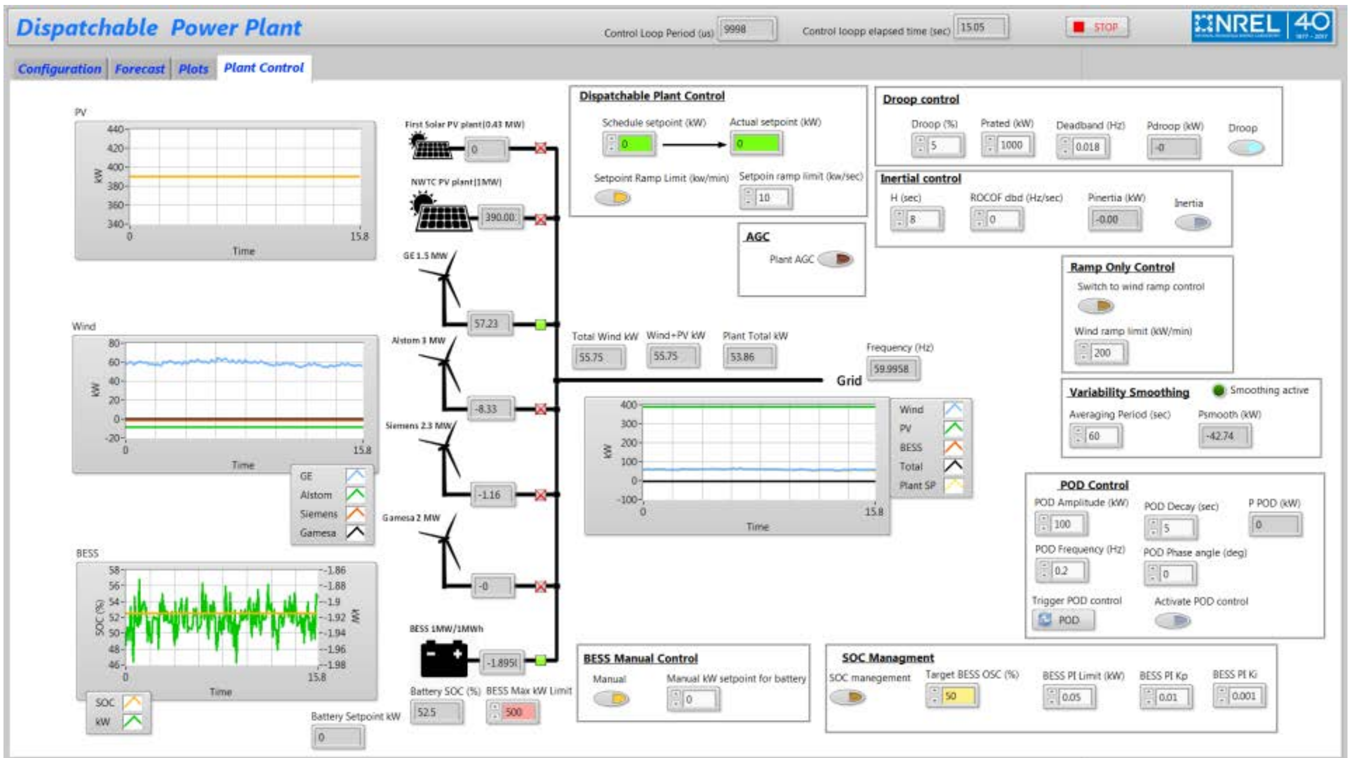

Figure 92. Main panel of the NREL dispatchable power plant with BESS

The following control features for a dispatchable renewable plant have been developed and implemented during this project.

- Dispatchable renewable plant operation: Ability to operate at active and reactive power external set points received from system operator
- Ramp limiting, variability smoothing, cloud-impact mitigation
- Provision of spinning reserve
- AGC functionality
- PFR (programmable droop control)
- FFR (fast frequency response)
- Inertial response: Programmable synthetic inertia for a wide range of H constants emulated by BESS

- Reactive power/voltage control
- Advanced controls—ability of the plant to modulate its output for provision of power system oscillations damping services was tested
- Stacked services (ability to provide several services at the same time)
- Battery SOC management controls

Simplified diagrams for some of the implemented controls, such as set point operation, plant ramp limiting, and variability smoothing, are shown in Figure 93, Figure 94, and Figure 95.

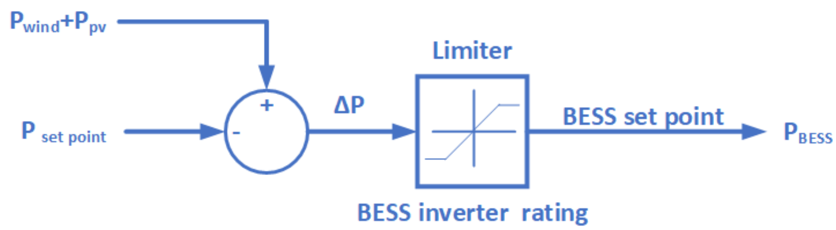

Figure 93. Simplified BESS control diagram to follow the plant dispatch set point

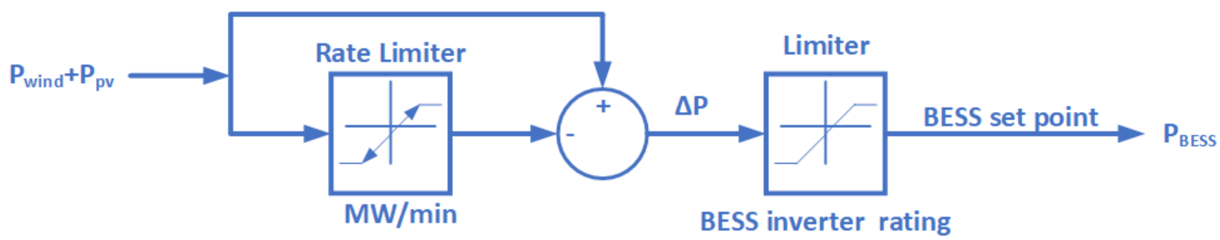

Figure 94. Diagram of ramp-limiting controller

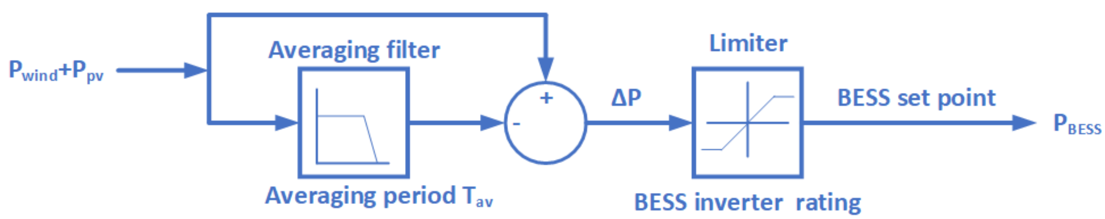

Figure 95. Variability-smoothing control

This dispatchable plant setup was used to conduct many different tests to demonstrate various BESS use cases for both renewables integration and standalone services. The summary of tests illustrating various use cases for BESS is provided below.

- Figure 96—Dispatchable operation tests: The BESS was providing capability to follow the plant dispatch set point. The plant maintained the set point operation even after one of two WTGs was intentionally disconnected from the grid.
- Figure 97—Ramp limiting tests: The plant was set to operate at ±50 kW/min (1.3% of installed plant capacity per minute) ramp rate. The plant maintained the ramp limit set point operation even after one of two WTGs was disconnected from the grid.
- Figure 98—Variability smoothing test: The plant was set to produce smoothed output using the 1-min averaging filter implemented in the controls. The BESS was adjusting its output based on the difference between actual variable wind plus solar production and calculated the smoothing set point.
- Figure 99—Stacked services test: The plant is capable of operating at dispatch set point and responds to AGC signals received from the utility. Historic area control error data from Public Service Company of Colorado (PSCo) were used to generate AGC signal for the plant.
- Figure 100—BESS providing AGC response: Ability of BESS alone to participate in frequency-regulation market has been demonstrated.
- Figure 101—BESS providing PFR (droop control): Ability of BESS to participate in future PFR markets has been demonstrated for different droop settings (3%, 5%) using historic frequency event data measured in Western Interconnection.
- Figure 102—Synthetic inertia tests: BESS demonstrated the ability to emulate the response of a rotating generator to frequency fluctuation.
- Figure 103—Power systems oscillations damping controls: BESS demonstrated the ability to modulate its active power output in accordance to various period set point signals for provision of power-systems oscillation-damping services. The ability of wind power to provide such services was demonstrated in our earlier work (Zayas et al.) [79].

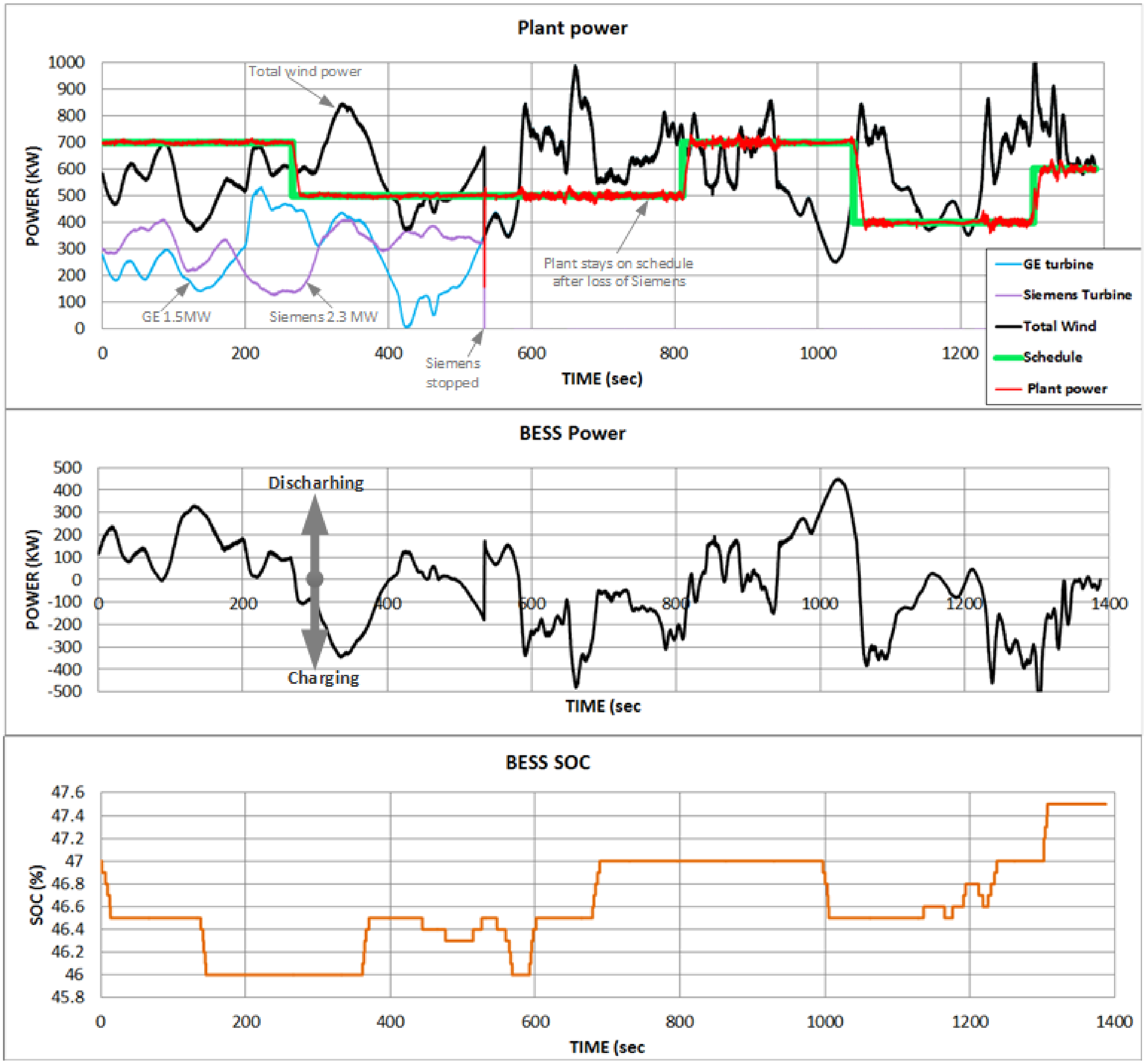

Figure 96. Dispatchable hybrid wind–BESS operation

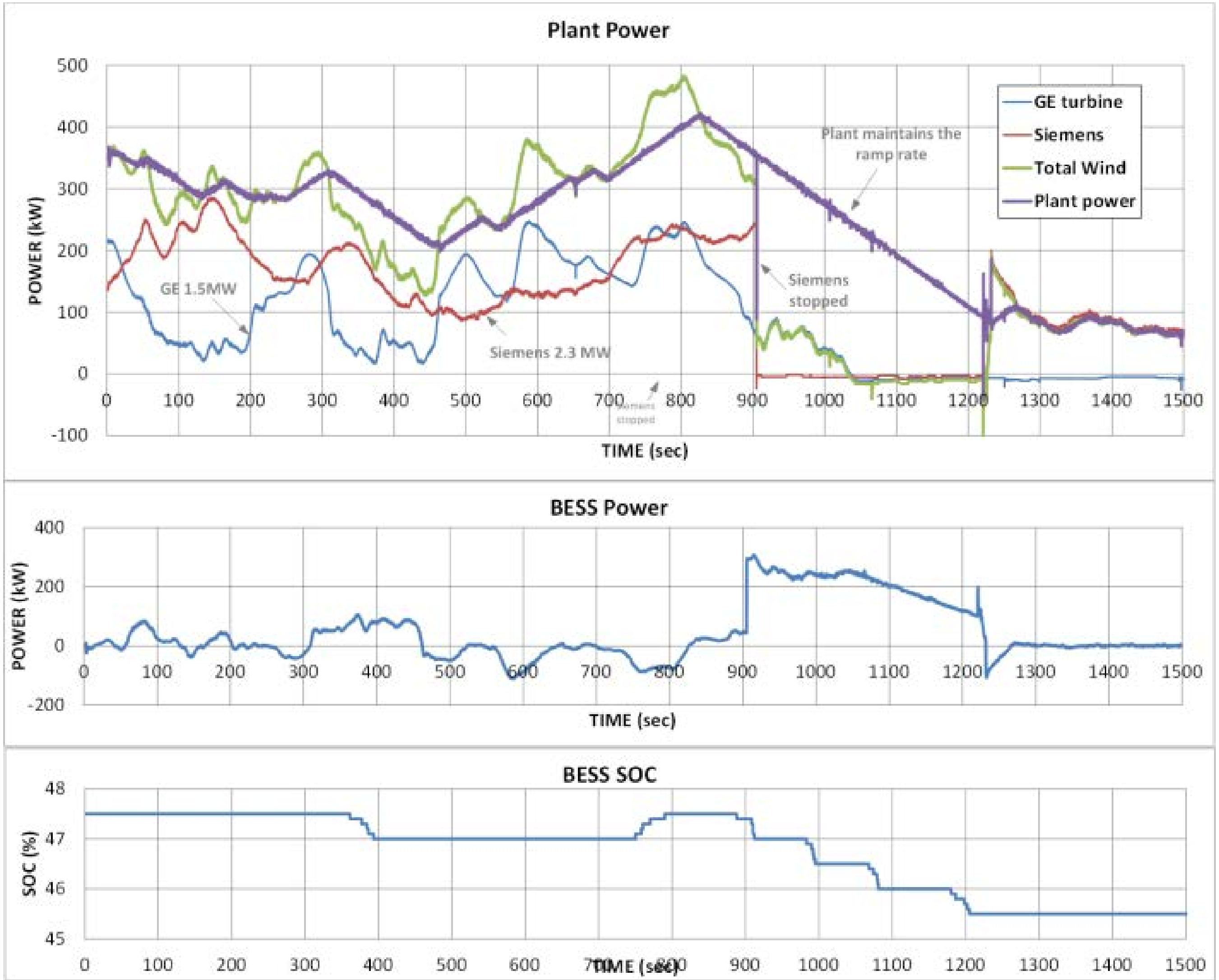

Figure 97. Wind-ramp limiting tests using BESS

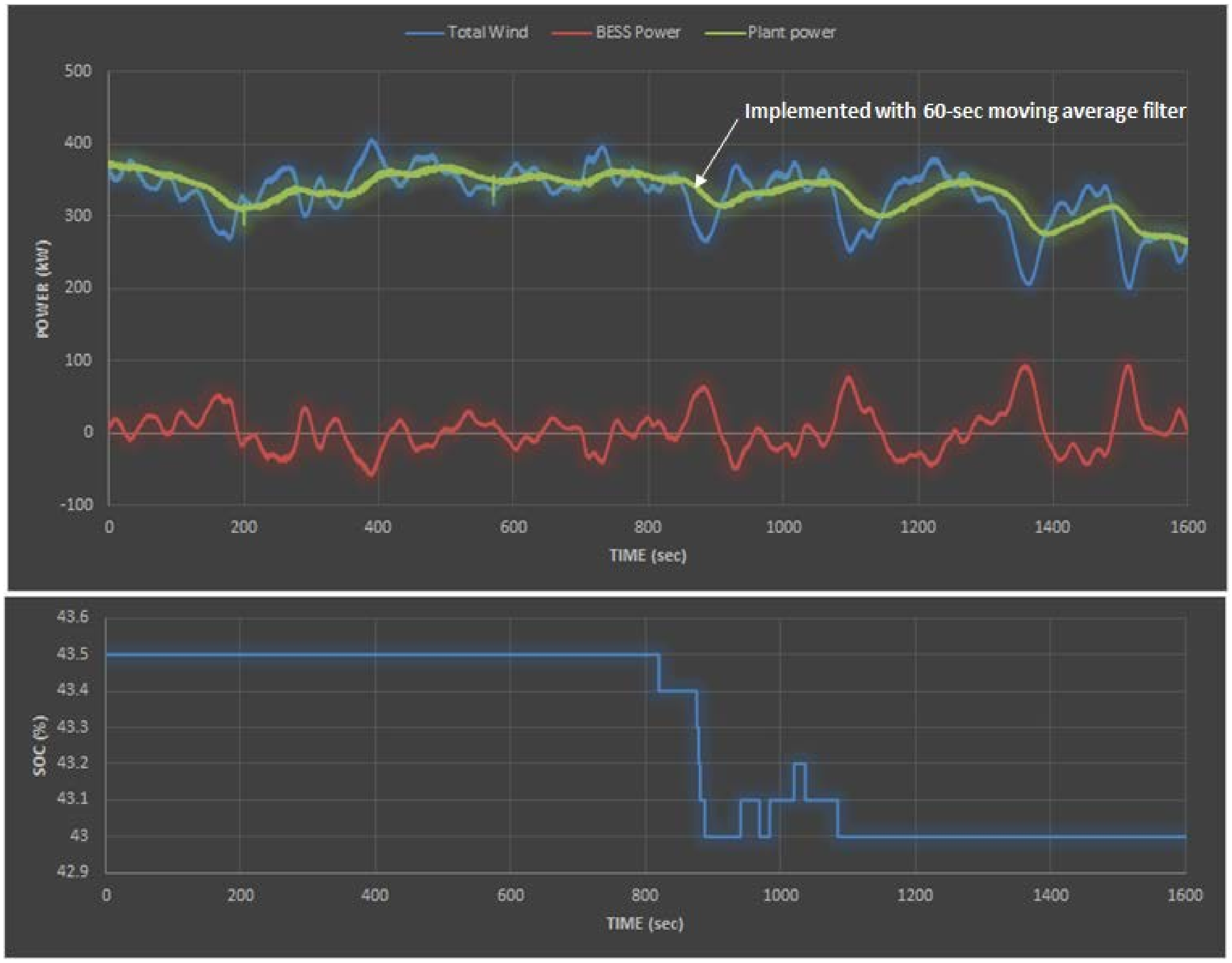

Figure 98. Variability-smoothing test with 60-sec averaging filter

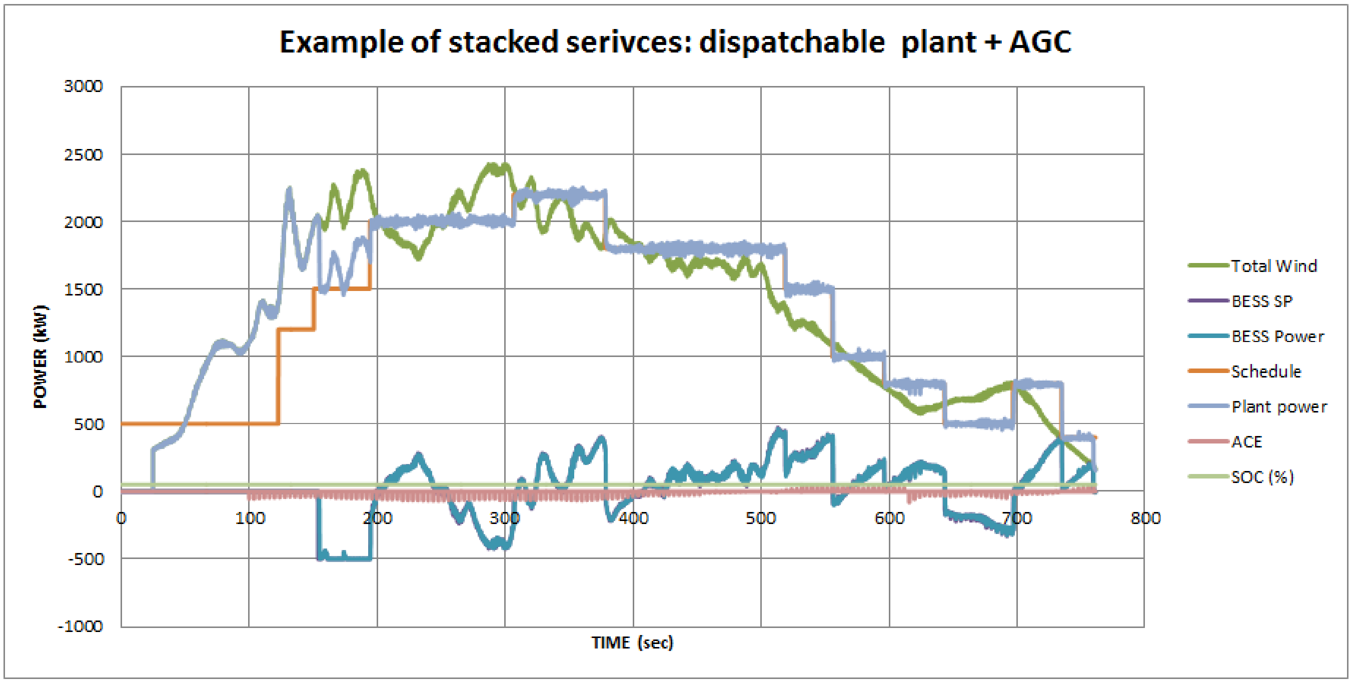

Figure 99. Example of stacked services tests

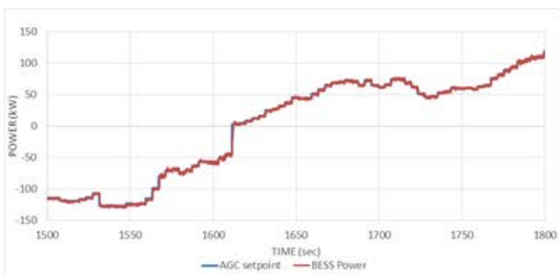

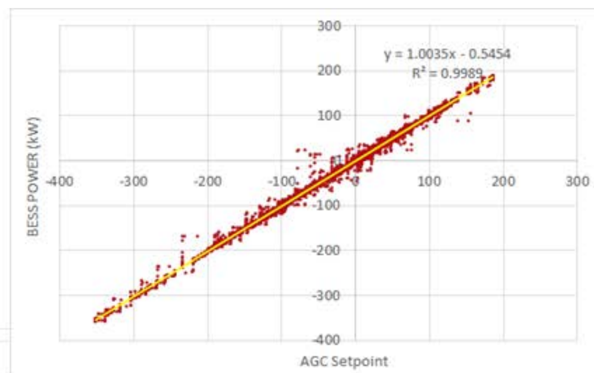

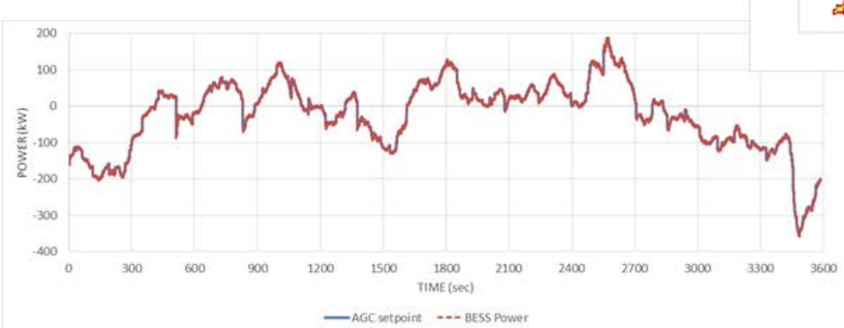

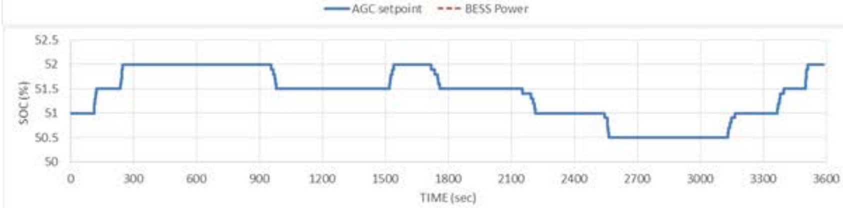

- PSCO historic ACE time series (updated every 4 sec)
- ACE is scaled down to match BESS rating

Figure 100. BESS participation in AGC tests

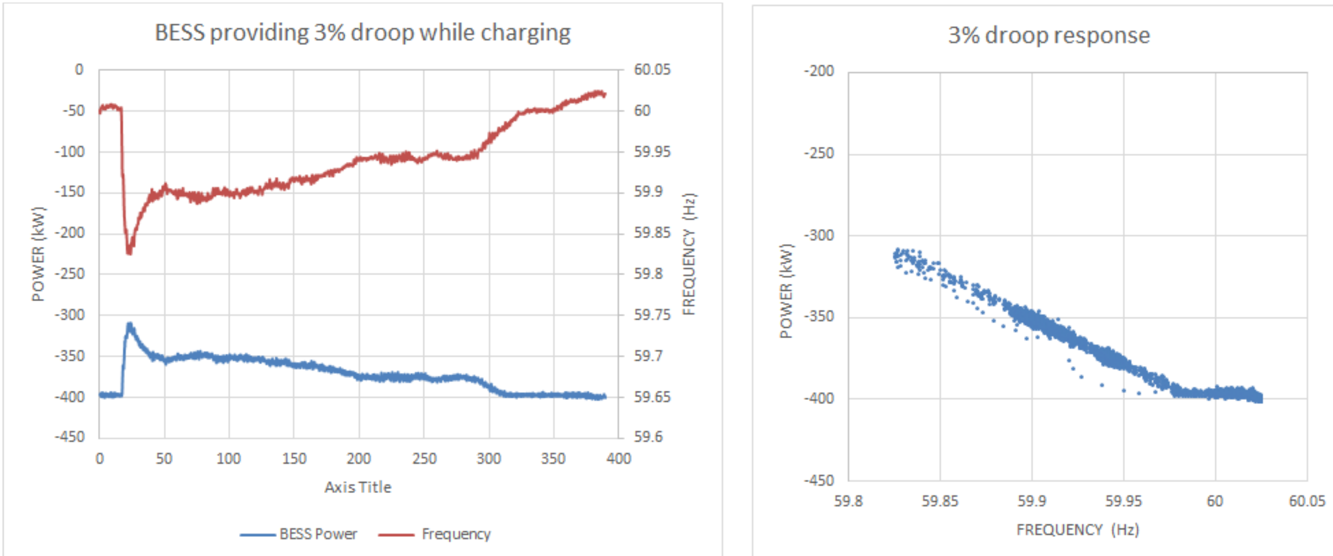

Figure 101. BESS providing frequency droop

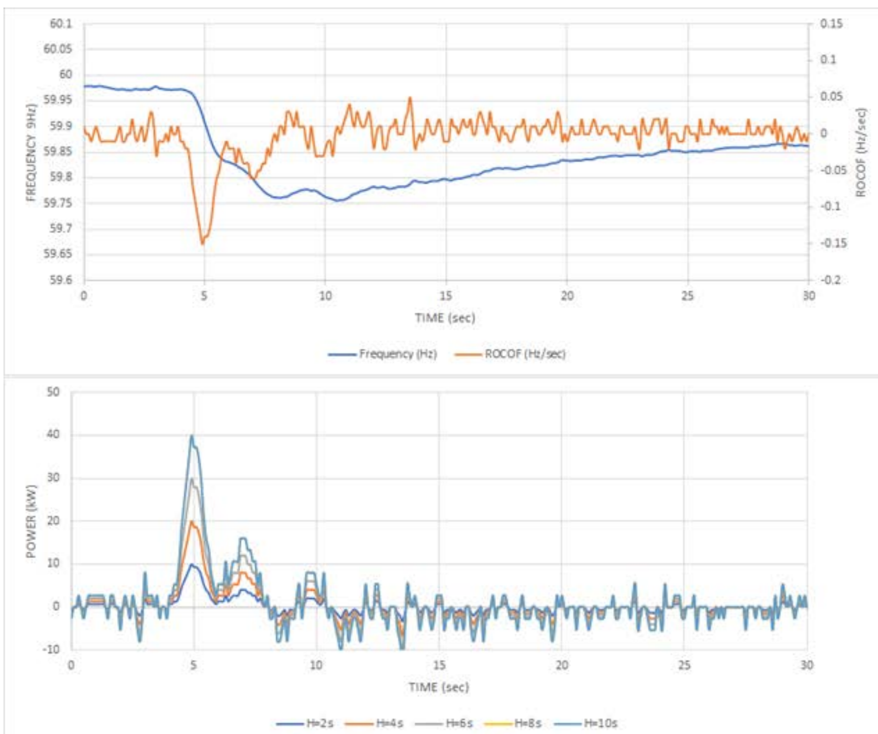

- BESS can operate with programmable H
- Other shapes of inertial response can be implemented
- ROCOF deadband can be implemented to eliminate impacts on battery life

$$\Delta P = -2H \cdot f \cdot \frac{df}{dt}$$

Unlike rotating generators, BESS offers a fully programmable H (within power limits of the converter).

Figure 102. BESS providing synthetic inertia test

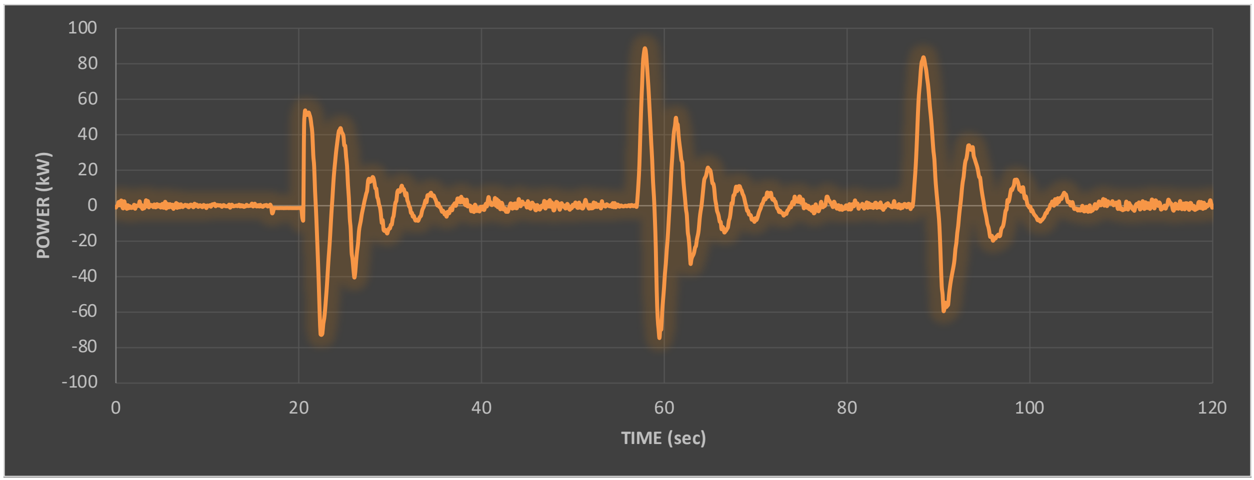

Figure 103. Modulating BESS output for power systems oscillation damping services

7.2 Concept of Hybrid Renewable Plants

Utility-scale solar photovoltaic (PV) generation rapidly is becoming cost-competitive with wind power. Consequently, hybrid renewable energy systems that combine variable wind and solar energy sources are well-positioned to lead the global scale-up of renewable generation at affordable cost levels, and offer new opportunities for equipment manufacturers, new revenue streams for plant operators, and new sources of **dispatchability, flexibility, and reliability** for utilities and system operators. Declining costs of BESS means that the introduction of an energy-storage component into such hybrid plants would transform variable renewable generation into a source of energy that potentially could revolutionize the renewable energy industry and disrupt the market for traditional single-technology players (Figure 104). Overall, the emerging concept of hybrid renewable power plants offers many new opportunities to existing industry stakeholders, and it could have transformational impacts on global renewable energy markets [68]–[70] . Several critical questions—related to both the technical and economic aspects of such a hybrid power plant—still must be addressed by the research community, including the following.

- How are the benefits of such multitechnology hybrid plants fully quantified in terms of generation cost, system reliability, and operational flexibility?
- What is the full set of use cases for hybrid plants including PV and wind generation coupled with energy storage?
- How should individual technology components (PV, wind, storage) be optimally sized in such plants?
- How do operators optimally control and operate individual hybrid plants, or clusters of hybrid plants, to provide the full set of economic and reliability benefits?

The results demonstrated in this project are the first stepping stones in answering these questions. Developing new tools to answer such questions is especially important now, because across the world there is a growing number of demonstrations for hybrid renewable energy projects (including PV and wind generation) and integrated battery-storage plants—proving the viability of the various emerging business models [68]. Hybrid plants are expected to scale-up in capacity and number to give rise to new business models and new integrated technology players. Hybrid systems that combine PV, wind, and energy storage are becoming a feasible option for large-scale power plants and can have significant economic, environmental, and social benefits. Combining wind and solar generation results in a significant increase in annual energy production for the same plant footprint without creating a need to expand transmission because of typical temporal differences in wind and solar resources.

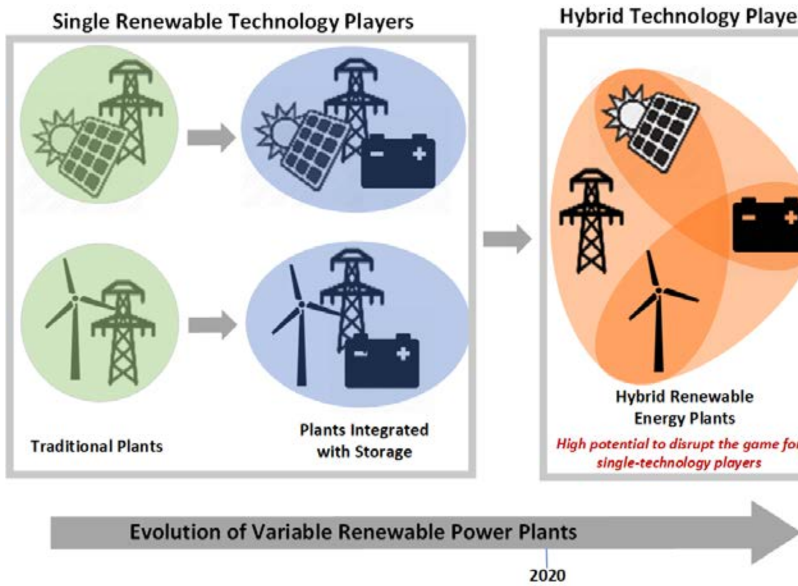

Figure 104. Thinking beyond traditional variable-generation renewable energy plants (image source: NREL)

Several enterprising renewable energy developers are now exploring how solar and wind might better work together, developing hybrid solar-wind projects to take advantage of the power-generating strengths of each—with the two technologies in tandem serving as a better replacement for conventional thermal generation than either could be alone [71]. A 2013 study conducted by RLI and Solarpraxis in Germany found that solar and wind power generation complement each other much better than previously thought [72]. The study examined the land area where solar PV systems and wind turbines were installed together. In that same land area, twice the amount of electricity was being generated, and the shading produced by the wind turbines accounted for a mere 1% to 2% loss in the PV system—which is much less than previously estimated. Some experience with hybrid PV-WPPs has been accumulated in the United States [73], [74]. For example, the EDF's 140-MW Pacific Wind Farm in the Tehachapi-Mohave region of Southern California is set to operate with the nearby 143-MW Catalina Solar project, mainly for cost-sharing and better use of transmission lines.

Countries such as China, Australia, and India are taking the lead in utility-connected hybrid systems and are piloting several farms to develop an understanding of the factors that will help drive policy [68], [75], [76]. The world's largest utility-scale PV-wind -storage hybrid power plant is being constructed in central north Queensland, Australia. This plant features 15 MW of solar combined with 43 MW of wind and a 2-MW/4-MWh Li-ion battery system. Brazil's government approved legislation to grant access to the country's energy auctions of large-scale hybrid renewable projects [76], and GE (a cost-shared partner in this proposal) already is planning to introduce a solar-wind hybrid system to Brazil's energy market. In fact, many global wind-technology players, such as Siemens and Suzlon, are "hybridizing" their generation portfolios by entering the solar markets in many emerging economies, such as India. Similar trends for developing demonstration projects are occurring in other regions of the world, such as Europe and the Caribbean [77], [78]. Despite such growing interest in hybrid plants worldwide, the co-optimized design and control theory is nonexistent for reliable and economic integration of such systems into the power grid.

In general, a strong complementarity combination of solar and wind generation is an advantage for renewables integration and is one of the main motivating factors behind the idea of hybrid plants. One example on complementary nature of solar and wind daily power production using CAISO data is shown in Figure 105.

Recent advances in wind turbine technology can vastly expand the geographic areas where the complementary nature between economic solar and wind resources can exist. Next-generation wind turbines can make reliable, cost-effective wind power a reality in all 50 states. Advanced wind turbines with taller towers and longer blades will enable the reaching of stronger, more consistent winds high above the ground, unlocking wind energy's potential across an additional 700,000 square miles (roughly one-fifth of the U.S. land mass) and allowing the advancing of affordable wind power into areas having high solar resource potential. Even a mere visual comparison of two NREL maps shown in Figure 106 highlights the geographical overlap between solar resource–rich areas and new land areas that can achieve a minimum 30% net capacity factor for wind generation at 140-m hub height (southeast United States and many new pockets of land area in the Southwest) [79]. This new technological advance has great promise for hybrid power plants in many regions in the United States and the world.

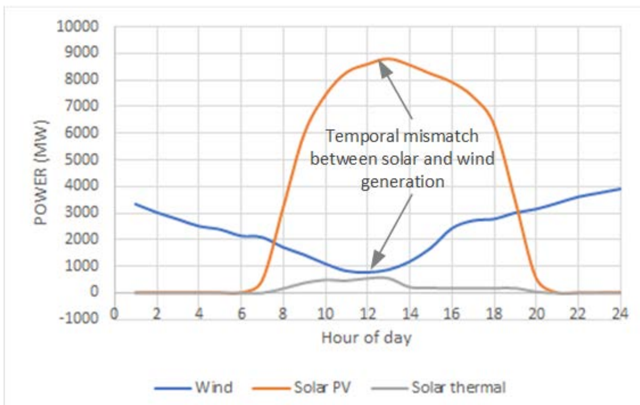

Figure 105. CAISO's typical wind and solar hourly production profiles; data for July 17, 2017 (source: NREL)

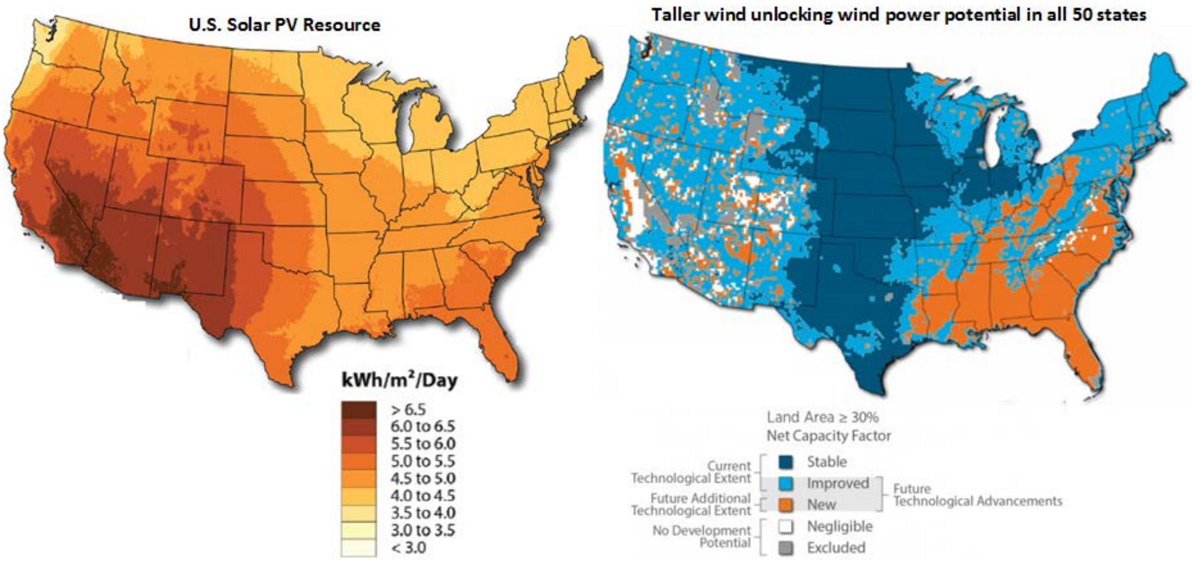

Figure 106. Bringing "taller" economic wind power to areas rich in solar resource (map source: NREL)

8.0 Impedance-Based Characterization of Power System Frequency Response

8.1 Introduction

Typically, the power system frequency response is characterized during unplanned transient events to verify compliance with reliability standards such as FERC BAL-003-1 and estimate frequency adequacy. This section presents an impedance-based noninvasive approach for the characterization of power system frequency response in real-time in the absence of a transient event. It uses the transfer function response from the injected active power to the frequency at the POI for the estimation of inertia and PFR of the system. The so-called frequency response function also shows the effects of the speed of primary frequency control. The section also helps in developing the relationship between the frequency response function and the network impedance seen from the POI. This relationship highlights how the network impedance captures the frequency response behavior. The proposed methodology is demonstrated on a modified IEEE 9-bus system with 25% penetration of renewable generation; a 5-MW BESS is used for the injection of active power perturbations for the measurement of the frequency response function.

The security and resilience implications of operating low inertia power systems require development of new real-time tools for the analysis of frequency-response adequacy, so system operators can ensure frequency stability of the system under any conceivable contingency and for any resource dispatch scenarios [61]. Unlike traditional statistical approaches for frequency-response adequacy estimation, the method proposed in this section has multipronged impact. It is capable of identifying system security issues arising from generation mixes prevailed by temporal and spatial stochastic characteristics of variable resources in real-time, at the beginning of any security-constrained units dispatch interval. It simultaneously identifies other potential resonance and stability problems that inverter-coupled energy storage and renewable generation can help mitigate. Additionally, the method enables the conducting of essentially a fundamental frequency response adequacy evaluation in real-time, a capability that never has existed within the energy industry.

Drop-in frequency following a transient event must be restricted to avoid triggering UFLS relays and to maintain stability [60]. Frequency response characteristics—including frequency nadir, rate-of-change-of-frequency, and settling frequency depend on system inertia and the PFR of generators and loads. The PFR of an interconnection typically is measured in MW/0.1 Hz. It shows the amount of power disturbance that will result in the change in frequency by 0.1 Hz during steady state following an event. Several studies have shown that both inertia and PFR gradually are declining in many power systems around the world, primarily because of the increasing penetration of power electronics–coupled renewable generation and the displacement of conventional generation [62], [63]. This limits the amount of the penetration of renewable generation an interconnection can absorb without raising significant reliability concerns. The Federal Energy Regulatory Commission (FERC) recently introduced BAL-003-1 standard, which requires each balancing authority (BA) within an interconnection to maintain a minimum PFR depending on its share of generation in the interconnection [51]. System inertia and PFR are periodically measured in the U.S. interconnections to check compliance with the BAL-003-1 standard [51]. Such measurements are carried out during unplanned transient events following the procedure described in the BAL-003-1 standard [51]. Frequency-response characterization using transient events do not provide analytical insights into the role of governor characteristics that shape the frequency response of the power system. It is not possible to characterize the power system frequency response whenever desired or in real-time. Finally, the frequency response characterization during transient events is agnostic to the system behavior looking from different locations; this information is critical for determining the optimum placement of an energy storage system for improving the system frequency response. The evaluation and design of the frequency support functions by renewable generation and storage is usually carried out using numerical simulations with high degree of simplifications [64], [65]. Frequency response characterization using unplanned transient events as well as using numerical simulations do not provide an analytical basis for the development of sophisticated control solutions for frequency support functions.

Impedance-based methods have proven effective for the evaluation of resonance and stability problems in converter-based power systems, such as wind and PV farms and high-voltage, direct current (HVDC) transmission networks [66], [67]. Because these methods follow measurement-based approach, they deliver distinct advantages as compared to state-space modeling and simulation-based methods. They expose the dynamic characteristics of a system looking from its terminals without needing the internal details of individual components. Such an approach can allow renewable generation and energy storage systems to shape the power system frequency response, depending on the impedance of the system at the POI. It is not yet understood, however, how impedance captures the frequency response behavior of a network.

In this work we present an impedance-based approach for the characterization of power system frequency response. The impedance-based approach addresses the drawbacks of the existing frequency-response characterization methods and provides analytical basis for the control development of frequency support function in renewable generation and storage. The proposed method is demonstrated on a modified IEEE 9-bus system with 33% of wind and PV penetration. It can estimate system inertia, PFR, and also the speed of primary frequency control in a noninvasive manner in the absence of a transient event. We also have shown how the network impedance embeds the information on the power system frequency-response behavior.

8.2 Impedance-Based Characterization Method

Because frequency support is provided by regulating the active power output, the proposed impedance-based characterization method measures frequency-domain transfer function response from the active power injected at the PCC to the measured frequency at the PCC. This requires injection of active power with sinusoidal perturbations of different frequencies. We used a 5-MW BESS, interfaced with the grid by a three-phase voltage source converter, for injecting the active power perturbations. Note that other converter-coupled devices such as wind turbines, PV inverters, and HVDC converters also can be programmed to inject active power perturbations. Figure 107 shows modified IEEE 9-bus system used to demonstrate the impedance-based frequency response characterization method. The inverter-coupled BESS at bus-5 is used for the injection of active power perturbations.

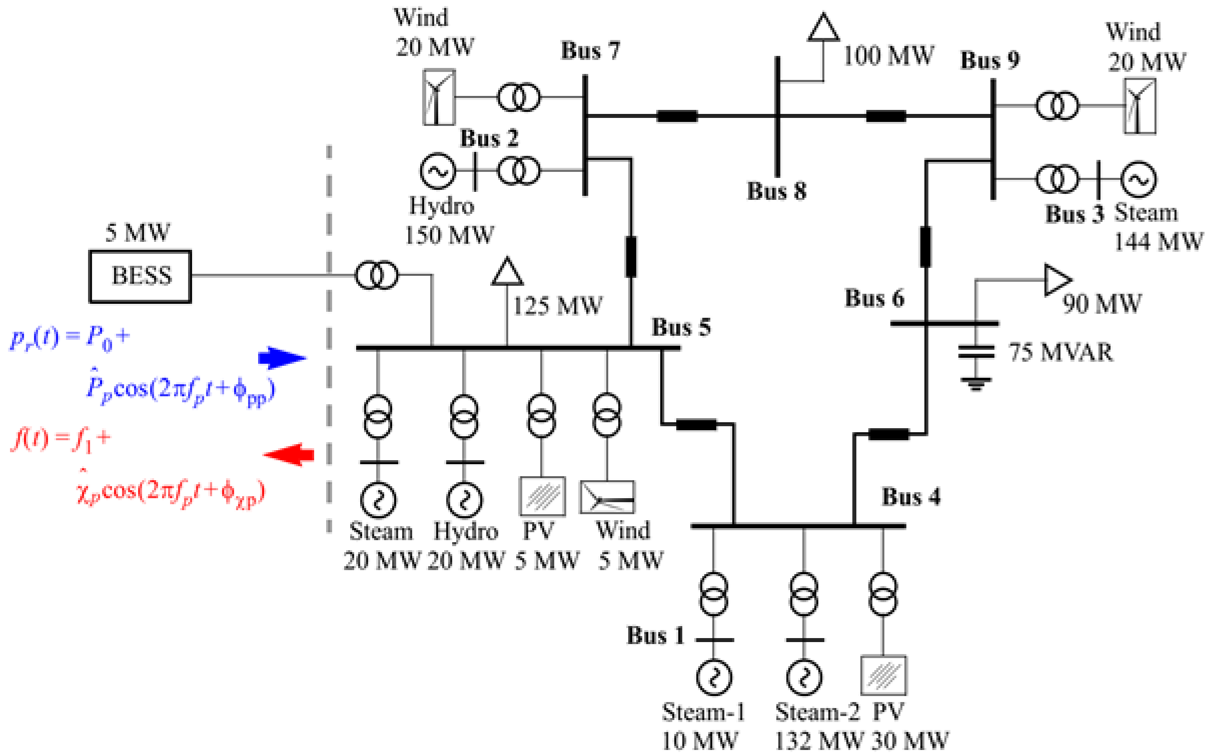

Figure 107. Simulated IEEE modified 9-bus system

Figure 108 shows implementation of the proposed method. Sinusoidal perturbation is injected in the reference for the active power (p_r) supplied by the battery. The active power reference with superimposed sinusoidal perturbation is given by Equation 8.1.

$$p_r(t) = P_0 + \hat{P}_p\cos\left(2\pi f_p t + \phi_{\mathrm{pp}}\right) \tag{8.1}$$

Where P_0 is the steady state active power supplied by the battery, $\hat{P}_p$ is the amplitude of the superimposed small-signal perturbation in the active-power reference, and f_p is the perturbation frequency. The d-axis current reference (i_{dr}) is derived from the power reference p_r and the d-axis voltage v_d at the PCC; the latter is obtained by a three-phase PLL shown in Figure 108b. Because the VSC current control dynamics are much faster than the frequency dynamics of a power system, the current controller is represented in the simulated model simply by a first-order low-pass filter with the time constant T_i of 4 ms. The BESS output currents i_{abc} enters into the IEEE 9-bus system and, depending on the network impedance $Z_{\mathrm{NET}}(s)$ as seen by the BESS, the perturbations in the BESS output currents result in the perturbations in the PCC voltages v_{abc}. As shown in Figure 108, a three-phase PLL is used to obtain the frequency measurement (f), grid-voltage angle (θ_{PLL}), and the d-axis voltage (v_d).

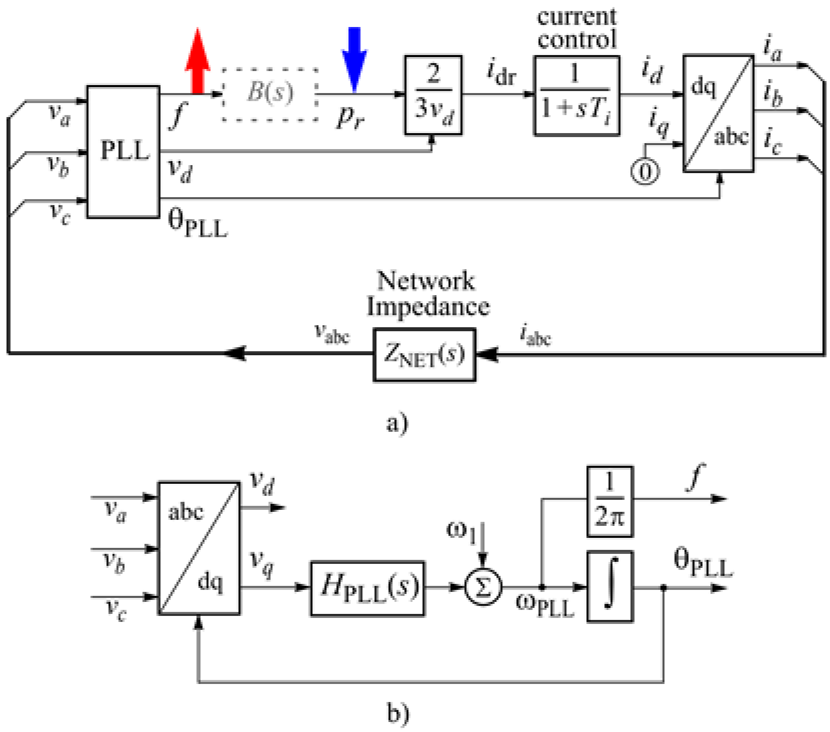

Figure 108. Active power injection using BESS: (a) implementation and (b) PLL.

During perturbation, the measured frequency (f) at PCC can be represented by considering only the steady state and perturbation frequency components as shown in Equation 8.2.

$$f(t) = f_1 + \hat{\chi}_p \cos(2\pi f_p t + \phi_{\chi p}) \tag{8.2}$$

The complex gain from the injected perturbation in the active power reference p_r to the response perturbation in f at the perturbation frequency f_p gives response of the desired frequency response transfer function at f_p. The proposed frequency response transfer function is defined as shown in Equation 8.3.

$$FR(s) = \frac{\mathbf{F}[f_p]}{\mathbf{P}_r[f_p]} \tag{8.3}$$

Where $s = j2\pi f_p$, and $\mathrm{F}[f_p] = \left(\frac{\hat{\chi}_p}{2}\right) exp(j \cdot \phi_{\chi p})$ and $\mathrm{P}_r[f_p] = \left(\frac{\hat{P}_p}{2}\right) exp(j \cdot \phi_{\mathrm{pp}})$ are Fourier components, respectively, of the measured frequency (f), and the active power reference (p_r) at the perturbation frequency (f_p). Note that the frequency support controller, *B(s)*, in Figure 108 can be designed once the frequency response transfer function, *FR(s)*, defined in Equation 8.3. is measured.

The frequency measurements for obtaining the responses of the frequency response transfer function $FR(s)$ are obtained using a PLL with 20 Hz bandwidth. The peak of the injected perturbation $\hat{P}_p$ in the active power reference is kept below 2.0 MW, to ensure small-signal condition. Table 10 summarizes the ratings and outputs of conventional generators in the IEEE 9-bus system. It also shows the nominal droop gain of each generator. The wind and PV generation outputs are summarized in Table 11. Note that 33% of the total load is supplied by wind and PV. Wind and PV generators are not programmed to participate in voltage and frequency control. Hence, they are modeled as sources with fixed active and reactive power outputs.

Table 10. Conventional Generation: Ratings, Active Power, Inertia Constants, and Droop Constants

Generator	Rating, S (MVA)	Active Power Output, P_o (MW)	Inertia Constant, H (s)	Nominal Droop Constant (R_p)
Hydro @ Bus-7	150	59.18	6.0	0.05
Hydro @ Bus-5	20	10.48	6.0	0.05
Steam @ Bus-5	20	11.49	3.117	0.20
Steam-1 @ Bus-4	10	5.70	3.117	0.20
Steam-2 @Bus-4	132	75.78	3.117	0.20
Steam @ Bus-9	144	82.66	3.117	0.20
Total	476	245.29	Equiv. Inertia: H_{sys} = 4.148 s	–

Table 11. Wind and PV Generation Power Output

Generator	Active Power Output, P_o (MW)
Wind @ Bus-7	20.0
Wind @ Bus-5	5.0
PV @ Bus-5	5.0
PV @ Bus-4	30.0
Wind @Bus-9	20.0
Total	80.0

The following sections present measurements of the frequency response transfer function for different governor settings in the IEEE 9-bus system shown in Figure 107.

8.3 Droop Gains: Primary Frequency Response

Figure 109 shows response of $FR(s)$ for three different droop gain settings in the steam power plants in Figure 107. Because steam power plants have the largest share of conventional generation in the IEEE 9-bus system in Figure 107, the system PFR is predominantly dependent on the droop settings of the steam power plants. Note that the magnitude in Figure 109 has the unit of mHz/MW. Figure 109 shows that the droop settings of generators mainly affect the low-frequency response of $FR(s)$. This is expected because droop-gains determine the steady-state frequency of the system following a transient event. The DC gain of the transfer function in Figure 109 is 28.85 mHz/MW (29.2 decibels [dB]), 20.64 mHz/MW (26.3 dB), and 10 mHz/MW (20 dB), respectively, for the droop gains of 20%, 10%, and 5% in steam power plants. Usually the PFR of a power system is measured as MW/0.1 Hz [60]. The PFR can be obtained simply by inverting the DC gains of the frequency response transfer function $FR(s)$.

Verifying that the DC gains of $FR(s)$ indeed estimate the PFR of the power system can be done in two ways. One way is to calculate the PFR of the system based on the ratings and droop gains of the conventional generators (hydro and thermal) in the IEEE 9-bus system. The calculated PFR of the system matches exactly with that predicted by the DC gains of *FR*(*s*) in Figure 109. The second approach used for the validation of the predicted PFR of the network is to simulate a generation-loss event and compare the steady-state frequency observed in simulations following the event with that predicted by the DC gain of *FR*(*s*) from Figure 109. Figure 110 compares the frequency response of the IEEE 9-bus system for different droop settings after the generator at bus-1 is tripped; this is obtained using dynamic simulations against that predicted by the frequency response transfer function *FR*(*s*). Note that the frequency response transfer function not only accurately predicts the steady-state frequency after the tripping of the generator, but it also accurately predicts nadir and ROCOF of the frequency response.

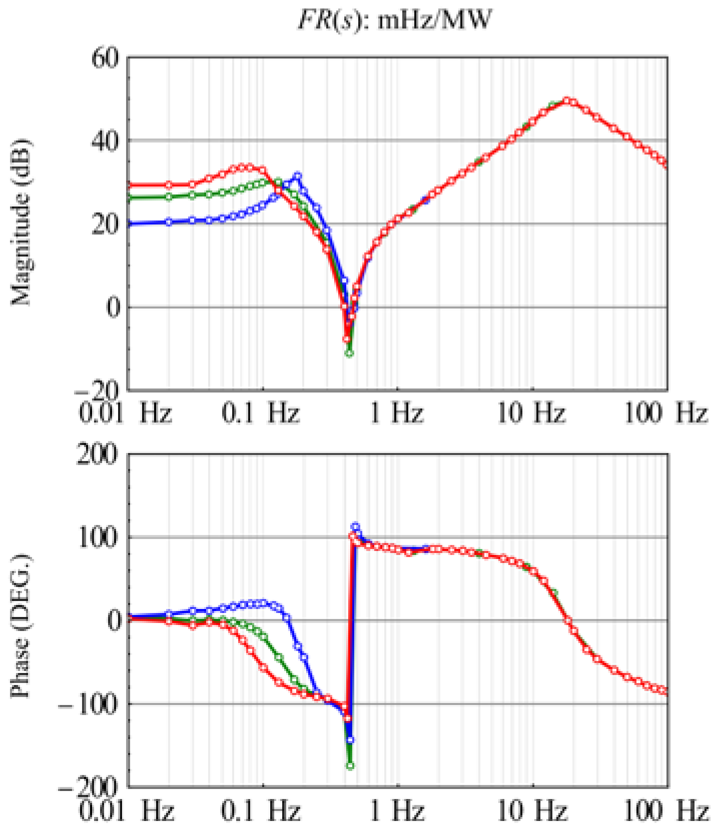

Figure 109. Measurements of the frequency response transfer function *FR*(*s*) for different droop settings in the steam power plants of the IEEE 9-bus system; (a) 20% droop (red lines), (b) 10% droop (green lines), and (c) 5% droop (blue lines)

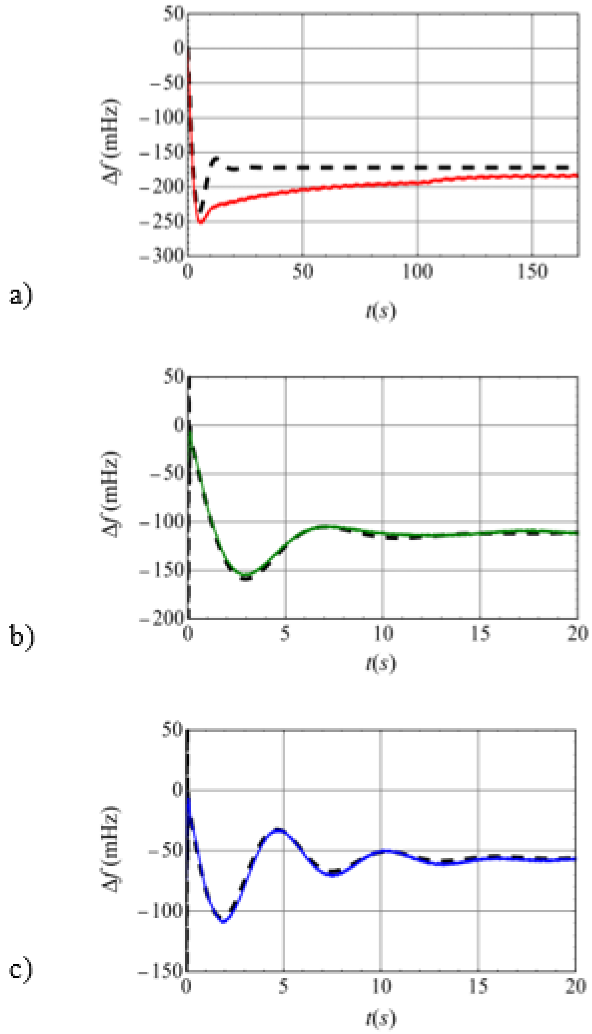

Figure 110. Prediction of frequency response following a generation drop event using frequency response transfer function *FR*(*s*); solid lines represent simulated response and dashed lines represent prediction by *FR*(*s*); (a) 20% droop, (b) 10% droop, and (c) 5% droop

8.4 Speed of Primary Frequency Control

Not only the amount of the primary frequency control of the system (i.e., equivalent droop-gain of the system), but also its speed is important for achieving desired frequency response following a transient event. The frequency response transfer function $FR(s)$ also can estimate the speed of the primary frequency control in addition to the equivalent droop gain. This is demonstrated in the following by leveraging the fact that the primary frequency control of hydro-generators usually is slower than that of the thermal generators. This different speed of primary frequency control is driven by the governor controls and setting of the hydro and steam generators.

Note that there are only two hydro generators in the IEEE 9-bus system shown in Figure 107. Among them, the 150-MVA hydro-generator at bus-7 has much greater capacity than the 20 MVA hydro-generator at bus-5. Hence, the response of the hydro generator at bus-7 dominates the response of the hydro generator at bus-5. In the simulated IEEE 9-bus system, the hydro generator at bus-7 initially does not participate in the primary frequency control because of its operation below the lower power limit of

0.4 p.u. The operation of the generator below the lower power limit renders it unresponsive during a frequency event. Hence, the PFR predicted by Figure 109 mostly is provided by the thermal generators in the system.

To demonstrate how the speed of the primary frequency control modifies $FR(s)$, the lower limit of hydro generators is reduced from 0.4 p.u. to 0.1 p.u. This allows the 150-MVA hydro generator to participate in the primary frequency control of the system. Figure 111 compares the response of $FR(s)$ before and after the change in the lower power limit of hydro generators. It is evident that the participation of the 150-MVA hydro-generators in the primary frequency control reduces the DC-gain to 20 dB (i.e., 10 mHz/MW). As shown in Figure 109, the PFR of 10 mHz/MW also can be achieved by reducing the droop gain of steam power plants from 20% to 5%. Hence, it is expected that the removal of the lower power limit in the hydro generator will result in the same settling frequency as reducing the droop slope of thermal generators from 20% to 5%. Nonetheless, note from Figure 111 that the PFR because of hydro generators is much slower than that of steam generators: The DC-gain of $FR(s)$ is realized at around 1 mHz in Figure 111 when the hydro generator is contributing to the PFR as compared to 10 mHz when most of the PFR is coming from thermal generators. This shows that the primary frequency control of hydro generators in the IEEE 9-bus system is approximately 10 times slower than that of the thermal generators.

This behavior also can be seen in Figure 112; it shows the frequency response of the IEEE 9-bus system after the loss of the generator at bus-1 for both scenarios, when the entire PFR is provided by thermal generators and when hydro generators also contribute to the PFR. For fair comparison, the droop gain of thermal generators for the first case when the PFR is provided solely by thermal generators is kept at 5%. Whereas, for the second case, when the 150-MVA hydro-generator participates in the primary frequency control, the droop gain of steam generators is kept at 20%. This results in the same DC-gain of $FR(s)$ under both scenarios (compare Figure 109 with Figure 111). As expected, the power system frequency settles to almost the same value after the event. Because of the slow primary frequency control by hydro generators, however, the settling time is much longer, and the frequency nadir is worse when the PFR is contributed partially by hydro generators.

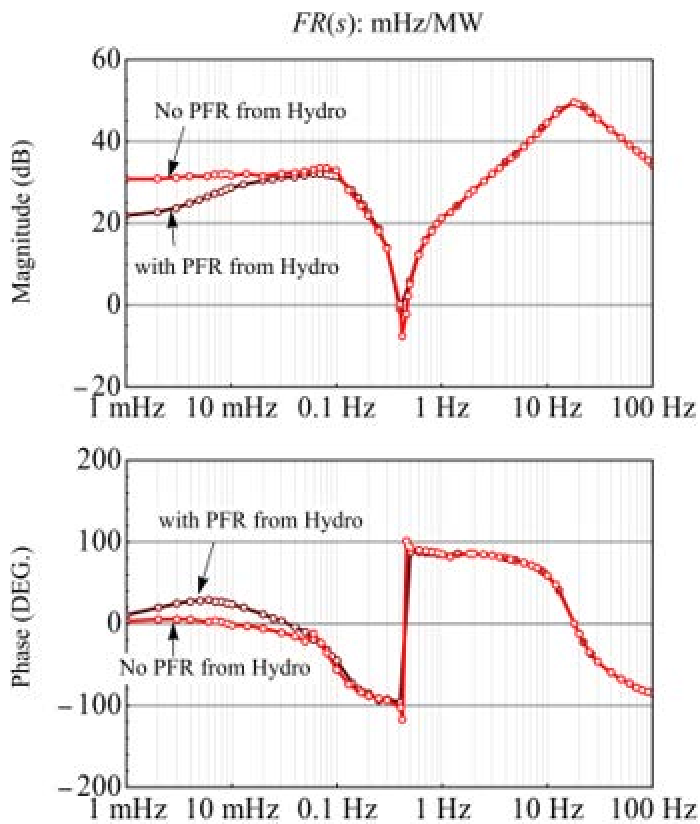

Figure 111. Effect of primary frequency control by hydro-generators on the PFR of the system and its speed

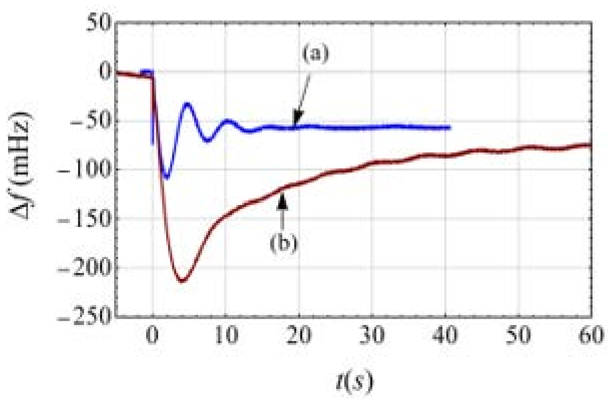

Figure 112. Frequency response of the IEEE 9-bus system after the loss of a generator at bus-1. (a) thermal generators operate with 5% droop and no PFR from hydro generators, (b) thermal generators operate with 20% droop and hydro generators operate with 5% droop

8.5 Rate of Change of Frequency: System Inertia

The response of $FR(s)$ in Figure 109 can be described using the following transfer function to extract the system parameters.

$$FR(s) = \left[\left(R_{droop} + sL_{droop} \right) \| \frac{1}{sC_H} \right] + sL_n \tag{8.4}$$

Where

- R_{droop} represents the DC gain of $FR(s)$ because of the droop gains in generators
- L_{droop} is because of the time-constant of the primary frequency control
- C_H represents the capacitive behavior of the power system because of the inertia of generators, and
- L_n represents the inductive impedance of the transmission network.

Note that peaking of $FR(s)$ in Figure 109 near 0.1 Hz to ~ 0.2 Hz is because of the parallel resonance between L_{droop} and C_H. The dipping of $FR(s)$ at 0.45 Hz, conversely, is because of the series resonance between C_H and L_n. The magnitude of $FR(s)$ starts decreasing beyond 20 Hz, which represents the bandwidth of the PLL used for frequency measurement in Figure 108b.

Based on the description of $FR(s)$ in Equation 8.4, the value of C_H can be obtained as 0.065 *F* by fitting the response of the transfer function in Equation 8.4 with the responses in Figure 109. If the effect of only the system inertia is considered, then the active power and frequency are related based on Equation 8.4 as follows.)

$$C_H \cdot \frac{df}{dt} = \Delta P \tag{8.5}$$

Note that f is in mHz and ΔP is in megawatts in Equation 8.5. Based on Equation 8.5, the measurements of $FR(s)$ predict the ROCOF to be $(0.065)^{-1}$, that is, 15.38 mHz per megawatt. This prediction is validated below by computing the system inertia based on the inertia of conventional generators in Table 10.

The power system swing equation can be written as follows.

$$\frac{1}{60 \times 1000} \cdot \frac{df}{dt} = \frac{1}{2H_{sys}} \frac{\Delta P}{S_{sys}} \tag{8.6}$$

Where the gain 1/(60·1,000) is to account for the conversion between the per-unit value of frequency to mHz, H_{sys} is the system inertia in seconds, S_{sys} is the MVA rating of the system, and ΔP is the change in power balance in megawatts.

As shown in Table 10, the equivalent inverter of the system H_{sys} is 4.148 sec. It is obtained as follows.

$$H_{sys} = \frac{\sum_{i=1}^{n} H_i \cdot S_i}{\sum_{i=1}^{n} S_i} \tag{8.7}$$

Where n is the total number of conventional generators in the system.

Using the value of H_{sys} in Equation 8.6 and comparing Equation 8.6 with Equation 8.5, the value of C_H is 0.0658. This matches the prediction using $FR(s)$. Hence, the frequency response transfer function measurements can accurately predict system inertia as well as the rate-of-change-of-frequency following a transient event. Future work will use the frequency response transfer function for the evaluation of the effects of steady state and transient synthetic inertia from inverter-coupled generation on the frequency response of a system.

8.6 Damping of Local Modes

The frequency response transfer function $FR(s)$ also can be used to estimate the frequency and damping of system resonant modes that are observable from the POI. Figure 113 shows dominant poles of the system estimated using the measured frequency response transfer function in Figure 109. It shows that the damping of a dominant mode starts reducing as the droop gain setting of thermal generators is reduced. This also is evident from the frequency responses in Figure 110.

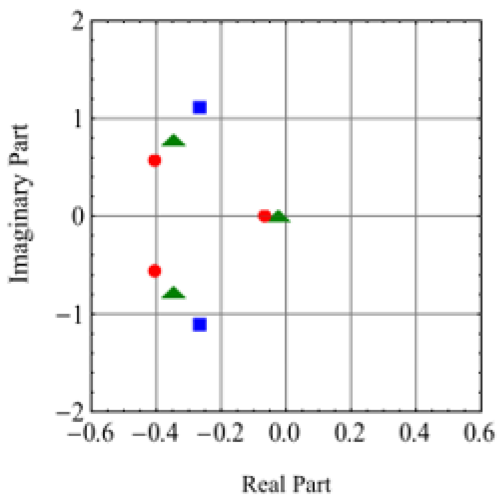

Figure 113. Estimation of dominant poles using frequency response transfer function for different droop settings in steam power plants: 20% droop (red circles), 10% droop (green triangles), and 5% droop (blue rectangles)

8.7 Relation with Impedance

By applying the harmonic linearization method to the block diagram in Figure 108b and using the relation between the sequence and direct-quadrature (dq) domain impedance of a three-phase network from Equation 8.2, the frequency response transfer function $FR(s)$ can be related with the network impedance as seen from the POI as follows.

$$\begin{aligned} FR(s) \equiv \frac{F(s)}{P_r(s)} &= \frac{3}{2V_1} \cdot \frac{s}{2\pi} \cdot T_{\text{PLL}}(s) \cdot \frac{1}{1+T_i s} \cdot \frac{1}{V_1} \cdot Z_{qd}(s) \\ &\approx \frac{3}{2V_1^2} \cdot \frac{s}{2\pi} \cdot Z_{qd}(s) \end{aligned} \tag{8.8}$$

Where

- $3/(2V_1)$ represents the gain from the perturbation in the active power reference p_r to the perturbation in the d-axis current reference i_{dr}.
- $s/(2\pi)$ represents conversion from the perturbation in the voltage angle in radians to the perturbation frequency in Hz.
- $T_{PLL}(s)$ is the closed-loop gain of PLL as defined in Shah [67]. It can be approximated by unity below the PLL bandwidth, which is 20 Hz for the responses discussed in this report.
- $1/(1+T_i s)$ is the first-order transfer that represents the dynamics of the current control in the BESS inverter. As can be done for the PLL, it also can be approximated by unity in the frequency range of interest, at low frequencies.
- 1/V1 gain represents the gain from the perturbation in the q-axis component of the PCC voltage (v_q) to the perturbation in the angle of the PCC voltages [67].
- $Z_{qd}(s)$ is the element of the dq-domain impedance of the IEEE 9-bus system looking from the POI. It relates perturbation in q-axis component of the PCC voltages (i.e., v_q) to the perturbation in the d-axis component of the BESS inverter output currents (i.e., i_d).

It is interesting to note from Equation 8.8 that the frequency response of a power system is shaped by $Z_{qd}(s)$. This indeed makes sense, because is equivalent to the perturbation in the active power input to network and the perturbation in v_q is equivalent to the perturbation in angle of the PCC voltages. This shows that the $Z_{qd}(s)$ elements of the dq-domain impedance of an inverter can be used to estimate its grid-forming functionality. Following the same arguments as presented above, it can be shown that the transfer function from the reactive power injection to the amplitude of the PCC voltages is shaped by the $Z_{dq}(s)$ element of the dq-domain impedance of a network.

9.0 New Capabilities

New unique testing concepts and capabilities have been developed at the NWTC during the course of this project.

9.1 PMU-Based Test Bed for Wide-Area Controls Validation

One new capability is in the area of development and testing of advanced control methods, algorithms, and modeling tools to guide coordinated and co-optimized provision of fast reliability services. Such capability will permit expanding the collective value proposition of nontraditional grid resources, including wind and solar PV generation, inverter-based storage systems, and other reliability-enhancing devices such as synchronous condensers (SC) and flexible AC transmission systems (FACTS) devices (Figure 115). The abundance of inertia and synchronous torque from synchronous machines allows for a variety of services to be supplied to the grid, including balance, voltage, and stability services. This fundamentally important characteristic of synchronous generation will negatively affect power systems, as it is displaced by growing penetrations of inverter-based generation. Therefore, new control strategies must be able to coordinate the different resource types within interconnected or islanded power systems, aiming to preserve or improve voltage and frequency stability. This new capability will allow developing and validating new real and reactive power modulation methods that will maintain or enhance the stability of power systems as conventional inertia is displaced by inverter-based wind and PV generation. These methods will be applied to wind and PV generation operating by themselves or in coordination with other technologies such as energy storage, SC, and FACTS, with a strong focus on improvements to resilient, secure, reliable, and efficient operation, An example this application is described in Section 6.2 (Figure 70).

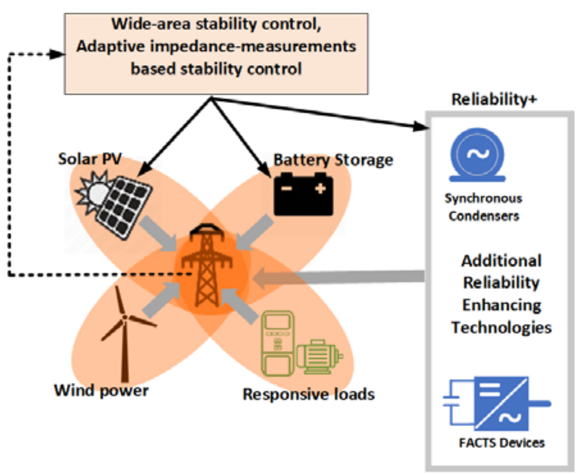

Figure 114. Provision of reliability services by wind and solar PV and BESS technologies

The diagram of the new test bed is shown in Figure 115. It consists of seven GPS-synchronized SEL PMU installed at the following locations.

- Medium-voltage sides of 1.5-MW wind turbine, 1-MW BESS, 430-kW PV plant, dynamometer test article
- Coupled with RTDS, so they can be virtually placed at any bus in RT power system model

The test bed also includes the following.

- SEL phasor data concentrator (PDC)
- SEL RTAC plant controllers
- PMU fiber network

It is fully integrated with the NWTC site controller and synchronized with advanced MV DAS 50 kHz data-acquisition system.

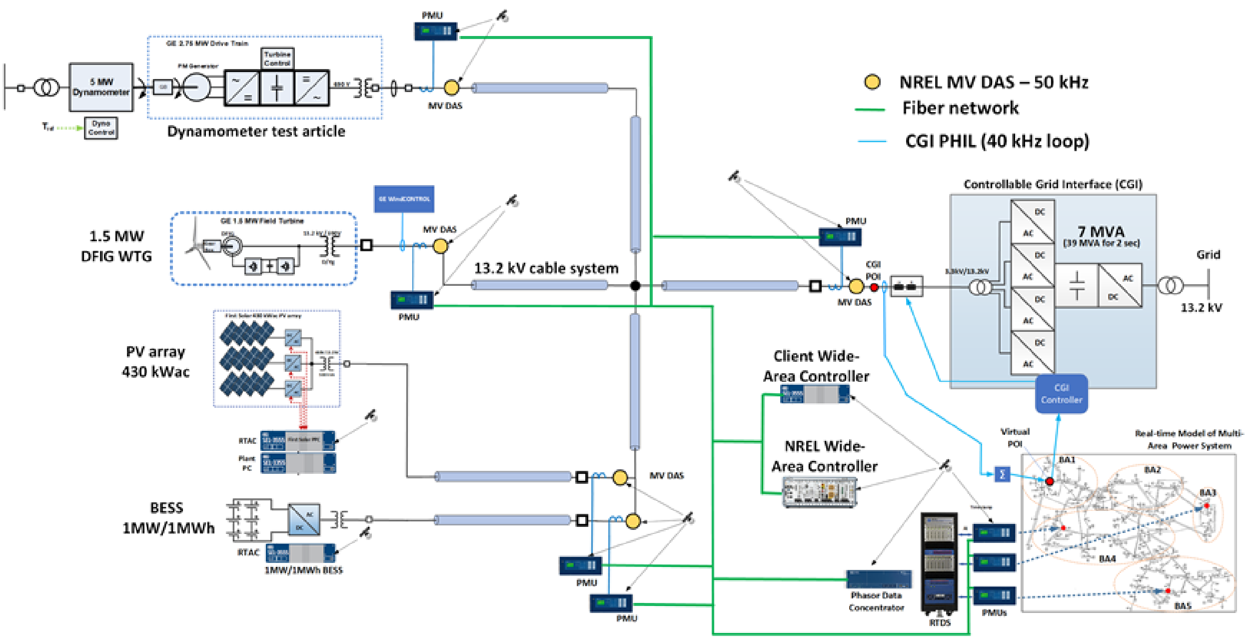

Figure 115. Platform for testing advanced wide-area controls

9.2 Impedance Characterization of Converter-Coupled Generation Using CGI

The NREL team developed and validated a new automated test method allowing the use of CGI for measuring small- and large-signal impedance response of multimegawatt-scale inverters. CGI injects voltage perturbations into its 13.2 kV bus, and our developed measurement system captures impedance response at different perturbation levels. One example of measured positive sequence impedance response of 1-MW BESS inverter from small-signal (0.5%) and large-signal (5%) voltage perturbations using CGI is shown in Figure 116.

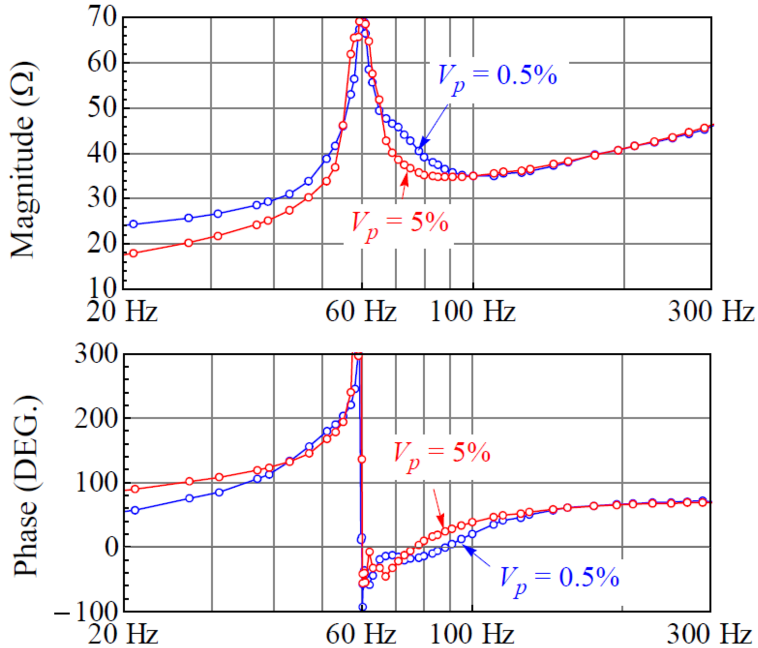

Figure 116. Measured impedance response of 1-MW BESS inverter

This is a new ground-breaking capability allowing small- and large-signal impedance-based characterization of full inverter-coupled resource (e.g., wind turbines, PV plants, storage systems) including their MV transformers (this cannot be done anywhere else in the world). The method developed by NREL also allows identification of true voltage and current control bandwidths of inverters. It also opens possibilities for a new field of grid-integration research: To develop and validate methods for shaping inverter-coupled resource impedances to reduce the resonance severities and mitigate oscillatory behavior in power systems.

10.0 Distributed Real-Time Simulations and Hardware-in-the-Loop Testing for Wind Energy Applications

This section describes a novel real-time simulations technique called geographically distributed real-time simulations (GD RTS) and using remote lab assets such as power and energy systems. The team has published several papers (Ren Liu 2017; Gevorgian 2018) on this very interesting research topic, including “Distributed Real-Time Simulations and Its Applications to Wind Energy Research,” which was presented at the 2018 Probabilistic Methods Applied to Power Systems (Steffen Vogel 2018). This section is based on the GD RTS performed between INL and NWTC, in addition to the research content and results from the aforementioned paper. The conference paper also was a deliverable for this current project.

10.1 Introduction to the Distributed Real-Time Simulations

10.1.1 Real-Time Simulations and Significance

Real-time simulations increasingly are being used to understand the complex device- and system-level interactions in power grids. The evolution of power grids with the introduction of distributed energy resources including wind and solar is rapid and complex. Wind and solar penetrations are increasing at both distribution and transmission levels of the power grids. With increasing penetration of distributed energy resources there are certain challenges with grid integration, including reduction of inertia and power-systems stability. Based on the previous sections, there is an emphasis of developing advanced inertia response capabilities with renewable energy generation including wind and solar. The current project focuses on the development and testing of the controllers that Based on the previous sections, there is an emphasis of developing advanced inertia response capabilities with renewable energy generation including wind and solar. can provide active power frequency (APF) response. The design and controls of large-scale electric grids must be reassessed and adapted to this changing paradigm with the support of new simulation and testing technologies. RTS and hardware-in-the-loop (HIL) are widely regarded as the next-generation assessment technique and very accurate to study distributed energy resources and other novel technologies.

Real-time simulations provide the capability to create a detailed, highly accurate, and diverse set of power and control system components at low time steps (on the order of microseconds) that are referenced using “real world clock-time.” Real-time simulator is a unique architecture with specialized processors and communication cards that enable time synchronization of simulations and the clock-time. Lean operating systems, specialized processors, and faster communications are the typical attributes of real-time simulators. Simulators provide a unique capability of interfacing with power and control components that are being integrated with the power grids, via analog and digital interfaces. Real-time simulators, however, have limited computational capability that constrains the size of power and control systems that can be simulated. In a conventional sense, multiple simulators connected locally are used to increase the computation capability; however, this is not always economical in cases of large-scale testing of technologies and systems, especially when a significantly large investment is needed to physically establish an energy technology-related test setup. In this case, for a local testing of the wind turbines, a significant investment is needed for both the wind turbine test facility and a large-scale set of real-time simulators.

10.1.2 Geographically Distributed Real-Time Simulations

Performing distributed RTS via the Internet can augment simulation capacity and leverage unique infrastructure that is dispersed in academia and research laboratories. The main challenges associated with geographically distributed real-time simulations (GD RTS) are outlined here. Although model partitioning and simulation stability did not represent a challenge for a simulation use case in this paper, uncertainty propagation of communication network is analyzed in detail. GD RTS refers to the use of multiple digital real-time simulators (DRTS) hosted at geographically dispersed locations and connected using a standard communication medium. The digital real-time simulators are interconnected across long distances for RTS of a system under study to analyze specific challenges and design solutions based on evolving dynamic conditions. The GD RTS enables distributed test beds and joint experiments with hardware and software assets hosted at multiple laboratories that are virtually interconnected. It is also a unique way of providing a flexible framework for joint work and leveraging domain expertise in various energy research and technology development groups. This interconnection between DRTS units hosted at geographically dispersed laboratories is typically established via wide area network (WAN). In addition to WAN interconnections, a robust communication interface is necessary to establish a GD RTS platform. Such a platform is not provided for by the commercially available DRTS and thus must either be created or adopted for experiments. This interface must support communication protocols which allow flexible implementation and configuration that might not be directly supported by DRTS systems, such as custom-tailored user datagram protocol (UDP). It also provides a flexible abstraction layer with advanced functionalities for the virtual interconnection of laboratories, such as multiplexing and demultiplexing of UDP messages. The distributed simulation setup introduced in this paper is based on the RWTH VILLAS framework which is described in following subsections. Design and performance reference for GD RTS is a monolithic RTS which is performed on a local setup of DRTS units. One of the challenges of the transition from monolithic RTS to GD RTS lies in the partitioning of a monolithic model into sub-models to be simulated on multiple geographically distributed DRTS systems. Next, transfer of interface quantities via communication network used for virtual interconnection of DRTS systems is influenced by the time delay and other characteristics such as packet loss, packet reordering, and time-varying delay.

These challenges represent the main sources of simulation stability and fidelity degradation in GD RTS. Interface algorithm (IA) is a method for interfacing partitioned sub-models by means of exchanging interface quantities representing the measurements at the interface terminals and providing the inputs to the sub-models based on these quantities with the objective of compensating the impact of the communication interface. IA plays a substantial role in ensuring simulation stability and fidelity in GD RTS with advanced methods for transformation of interface quantities and design of compensation methods. The most widely used co-simulation IA is the Ideal Transformer Model (ITM). This method uses controlled current and voltage sources that impose the behavior of the remote subsystems at the local subsystems. In GD RTS, interface quantities are not transferred via WAN directly as instantaneous values, but they are at first transformed to the form that is characterized by slower time-varying of quantities. This transformation is particularly important for compensation of time-varying characteristic of the delay.

In this work, we use IA based on root mean square (RMS), frequency, and phase angle for the controlled voltage source, and current injection based on active and reactive power measurements for the controlled current source, as illustrated in the Figure 6. An important challenge in GD RTS is stochastic characteristics of a WAN and its impact on the simulation results. The IA used here contributes to the compensation of the time-varying characteristics of the WAN, however it is necessary to analyze uncertainty propagation, as described in the next section. A potential solution to address the lack of access to larger cluster of locally available real-time (RT) simulators for larger system simulations is the fast-paced evolution of the processor capacity and related design of the RT simulator. This development requires equally critical development of robust communication mechanism between the processors to support the increased bandwidth. The cost of processor-based computations is decreasing and eventually will lead to a lower cost of RT simulators as well. Thus, RT simulators with a greater computation capacity and comparatively lower costs might make locally available clusters of RT simulators more economically viable. This progression is well-driven by the commercial processor businesses as well as commercial RT simulator vendors.

10.2 Distributed Real-Time Simulations Setup

10.2.1 Idaho National Laboratory Real-Time Simulations for Wind Assessment

At the Real-Time Power and Energy Systems Laboratory (RTPESIL) at INL, several DRTS are installed and commissioned. These simulators allow the transient and dynamic assessment of power and energy systems along with the interconnection of diverse distributed energy resource as either software models or hardware equipment or any combination. At the RTPESIL, a commercially available DRTS called the real-time digital simulator is used for this project and is shown in Figure 117. Dynamic models of wind turbines, generalization to WPPs, and test electric grids are created within the RTDS to enable the inertial testing and response analysis. Another capability of a bank of controller cards as shown in Figure 118 was used for this project as well. The bank of controller cards is used to simulate dynamic models of wind turbines that are based on the characterization of the 1.5-MW wind turbine at NWTC. This modeling representation enables the testing of wind turbines on a larger scale as well as extrapolation toward extremely high levels of penetration of wind energy and assessment in a dynamic and transient sense. The dynamic and transient stability of power systems with high renewable penetration is a very important topic that is investigated in this research; the inertial response analysis of wind turbines with the use of the APC especially is explored.

Figure 117. DRTS at the RTPESIL (INL) used to simulate real-time models of wind turbines and power systems

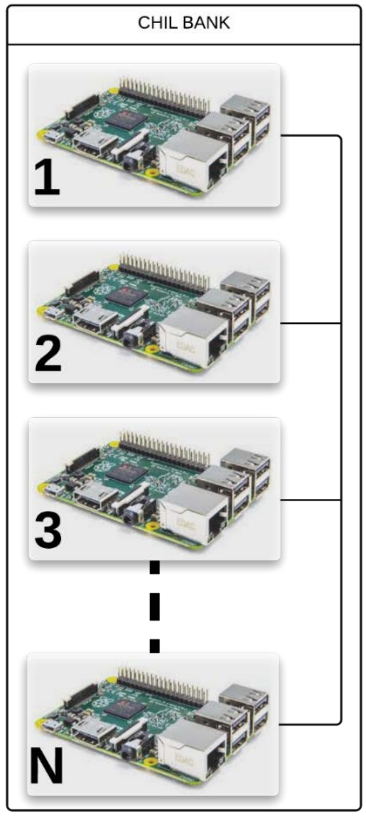

Figure 118. Hundreds of controller cards connected as controller-hardware-in-the-loop used to simulate hundreds to thousands of wind turbines as dynamic models

The description of the APC and its deployment with the test wind turbines at NWTC is described in earlier sections of this report.

10.2.2 National Wind Technology Center Setup for Wind Research

For the details of wind and other related lab and experimentation facilities at NWTC that are used for this research, please refer to the earlier sections of the report.

10.2.3 Distributed RTS Between INL and NREL

The distributed RTS or GD RTS between INL and NWTC is one of the more technically challenging tasks of this project. It essentially involves performing a large power systems simulation in real-time with two DRTS that are located at different places. In this context, the two simulators are located at INL and NREL. A power systems model is partitioned in a suitable technical manner to create two subsystems to enable the GD RTS. The power systems portion that is simulated at NWTC connects with the GE 1.5-MW wind turbine with the proposed APC connected. The subsystems simulated at INL connects to the hundreds of controller cards that model a WPP that is based on the characterization of the GE 1.5-MW and also has a significantly larger grid portion. More details are explained in the following section. The significance of this simulation is the enhanced computation capability and enabling remote characterization and use of the NWTC.

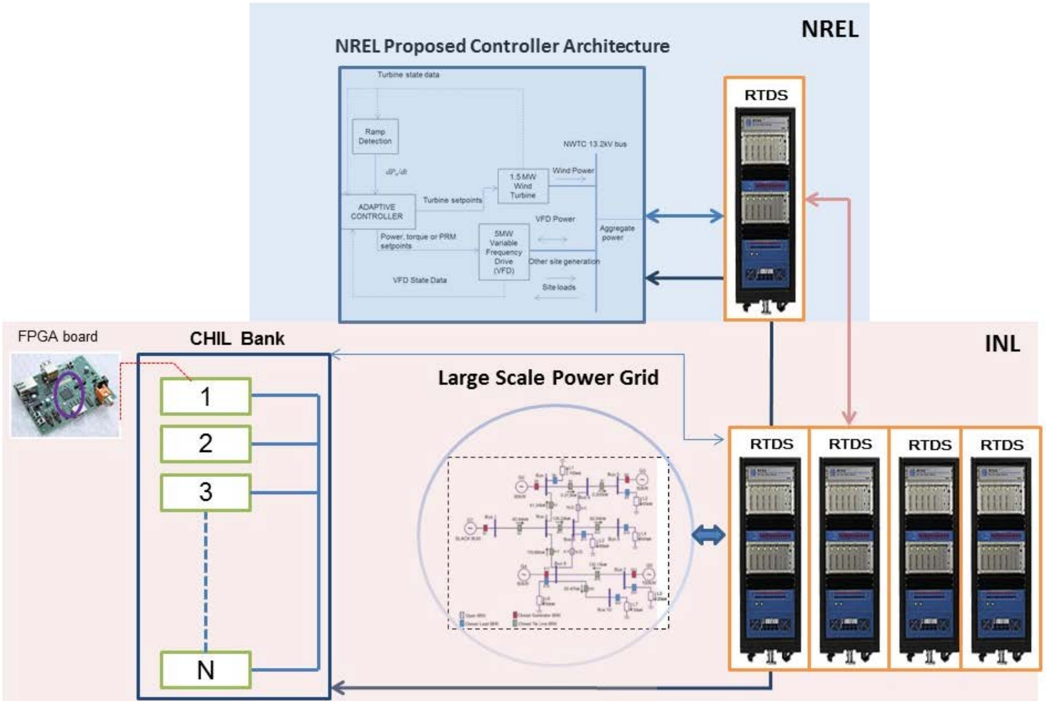

Figure 119. GD RTS between INL and NREL to characterize the APC with large-scale power systems and hundreds of controller cards as controller-hardware-in-the-loop

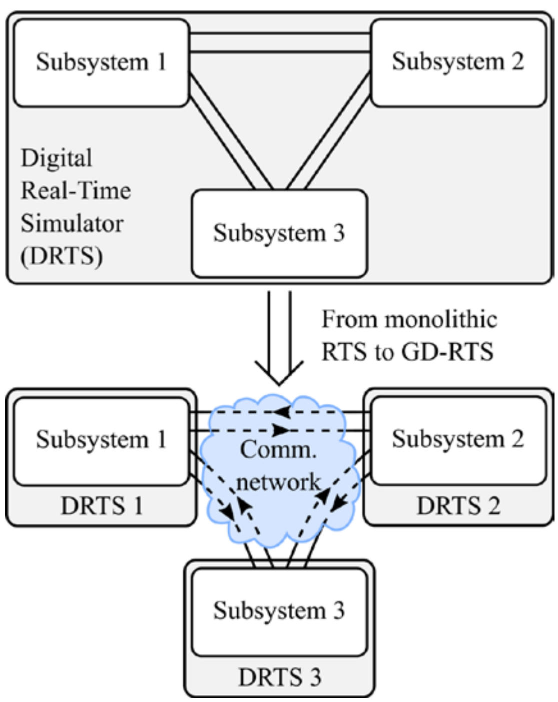

Figure 120. The principles of design of experiments for the proposed GD RTS to test the APC capabilities of the controller

As shown in Figure 119, the real-time simulation setup includes both the INL- and NREL-based simulations and hardware including DRTS, CGI, and wind turbines that are used for this research. Figure

120, shows the fundamental mechanism of GD RTS used for this research, to aid understanding and analysis of the APC aspects of the novel controller for wind turbines. The communication medium used in this case is the Internet with UDP to connect the two DRTS. The VILLAS framework used to facilitate this interconnection provides a flexible abstraction layer with advanced functionalities for the virtual interconnection of laboratories, such as multiplexing and demultiplexing of UDP messages, as shown in Figure 121.

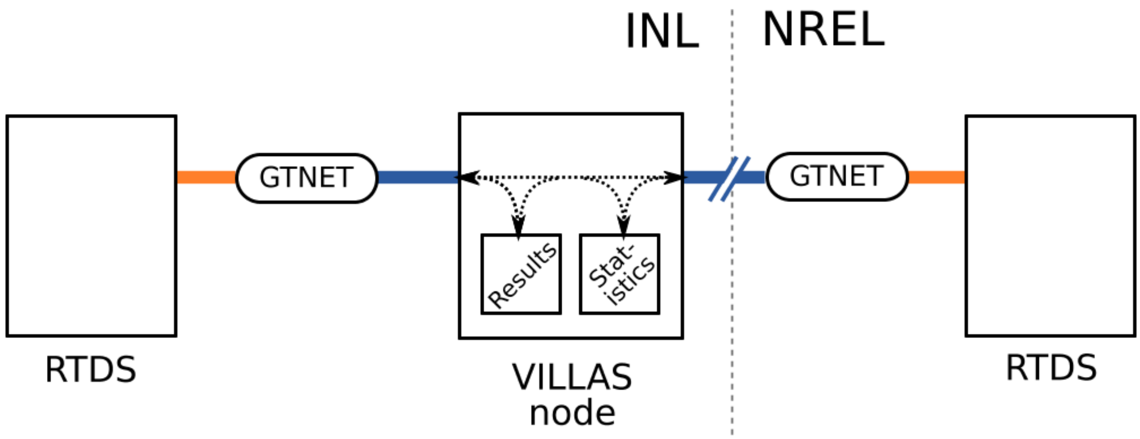

Figure 121. RTDS connectivity between INL and NWTC using the communication cards and the VILLAS framework

10.3 Assessment of the INL-NREL (NWTC) Connectivity

VILLASnode is the main component of VILLAS framework, a set of co-simulation tools developed by the Institute for Automation of Complex Power Systems at RWTH Aachen University and is a publicly available set of tools. VILLASnode is the gateway for interfacing with DRTS locally as well as in geographically disperse locations. Simulation data are exchanged in UDP packets between communication cards of the simulators and the simulation gateway. For bandwidth efficiency, data values are encoded as binary floating-point numbers and supplemented by a small header carrying a time stamp and sequence number which allows filtering for reordered packets. The co-simulation interface quantities including RMS voltage, frequency, and phase are exchanged at a fixed rate of 1,000 packets/sec between the DRTS. This value has been determined empirically to keep network congestion and the associated packet loss to a minimum. Higher rates show an increased probability greater than 1% of packet loss which affects the stability of the simulation. As a result, every twentieth simulation time step triggers the transmission of new interface quantities to the remote site. Beside the interconnection of DRTS, VILLASnode gathers the results and collects the statistics about communication delay, packet loss, and reordering, as well as configures the network emulation. With the given rate of 1,000 packets/sec, several runs of data exchange between the two labs was performed. This is necessary to understand the communication network characteristics prior to approaching the actual distributed RTS. The primary reason for this assessment is to understand the stochasticity of communication latency and then account for its impact on GD RTS.

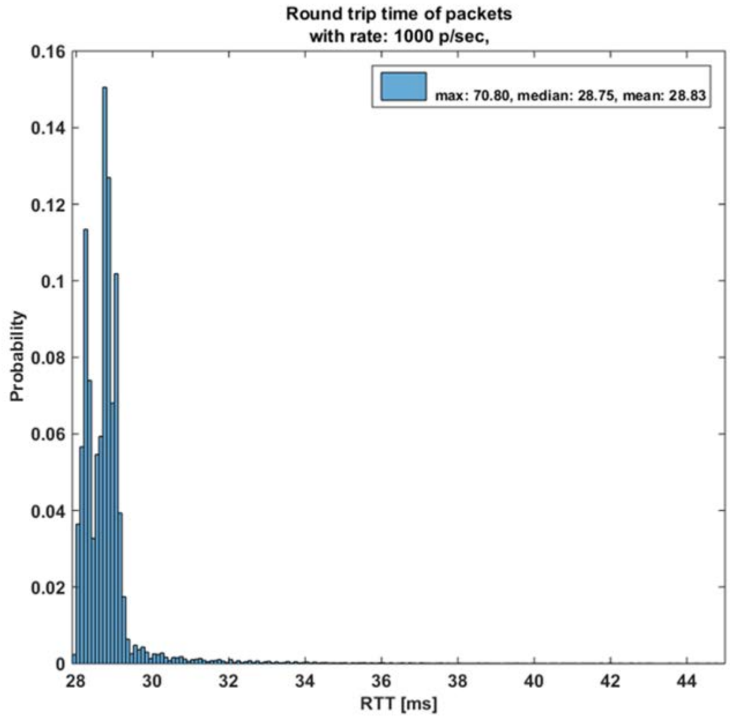

Figure 122. Roundtrip latency statsitics between INL and NREL based on a single-day test

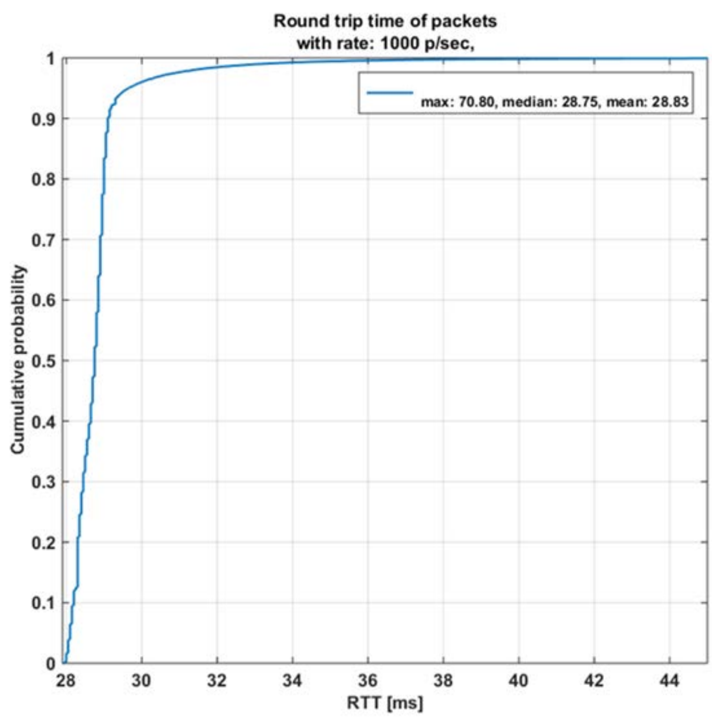

Figure 123. Cumulative probility distribution function for the RTT measurements for roundtrip latency statsitics between INL and NREL based on a single-day test

As observed in Figure 122 and Figure 123, the concept of roundtrip time (RTT) latency can be best described as a stochastic variable and is governed by a stochastic process. Although a secured IP tunnel runs between the labs, there is a nontrivial amount of variabilty and uncertainty for the RTT. The challenge of keeping the distributed DRTS in this case synchronized with a variable RTT is a critical challenge. The team leveraged past work of compensation of RTT stochasticity and still performed a synchronized and accurate GD RTS. The team also has published several manuscripts on the latency mitigation approaches; however, these are slightly out of context to be described in details of this report. As needed, however, such techniques and algorithms have been implemented and adopted. While studying such a critical stochastic process, a communciation simulation environment was created based on the characterized data obtained from several tests. This simulation environment with an acceptable accuracy mimics the communication channel between INL and NREL. Figure 124 shows the integration of RTDS communication cards with the NetEm, performance accuracy is showed in Figure 125 through Figure 127. As it is quite easy to observe, the emulation peformance is very close to actual data and information recorded. This setup within RTPESIL was fundamental to perform several GD RTS simulations prior being executed between the two labs.

For this estimation, a significant number of RTT measurements during an extended period must be collected. For this, three methods have been considered.

1. The Internet Control Message Protocol (ICMP) echo/reply (ping): The ICMP provides an echo request/reply mechanism usually used to test connectivity between two endpoints with the utility. Similar to the first method, the one-way delay is estimated by half the RTT. ICMP echo request/reply messages transport an additional payload which can be used to correlate request and reply packets and track packet loss. ICMP traffic usually is prioritized differently because of its importance as an Internet control protocol and as such does not provide realistic results.
2. TCP (Transmission Control Protocol) 3-way handshake: The RTT measurement techniques require the remote site to loop back packets as soon as they have been received. The TCP 3-way handshake can be used to estimate the RTT by measuring the time between the first sent SYN and the ACK reply of the remote. After these two initial packets have been received, the handshake is aborted.
3. UDP (User Datagram Protocol) loop back: The last method is using the User Datagram Protocol (UDP)and a custom model running on the DRTS which performs the loop back. This model is required as the UDP protocol itself does not send any reply packets by default.

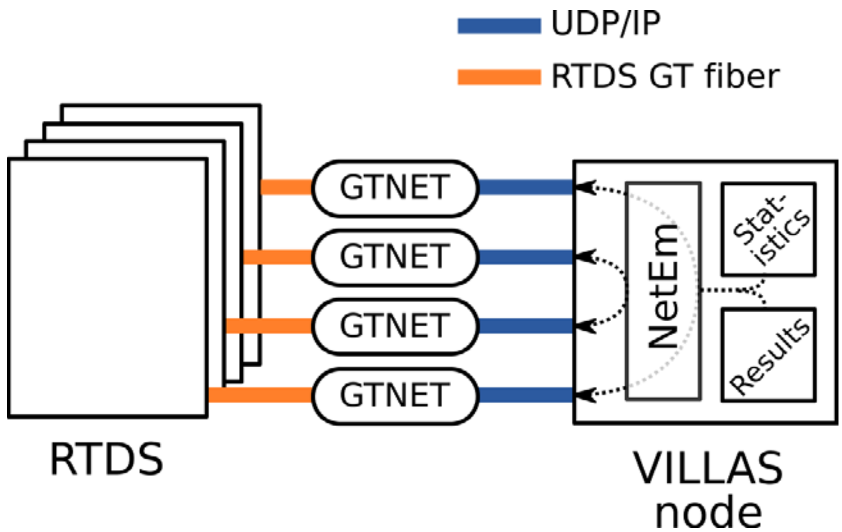

Figure 124. Emulation of the communication network channel between INL and NREL was created using NetEm at the RTPESIL at INL to study GD RTS in greater detail

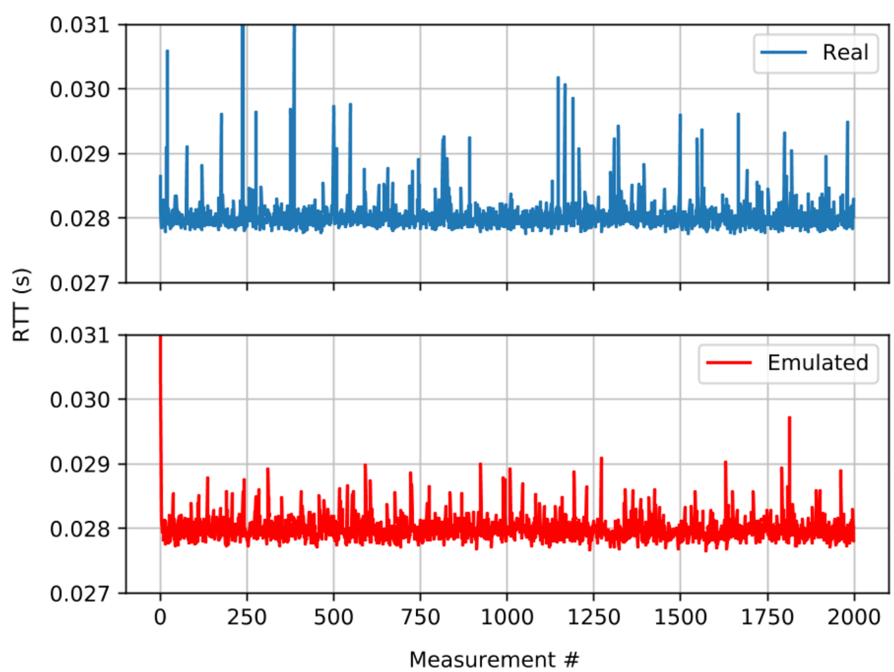

Figure 125. A time series plot of 2,000 sample data packets exchanged

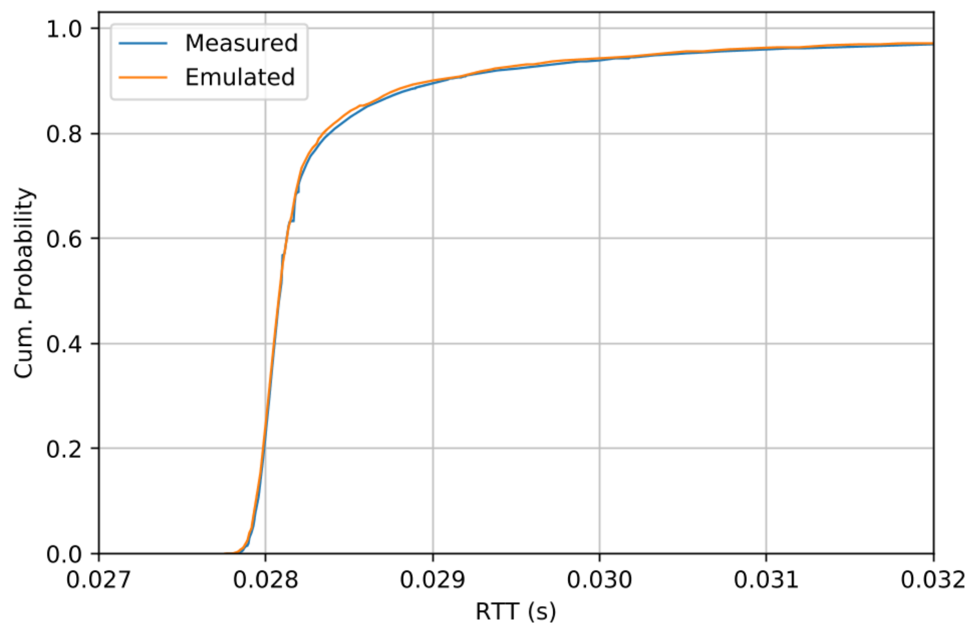

Figure 126. Cumulative probability distribution function of measured and emulated RTT

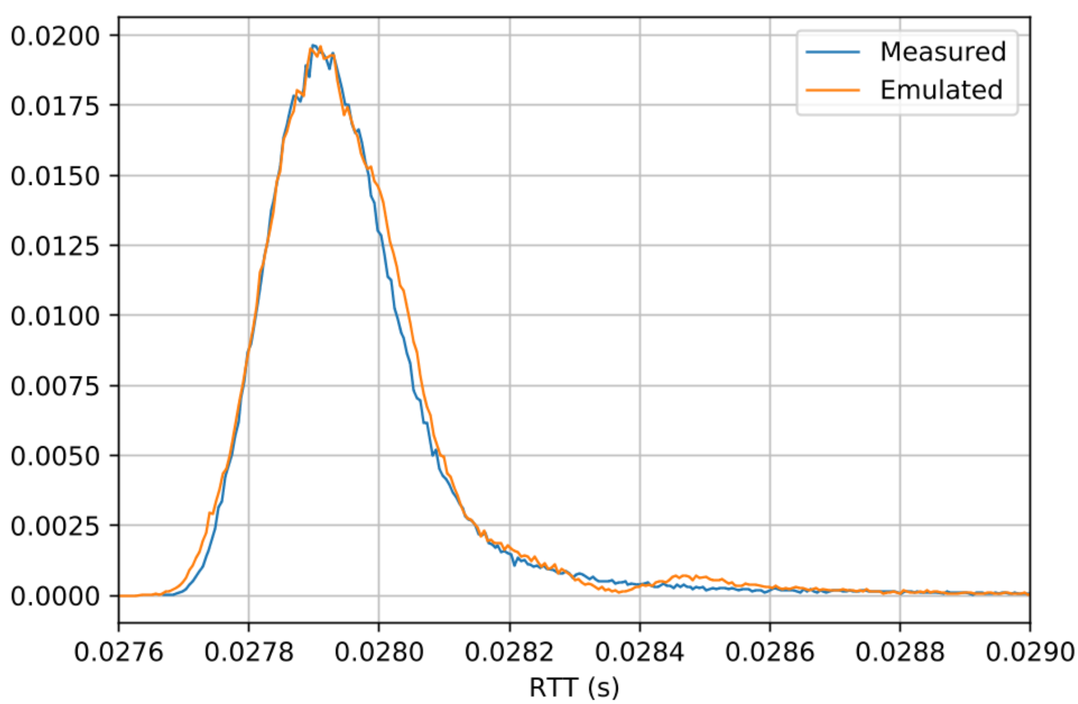

Figure 127. Probability density function of measured and emulated RTT

10.4 Observations

Results show that wired connections have a very low probability of packet loss and reordering ≤1% as long as the network is not congested. Under this assumption, packet loss and reordering are not considered in the following emulation. Under normal conditions, the RTT between INL and NREL is measured to be approximately 28 ms with a relatively small standard deviation of σ = 0.7 ms and a

Spearsman correlation coefficient of ρ = 0.48. For certain periods ≤2 minutes, however, RTT can increase by a factor of 50. It is to be assumed that Deep Packet Inspection (DPI) or Intrusion Detection Systems (IDS) are accountable for these jumps in RTT. Such events of DPI and IDS activation have been removed from the measurements and are not considered here.

10.5 Results and Discussion

A very methodical and systematic approach was developed and adopted for the characterization of the APC in this project. A framework for GD RTS (described elsewhere in this report) was deployed to enhance the computation capability and leverage remote assets and, in this case, also the NWTC wind turbines and CGI. The case study selected for this work is designed for analysis of grid integration of wind energy systems. To this end, the IEEE 14-bus test system is simulated on RTDS at INL, and wind turbine/hardware is simulated as PHIL at NREL. Partitioning of a monolithic model has been performed based on the research focus of each lab. Output power of the wind turbine is scaled appropriately to represent the greater level of wind energy penetration in the transmission system. Scaled output of the wind turbine (referred to as a wind power plant in this approach) is directly adopted from past NREL work. Integration of a wind turbine into the IEEE 14-bus test is realized with a transformer connected to the bus 5. Application of co-simulation IA for the interconnection of the sub-models at INL and NREL.

10.5.1 Unit Testing

The unit testing was associated with the basics of GD RTS that starts with processing of the communication latency, both one- and two-way. Based on the understanding of latency and the NetEm setup, basic analysis of GD RTS and its impacts on sending real-time signals was performed. Boundary-layer conditions including real power, reactive power, frequency, phase, and voltage values are shared. There are several approaches and domains in which these boundary-level conditions can be exchanged for performing GD RTS. Detailed discussions, theory, and criteria of selection for these different approaches are very interesting research fields and require rigorous signal-processing information. The work presented here uses the IA based on RMS, frequency, and phase angle for the controlled voltage source, and current injection based on active and reactive power measurements for the controlled current source. Simplified models are chosen to understand the impact of variable latency on the IA quantities and for understanding the impacts of the communication link.

This work includes the loopback communication tests which include sending a data value from INL to NREL and back to INL using the RTDS communication cards. The total time to perform this loopback task is critical to keeping the two RTDS simulations and the subsystems synchronized to perform accurate GD RTS. The loopback test used in unit testing is shown in Figure 128, and representative results are given in Figure 129. Figure 130 shows the simplified Thevenin approach that enables the study of latency analysis.

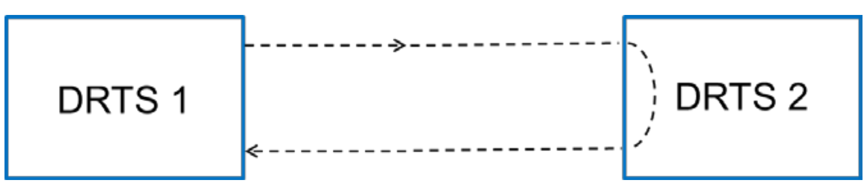

Figure 128. Loopback test setup for computing the RTT values from the RTDS at INL and NWTC

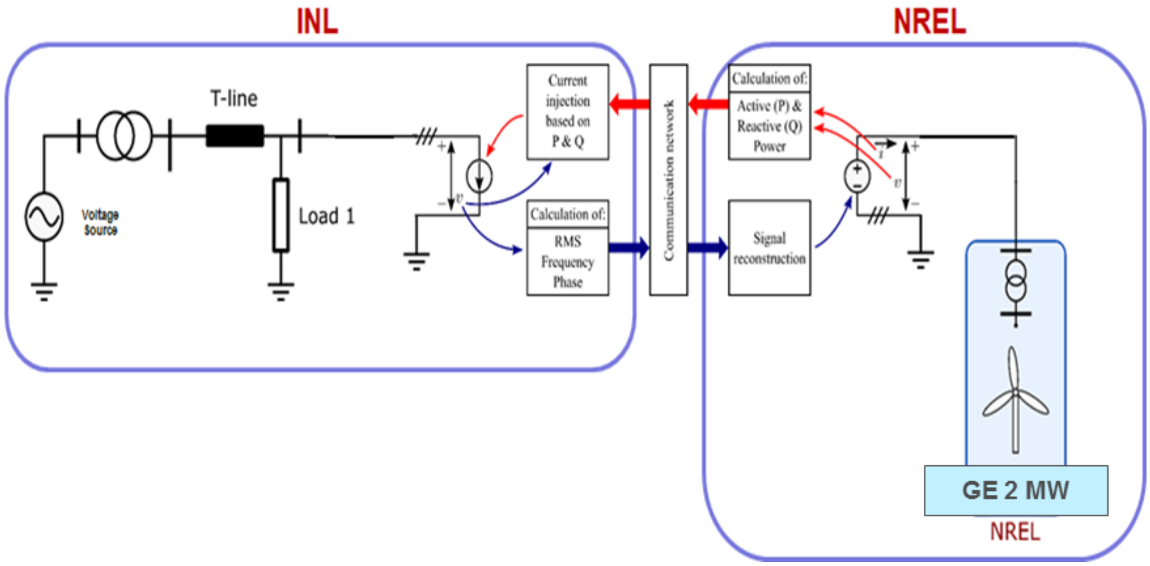

Figure 129. Experimental setup for the performing detailed assessment of impacts of latency on exchange of boundary level conditions on a simplified network

10.5.2 Integrated Testing

The integrated testing is based on a full-blown power systems representation of transmission networks. In this case, the IEEE 14-bus test system and Western Electricity Coordinating Council 9-bus test system was used. For the integrated testing, a wind turbine model at NREL is used along with the controller representation as shown in Figure 130. This provides the first environment to assess the functionalities of the controller to provide frequency regulation. The controller also is replaced by a hardware representation commonly known as controller-hardware-in-the-loop (CHIL).

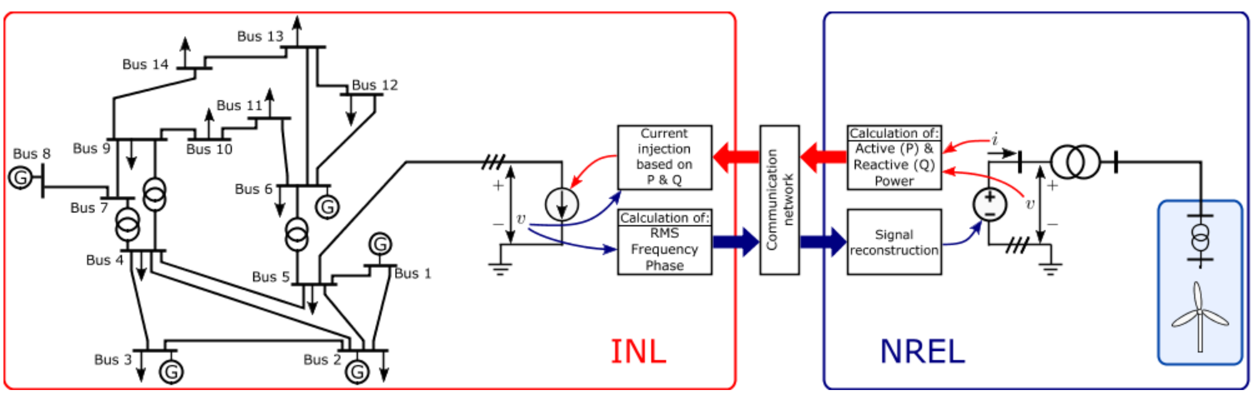

Figure 130. GD RTS setup for performing the integrated testing to enable wind turbine testing and characterization of the APC

10.5.3 Integrated Testing with PHIL

Final integrated testing includes replacing the wind turbine representation using the actual wind turbine at NREL connected through CGI as a power-hardware-in-the-loop (PHIL). This is the full-blown application of the GD RTS to enable the use and characterization of a remote asset under dynamic and transient conditions. The APC capabilities of the controller are tested for both integrated testing and integrated testing with PHIL to provide a very accurate representation of its functionalities. A test plan was created and executed to obtain the final observations and results.

10.5.4 Test Plan for Running Distributed Wind Simulation at INL

The objective of the plan is to develop and test coordinated controls using wind generation by multiple CHIL (hundreds of controller cards) and NREL's wind turbine as PHIL (1.5-MW GE wind turbine and CGI). This plan is used to test and verify the functionality of the distributed WPP simulation to provide grid support.

10.5.4.1 Test Framework

A standard test system (IEEE 9-bus or 4-bus) modeled in RTDS is run as the benchmark power system at INL. Multiple CHILs characterized as a wind turbine (WT) are interfaced with the benchmark power system to emulate the interaction and coordinated control action of individual WTs in a wind power plant. NREL's CGI-connected WT is integrated as a PHIL at INL via an existing inter-lab remote connection. The communication backbone for the integrated power system simulation is based on the VILLASnode framework that establishes the gateway for interconnecting DRTS locally as well as in geographically dispersed locations. Detailed technical steps (discussed in the following sections) are followed to perform characterization and testing under dynamic and transient conditions.

10.5.4.2 Test Scenarios

1. Communications Test: This test ensures the signal exchange between the CHIL bank and RTDS at INL with the PHIL running at NREL. Data from the simulation is measured and analyzed to understand latency along with its impact on real-time simulation.
   a. Start the communication bus on VILLASnode
   b. Initialize the 100 controller cards
   c. Start RTDS power system simulation at INL
   d. Start PHIL simulation at NREL
   e. Synchronize PHIL at NREL with VILLASnode
   f. Operator at RTDS observes the power system for signal exchange
   g. Record and evaluate the measurements
2. Power System Scenarios: In this test, the capability of WT characterized as CHIL and PHIL to provide grid support are verified.
3. Load Imbalance Scenario: This test verifies the fast response time of the CHIL and PHIL to support the power system frequency and voltages by running a step load change (step load add or reduce).
   a. Start the communication bus on VILLASnode
   b. Initialize the 100 controller cards
   c. Start RTDS power system simulation at INL
   d. Start PHIL simulation at NREL
   e. Synchronize PHIL at NREL with VILLASnode

f. Operator at RTDS observes the power system for signal exchange

g. Remove the system load and observe the response from the emulated WPPs

h. Record and evaluate the measurements

i. Add the load in the power system and observe the response from the emulated WPPs

j. Record and evaluate the measurements

4. Generation Loss: In this test, existing generator units in the power system are turned off randomly to simulate a generation loss event caused by fault or planned outage, and the response from the emulated WPPs are recorded and evaluated.

5. Power System Faults: In this test, single phase and three phase faults are injected to introduce disturbance into the benchmark power system and the response from the emulated WPPs is recorded and verified.

6. All results and responses from NWTC's WT and CHIL representation of WT are recorded and analyzed to study the impact of WPP for grid support.

10.5.5 Discussion

As described above, the distributed INL-NREL setup is used here for assessing the frequency support of a wind energy system following a contingency event based on the test plan described above. First, RTS is performed under deterministic conditions of data exchange between DRTS units. Figure 131 shows frequency response at bus 5 of a reference transmission system following the loss of a generator. Bus 5 represents the PCC of WPP, as illustrated in Figure 132.

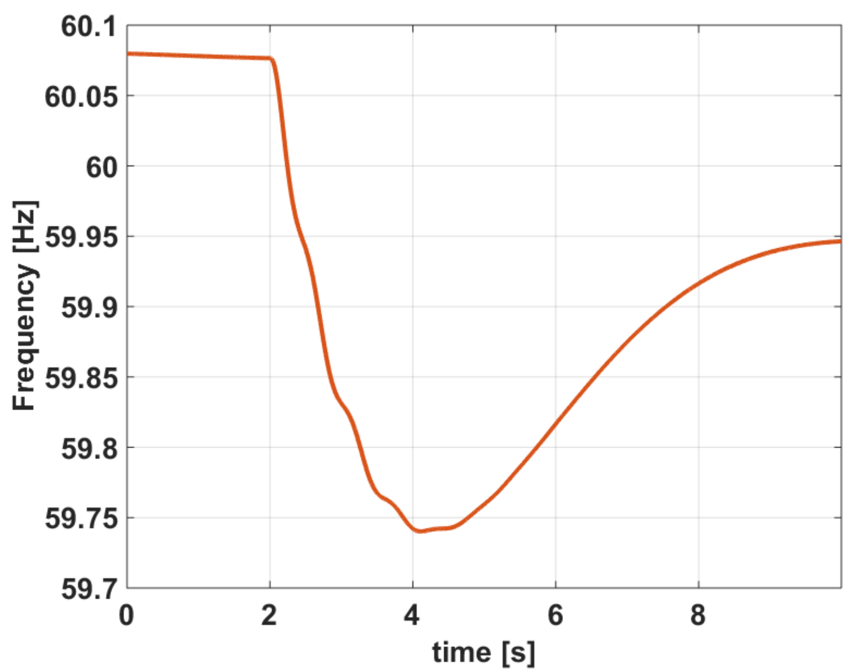

Figure 131. Frequency response obtained from WPP as a whole to a grid event

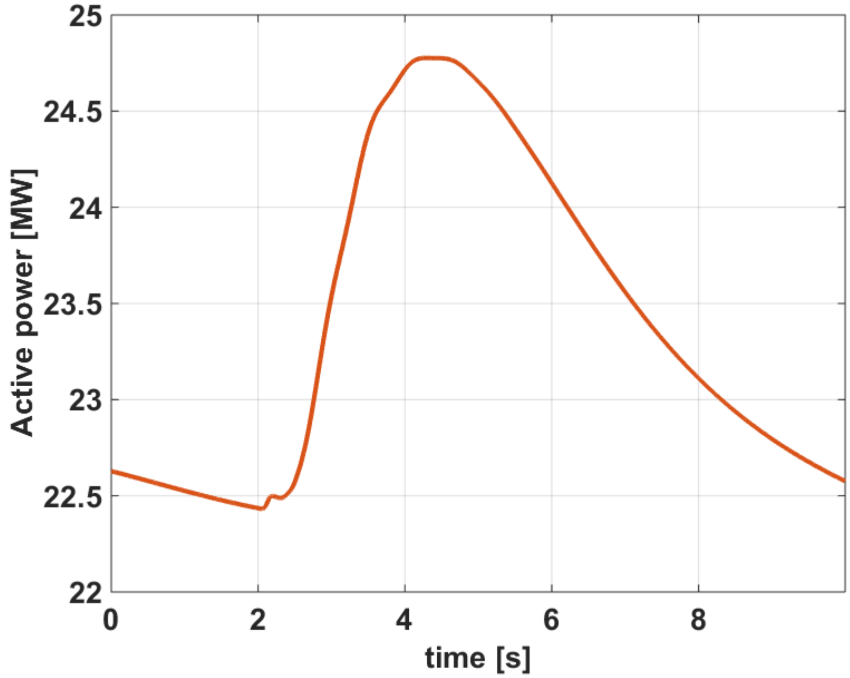

Figure 132. Active power response provided by the WPP to a grid event

One thousand simulations are performed with the setup described in this section. We chose to analyze the uncertainty for t = 3.0 seconds to account for the frequency decrease and for t = 4.35 seconds to analyze one of the lowest values in frequency response. Figure 133 shows histograms with empirical probability density functions of frequency for t = 3.0 seconds and t = 4.35 seconds. The resulting uncertainty is relatively small for both cases considering the dynamics of overall frequency response, where frequency decreased for more than σ_1 = 0.25 Hz. Namely, the main characteristics of uncertainty at t = 3.0 seconds are μ_1 = 59.85 Hz and σ_1 = 0.0007 Hz. Standard deviation of the same order is observed for uncertainty at t = 4.35 seconds, that is σ_1 = 0.0006 Hz and μ_1 = 59.75 Hz. Histograms with empirical probability density of active power of WPP for t = 3.0 seconds and t = 4.35 seconds are illustrated in Figure 134. It is observed that standard deviations of uncertainty at t =3.0 seconds and at t = 4.35 seconds are relatively small with respect to the transient of the variable of interest. Mean value and standard deviation characterizing uncertainty at t = 3.0 seconds are μ_1 = 22.75 MW and σ_1 = 0.0581 MW, and for t = 4.35 seconds the parameters are μ_2 = 24.36 MW and σ_2 = 0.0644 MW. One result from the several thousand runs is shown in Figure 135 and Figure 136 with the performance characterization of APC.

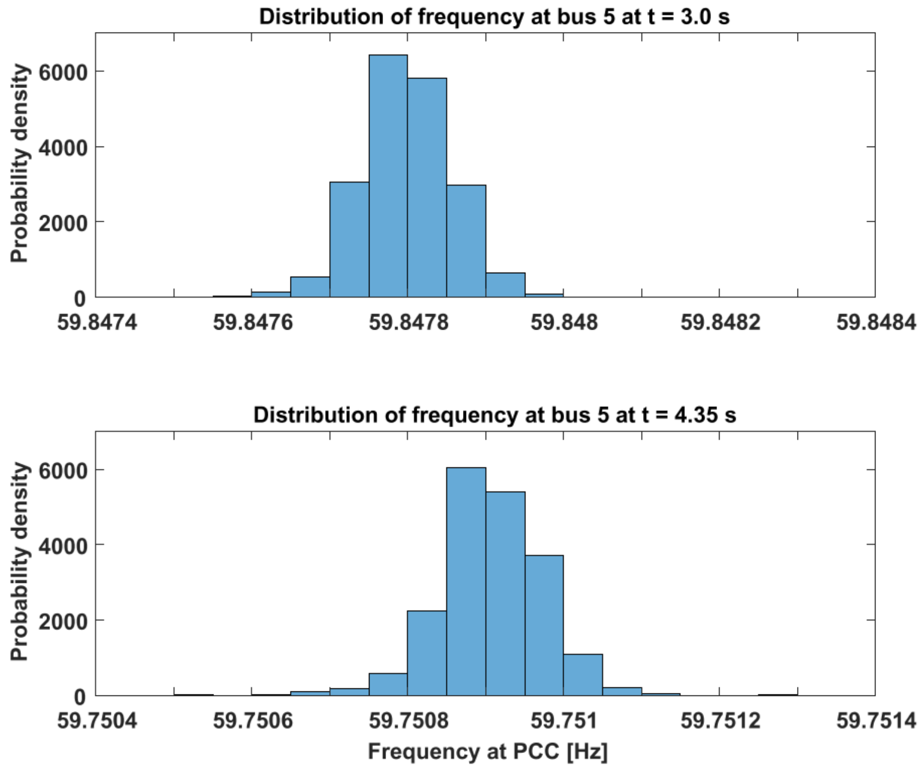

Figure 133. Frequency variation of the 1,000 runs performed to obtain a variation and impact analysis of data latency in GD RTS

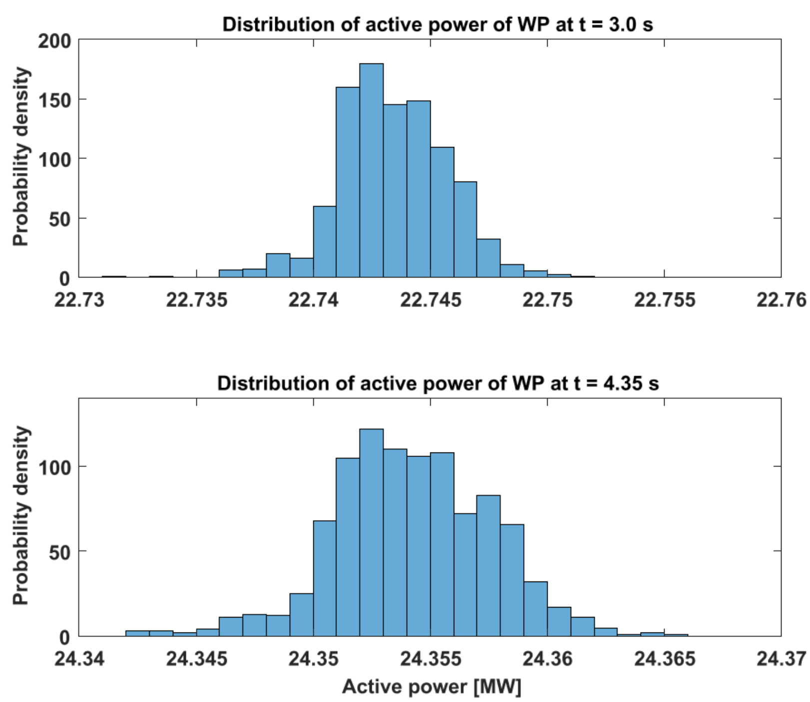

Figure 134. Power variation of the 1,000 runs performed to obtain a variation and impact analysis of data latency in GD RTS

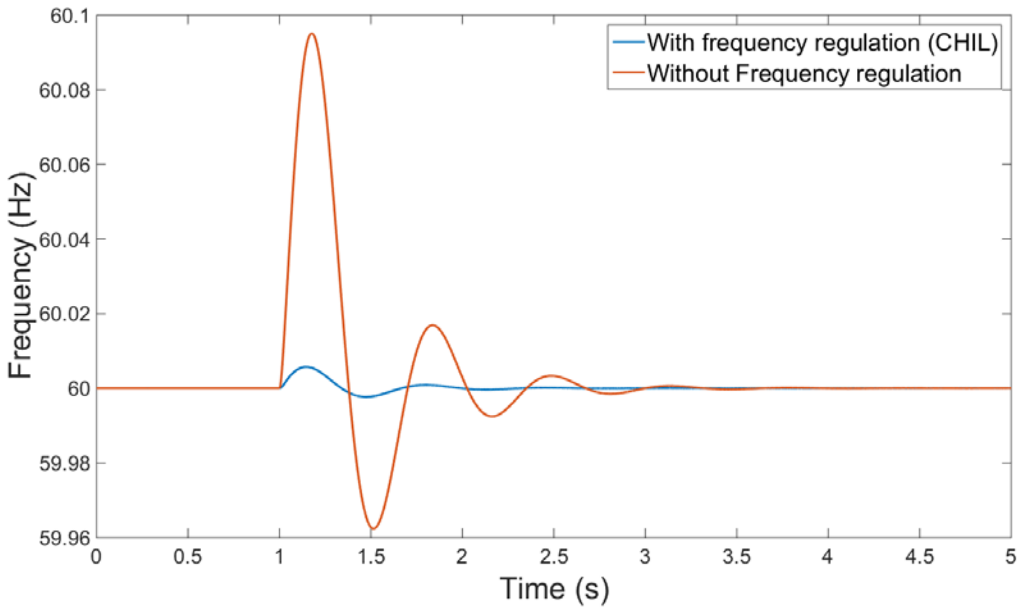

Figure 135. CHIL-based integrated wind turbine model providing frequency support when there is a sudden change in system load (90 MW to 0.1 MW) and response of the wind turbine

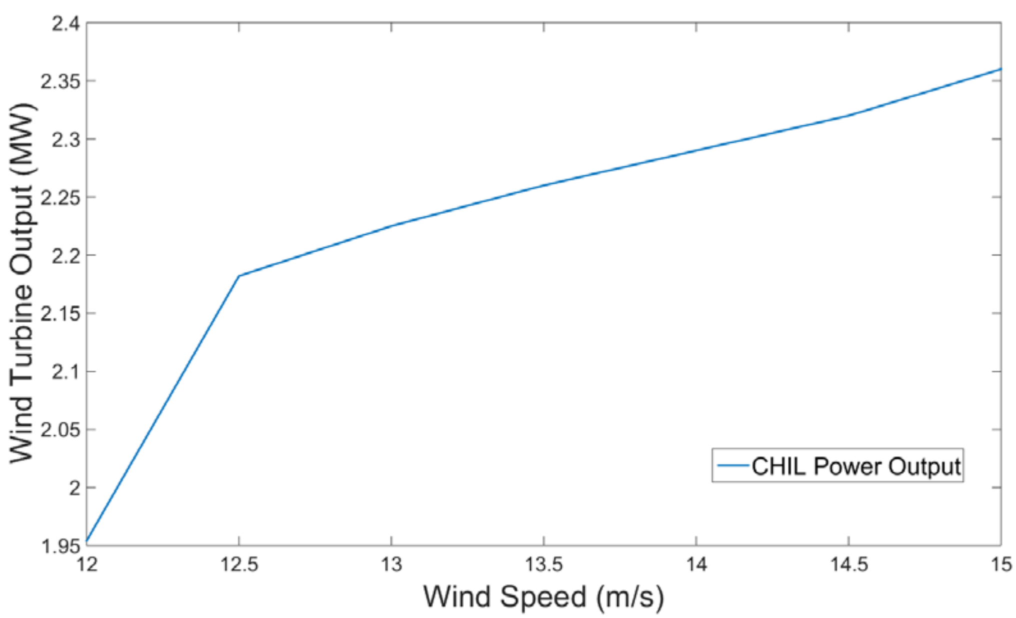

Figure 136. CHIL-based integrated wind turbine providing frequency support and its response to a grid event

11. Conclusions

Simulations and field tests using wind turbines with BESS, VFDs, and PV coupled with advanced controls showed that wind power inertial and primary responses and AGC participation can be significantly enhanced with the assistance of these technologies. Power system dynamics studies show that wind generally can improve the reliability of the power system when providing primary frequency and synthetic inertial control. Coordinated control with other technologies allows notable improvements in system reliability in terms of frequency response. Control simulations show that providing these responses has a negligible effect on the structural loading of WTGs.

In particular, it was demonstrated that the symbiosis of frequency-responsive technologies can notably improve the frequency performance of power systems. In particular, wind, storage, and pumping stations can provide a significant amount of synthetic frequency response to power systems. These technologies have been furnished with control loops that respond in proportion to the ROCOF; hence, these assets can reliably emulate the inertial response of synchronous machines to frequency events. To compensate for the power changes that wind turbines can introduce when losing optimality after providing synthetic inertia, pumping stations are proposed to be furnished with droop-like frequency control strategies. This control strategy in addition to a synthetic inertia control loop, imply that pumped flow will be impacted momentarily, which might not be problematic—for example, for irrigation subsystems.

In this work, the control constants that determine the synthetic inertia response for the considered assets originate from rational choices only. A rigorous framework to tune these constants—for example, as a function of displaced synchronous inertia—is a future research direction. A possible course could be to rely on system identification theory, because control constants could be identified to match a desired frequency trajectory in time. Another possibility is to rely on optimal control to minimize the perturbed pumped flow in pumping stations and changes of the performance coefficient in wind turbines and maintain the power system frequency within desirable bounds. Another line of research pertains to ascertaining whether a particular penetration of wind, pumping, and battery capacity could be appropriate to compensate for the displaced synchronous inertia. In particular, it could be useful to elucidate the capability of these assets to replace synchronous inertia in a one-to-one manner.

We also demonstrated a use of a new impedance-based noninvasive approach for the characterization of frequency response of a power system in real-time in the absence of a transient event. It showed that the transfer function from the active power injected at the POI to the frequency at the same bus can be used to characterize the power system frequency response and estimate system inertia, PFR, and the speed of the primary frequency control. The method essentially performs the fundamental frequency response adequacy evaluation in real time—a capability that never before has existed within the energy industry. We also showed how the frequency response function is related with the network impedance. Such a relationship can support the development of grid-friendly controls for inverters and simultaneously optimize the inverter behavior for resonance or stability and frequency adequacy. Future work will use the proposed frequency response function for the frequency support control design using the BESS and renewable generation. An equivalent approach for the characterization of the voltage response of a power system also will be developed.

The following control features for a dispatchable renewable plant have been developed and successfully implemented during this project

- Dispatchable renewable plant operation (ability to operate at active and reactive power external set points received from system operator)
- Ramp limiting, variability smoothing, cloud-impact mitigation
- Provision of spinning reserve

- AGC functionality
- PFR (programmable droop control)
- Fast frequency response (FFR)
- Inertial response (programmable synthetic inertia for a wide range of H constants emulated by BESS)
- Reactive power and voltage control
- Advanced controls (the ability of the plant to modulate its output for the provision of power system oscillations damping services was tested)
- Stacked services (ability to provide several services at the same time)
- Battery SOC management controls

Additionally, new unique testing concepts and capabilities were developed at the NWTC during the course of this project, including a test bed for PMU-based wide-area controls validation and a novel method for impedance characterization of converter-coupled generation using CGI.

The research under this project will continue through FY 2019 with the expectation to produce more interesting results and concept-validation activities.

References

1. E. Ela, V. Gevorgian, P. Fleming, Y. Zhang et al., *Active Power Controls from Wind Power: Bridging the Gaps,* NREL Technical Report (Golden, CO, January 2014).
2. A. Monti et al., "A Global Real-Time Superlab: Enabling High Penetration of Power Electronics in the Electric Grid," *IEEE Power Electronics Magazine* 5, no. 3 (September 2018): 35–44.
3. P. Sullivan, W. Cole, N. Blair, and E. Lantz, *2015 Standard Scenarios Annual Report: U.S. Electric Sector Scenario Exploration* (NREL/TP-6A20-64072), NREL Technical Report (Golden, CO, July 2015).
4. North American Electric Reliability Corporation, *2013 Special Reliability Assessment: Maintaining Bulk Power System Reliability While Integrating Variable Energy Resources* (Washington, DC, November 2013).
5. International Electrotechnical Commission, IEC 61400-21, Edition 2, *Measurement and Assessment of Power Quality Characteristics of Grid-Connected Wind Turbines* (2008).
6. V. Gevorgian, R. Wallen, and M. McDade, *NREL Controllable Grid Interface for Testing of Renewable Energy Technologies* (paper presented at the 3rd International Workshop on Grid Simulator Testing, Tallahassee, TN, November 2015).
7. L. Zeni, P. E. Sorensen, A. D. Hansen, B. Hesselbaek, and P. C. Kjaer, *Power System Integration of VSC-HVDC Connected Offshore Wind Power Plants* (Kongens Lyngby, Denmark: Technical University of Denmark/DONG Energy, July 2015).
8. L. Zeni, V. Gevorgian, R. Wallen, J. Bech, P. E. Sorensen, and B. Hesselbaek, "Utilization of Real-Scale Renewable Energy Test Facility for Validation of Generic Wind Turbine and Wind Power Plant Controller Models," *IET Renewable Power Generation* (May 2016).
9. E. Muljadi and V. Gevorgian, *Short-Circuit Modeling of a Wind Power Plant* (paper presented at the 2011 IEEE PES GM, Detroit, MI, July 24–28, 2011).
10. W. Ren, M. Steurer, and T. L. Baldwin, "Improve the Stability and the Accuracy of Power Hardware-in-the-Loop Simulation by Selecting Appropriate Interface Algorithms," *IEEE Transactions on Industry Applications* 44, no. 4 (2008): 1286–1294.
11. N. Ainsworth, A. Hariri, K. Prabakar, A. Pratt, and M. Baggu, *Modeling and Compensation Design for a Power Hardware-in-the-Loop Simulation of an AC Distribution System*, 2016 North American Power Symposium (NAPS): 1–6.
12. F. Huerta, R. L. Tello, and M. Prodanovic, "Real-Time Power Hardware-in-the-Loop Implementation of Variable-Speed Wind Turbines," *IEEE Transactions on Industrial Electronics* (2017): 1893–1904.
13. North American Electric Reliability Corporation (NERC), *[Draft] Reliability Guideline: BPS-Connected Inverter-Based Resource Performance* (Atlanta, GA: NERC Technical Report, May 2018).
14. A. J. Wood, B. F. Wollenberg, and G. Sheblé, *Power Generation, Operation, and Control 3rd ed.* (New York: Wiley, 2013).

15. P. Anderson and M. Mirheydar, "A Low-Order System Frequency Response Model," *IEEE Trans. Power Syst.* 5 (August 1990): 720–729.

16. P. W. Sauer and M. A. Pai, *Power System Dynamics and Stability* (Champaign, IL: Stipes Publishing L.L.C., 2006).

17. P. Kundur, J. Paserba, V. Ajjarapu, G. Andersson, A. Bose, C. Canizares, N. Hatziargyriou, D. Hill, A. Stankovic, C. Taylor, T. Van Cutsem, and V. Vittal, "Definition aand Classification of Power System Stability IEEE/CIGRE Joint Task Force on Stability Terms and Definitions," *IEEE Trans. Power Syst.* 19, no. 3 (August 2004): 1387–1401.

18. North American Electric Reliability Corporation (NERC)/ Western Electricity Coordinating Council (WECC) Inverter Task Force, *1200 MW Fault Induced Solar Photovoltaic Resource Interruption Disturbance Report: Southern California 8/16/2016 Event* (Atlanta, GA: NERC, June 2017).

19. NERC/WECC, *900 MW Fault Induced Solar Photovoltaic Resource Interruption Disturbance* (Atlanta, GA: NERC, February 2018).

20. AEMO, *Black System South Australia: 28 September 2016* (Australia: Australian Energy Market Operator Ltd., 2017).

21. NERC, *State of Reliability 2018* (Atlanta, GA: North American Electric Reliability Corporation, June 2018).

22. B. Kroposki et al., "Achieving a 100% Renewable Grid: Operating Electric Power Systems with Extremely High Levels of Variable Renewable Energy," *IEEE Power Energy Mag.* 15, no. 2 (March-April 2017): 61–73.

23. D. Yang, J. Kim, Y. C. Kang, E. Muljadi, N. Zhang, J. Hong, S.-H. Song, and T. Zheng, "Temporary Frequency Support of a DFIG for High Wind Power Penetration," *IEEE Trans. Power Syst.* 33, no. 3 (May 2018): 3428–3437.

24. M. Kayikçi and J. V. Milanović, "Dynamic Contribution of DFIG-Based Wind Plants to System Frequency Disturbances," *IEEE Trans. Power Syst.* 24, no. 2 (May 2009): 859–867.

25. M. A. Pelletier, M. E. Phethean, and S. Nutt, *Grid Code Requirements for Artificial Inertia Control Systems in the New Zealand Power System* (IEEE Power and Energy Society General Meeting, San Diego, CA, July 2012).

26. J. O'Sullivan, A. Rogers, D. Flynn, P. Smith, A. Mullane, and M. O'Malley, "Studying the Maximum Instantaneous Non-Synchronous Generation in an Island System—Frequency Stability Challenges in Ireland," *IEEE Trans. Power Syst.* 29, no. 6 (November 2014): 2943–2951.

27. R. Eriksson, N. Modig, and K. Elkington, "Synthetic Inertia Versus Fast Frequency Response: A Definition," *IET Renewable Power Generation* 15, no. 5 (September 2018): 507–514.

28. Y. Bian et al., "Demand Side Contributions for System Inertia in the GB Power System," *IEEE Trans. Power Syst.* 33, no. 4 (July 2018): 3521–3530.

29. K. Aström and T. Hagglünd, *PID Controllers, Theory, Design, and Tuning*, *2nd ed.* (The Instrumentation, Systems, and Automation Society, 1994).

30. S. Skogestad and I. Postlethwaite, *Multivariable Feedback Control*, *2nd ed.* (Chichester, UK: John Wiley & Sons, 2007).

31. J. Ma, Z. Song, Z. Song, Y. Shen, and J. S. Thorp, “Model Order Reduction Analysis of DFIG Integration on the Power System Small-Signal Stability Considering the Virtual Inertia Control,” *IET Generation, Transmission & Distribution* 11, no. 16 (November 2017): 4087–4095.
32. IEEE Power & Energy Society, *Dynamic Models for Turbine-Governors in Power System Studies* (Tech. Rep. PES-TR1, January 2013).
33. P. Kundur, “Power System Stability and Control,” *The EPRI Power System Engineering*, ed. N. J. Balu and M. G. Lauby (Palo Alto, CA: McGraw-Hill, Inc., 1994).
34. S. Heier, *Grid Integration of Wind Energy, 3rd ed.* (United Kingdom: Wiley, 2014).
35. R. Guttromson, J. White, J. Berg, F. Wilches-Bernal, C. Hansen, J. Paquette, and I. Gravagne, *Use of Wind Turbine Kinetic Energy to Supply Transmission Level Services,* Tech. Rep. SAND2018-772151 (Albuquerque, NM: Sandia National Laboratories, February 2018).
36. B. Shen, B. Mwinyiwiwa, Y. Zhang, and B.-T. Ooi, “Sensorless Maximum Power Point Tracking of Wind by DFIG Using Rotor Position Phase Lock Loop (PLL),” *IEEE Trans. Power Electron.* 24 (4) (April 2009): 942–951.
37. L. Tian, W. Zhu, W. Shen, N. Zhao, and Z. Shen, “Development and Validation of a New Two-Dimensional Wake Model for Wind Turbine Wakes,” *J. Wind Eng. Ind. Aerodyn.* 15 (February 2015): 90–99.
38. M. H. Johnson and D. C. Aliprantis, “Analysis of Series-DC Offshore Wind Plants with Aerodynamic Wake Effects,” *IEEE Trans. Sustain. Energ* 8, no. 4 (October 2017): 1706–1714.
39. “Centrifugal Pump,” MathWorks, https://www.mathworks.com/help/physmod/hydro/ref/centrifugalpump.html (August 2018).
40. M. Schimpe et al., “Energy Efficiency Evaluation of a Stationary Lithium-Ion Battery Container Storage System via Electro-Thermal Modeling and Detailed Component Analysis,” *Applied Energy* 210, no. 15 (January 2018): 211–229.
41. Western Electricity Coordinating Council, *State of Interconnection Digest* (Tech. Rep.) (2017–2018).
42. J. Morren and S. W. H. de Haan, “Short-Circuit Current of Wind Turbines with Doubly Fed Induction Generator,” *IEEE Trans. Energy Convers.* 20 (June 2005).
43. A. McKane, I. Rhyne, A. Lekov, L. Thompson, and M. A. Piette, “Automating Demand Response: The Missing Link in the Electricity Value Chain.” In the *Proceedings of the 2008 ACEEE Summer Study on Energy Efficiency in Buildings, Pacific Grove, CA, August 17–22, 2008*, LBNL-2736E (August 2008).
44. L. Thompson, A. Lekov, A. McKane, and M. A. Piette, “Study Examines Automated Demand Response in Wastewater Facilities,” *Water World* 27, no. 3 (2016).
45. V. M. Zavala, D. Celinski, P. Dickinson, *Techno-Economic Evaluation of a Next-Generation Building Energy Management System*, Technical Report ANL/MCS-TM-313 (Argonne National Laboratory, 2011).
46. Y. M. Lee, R. Horesh, and Leo Liberti, “Optimal HVAC Control as Demand Response with On-Site Energy Storage and Generation System,” *ELSEVIER Energy Proceedings,* 78 (November 2015): 2106–2111.

47. “Siemens Answers with a List of Drives Capable of Power Regeneration,” http://www.industry.usa.siemens.com/drives

48. B. Kroposki, B. Johnson, Y. Zhang, V. Gevorgian, et. al. “Achieving 100% Renewable Grid,” *IEEE Power and Energy Magazine* (March/April 2017).

49. F. Daz-Gonzlez, A. Sumper, O. Gomis-Bellmunt, and R. Villaffila-Robles, “A Review of Energy Storage Technologies for Wind Power Applications,” *Renewable and Sustainable Energy Reviews,* 16, no. 4 (2012): 2154–2171.

50. Federal Enegy Regulatory Commission, *BAL-003-1—Frequency* Response and *Frequency Bias Setting* (Washington, DC, March 2013).

51. *NERC 2017 Frequency Response Annual Analysis Report*, www.nerc.com

52. I. P. Grisang, J. Dhupia, M. Sigh, & V. Gevorgian, “Impacts of Providing Inertial Response on Dynamic Loads of Wind Turbine Drivetrains” (presented at IEEE ECC, Pittsburgh, PA, September 11–14, 2014).

53. J. Keller, S. Lambert*, Gearbox Instrumentation for the Investigation of Bearing Axial Cracking,* NREL technical report (March 2018).

54. North American Electric Reliability Corporation (NERC)*, Balancing and Frequency Control* (Technical Report) (Atlanta, GA: January 2011).

55. Federal Energy Regulatory Commission (FERC), “Large Generator Interconnection Agreement,” www.ferc.gov/industries/electric/indus-act/gi/stnd-gen.asp.

56. Federal Energy Regulatory Commission (FERC) Order 661-A, https://www.ferc.gov/CalendarFiles/20051212171744-RM05-4-001.pdf (accessed June 23, 2019).

57. Federal Energy Regulatory Commission (FERC), *Order 827: Reactive Power Requirements for Non-Synchronous Generation* (June 2016).

58. CAISO, *Reactive Power and Financial Compensation: Draft Final Proposal* (Folsom, CA: November 2015).

59. V. Gevorgian, Y. Zhang, and E. Ela, “Investigating the Impacts of Wind Generation Participation in Interconnection Frequency Response,” *IEEE Transactions on Sustainable Energy* 6, no. 3 (July 2015)

60. North American Electric Reliability Corporation (NERC), “State of Reliability” (Atlanta, GA, June 2018).

61. J. W. Ingleson and D. M. Ellis, “Tracking the Eastern Interconnection Frequency Governing Characteristics,” in *Proceedings 2005 IEEE Power Eng.Soc. General Meeting* (San Francisco, CA, June 2005).

62. P. M. Ashton et al., “Inertia Estimation of the GB Power System Using Synchrophasor Measurements,” *IEEE Trans. Power Syst.* 30, no. 2 (March 2015): 701–709.

63. F. Wilches-Bernal, J. H. Chow, and J. J. Sanchez-Gasca, “A Fundamental Study of Applying Wind Turbines for Power System Frequency Support,” *IEEE Trans. Power Syst.*. 31, no. 2 (Mar. 2016): 1496–1505.

64. J. Undrill, "Primary Frequency Response and Control of Power System Frequency," (Lawrence Berkeley National Laboratory, CA, Rep. LBNL-2001105, February 2018).

65. J. Sun, M. Li, Z. Zhang, T. Xu, J. He, H. Wang, and G. Li, "Renewable Energy Transmission by HVDC Across the Continent: System Challenges and Opportunities," *CSEE J. Power and Energy Syst.* 3, no. 4 (December 2017): 353–364.

66. S. Shah, "Small and Large Signal Impedance Modeling for Stability Analysis of Grid-Connected Voltage Source Converters" (Ph.D. dissertation, Dept. of Elect. Comput. Syst. Eng., Rensselaer Polytechnic Institute, Troy, NY, 2018).

67. *Emergence of Hybrid Renewable Energy Systems*, QVARTZ white paper (February 2016).

68. R. de Azevedo and O. Mohammed, *"Profit*-Maximizing Utility-Scale Hybrid Wind-PV Farm Modeling and Optimization" (conference paper, IEEE Southeast Con 2015, Fort Lauderdale, FL, April 2015).

69. F. Bizzarri, "Combining Solar PV Plants and Wind Farms" (IEA Technology Roadmaps for Solar Electricity Workshop, February 2014).

70. B. Jervey, "Wind and Solar Are Better Together," *Scientific American* (December 2016).

71. D. Ludwig, "Solar-Wind Power Plants Approximately Twice As Efficient," *PV Magazine* (April 2013).

72. T. Woody, "California's New Solar-Wind Hybrid Power Plant Greens the Grid," *Forbes* (November 2012).

73. F. Jossi," Nation's First Integrated Wind and Solar Project Takes Shape in Minnesota," *Midwest Energy News* (March 2017).

74. T. Kenning, "Construction Imminent on Major Solar-Wind-Storage Hybrid Plant in Queensland," *PVTECH Magazine* (Deccember 11, 2017).

75. B. D. Lopez, "Brazil Assesses Potential of Hybrid Solar-Wind Power Plants," *PV Magazine* (May 1, 2017).

76. M. Cuff, "Vattenfall Starts Work on UK Hybrid Wind Solar Farm," *The Guardian Solar Power* (January 2016).

77. "Haiti to Build Hybrid Solar-Wind Power Plant," *CREF Market News* (August 2017).

78. J. Zayas et al., *Enabling Wind Power Nationwide* (U.S. Department of Energy technical report, May 20, 2015).

79. L. Zeni, V. Gevorgian et al., "Utilization of Real-Scale Renewable Energy Test Facitlity for Validation of Generic Wind Turbine and Wind Power Plant Controller Models," *IET Renewable Power Generation* (2016).

GRID
MODERNIZATION
LABORATORY
CONSORTIUM
U.S. Department of Energy

http://gridmodernization.labworks.org/